# Assessing the correlation of Aviation Nitrogen Oxides and Ozone with respect to Specific Weather Patterns

*MSc. Thesis Report*

Kinanthi Sutopo 4227069

Aerospace Enginering
MSc. thesis

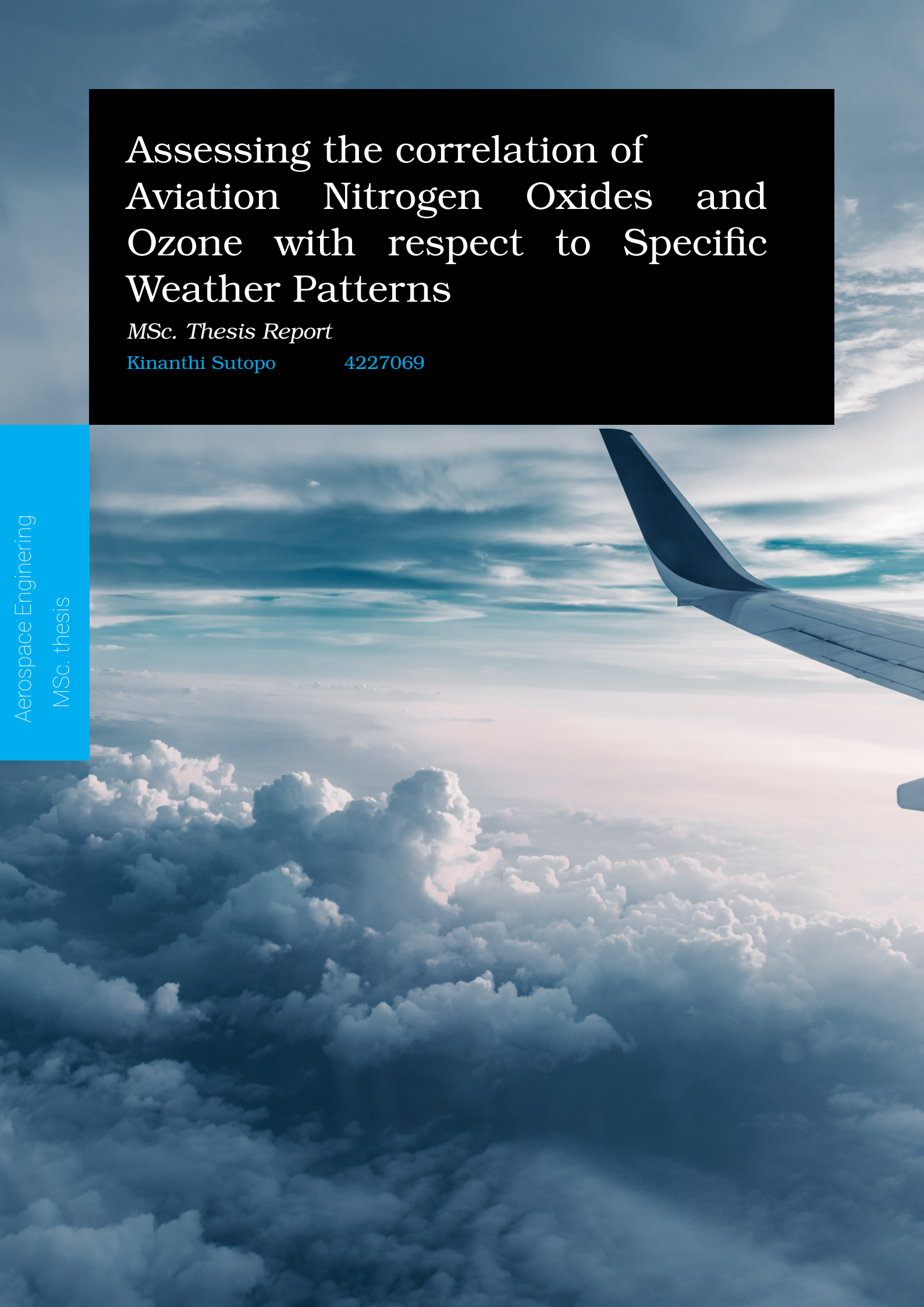

# Final MSc. Thesis Report

**by**

N.D.K. Sutopo 4227069

**Supervisor**

TU Delft and DLR: Prof. dr. Volker Grewe

**Thesis Committee**

| | | |
|---|---|---|
| Chair of the committee: | Prof. dr. V. Grewe | TU Delft (C&O, ANCE), DLR |
| | Dr. I.C. Dedoussi | TU Delft (C&O, ANCE) |
| | Dr. V. Dhanisetty | TU Delft (C&O, ATO) |
| | ir. P. Roling | TU Delft (C&O, ATO) |

*Front page figure:* Courtesy of https://unsplash.com

TU Delft Delft University of Technology

# Preface

This Master thesis is written to obtain my master's degree in Aerospace Engineering at the Delft University of Technology. As a student in the track of Air Transport and Operations I felt a growing interest and concern in the climate effects of aviation which resulted in performing a Master's thesis at the track of Aircraft Noise and Climate Effects. This thesis focuses on the correlation between ozone production and aviation $NO_x$ emissions in the atmosphere, with respect to specific weather patterns. Finding this correlation could aid in better understanding the behaviour of aviation $NO_x$ in the atmosphere and the produced ozone that results from these emissions. As these emissions and its produced ozone are large contributors to the climate effects of aviation, contributing to the research of climate effects of aviation through this thesis has been a large motivator for me.

I would like to express my gratitude towards Professor Grewe for his supervision throughout this thesis. It was an honour to work with him and learn from him. Furthermore, I would like to thank Lisette for her intensive help to organise everything needed throughout my thesis and for helping me carry around my stuff when I was walking around on crutches. Thank you to my thesis buddies and friends who have always listened to my complaints and who have shared coffee breaks with me, or went off to do sports with me to blow off some steam. A large gratitude goes out to my parents and my brother, who have always supported me and provided a warm home for me to come home to. Lastly, my thanks go out to my boyfriend who has supported me incredibly much. From mental support to challenging discussions, thanks for always being there and being the one I can always count on.

*N.D.K. Sutopo,*
*Delft, October 2019*

# Contents

# List of Figures

# List of Tables

# List of Abbreviations

| | |
|---|---|
| $T_{dry}$ | Dry air temperature |
| $q$ | Specific humidity |
| $q_*$ | Saturation-specific humidity |
| **BMIL** | Base Model Interface Layer |
| **BML** | Base Model Layer |
| **CTM** | Chemistry Climate Model |
| **DJF** | December, January, February |
| **DKRZ** | German Climate Cooperation Center |
| **DLR** | German Aerospace Center |
| **ECHAM5** | General circulation model developed by the Max Planck Institute |
| **ECMWF** | European Centre for Medium-range Weather Forceast |
| **EMAC** | ECHAM/MESSy Atmospheric Chemistry |
| **GCM** | General Circulation Model |
| **GTP** | Global Temperature change Potential |
| **GWP** | Global Warming Potential |
| **JJA** | June, July, August |
| **MECCA** | Module Efficiently Calculating the Chemistry of the Atmosphere |
| **MESSy** | Modular Earth Submodel System |
| **NH** | Northern hemispheric |
| **PV** | Potential vorticity |
| **RF** | Radiative Forcing |
| **RH** | Relative humidity |
| **SH** | Southern hemispheric |
| **SMCL** | Submodel Core Layer |
| **SMIL** | Submodel Interface Layer |
| **TAGGING** | TAGGING submodel implementing the tagging method |

# Abstract

Aviation contributes to about 4.9 % to the anthropogenic forcing through its emissions and the formation of contrails [2]. The effect of the emissions occur both directly through the emissions of $CO_2$ and water vapour, and indirectly through the emissions of nitrogen oxides ($NO_x$). For this research the focus is on the effects of the emissions of the latter species. In the atmosphere aviation $NO_x$ ($NO_{x_{air}}$) has a short-term and a long-term effect. The short-term effect (in the order of months) of this species is that it produces an increase in ozone ($O_{3_{air}}$) which causes positive radiative forcing. Both $NO_x$ and ozone generate $OH$, which on a long term (years) results in a reduction of $CH_4$ in the atmosphere, causing a negative forcing. It has not yet been successfully measured to what extent these budgets are disturbed through aviation emissions. Measuring these species greatly contributes to understanding the mechanism of aviation ozone production from aviation $NO_x$ in the atmosphere. If this mechanism is better understood, mitigation measures can be designed to reduce the effect of aviation $NO_x$ on the $O_3$ and $CH_4$ budgets. Currently, the concentration changes and contribution of aviation $NO_x$ and $O_3$ have been successfully modelled in 3D climate-chemistry models which is a great aid in understanding their behaviour. The current understanding is that the background concentrations of $NO_x$ and ozone are larger than the perturbations caused by aviation $NO_x$ and ozone, making it hardly measurable in the atmosphere, except for under special meteorological conditions such as high-pressure systems [42]. High ozone concentrations are found in areas where high-pressure systems exist, as favourable conditions for the production of ozone are found in these systems [33]. Emitted $NO_x$ from aviation into high-pressure systems could accumulate here which may result in an increased production of aviation $O_3$. The hypothesis for this research is that elevated ozone production due to aviation is found in high-pressure weather systems. In order to test this hypothesis, it is investigated whether a correlation exists between aviation $NO_x$ and $O_3$ and specific weather patterns.

In this MSc. thesis the relationship between weather patterns and the concentration changes of aviation nitrogen oxides and its chemically produced ozone is investigated. It is investigated whether a perturbation in ozone due to aviation is detectable under high-pressure weather systems. First a general variability analysis is performed where the variability of the mixing ratios of aviation $NO_x$ and $O_3$ is assessed with respect to latitude and season. This is followed by an analysis of the variability of these species with respect to dry air temperature, relative humidity and potential vorticity (PV). By performing this analysis it is assessed whether these variables are correlated to the behaviour of $NO_{x_{air}}$ and $O_{3_{air}}$ or whether these effects are negligible. Aviation $NO_x$ shows to be insensitive to relative humidity and dry air temperature, but a strong correlation to PV is found for $NO_{x_{air}}$. Aviation $O_{3_{air}}$ also exhibits a correlation with PV, but less strong compared to the correlation of $NO_{x_{air}}$ with PV.

High-pressure weather patterns are filtered and the behaviour of $NO_{x_{air}}$ and $O_{3_{air}}$ within these patterns is investigated. In these specific weather patterns an increase in aviation $NO_x$ only occurs if a high-pressure weather system is stable for at least 50 hours. Additionally, elevated $O_{3_{air}}$ levels are only found for elevated PV values, which allows transport of additional $NO_{x_{air}}$ into the weather system. The elevated $O_{3_{air}}$ levels are found at average and lower flight levels.

Dry air temperature ($T_{dry}$) and relative humidity (RH) exhibit a positive influence on the production of $O_{3_{air}}$. For higher $T_{dry}$ and RH conditions elevated $O_{3_{air}}$ mixing ratios are established. Thus, in weather patterns with elevated dry air temperatures and elevated RH conditions, the conversion of aviation $NO_y$ to ozone will be more efficient and increased aviation $O_3$ mixing ratios are found. The increased $O_{3_{air}}$ ratios extend even to lower flight levels, while $NO_{x_{air}}$ levels have decreased at lower flight levels. The increase in aviation $O_3$ in a stable high-pressure system is potentially detectable at lower flight levels as here the influence of stratospheric ozone has largely reduced, and the aviation ozone concentrations are still relatively large (although still smaller than stratospheric ozone).

Finally, from these results recommendations for future measurement campaigns are formulated. Aviation ozone concentrations increase at locations where a high-pressure system is found with PV values close to 0 pvu at the establishment of the high-pressure system, after which elevated PV values arise due to transport from higher altitudes. Under these conditions an increase in aviation $NO_x$ is found at flight levels. Only at lower flight levels there is a possibility that the increase in aviation ozone is detectable by an increase in total ozone, as the stratospheric ozone has reduced largerely here relative to the aviation ozone concentrations. Additionally, $T_{dry}$ and RH positively affect the production of ozone so these factor should be taken into account as well.

# 1 Introduction

Aviation is a large contributor to anthropogenic climate change through the emissions of carbon dioxide, water vapour, nitrogen oxides ($NO_x$) and by forming contrails (Brasseur et al. 1998, Irvine et al. 2012, Grewe et al. 2014). It has been estimated that in 2005 aviation has contributed to about 4.9% of the total man-made radiative forcing, which increases with the continuing growth of aviation [1][7][16][12]. The additional emissions of aviation $NO_x$ result in an increased $NO_x$ budget of the atmosphere, which influences the chemical composition of the atmosphere as it induces the loss of $CH_4$ and production of ozone, which are dominant greenhouse gasses. These changes in $CH_4$ and ozone cause a negative and positive radiative forcing, respectively. In order to restore the imbalance in outgoing and incoming radiation, the Earth adapts its surface temperature such that the outgoing radiation balances the incoming radiation. The positive radiative forcing that results from the increase in ozone due to aviation $NO_x$ requires an increase in surface temperature in order to restore the radiative balance, which is experienced as global warming.

In order to mitigate the effects of aviation $NO_x$ and aviation ozone, establishing and understanding the variability of these species in the atmosphere is of high importance. The chemistry and transport of these species have been successfully simulated in chemistry-climate models, but up to date no party has succeeded in measuring the footprint of aviation ozone in the atmosphere [21][22][18]. This is due to the fact that aviation $NO_x$ mixes rapidly with other $NO_x$ particles and then reacts with other species once it is released in the atmosphere. Therefore, even though aviation $NO_x$ can be measured in fresh plumes, due to the variability of the atmosphere and background concentrations, it is challenging to predict where and when it will react to ozone. Research has established that the perturbation of aviation $NO_x$ and ozone are generally smaller than the standard deviations of their background constituents and might therefore not be detectable in the atmosphere except under special meteorological conditions [42]. These meteorological conditions, such as stable high-pressure systems, could influence the $NO_x$ - ozone chemistry and are therefore of interest for further research. Therefore, a Msc. thesis research is proposed to investigate aviation $NO_x$ and ozone impacts with respect to specific weather patterns. The aim of this research is to find relationships between the variability of aviation $NO_x$ and ozone and specific weather patterns, such that these relationships can be used in the formulation of recommendations for future aviation ozone measurement campaigns.

The purpose of this the MSc. Thesis is to establish whether there is a relationship between specific weather patterns and $NO_x$ and ozone emanating from aviation. The problem statement, research goals, research question and structure of the research are detailed in Chapter 2. Chapter 3 presents an overview on climate and weather characteristics that are relevant for this research. To provide a better understanding of the chemical processes of nitrogen oxides and ozone in the atmosphere, the chemistry of these species in the troposphere and lower stratosphere are explained in the first part of Chapter 4. In the second part of this chapter the variability of these species in the atmosphere is discussed. In Chapter 6 the numerical chemistry climate model EMAC is introduced, which provides the simulation data for the data analysis of this research. The methodology applied for this research is set out in Chapter 7. This entails a discussion on the data used, the methods of data processing and analysis, statistical tools used, and the general methods applied for the research. In Chapter 8 the results of a variability analysis of aviation $NO_x$ and $O_3$ are presented, where the variability of these species are analysed with respect to latitude, season, relative humidity, dry air temperature and potential vorticity. Chapter 9 follows with a detailed analysis of the development of aviation $NO_y$ and $O_3$ in weather patterns and analyses the concentration and concentration changes of these species with respect to relative humidity, dry air temperature and potential vorticity. Then, in Chapter 10 it is assessed whether the increase in aviation $O_3$ found for specific weather patterns is detectable in the local total ozone budget. Subsequently it is assessed how these results could aid in formulating recommendations for future aviation ozone measurement campaigns, which is set out in Chapter 11. Lastly, in Chapter 12 the Conclusions and Discussion of this thesis research are set out, respectively.

# 2

# Thesis Project definition

In this chapter the research is firstly detailed in terms of the research context and motivation. This is followed by the research objective and goals in Section 2.2. Section 2.3 concludes this Chapter with an elaboration on the structure of the research.

## 2.1. Research Motivation

As stated in Chapter 1, aviation emissions change the chemical composition of the atmosphere by emitting $NO_x$ which results in an adjusted methane and ozone budget of the atmosphere, that in turn leads to a negative or positive disturbance in the radiative balance of the atmosphere. In order to propose effective mitigation measures for this effect, the variability of aviation $NO_x$ and aviation $O_3$ must be better understood, which could be achieved by performing measurements. Aviation $NO_x$ has been successfully measured in fresh plumes from aircraft, but aviation $O_3$ has not yet been successfully measured. As stated in the previous Chapter, the hypothesis is that the perturbation in ozone due to aviation could potentially be detectable under special meteorological conditions, specifically in high-pressure systems. If this is true, measurement campaigns could be designed to measure aviation $O_3$ in the atmosphere. This leads to the aim of this research, which was stated in Chapter 1:

*"To find relationships between the variability of aviation $NO_x$ and ozone and specific weather patterns, such that these relationships can be used in the formulation of recommendations for future measurement campaigns of aviation ozone."*

In order to achieve this research aim, the following three research questions were formulated:

***RQ 1:*** *How do aviation $NO_x$ and aviation Ozone vary in the Northern Hemisphere with respect to season, latitude and relevant weather factors?*

***RQ 2:*** *How do aviation $NO_x$ and aviation Ozone vary in specific weather patterns with respect to season and relevant weather factors?*

***RQ 3:*** *Is there a correlation between the change in aviation Ozone and total Ozone in a specific weather pattern that can aid in formulating recommendations for future aviation Ozone measurement campaigns?*
If these questions are answered positively, the research aim is achieved.

## 2.2. Research Objective and Goals

For this MSc. thesis, Chemistry Transport Model (CTM) and General Circulation Model (GCM) data is made available by the German Aerospace Center (DLR) and the German Climate Cooperation Cener (DKRZ). This data contains information on the chemistry in the atmosphere, general atmospheric specifications information, and information on the concentrations, concentration changes and contributions of trace gases and species in the atmosphere, simulated through the tagging and tracing method, emanating from both natural and anthropogenic sources [22][31][37]. This data is used to perform a data analysis to find correlations for the variability of aviation $NO_x$ and ozone with respect to specific weather patterns. Therefore, a MSc. thesis is proposed with the following research objective:

*"To identify the impact of aviation $NO_x$ and ozone with respect to specific weather patterns, by comparing specific aviation $NO_x$ and ozone changes from tagging and tracing data simulated by the EMAC model to specific weather patterns, to ultimately formulate recommendations for future aviation $NO_x$ and ozone measurement campaigns".*

To break this research objective down into concrete, unique goals, three research goals have been defined which are closely related to the research questions that were introduced in the previous section. By completing these research goals, the research objective will be achieved. These research goals are the following:

1. Analyse the variability of aviation $NO_x$ and ozone
2. Identify the relationship of aviation $NO_x$ and ozone with specific weather patterns
3. Formulate recommendations for future measurement campaigns

The structure of the MSc. thesis follows these three research goals. This structure is discussed in the following section.

## 2.3. Research Structure

This research is set up in cooperation with the DLR. The DLR has researched the climate impact of aviation for many decades throughout various projects [20][21]. For this research simulations have been performed using the EMAC model configured with the TAGGING and MECCA submodels, which are based on the Modular Earth Submodel System (MESSy 2.52) and the ECHAM5 atmospheric circulation model[22][36]. The data contains information on the atmospheric constituents and chemical behaviour and concentrations of the various trace gases and species in the atmosphere over a timespan of 10 years. In these 10 years, a time step of 10 hours is used to record the concentrations which includes the diurnal variability. The simulations were performed with a spectral resolution of T42 and a vertical resolution of 90 levels, up to 0.01 hPa. In Chapter 7 an elaboration on the simulations used is given [22]. The simulations are run and stored on the supercomputer "Mistral" of the DKRZ. Mistral is DKRZ's first petascale supercomputer containing 3.300 compute nodes, 100.000 compute cores, 266 Terabytes of memory and 54 Petabytes of disk.

This research is structured according to the structure of the Research Goals mentioned in Section 2.2 . This means that first, using the data provided, the variability of aviation $NO_x$ and ozone is assessed with respect to various variables, which is discussed in Chapter 8. After this, the data is further processed and analysed with respect to specific weather patterns. High-pressure weather systems are selected and filtered for analysis. For this a diagnostic tool has been developed. When this is done, it is established, whether a relationship between weather patterns and aviation $NO_x$ and ozone behaviour exists, which is discussed in Chapter 9. Furthermore, it is investigated whether the perturbation in ozone in a weather pattern caused by aviation is detectable in the total ozone budget of this weather pattern. This is discussed in Chapter 10. With the findings of this research, recommendations for future aviation ozone measurement campaigns are formulated, which are given in Chapter 11.

# 3

# Climate and Weather characteristics

Chemical species and their relative chemical interaction in the atmosphere are subject to the dynamical properties of the atmosphere. Chemical species are subject to horizontal transport, convection within the atmosphere and they are influenced by atmospheric characteristics such as temperature, humidity and radiation. The relevant climate and weather characteristics, specifically those influencing the behaviour of chemical species in the atmosphere, are discussed in this chapter. Firstly the Earth's atmosphere is discussed in Section 3.1. Here the dynamical processes in the Troposphere and Stratosphere will be highlighted. This is followed by a brief discussion of the effect of aviation on climate change in Section 3.3.1. Lastly in Section 3.2 specific weather pattern characteristics are set out and their influence on chemical reactions are discussed.

## 3.1. The Earth's Atmosphere

The atmosphere can be divided in five layers based on their chemical properties and temperature variations. These are, from the outermost layer down to the Earth's surface:

1. Ionosphere or Thermosphere
2. Mesosphere
3. Stratosphere
4. Troposphere

These layers are seperated by boundaries where one can distinguish a temperature rate change. These are the Mesopause, Stratopause and Tropopause. These boundaries and the layers along with their respective lapse rates are depicted in Figure 3.5. Additionally at the top of the atmosphere the Exosphere is located. The Exosphere is not depicted in this figure, but it extends from the top of the thermosphere to about 10.000 km above the Earth.

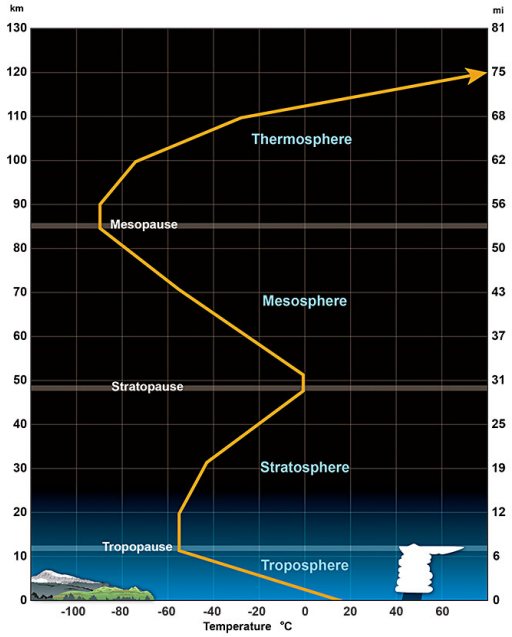


Figure 3.1: Structure of the Earth's atmosphere indicating the temperature layers and temperature gradients. Source: https://www.weather.gov/jetstream/layers

### 3.1.1. The Stratosphere and Troposphere

The most interaction between the Earth's surface and atmosphere and where aviation exercises the most influence are the Troposphere and Stratosphere. The Stratosphere extends from 20 km to 50 km altitude above the Earth's surface, where the temperature is about -15 ° C at the top (Stratopause) and decreases to about -51 ° C at the bottom (Tropopause). In this layer the density of the gases is relatively higher than the layer above it such that about 19% of the gases of the atmosphere is situated here. The Stratosphere contains about 90% of the atmospheric ozone, and the process of the formation of ozone takes place in the mid-high stratosphere. Ozone absorbs the radiation emitted by the sun causing the temperature at the mid- and high Stratosphere to increase. Towards the Tropopause the temperature is at a minimum of about -51 ° C. This means that "warmer" air can be found above cooler air which prevents convection in the Stratosphere.

The transition from the Stratosphere to the Troposphere is characterized by the Tropopause. This boundary is a dynamically stable layer which indicates another temperature gradient inversion. The Tropopause typically lies between 9 km and 17 km above the Earth's surface, around the polar regions and the equator, respectively. The Tropopause is at the top of the Troposphere, which is a dynamically very unstable layer and enjoys transport from the Stratosphere in terms of ozone and other species. The Troposphere holds the majority of the atmosphere's mass, namely about 80-85%. Since the total mass of the atmosphere is estimated to be around $5.26 \cdot 10^{18}$ kg, one can imagine that the density of the air increases strongly with decreasing height [29]. Additionally the temperature increases towards the Earth's surface from about -51 ° C at the top to an average temperature of 17 ° C at the surface. Since the lower layer of the Troposphere contains warmer air, rapid vertical exchanges of energy and mass take place, associated with convection. Much of the variability observed in the atmosphere occurs within this layer, including the weather patterns for example associated with the passage of fronts and the formation of thunderstorms. In the Troposphere most of the Earth's weather takes place. Weather is characterized by for example precipitation, cloud formation, winds and temperatures. More on this will be discussed in Section 3.2.

The dry air of the Troposphere contains (by volume) about 78% nitrogen, 21% oxygen, 1% of argon, 0.04% carbon and even smaller amounts of other gases (trace gases). A complete overview of the mean composition of the troposphere is given in Table 3.1 where both the volume mixing ratio and the lifetime of the trace gases is given.

Table 3.1: Mean composition of the troposphere of trace gaces with their respective volume mixing ratio and lifetime [3]

| **Species** | **Formula** | **Volume mixing ratio** | **Lifetime** |
|---|---|---|---|
| Nitrogen | $N_2$ | 0.781 | 1.5 x $10^7$ yr |
| Oxygen | $O_2$ | 0.209 | 40000 yr |
| Water vapour | $H_2O$ (surface) | 0.01 | days |
| | $H_2O$ (tropopause) | 10 ppmv | weeks |
| Argon | Ar | 9.3 x 106−3 | accumulates |
| Carbon dioxide | $CO_2$ | 360 ppmv | 50-200 yr |
| Methane | $CH_4$ | 1.73 ppmv | 9 yr |
| Nitrous oxide | $N_2O$ | 313 ppbv | 130 yr |
| Ozone | $O_3$ (surface) | 5-50 ppbv | weeks |
| | $O_3$ (tropopause) | 100 ppbv | months |
| Carbon monoxide | CO (surface) | 50-200 ppbv | 2 months |
| | CO (tropopause) | 50-100 ppbv | 0.05 yr |
| Nitrogen oxides | $NO_x$ (surface) | 0.01-1 ppbv | days |
| ($NO_x$ = NO + $NO_2$) | $NO_x$ (tropopause) | 0.05-05 ppbv | weeks |
| Sulphur dioxide | $SO_2$ (surface) | 0.01-1 ppbv | days |
| | $SO_2$ (tropopause) | 10-50 pptv | weeks |

### 3.1.2. Transport of Trace Gases in the Troposphere

The dynamics of the atmosphere can be attributed to differences in solar radiation and temperature differences. In the Troposphere, these phenomena together with differences in latent and sensible heat result in convection and horizontal transport of the air. These vertical and horizontal dynamics transport the species which influences the chemical compositions and reactions occuring in the atmosphere, and are therefore important to discuss.

#### Vertical mixing in the atmosphere

The lower layer of the Troposphere near the Earth's surface contains a higher absorption efficiency of incoming solar radiation than the higher layers of the Troposphere. This results in upwelling Infrared Radiation (IR) that heats the atmosphere from below, while at higher altitudes radiative cooling takes place which destabilises the atmosphere as it

increases the temperature lapse rate resulting in varying temperature lapse rates within the atmosphere. This causes convection to take place: the warmer, moist air of the lower layers is transported to higher altitudes, whereas colder and dry air from higher altitudes is transported downwards. Additionally, the condensation of water vapor can lead to precipitation which enhances convection.

In a global perspective, the mean result of convection is that the Troposphere mixes vertically in about one month. A result of this is that short-lived species such as $NO_x$ influence the ozone chemistry mostly at the altitude of their release, since their lifetimes is shorter than the global mean of convection. On the other hand, deep convection caused by for example thunderstorms can cause vertical exchange that also effectively redistributes short-lived species. In this way $NO_x$ with a relatively short lifetime can be redistributed from the upper Troposphere to the lower Troposphere, and vice versa, in times shorter than their lifetimes. An important effect of this is that surface emitted $NO_x$ can thus reach the upper troposphere, which affects ozone production. Therefore, in this research it is important to distinguish $NO_x$ emitted by aviation (*foreground concentrations*) from the $NO_x$ from other sources (*background concentrations*).

### Horizontal transport in the atmosphere

The horizontal dynamics in the Troposphere are attributed to the latitudinal differences in incoming solar radiation which lead to redistribution of heat and trace components. The latitudinal distribution of incoming solar radiation is a result of the spherical geometry of the Earth and the tilt of the spin axis. Because of this tilt it is possible for the poles to receive solar radiation in their summer half-years. Furthermore, as the Earth's orbit is not circular but rather elliptic, the distance from the Earth to the sun varies throughout its orbit. This means that also the solar flux incident at the top of the atmosphere varies, causing a variation in solar flux received. However, its contribution to the annual variation of the local solar flux per unit area at any point on Earth is much less compared to the contribution that arises from the tilt of the Earth's rotation axis. This is due to its current offset from the vertical of 23.5 °. Averaged over the year, the absorbed solar radiation has a strong maximum at the tropics, where it is about six times larger than at the poles. Furthermore, a net surplus is found of incoming radiation at the tropics, and a net deficit at high latitudes. In order to maintain equilibrium in terms of local energy balance, there must be some sort of transport of energy from low to high latitudes.

This transport is achieved by the motion of air parcels in the atmosphere. These motions cause latitudinal exchange by transporting warm air from the tropics poleward, and cold air from the poles towards the Equator. Additionally, the Coriolis force deflects meridional motions in the zonal direction. These motions drive the global circulation, which consists of three distinct cells: the Hadley, Ferrel and polar cells (see Figure 3.2).

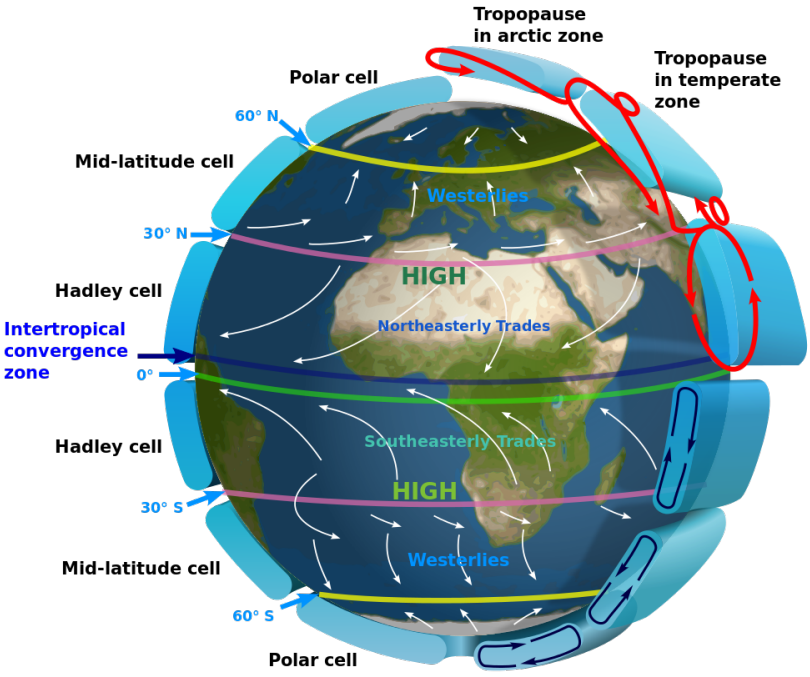


Figure 3.2: Hadley circulation with the Hadley cells, Mid-latitude cells (or Ferrel cells) and the polar cells. The westerly winds are also depicted in this figure. Source: https://en.wikipedia.org/wiki/Hadley_cell

In this figure the easterly winds near the equator can be identified. These winds carry moisture to the tropics, where deep convective clouds are formed in a region called the Intertropical Convergence Zone (ITCZ). Furthermore, these easterlies calm the weather experienced in the subtropical regions, in the downward branch of the tropical Hadley cells. In higher latitudes westerly winds can be distinguished, around 30 ° N and 30 ° S. These result from the fact that the Coriolis force increases with latitude, making the zonal wind component stronger. These dominating transient synoptic systems cause highly variable weather. This highly variable weather is expressed in cyclones and anticyclones, which reduce the large latitudinal temperature contrasts.

These motions of the air near the surface reflect closed cell-like structures where in the middle and upper Troposphere the intermittent cyclones and anitcyclones form planetary waves. In these planetary waves air motions are eastward. At higher altitudes, near the tropopause, two jet streams can be identified. One can be observed as a narrow band with wind speeds that reach about 40 $ms^{-1}$ at latitudes around 30 ° N and 30 ° S. A less persistent jet stream is found at higher latitudes, at around 60 ° N and 60 ° S, which is due to the interaction between polar and tropical air. The center of the jet stream is known as the core. This core occurs in a region that is idealized as a fold in the tropopause, also known as tropopause folding. This tropopause folding facilitates transport between the Troposphere and Stratosphere, which is discussed in the following subsection

### 3.1.3. Troposphere and Stratosphere interaction

The Troposphere and the Stratosphere are coupled through the Tropopause dynamically, radiatively and chemically. Mass and trace species are transported between the two layers which constitute an important coupling process [5]. Around the equator, mass is transported upwards from the Troposphere into the stratosphere. Through this transportation process, anthropogenic chlorine gases are deposited in the Stratosphere, which eventually leads to ozone depletion. In the subtropics downward transport from the Stratosphere to the Troposphere takes place through tropopause folding (see Subsection 3.1.2). In the extratropics downward transport takes place through tropopause foldings associated with cyclones and cut-off lows. In this way ozone is transported from the Stratosphere to the Troposphere. In the Northern hemisphere this downward transport is about twice as large as in the Southern hemisphere. Because the majority of aviation is located in the Northern Hemisphere and tropopause folding occurs significantly more here than in the Southern Hemisphere, it is expected that the impact of tropopause folding on aviation $NO_x$ and ozone can be better identified in the Northern Hemisphere. Overall, the transport of ozone between the Troposphere and Stratosphere is maximum in spring [23].

## 3.2. Weather Patterns

The conditions of the atmosphere at a certain geographical location over a short period of time is described by the weather. The weather is generally expressed in air temperature, air pressure, precipitation, wind speed and direction, cloud cover and type, and humidity. Weather is driven by the differences in air pressure, temperature and moisture between the moving air masses in the atmosphere. This occurs predominantly in the Troposphere.

As explained in Subsection 3.1.2 the difference in incoming solar radiation and net radiation absorbed by air masses cause air masses to move horizontally and vertically throughout the atmosphere. As an air mass warms up, its densitity decreases. As its density decreases below the density of its surrounding air masses it rises to higher altitudes. While rising to higher altitudes also its humidity increases. On the contrary, an air mass at higher altitudes with a large density can sink and cool down. As the air mass is sinking and cooling down, its density increases even more, and the air mass continues to cool down and travel to lower altitudes. Due to these mechanisms air masses with different pressures meet and interact, resulting in winds that have a tendency to blow from high-pressure areas to low-pressure areas. A sketch of this mechanism is illustrated in Figure 3.3 (top view) and Figure 3.4 (side view). If the movement of air masses are fast and take place in the upper atmosphere, one speaks of jet streams (see Subsection 3.1.2) which move weather systems throughout the atmosphere.

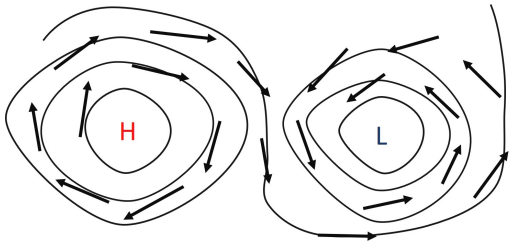


Figure 3.3: Schematic top view of a air flowing from a high-pressure system to a low-pressure systen

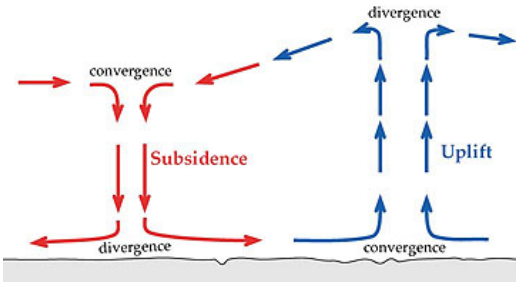


Figure 3.4: Schematic side view of air flowing from high pressure systems to low pressure systems

When weather patterns in the order of a synoptic scale contain a low-pressure centre, they are called "cyclones". Cyclones rotate counter clockwise in the Northern Hemisphere and clouds, precipitation and low temperatures are usually associated with these low-pressure systems. On the other hand, when weather systems on this scale contain high-pressure centers, they are called anti-cyclones. These high-pressure systems rotate in the oposite direction from cyclones and are associated with clearer skies, less dynamic weather and warmer temperatures.

The region where two air masses meet is called a weather front. In this region the weather characteristics change abruptly: temperature drops or rises, winds change direction and magnitude and humidity can change abruptly. This results in an atmospheric instability and storms can develop.

When the movement of air masses causes a stable situation of atmospheric conditions at a geographical location in time, one can speak of a weather pattern. A weather pattern can be defined predominantly by a high-pressure or low-pressure system, which imply warmer and cooler temperatures, respectively. This could be paired with certain humidity conditions precipitation, and wind speeds in the pressure system. Such a weather pattern can be viewed as an enclosed system in itself where transport and chemical reactions occur within the weather pattern, and where transport into and out of the weather pattern can take place.

## 3.3. Climate change and aviation

Climate change is often expressed in temperature increase (global warming) which is a result of Radiative Forcing (RF). Radiative Forcing is the imbalance of radiation emitted by the Earth into space and solar radiation received by the Earth. This imbalance needs to be restored, which the Earth resolves by adapting its temperature. In the following Section this will be discussed in detail. First an overview of climate and its influencing factors is given in Subsection 3.3.1, after which Subsection 3.3.2 discusses radiative forcing and global warming in more detail. Finally, in Subsection 3.3.3 it is explained how aviation contributes to this mechanism.

### 3.3.1. Climate and influencing factors

When weather conditions over a global or synoptic scale prevail over a long period of time, generally thirty years or more, one speaks of a climate. The climate on a certain location on Earth is influenced by properties of that location.

- **Latitude** - As discussed in Subsection 3.1.2 the Earth circles the sun in an elliptic fashion with its axis under a tilt of approximately 23 degrees. This causes a varying incoming solar radiation with respect to latitude which results varying temperatures with respect to latitude and horizontal transport of air masses.
- **Elevation** - The temperature of air masses at higher altitudes are generally lower than of air masses at lower altitudes. This effects the climate and thus the flora and fauna with respect to elevation considerably.
- **Direction of prevailing winds** - Winds blowing in from different directions bring air with different properties. For example, winds that blow from the sea are often associated with rain at coastal areas but dry weather at inland areas. Wind that blows from warm inland areas such as Africa bring warm and dry weather, etc.
- **Topography and geography** - The topography of an area greatly influences its climate. Winds blowing in from neighbouring seas affect the climate but also mountain ranges affect the climate by acting as barriers to air movement.
- **Ocean currents** - Ocean currents affect temperatures that are experienced through winds blowing inland from specific locations above the oceans. Winds blowing from warm currents bring warmer and more humid air, whereas winds blowing from colder currents bring colder and drier air.

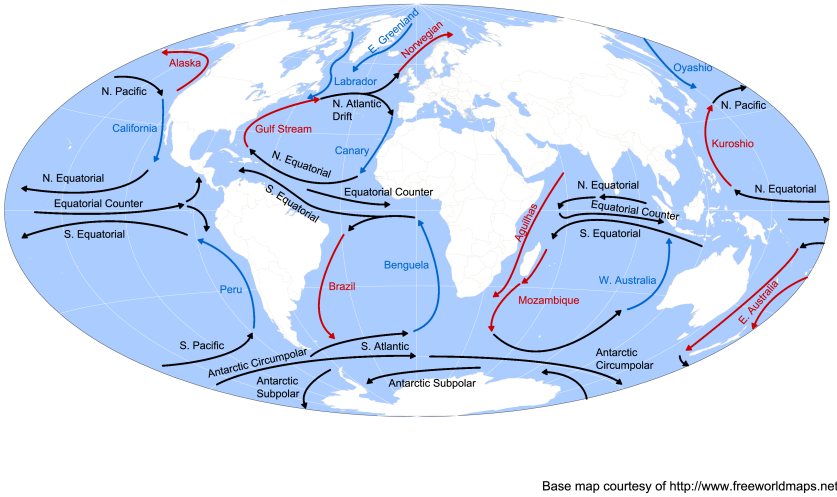


Figure 3.5: Global ocean currents. Source:http://www.physicalgeography.net/fundamentals/8q1.*html*

- **El Nino phenomenon** - This phenomenon describes the irregular warming of the surface water of the Pacific Ocean. The warmer water that results from this irregular warming pumps energy and moisture into the atmosphere, which alters the global wind and rainfall patterns which results in dynamical weather phenomena.
- **Anthropogenic factors** - A continuously increasing source affecting the climate are the anthropogenic factors. Notorious examples are the human-driven deforestation that leads to increased carbon dioxide in the atmosphere,along with the Industrial Revolution which resulted in a significant increase in the burning of fossil fuels, leading again to an increased carbon dioxide budget in the atmosphere. A notorious anthropogenic source which currently experiences increasing attention is aviation. The effect of aviation on climate change will be detailed in Section 3.3.3.

### 3.3.2. Radiative Forcing and global warming

The incoming short wave radiation from the Sun is absorbed by the Earth, and the Earth itself emits long wave radiation due to its low temperature. This incoming and outgoing radiation results in a radiation equilibrium at the top of the Earth's atmosphere. However, due to particles and species in the atmosphere that may absorb, scatter and re-emit long- and short wave radiation, the net incoming radiation may deviate from the net outgoing emitted radiation from the Earth which is known as Radiative Forcing (RF). This phenomenon is known as the greenhouse effect and the gases that cause this effect are called greenhouse gases [13]. The greenhouse effect is amplified when the concentration of greenhouse gasses increases.

In order to restore this balance, the Earth adapts its temperature. By adapting its temperature, the outgoing radiation can be controlled, such that the energy balance at the top of the atmosphere can be restored. This mechanism is based on the Stefan-Boltzmann law and it results in a change of near surface temperature of the Earth, which is approximated by:

$$\Delta T_s \approx \lambda \cdot RF \tag{3.1}$$

Where $\Delta\ T_s$ denotes the change in surface temperature, $\lambda$ denotes the climate sensitivity factor and $RF$ is the radiative forcing.

### 3.3.3. Effects of aviation on climate change

Aviation contributes to climate change through emissions of carbon dioxide ($CO_2$), carbon monoxide ($CO$), water vapour ($H_2O$), nitrogen oxides ($NOx$), soot and unburned hydrocarbons and through the formation of contrails[24][20][21]. The effect that these emissions have on the greenhouse gases are both direct and indirect. As such, the additional $CO_2$ and $H_2O$ emitted by aviation increases the $CO_2$ and $H_2O$ budgets respectively. Indirect effects are expressed through the formation of the greenhouse gas ozone ($O_3$) which is influenced by the presence of additional emitted $NO_x$ and the formation of contrails. Contrails can have both a cooling and warming effect by reflecting sunlight back into space (cooling) and absorbing terrestrial radiation which results in a positive RF (warming).

The extent to which aviation affects climate change can be attributed to the location and altitude at which the emissions are released. Location and altitude determine the lifetime of the species and whether they will be transported and have their effect elsewhere or whether they affect the atmosphere more locally. Therefore, in order to design mitigation measures the dynamics and footprint of aviation emissions in the atmosphere must be well understood.

# 4

# Nitrogen Oxides and Ozone Chemistry

Odd nitrogen constituents are relevant in the oxidation processes in the Earth's atmosphere. This group is often denoted as $NO_y$ and constitutes $N$, $NO + NO_2$, $NO_3$, $N_2O_5$, $HNO_3$, $HONO$, $HO_2NO_2$, $RC(O)O_2NO_2$ (peroxyacetyl nitrates), $RONO_2$ (alkyl nitrates), and $XONO_2$. The 'R' and 'X' groups are as follows: the 'R' denotes an alkyl group ($C_nH_{2n+1}$), $C(O)O_2$ denotes the peroxyacetyl group, and 'X' represents $Br$, $OBr$, or $O_2Br$ [38].
From these constituents nitric oxide ($NO$) and nitrogen dioxide ($NO_2$) are necessary for the photochemical production of ozone in the troposphere [10][9]. Due to the rapid interconversion of these two species, they are often grouped together as $NO_x$. The concentration of ozone in the troposphere is determined by photochemical production of ozone in the troposphere and by transport of ozone from the stratosphere. Therefore, in order to assess the variability of aviation $NO_x$ and ozone in the troposphere, the relationship between $NO_x$ and ozone in the troposphere must be thoroughly understood, both in terms of chemical relationships and through transportation.

## 4.1. Stratospheric Chemistry

In the Stratosphere, above 30km altitude, ozone is produced by the dissociation of molecular oxygen due to the solar radiation of wavelengths less than 242 nm [38]. The oxygen atom reacts rapidly with other $O_2$, under the condition that another molecule (denoted by $M$) is present. $M$ usually is another $O_2$ or $N_2$ molecule. This is given by the following equation:

$$O_2 + h\nu \rightarrow O + O \tag{4.1}$$
$$O + O_2 + M \rightarrow O_3 + M \tag{4.2}$$

In the stratosphere, odd nitrogen plays an important role in the destruction of ozone. This is done through photochemical reactions and are called "catalytic cylces". The photochemical balance of ozone in the stratosphere is governed by a combination of those destruction cycles and those involving odd chlorine and bromine, odd oxygen and odd hydrogen [5].
For this text the ozone catalytic destruction cycles as described by Brasseur (1998) are discussed [5][4]. Atmospheric ozone oxidizes $NO$ to $NO_2$. The latter is then photolysed at wavelengts shorter than 420 nm. This returns $NO$ and a ground-state oxygen atom as follows:

$$NO + O_3 \rightarrow NO_2 + O_2 \tag{4.3}$$
$$NO_2 + O_3 \rightarrow NO_3 + O_2 \tag{4.4}$$
$$NO_3 + h\nu \rightarrow NO + O_2 \tag{4.5}$$

Which gives a net reaction of:

$$2O_3 \rightarrow 3O_2 \tag{4.6}$$

The $O$ atom and $O_2$ can actually recombine to $O_3$. However, since the concentration of $O$ atoms throughout the stratosphere is relatively low compared to the concentration of $O_3$, the destruction of $O_3$ is dominant.

At higher altitudes, around the mid- to high stratospheric regions, the concentration of $O$ atoms becomes sufficiently high such that their reaction with $NO_2$ forms the following catalytic destruction cycle:

$$NO + O_3 \rightarrow NO_2 + O_2 \tag{4.7}$$
$$NO_2 + O \rightarrow NO + O_2 \tag{4.8}$$

Which gives the following net reaction:

$$O + O_3 \rightarrow 2O_2 \tag{4.9}$$

## 4.2. Tropospheric Chemistry

In the troposphere interaction of $NO_x$ with odd-hydrogen molecules have a large influence on the concentration of $OH$. $OH$ is considered a relevant "cleanser" of the atmosphere as it is able to transform primary emissions into secondary species which can be removed from the atmosphere through dry- and wet deposition. In the troposphere the $O$ concentration and the catalytic destruction of $O_3$ by $NO_x$ are negligible. Therefore, in the troposphere the production of ozone is most important.

In the urban atmosphere, the formation of ozone is dominated by the presence of non-methane hydrocarbons ($NMHC$) emanating from for example vehicles. In literature this family is often abbreviated to $RH$ when denoted in reaction schemes, and carbonyl products are denoted as $R'CHO$. For clarity the reaction scheme is simplified:

$$OH + RH \rightarrow R + H_2O \tag{4.10}$$
$$R + O_2 + M \rightarrow RO_2 + M \tag{4.11}$$
$$RO_2 + NO \rightarrow RO + NO_2 \tag{4.12}$$
$$RO + O_2 \rightarrow HO_2 + R'CHO \tag{4.13}$$
$$HO_2 + NO \rightarrow OH + NO_2 \tag{4.14}$$
$$2NO_2 + 2O_2 \rightarrow 2NO + 2O \tag{4.15}$$
$$2O + 2O_2 + 2M \rightarrow 2O_3 + 2M \tag{4.16}$$

Which gives a net reaction of:

$$RH + 4O_2 + h\nu \rightarrow R'CHO + H_2O + 2O_3 \tag{4.17}$$

The $R'CHO$ group undergoes more photochemical reactions which eventually result in the production of more ozone. When moving up to the free troposphere, the concentration of $NMHC$ decreases and the ozone production is governed by the oxidation of $CO$ and $CH_4$. This results in the following catalytic production cycles for $CO$ (4.18 - 4.23):

$$OH + CO \rightarrow CO_2 + H \tag{4.18}$$
$$H + O_2 + M \rightarrow HO_2 + M \tag{4.19}$$
$$HO_2 + NO \rightarrow OH + NO_2 \tag{4.20}$$
$$NO_2 + h\nu \rightarrow NO + O \tag{4.21}$$
$$O + O_2 + M \rightarrow O_3 + M \tag{4.22}$$

Which gives the following net reaction:

$$CO + 2O_2 + h\nu \rightarrow CO_2 + O_3 \tag{4.23}$$

The catalytic production cycle through the oxidation of $CH_4$ is of the similar form:

$$OH + CH_4 \rightarrow CH_3 + H_2O \tag{4.24}$$
$$CH_3 + O_2 + M \rightarrow CH_3O_2 + M \tag{4.25}$$
$$CH_3O_2 + NO \rightarrow CH_3O + NO_2 \tag{4.26}$$
$$CH_3O + O_2 \rightarrow HO_2 + CH_2O \tag{4.27}$$
$$HO_2 + NO \rightarrow OH + NO_2 \tag{4.28}$$
$$2NO_2 + h\nu \rightarrow 2NO + 2O \tag{4.29}$$
$$2(O + 2O_2) + 2M \rightarrow 2O_3 + 2M \tag{4.30}$$

Which results in the overall reaction:

$$CH_4 + 4O_2 + h\nu \rightarrow CH_2O + H_2O + 2O_3 \tag{4.31}$$

In the troposphere the concentrations of $CH_4$ and $CO$ are significantly higher than the $NO_x$ concentrations (see Table 3.1). Therefore the presence of $NO_x$ is usually the rate limiting step in the troposphere in the production of ozone. Therefore, when the oxidation of $CO$ takes place in an $NO_x$-poor environment, no ozone is produced.

$$OH + CO \rightarrow CO_2 + H \tag{4.32}$$
$$H + O_2 + M \rightarrow HO_2 + M \tag{4.33}$$
$$HO_2 + O_3 \rightarrow OH + 2O_2 \tag{4.34}$$

The net reaction is:

$$CO + O_3 \rightarrow CO_2 + O_2 \tag{4.35}$$

## 4.3. Reaction productivity

The rate in which a chemical reaction takes place is defined as the *chemical reaction rate*. This reaction rate is by definition the change in concentration of the reactants or products per unit time. In general chemical reaction rates are described by the power law, which is:

$$\frac{d[A]}{dt} = k \cdot [B]^n [C]^m \tag{4.36}$$

Here the chemical reaction rate is given as the change of the concentration of the product $[A]$ with respect to time. This rate depends on a certain reaction rate coefficient $k$ and the concentrations of the reactants $[B]$ and $[C]$ which are raised the power $n$ and $m$ respectively, which represent partial reaction order. The reaction rate coefficient $k$ is influenced by multiple atmospheric factors such as the pressure, ambient temperature and incoming solar radiation.

### 4.3.1. Influence of pressure on chemical reaction rates

Pressure is defined as the force applied perpendicularly to the surface of an object per unit area over which that force is distributed. When increasing the pressure of an air parcel, the molecules inside that air parcel are pressed closer together than in an air parcel with lower pressure. Therefore, the local pressure in the atmosphere influences gaseous reactions and thus the reaction rate coefficient. In this sense, the reaction rate coefficient increases with increasing pressure. For each chemical species the dependency on pressure differs, making this a complex relationship. In general however, the chemical reaction rates are not sensitive to pressure changes unless the ambient pressure is higher than that at sea level.

### 4.3.2. Influence of temperature on chemical reaction rates

In an ideal gas, temperature is proportional to the average kinetic energy of the random motions of the particles the gas consist of. Therefore, the higher this kinetic energy is, the higher the respective temperature of the gas is. Not only does a higher energy imply a higher temperature, it also implies elevated velocities of the particles. This increased velocity leads to a higher chance of colliding molecules, resulting in a higher reaction rate. Also, due to a higher energy state of the molecules, there is a higher chance that they have sufficient activation energy needed for a reaction to succeed.

### 4.3.3. Influence of solar radiation on chemical reaction rates

Incoming solar radiation increases the energy of molecules with their electromagnetic radiation. The photolysis of ozone only happens when there is solar radiation present with a certain maximum wavelength (<410$nm$ in the troposphere). The destruction of ozone happens in the stratosphere for wavelengths <420$nm$ [4][10]. This means that these reactions have strong variation between day and night. Since the incoming radiation also varies with respect to latitude (see Section 3.1), the chemical reaction rates of the production and depletion of ozone also vary with respect to latitude. The impact that this has on the atmospheric concentrations of $NO_x$ and $O_3$ is discussed in Section 8.1.

### 4.3.4. Influence of background concentrations on chemical reaction rates

As was seen in the beginning of this Section, the chemical reaction rate also depends on the concentrations of the reactants involved. Therefore, the reaction rates of the chemical reactions of ozone production depend on the concentrations of the constituents involved in these chemical reactions.
Specifically, the $NO_x$ background concentration influences the ozone net production rate significantly [3][39]. When the $NO_x$ volume mixing ratios are low, additional $NO_x$ emissions enhance the net production of $O_3$. In contrast, additional $NO_x$ emissions can reduce the net production of $O_3$ when the background concentrations of $NO_x$ are sufficiently high. Thus, the increase of $O_3$ production with additional $NO_x$ emissions increases steadily until it reaches a maximum. Here the ambient is $NO_x$ saturated. When even more $NO_x$ is then added, the net production of $O_3$ decreases again. A strong relation is found between the background concentration of $NO_x$ and the ozone production rate and $OH$ concentration. This is shown in Figure 4.1.

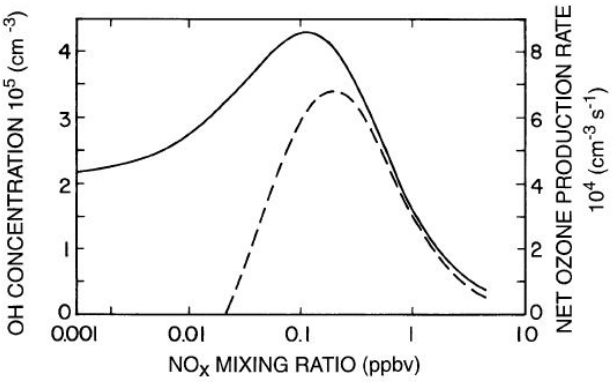


Figure 4.1: *OH* concentrations calculated by a model (solid curve) and the net photochemical production rate as a function of the *NO* background concentration (dashed line) in lower mid-latitude tropospheric conditions. This figure is obtained from Brasseur et al. 1998 [3].

In Figure 4.1 it can be seen that for very low $NO_x$ mixing ratios the net production of ozone is actually negative. This is because in this case the depletion of ozone is dominant.

A similar relationship was established by Sillman (1998), where the relationship between ozone and its main precursors $NO_x$ and volatile organic compounds ($VOC$) was inbestigated[39]. According to this study the ozone-precursor mechanisms can be split into a $NO_x$-sensitive and $VOC$-sensitive regime. The first being the regime where $NO_x$ mixing ratios are relatively low and thus ozone production is efficient and increasing, and the latter being the regime where $NO_x$ mixing ratios are relatively high and thus ozone production efficiency decreases. This split is determined by the $VOC/NO_x$ ratios, the $VOC$ reactivity and rates of meteorological dispersion. The latter indicates that a detailed research to the correlation of meteorological patterns with aviation $NO_x$ and ozone may aid in understanding the aviation $NO_x$ and ozone variability better.

## 4.4. Lifetimes of Species in the Stratosphere and Troposphere

The lifetime of species in the Stratosphere differs considerably from their lifetime in the Troposphere. This is due the dynamic characteristics of the Troposphere. In Section 3.1 in Table 3.1 the lifetimes of important species was listed for both the surface layer and higher in the troposphere. Here already a considerable difference was identified between the lifetime of for example $NO_x$ at the surface (days) compared to its lifetime in the free Troposphere (weeks). This is summarized in Table 4.1 for the relevant species involved in the production of ozone.

Table 4.1: Mean composition of the troposphere of trace gaces with their respective volume mixing ratio and lifetime [3][13]

| **Species** | **Formula** | **Lifetime** |
|---|---|---|
| Oxygen | $O_2$ | 40000 yr |
| Ozone | $O_3$ (surface) | weeks |
| | $O_3$ (tropopause) | months |
| Carbon dioxide | $CO_2$ | 50-200 yr |
| Methane | $CH_4$ | 9 yr |
| Carbon monoxide | $CO$ (surface) | 2 months |
| | $CO$ (tropopause) | 0.05 yr |
| Nitrogen oxides | $NO_x$ (surface) | days |
| ($NO_x$ = NO + $NO_2$) | $NO_x$ (tropopause) | weeks |
| Water vapour | $H_2O$ (surface) | days |
| | $H_2O$ (tropopause) | weeks |
| Hydroperoxyl Radical | $HO_2$ | seconds |

In the Stratosphere the lifetime of species increases even more due to the more stable characteristics of the Stratosphere resulting in a longer dynamical and chemical lifetime. Because the lifetime of $NO_x$ decreases towards the surface of the Earth, the impact of $NO_x$ decreases with decreasing altitude (see Section 5.3).

## 4.5. Nitrogen oxides and ozone variability in the atmosphere

The background $NO_x$ and ozone concentrations and variability vary significantly with latitude due to varying latitudinal incoming radiation, which results in varying chemical compositions of the atmosphere [5][42]. In the lower

stratosphere polar region the standard deviation of $NO_x$ background concentrations vary up to 70% in winter, and the lower and middle troposphere this varies up to even 90% [42]. Furthermore, in the Northern Hemisphere the $NO_x$ concentrations are significantly more abundant than in the Southern Hemisphere [5].

Because of the higher concentrations of $NO_x$ in the Northern Hemisphere, the photochemical production rate of ozone is also higher in the Northern Hemisphere. This results in twice as large ozone mixing ratios in the Northern Hemisphere mid-latitudes compared to the mixing ratios in the Southern Hemisphere. Greater stratospheric fluxes in the Northern Hemisphere also play an important role in this mechanism. This transport flux takes place through tropopause folding and other processes at mid- and high latitudes. In the Northern Hemisphere this transport flux is estimated to be about double than that of the Southern Hemisphere. The standard deviation of both $NO_x$ and ozone background concentrations at cruise altitudes at mid-latitudes are roughly 30% [42].

## 4.6. Nitrogen oxides and ozone accumulation in a high pressure system

High-pressure weather systems are believed to provide advantageous conditions for species to accumulate in. In high-pressure systems often low potential vorticity values are found, implying weak winds and allowing species to accumulate without being transported away [33]. The correlation for high ozone and pressure is not one-to-one, meaning that the highest pressure does not necessarily entail the highest concentration. This is mostly due to the fact that pressure does not affect the ozone production primarily or vertical mixing. Thus, other factors influence the increase in ozone in a high-pressure system. For the research at hand it is of interest to investigate whether aviation $NO_x$ accumulates in high-pressure weather systems which would lead to an increase in aviation ozone.

# 5

# Aviation Nitrogen Oxides and Ozone in the Atmosphere

As the relationship between tropospheric and stratospheric ozone and nitrogen oxides became clear ([3][4][5][9][10]) research focused on the variability of aviation $NO_x$ and ozone in the atmosphere. Various relationships were found, such as dependency on season, latitude, altitude and geographical location. In this Section the fundamental researches that established these relationships are discussed.

## 5.1. Latitudinal variability

The contribution of aviation $NO_x$ amounts to about 20-100 $pptv$ in northern mid-latitudes. In contrast, the contribution of aviation $NO_x$ on the Southern Hemisphere is rather small, as this amounts to less than 5 $pptv$ [42]. This results in an increase of ozone in the upper troposphere of about 2-3 $ppbv$ in Winter, and 5-10 $ppbv$ in Summer, in the Northern hemisphere from about 30 °N poleward.

The climate impact of aviation $NO_x$-induced ozone shows to be largest at the equator and decreases towards the poles [24][25]. In the zonal direction, the ozone perturbation is almost symmetric and in the northern mid-latitudes it reaches a maximum during the Northern Hemispheric Winter. In the polar regions it attains a maximum in the Northern Hemispheric Summer. This suggests a strong seasonal dependence of the perturbations. The relatively high contribution of aviation $NO_x$ in the Northern Hemisphere suggests a possibility to distinguish aviation $NO_x$ at northern mid-latitudes. However, since the standard deviation is also rather large at these latitudes (30 %), it is doubtful whether the ozone perturbation caused by aviation is detectable except under specific meteorological conditions [42]. Therefore, assessing the variability of aviation $NO_x$ and ozone with respect to specific meteorological conditions can provide valuable insights.

The impact variation of aviation $NO_x$ and ozone with respect to latitude can be assessed by comparing associated radiative forcings induced by aviation $NO_x$. Using the perturbation method (see Appendix A) and a global chemistry transport model this analysis is carried out [31]. By emitting aircraft(-like) $NO_x$ emissions, the ozone- and methane budgets are disturbed, which causes a change in radiative forcings. Calculating these over various latitudes gives the radiative forcings due to short-lived $O_3$, due to methane induced $O_3$ and the methane and net $NO_x$ forcings. These are given in Table 5.1 [25].

Table 5.1: Steady-state radiative forcings (in $mWm^{-2}(Tg(N)yr^{-1})^{-1}$) induced by short-lived $O_3$, $CH_4$ induced $O_3$, $CH_4$ and the net $NO_x$ forcing, with applied feedback factor that account for sustained aviation emissions by the present-day global fleet. In this experiment constant percentage increases in aviation emissions at near-cruise altitudes at various latitudes were considered as seen in [25].

| **Latitude bands** | **Short-lived $O_3$ forcing** | **$CH_4$-induced $O_3$ forcing** | **$CH_4$ forcing** | **Net $NO_x$ forcing** |
|---|---|---|---|---|
| 60 - 80 °N | 18.4 | -2.96 | -8.11 | 7.34 |
| 40 - 60 °N | 24.5 | -4.26 | -11.7 | 8.55 |
| 20 - 40 °N | 52.6 | -9.81 | -26.8 | 16.0 |
| 0 - 20 °N | 124 | -19.1 | -52.4 | 52.2 |
| 0 - 20 °S | 132 | -22.3 | -61.0 | 48.3 |
| 20 - 40 °S | 65.8 | -15.4 | -42.1 | 8.25 |
| 40 - 60 °S | 42.1 | -10.3 | -28.2 | 3.60 |
| 60 - 80 °S | 39.5 | -8.90 | -24.4 | 6.19 |

The values from Table 5.1 are obtained from the research by Köhler et al. (2012) [25]. Here the radiative forcings are given due to the aviation emissions by the present-day subsonic fleet in $mWm^{-2}$ per $Tg(N)yr^{-1}$. In this research

constant percentages increases in aviation emissions at near-cruise altitudes were considered at various latitudes. As expected from the higher photochemical efficiency near the tropics (see Chapter 3.1.2), the radiative forcings near the equator are larger than at higher latitude bands. Examining this table shows that lower latitude emission changes cause ozone- and methane radiative forings that are roughly a factor 6 larger than those from higher latitude emission changes.

To better illustrate the impact of aviation $NO_x$ emissions with respect to latitudinal variations, in Figure 5.1 the net global-mean radiative forcing is depicted in $mWm^{-2}$ with the black crosses. The red bars indicate the contributions to this mean value due to short-lived $O_3$, and the blue and green bars show the contributions due to the reduction in methane lifetime and methane-induced ozone decrease, respectively.

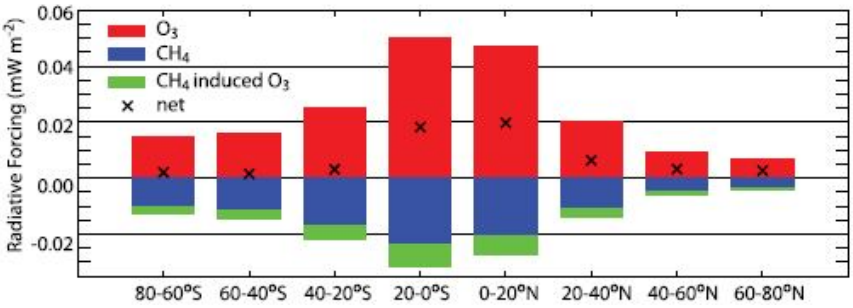


Figure 5.1: The net global-mean radiative forcing (in $mWm^{-2}$) due to an increase of $NO_x$ (aircraft) emissions by $3.8 \cdot 10^{-4}$ Tg(N) per year at cruise altitudes at the latitudes shown in Table 5.1, indicated by the black crosses. The red bars indicate the contributions due to short-lived ozone, the blue bars indicate the contribution due to the reduction of methane lifetime and the green bars indicuate the contribution due to methane-induced ozone decrease.

From Figure 5.1 it is concluded that the net global-mean radiative forcings (RF) due to the aircraft $NO_x$ increase near cruise altitudes are close to zero and positive. This is in accordance with the by Stevenson et al. (2004) which showed a slightly positive net forcing [41]. The net radiative forcings found in literature differe slightly due to the strong correlation between the long-lived methane induced and short-lived ozone changes, which yield a negative and positive RF, respectively. Small differences in these values lead to large impacts on the net RF, the Global Warming Potential GWP and the Global Temperature change Potential GTP. Most likely, these differences are attributed to the different chemical responses incorporated in the used models.

Analogously to the composition changes, where the impact of composition changes at the Southern Hemisphere are larger than at the Northern Hemisphere for the same latitude bands, the corresponding radiative forcings are also larger at given SH latitude bands compared to the respective NH latitude bands. The lower background concentrations of $NO_x$ in the Southern Hemisphere influence the ozone and methane sensitivities to changes in $NO_x$. Therefore, the Southern Hemisphere ozone and methane is more sensitive to changes in $NO_x$ concentration than the corresponding Northern Hemisphere latitudes.

## 5.2. Seasonal variability

The impact of aviation $NO_x$ and ozone have a strong dependence on season [42] [41]. This is most prominently related to the varying solar radiation absorption with respect to season (see Chapter 3) which influences the photochemical efficiency and lifetimes of species in the atmosphere. Therefore, also the background concentrations of $NO_x$ and ozone vary seasonally. In this context, the Summer season is defined as the period where the Northern Hemisphere experiences Summer, thus the months June, July, August, whereas the Winter season is defined as the months December, January, February. In Summer, convection activities are largest which causes the $NO_x$ concentrations near cruise altitude to be highest in July for the Northern Hemisphere [42]. This is due to the fact that the increased convection activity transports more $NO_x$ emitted at the surface of the Earth to higher altitudes. The $O_3$ concentrations near cruise altitudes on the other hand are lower for the Summer months than for the Winter months which is related to the shorter lifetime of ozone in Summer [41][42].

The difference in aviation $NO_x$ and ozone impact lies in the seasonal differences in the response of $O_3$ and $OH$ to aircraft $NO_x$ which is related to the annual photochemistry cycle. The ozone radiative forcing calculations also have a seasonal dependence. Aircraft $NO_x$ emissions lead to short-lived ozone pulses, which imply a positive radiative forcing. The $NO_x$ and $O_3$ concentrations generate $OH$ which ultimately leads to a reduction in $CH_4$. Therefore, aircraft $NO_x$ emissions cause negative $CH_4$ anomalies. This negative $CH_4$ anomaly causes a negative $O_3$ anomaly on the long term, which causes a negative radiative forcing. Therefore, short-lived $O_3$ imply positive radiative forcing,

whereas long-lived $O_3$ imply a negative radiative forcing.

The sensitivity of the response of $O_3$ and $OH$ to aircraft $NO_x$ is dependent on the season. Since during Winter months the lifetime of $NO_x$ and $O_3$ is largest, the largest $O_3$ anomaly occurs in Winter from aviation emissions emitted in October. In contrast, the smallest $O_3$ anomaly occurs in Summer due to the shorter lifetimes, from the aviation emissions emitted in July [41]. When translated into radiative forcing, the largest response occurs in Spring (April), whereas the smallest occurs for Winter (January) [41]. The long-lived response caused by the $OH$ anomalies are dependent on the $NO_x$ and $O_3$ anomalies and on the availability of sunlight. A maximum peak response of the $OH$ anomaly can therefore be found in Summer, in July, and a minimum in Winter, in January. The $OH$ anomalies translate into the aforementioned $CH_4$ anomalies, which are maximum in July and minimum in October. These anomalies result in positive and negative radiative forcings due to the short-lived $O_3$ and long-lived negative $CH_4$ anomalies, respectively. Their absolute values are rather similar, which results in a net positive radiative forcing. However, they are variable for the Winter and Summer season, resulting in a positive forcing for the months April and October and a negative net forcing for the months January and July. The maximum difference between the seasons are roughly 0.8 $mWm^{-2}$ per year [42][4][41].

## 5.3. Altitudinal variability

In Chapter 4 it was discussed that the $NO_x$ - ozone chemistry in the troposphere differs from that in the stratosphere due to the variable background concentrations and species present, and varying radiative absorption which results in different dominating chemical reactions. When looking at the variation of aviation $NO_x$ and ozone an important factor contributing to this variation is the lifetime of the emitted $NO_x$ at the different altitudes, and to a certain extent also the efficiency of the engines of the aircraft with respect to altitude. To a certain extent, the climate impact of $NO_x$ emissions is increased if the emissions are made directly into the stratosphere where they have a longer lifetime [24].

In the troposphere, reducing the cruise altitudes of a subsonic fleet by 1 km and keeping the amount of aircraft emissions constant, the impact of aircraft $NO_x$emissions decreases due to its shorter lifetime with decreasing height [19]. Lowering the cruise altitude causes a decrease of 30% of the $NO_x$ concentrations at the old flight altitude, while at the new, lowered flight altitude the concentrations increases with only 5-10% [15]. Therefore, the ozone production increases at the lower altitude, while at the standard cruise level it decreases. However, due to the shorter lifetime of ozone at lower altitudes, the ozone production at the same geographical location at elevated altitudes overcompensates for this increase [15]. When not taking the shorter lifetimes of $NO_x$ and ozone at lower altitudes into account, a similar result can be obtained [27]. However, in this case the ozone production at lower altitudes are overestimated, since no shorter lifetimes of the species at the lower altitudes are taken into account.

When analysing the impact variations of aviation $NO_x$ and ozone with respect to altitude one can look at the respective RF changes. In a more recent study by Søvde et al (2014) the altitudinal impact variations of aviation $NO_x$ emission impacts were assessed by analysing the short-lived radiative forcing caused by $NO_x$ and long-lived radiatve forcing caused by $CH_4$ [40]. Three chemistry-climate models (CTM) and two climate-chemistry models (CCTM) in CTM mode were applied, which all included detailed tropospheric and stratospheric chemistry, to estimate the short-lived RF from $O_3$. This ranged on average between 16.4 $mWm^{-2}$ and 23.5 $mWm^{-2}$ and including the long-lived RF caused by changes in $CH_4$, the total $NO_x$ related RF was estimated to range between 1 and 8 $mWm^{-2}$ with an average of 5 $mWm^{-2}$. This study showed that in terms of RF, increasing the cruise altitude with 2000 $ft$ results in an increase of the total RF due to aircraft $NO_x$ emissions by $2 \pm 1$ $mWm^{-2}$. Decreasing the cruise altitude with 2000 $ft$ on the other hand results in a decrease of the total RF of $2 \pm 1$ $mWm^{-2}$. This change is mainly controlled by the short-lived $O_3$. These chemical ozone perturbation and sensitivities to the altitude of aircraft $NO_x$ emissions are consistent with earlier studies [15][26].

## 5.4. Geographical variability

Since the background $NO_x$ concentrations have a significant effect on the chemical reactions converting $NO_x$ to $O_3$, one can imagine that the impact of aviation $NO_x$ and ozone varies with respect to geographical location. Generally, when the $NO_x$ background concentrations are low, the ozone formation rate increases with increasing $NO_x$, nearly linearly [39]. As the $NO_x$ concentration increases even more, the production rate of ozone still increases, but with an decreasing rate until it reaches a local maximum. After this maximum, the production efficiency decreases with increasing $NO_x$ background concentrations. With respect to geographical locations this is translated to the background $NO_x$ concentrations present at different types of locations. Rural areas have lower $NO_x$ backgrounds due to the lack of anthropogenic sources. Therefore, these are so-called "$NO_x$-sensitive" areas. Urban areas contain elevated $NO_x$ background concentrations, causing a lower ozone production rate than in rural areas [39]. Additionally to this, a geographical location's sensitivity to aviation $NO_x$ disturbances is of course also dependent on the latitude band in

which it is located (see Section 8.1).

The relative contribution of aviation $NO_x$ is found to be largest over Europe and smallest over India [25]. Emission increases over Inda and China on the other hand appear to increase $O_3$ columns which are roughly a factor 2 higher than over the USA and Europe. This is most probably due to the dfference of solar irradiance, which is higher at lower latitudes and thus increases the photochemical production of ozone. In the mid-latitudes, emission perturbations are picked up by prevalent westerlies. Due to these westerlies they get transported and the associated $O_3$ changes occur elsewhere to the East. The same concept applies to $NO_x$ aviation emissions above India, where the associated peak ozone increases occur over the north-eastern Indian Ocian. Additionally important in this case is that a large seasonal effect is in place due to the monsoon phase.

## 5.5. Variability with respect to emission location in a weather pattern

The location within a specific weather pattern at which aircraft $NO_x$ is emitted is of great influence of the ozone production. Larger ozone values are found in the area of high pressure ridges and in the vicinity of jet streams [21]. Depending on the location with respect to a high pressure ridge, distinctive pathways and chemistry along the trajectories of air parcels are found.

To illustrate this, the weather situation depicted in Figure 5.2 is analysed in the DLR WeCare project [21]. In this figure a high pressure ridge (HPR) can be identified from western Africa to the tip of Greenland. For the analysis 150 air parcel trajectories were assessed which started both inside the area of the HPR and west of it (both at 40°N to 50°N and at 15 W and 30 °W, respectively), and the same was performed for a similar blocking situation. On the right in Figure 5.2 one can see a clear distinction in the transport pathway of an air parcel tracked within and west of the HPR. The red trajectory depicting the air parcels within the pressure ridge shows that these are transported to lower altitudes and more southward towards the tropics. These trajetories show an adjusted radiative forcing and climate cost function from the ozone change which was found to be roughly 50% larger than that of the trajectories starting west of the HPR (the blue line in Figure 5.2[21].

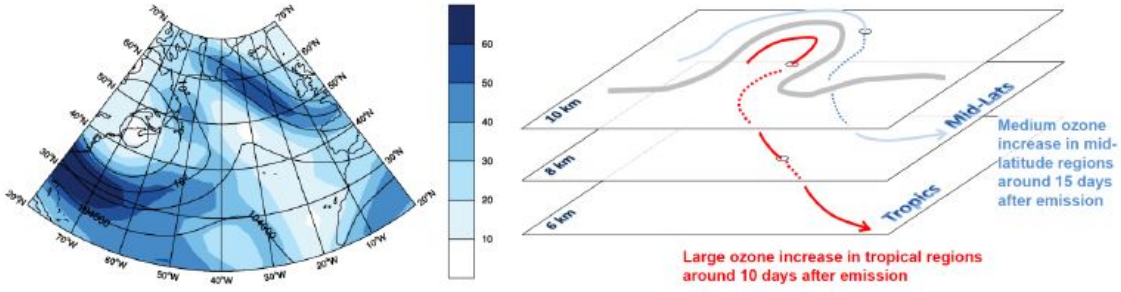


Figure 5.2: Illustrative weather situation over the Atlantic with on the left the geopotentials at 250 hPa in isolines and the wind velocity (in m/s) in blue gradients. On the right a sketch of the transport pattern

The increased radiative forcing is attributed to the higher ozone production efficiency at lower latitudes 8.1, which leads to larger contributions of the aviation $NO_x$ to ozone in those regions.

# 6

# Numerical Chemistry-Climate Model EMAC

Numerical chemistry-climate models are used to simulate the Earth's chemistry and climate systems and the interaction between these systems. These models are used to investigate the conditions and behaviour of the atmosphere and are used in combination with observational data. Performing analyses using numerical models and observational data allows for a better understanding of processes that determine the dynamical and chemical state of the atmosphere. These processes are significant for the variability of atmospheric quantities. Such a numerical model is the ECHAM/MESSy Atmospheric model, or EMAC model [35]. This is a modular global climate and chemistry simulation system consisting of various submodels which calculate the processes in the troposphere and middle atmosphere and their interactions with land surfaces, the ocean and with human influences. The data provided by the DLR was simulated by the EMAC model and therefore this model will be elaborated on in this chapter.

## 6.1. The configuration of the numerical chemistry-climate model EMAC

The EMAC model is a modular chemistry-climate model which generates multi-annual simulations using different submodels. The structure of the EMAC model is illustrated in Figure 6.1. The model calculates the processes in the troposphere and middle atmosphere and their interactions with land surfaces, the ocean and with human influences. This allows to find relationships between impacts of specific emission sources and for example specific meteorological conditions. The structure of the model consists of three levels: a base layer, an interface layer, and a submodel layer. The base layer is a model that calculates and simulates the physics of the Earth's atmosphere and this layer is coupled to various submodels that feed calculations and simulations to the base layer through an interface layer. The submodels that are linked to the base layer calculate and simulate mechanisms such as chemical processes in the atmosphere from different sources, both natural and anthropogenic, for which continuous data exchange between the base layer and the submodel layer is required.

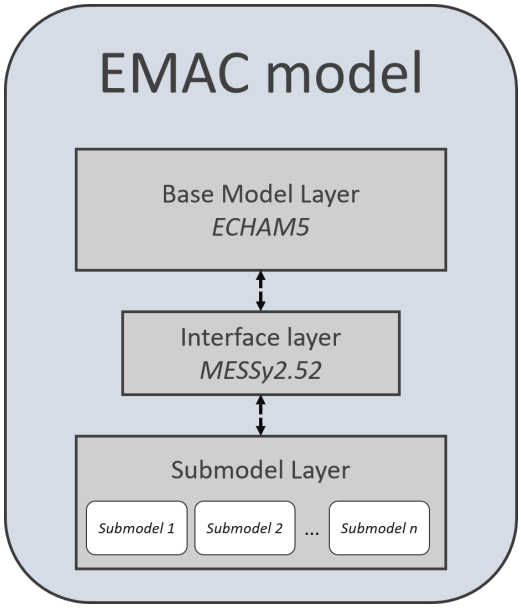


Figure 6.1: EMAC model structure consisting of the Base Model Layer, Interface Layer and the Submodel Layer

The base layer in the EMAC model is the 5th generation of the dynamic model ECHAM (ECHAM5). The ECHAM5 model is based on the weather forecast model of the European Centre for Medium-Range Weather Forecasts (ECMWF)

and is developed by the Max-Planck Institute for Meteorology and the University of Hamburg[34]. The ECHAM model is further detailed in Subsection 6.2. The interface layer in the EMAC model couples the base layer to the submodels. This interface layer is the Modular Earth Submodel System (MESSy2.52). It is a software which allows to link multi-institutional compure codes by facilitating an infrastructure with generalized interfaces for the coupling of different submodels[1]. This software is further discussed in Subsection 6.3.

EMAC can be applied both as a pure atmospheric general circulation model (GCM), as an atmospheric-chemistry transport model (CTM) or as a quasi atmospheric-chemistry transport model (QCTM). When applied as an atmospheric-chemistry model, EMAC can also be applied with full feedback between atmospheric chemistry and atmospheric dynamics [37]. Furthermore, the dynamics of the EMAC model can be relaxed towards analysis and re-analysis (forecast and hindcast, respectively) data of the ECMWF.

Different submodels are used in the EMAC model for the current research, most notably the TAGGING submodel which governs the tagged tracers in the atmosphere (see the elaboration of the TAGGING submodel in Section 6.4). The sub-model MECCA is used for simulating the chemistry processes in the atmosphere [36]. This sub-model considers combined chemical reactions as a rigid system of ordinary differential equations. More details on this submodel and others applied for the current research are given in Subsection 6.4.

Due to the ability to link multiple submodels EMAC disposes of a modular structure which allows the model to be applied to a wide variety of applications in the scientific field. Additionally, EMAC follows some important standards: Fortran95, ISO/IEC-1539-1, Message Passing Interface standard for parallel computation (MPI-2), and Network Common Data Form data format (NetCDF) [37]. Therefore, EMAC is well applicable in various architectures.

## 6.2. The ECHAM5 Atmospheric Model

The core of EMAC is the general atmospheric circulation model ECHAM5. This model solves the primitive atmospheric equations and is used as the base layer of the EMAC model. In the horizontal dimension it solves the primitive equations through a spectral transform technique and in the vertical dimension it solves the primitive equations for the troposphere and stratosphere through the method of finite differences. In the time dimension the equations are solved using a semi-implicit leap-frog scheme with a time filter. In this way ECHAM5 calculates the development of global weather situations and optionally it can calculate the chemical composition of the atmosphere around the globe. This is done in time steps of 20 to 40 minutes when a spatial resolution of 300 to 500 km is employed. The dynamic model simulates typical characteristics of the atmospheric circulation and not selected observed weather situations. The data is output and stored for every 10 hours to account for diurnal variability.

The latitudes and longitudes in the ECHAM5 model are defined for different truncation levels on a Gaussian grid, also called the "T-value". These T-values and respective numbers of latitudes and longitudes on the grid are given in Table 6.1. For the simulation at hand the resolution T42L90MA is applied. T42 indicates that in the longitudinal direction the grid is divided in 128 longitudes, and in the latitudinal direction the grid is divided in 64 latitudes. This corresponds to a Gaussian grid with a resolution of approximately 2.8° by 2.8° which provides sufficient resolution for mesoscale and synoptic scale events.

Table 6.1: Truncation levels and respective latitudes and longitudes options of the ECHAM5 model from Roeckner et al. (2003) [35]

| Truncation | Number of longitudes | Number of latitudes |
|---|---|---|
| T21 | 64 | 32 |
| T31 | 96 | 48 |
| T42 | 128 | 64 |
| T63 | 192 | 96 |
| T85 | 256 | 128 |
| T106 | 320 | 160 |
| T159 | 480 | 240 |

T42L90MA indicates that for the simlation at hand 90 hybrid pressure levels were set in the vertical direction, where the top layer was situated at 0.01 hPa (about 80 km). This configuration is used when simulating processes in the middle atmosphere. In the standard configuration however, the model simulates 19 or 31 vertical layers where the top level is at 10 hPa. These vertical layers represent hybrid pressure levels which follow the relief of the Earth's surface close to the surface, whereas away from the surface at higher altitudes it follows the dominance of the ambient pressure levels. This relationship is given by Equation 6.1 where the downward direction is positive.

[1] https://www.messy-interface.org/

$$press = hyam + hybm * aps \tag{6.1}$$

In this equation $press$ indicates the "hybrid pressure level at layer midpoints" or "hybrid sigma pressure" and $aps$ is the surface pressure at a specific grid point in Pa. The variables $hyam$ and $hybm$ are the hybrid $a$ and $b$ coefficients at layer midpoints. The values of these coefficients are depicted in the graphs of Figure 6.2 and 6.3. Here it can be seen that around the lower Stratosphere - upper Troposphere the hyam coefficient becomes dominant and towards the surface its dominance decreases. Towards the surface the hybm coefficient reaches 1, meaning that the surface pressure becomes dominant.

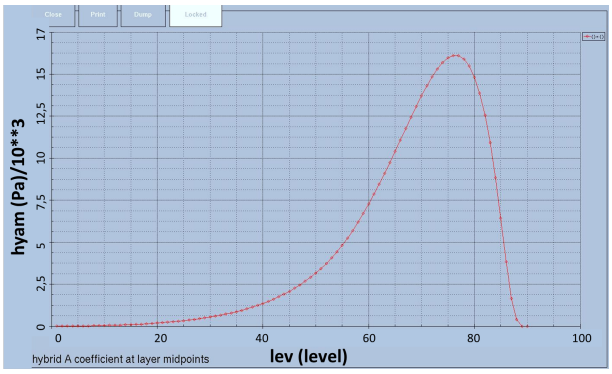


Figure 6.2: hyam values for the ECHAM5 model configurated with 90 levels

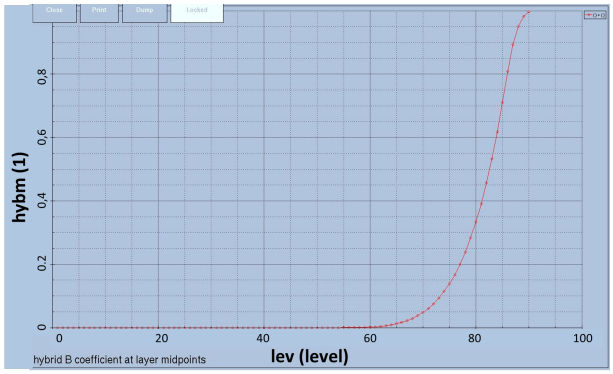


Figure 6.3: hybm values for the ECHAM5 model configurated with 90 levels

## 6.3. MESSy2.52 Software

As previously stated, the MESSy software facilitates an interface that allows the coupling of computer codes of multiple institutions by providing an infrastructure with generalized interfaces that can couple different submodels. At the moment MESSy comprises around 60 submodels which are infrastructure submodels, diagnostic submodels, atmospheric chemistry related submodels and model physics related submodels. The main design concept of MESSy keeping the infrastructure clear is the strict separation of process description from the model infrastructure. These two are separated but linked by the standardized interface of MESSy.

The coupling infrastructure of MESSy comprises 4 layers. These are the Base Model Layer (BML), Base Model Interface Layer (BMIL), Submodel Interfacel Layer (SMIL) and the Submodel Core Layer (SMCL). The infrastructure can be regarded as a multiple socket outlet connected to a power supply, supplying power to multiple appliances (Figure 6.4).

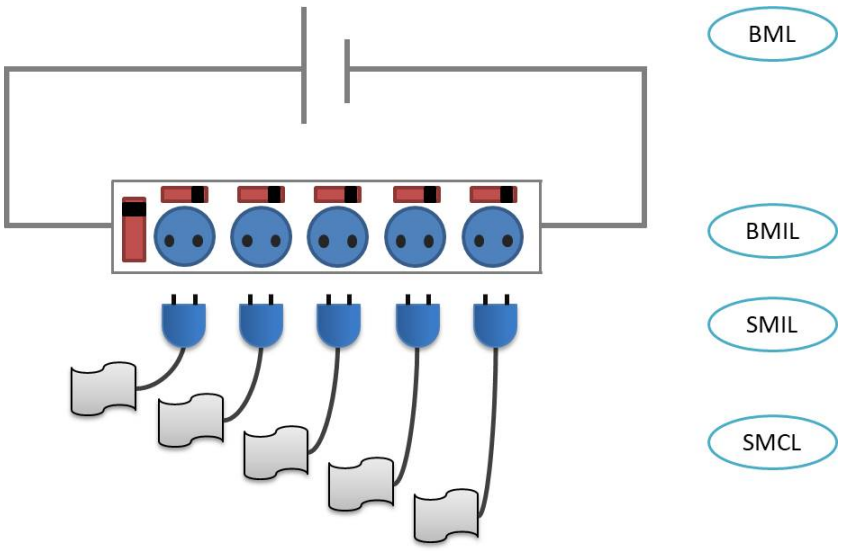


Figure 6.4: Coupling infrastructure representation of MESSy by illustrating the BML as a power supply, the BMIL as a multiple power socket outlet, the SMIL as the connectors and the SMCL as various appliances.

The Base Model Layer has two possible states: a final develop,ent state and a transition state. In the first state the layer makes sure that the processes involved can run smoothly by providing a central time integration management and a run control facility. In the transition state the layer does not run the modularized parts but it is solely the domain specific model. The Base Model Interface Layer is illustrated as a multiple socket outlet as it couples multiple submodels to the BML. The BMIL comprises three functionalities: one where it allows the BML to control the submodels, one where it organizes the data transfer between the layers and between the submodels and the export of data, and the third functionality concerns the data import interface. These functionalities are organized in generic submodels.

The Submodel Interface Layer is depicted as a connector from the appliance into the BMIL from which it collects relevant data. The SMIL is a submodel-specific interface that transfers this data from the BML through parameter lists to the Submodel Core Layer, which is depicted as the group of appliances, representing the submodels. The SMIL then calls the SMCL routines and redistributes the calculated results back to the BMIL. Besides the communication from the SMCL to the BMIL, the SMIL also performs the coupling and/or feedback between submodels that are managed within this SMIL. Lastly, the SMCL is indicated by the group of different appliances which represent the self-consistent core routines of a certain submodel. The output of a submodel is dependent solely on the input.

## 6.4. EMAC Submodel Configuration for the Current Research

The current version of MESSy (2.52) disposes of approximately 60 submodels that are grouped into: infrastructure (generic) submodels, chemistry submodels, physics submodels and diagnostic submodels. For the current research the interest lies with the tagged tracers and the chemistry in the atmosphere. A total of 38 submodels is used for the current research (see the Supplement of Mertens 2016) [30]. The TAGGING submodel and the MECCA submodel are of most interest [22]. Therefore, these two are discussed in the following subsection, which follows the description of the submodels as published by Grewe et al. (2017) [22].

### 6.4.1. TAGGING and MECCA submodels

The TAGGING submodel gives the abundance of species, it indicates the sources (anthropogenic and natural sources) the species emanate from, the origin location and the deposition (dry and wet) of it. In this way it is possible to assess the contribution of an emission source and its impact to the atmospheric chemical composition. In the TAGGING submodel ten different sources are distinguished, of which four are anthropogenic, five natural sources and a last mixed class source. A configuration of the chemical submodel MECCA is used which consists of 72 species [36]. However, in order to limit the required memory only a reduced set of species is tagged which resemble the main species and families for tropospheric chemistry. The set of species that are considered consists of the following seven: $CO$, $O_3$, $PAN$, $HO_2$, $OH$, $NO_y$ and $NMHC$. This results in a tagging scheme of 70 tagged tracers since there are ten emission sectors considered.

For the initialization of each tracer the chemical conversions, emissions, dry- and wet depositions and transport processes (except for $OH$ and $HO_2$) are deduced from the MECCA submodel. The information deduced from MECCA is processed in the core routines of the TAGGING submodel. To initialize the tagged tracers there are two options: initialize the variables from files, or, initialize the variables according to their key characteristics. By calculating the difference in concentrations of the chemical. The concentration changes of the chemical species are determined by calculating the difference of the concentrations of each species before and after dry and wet deposition. This calculation is performed in the MECCA submodel. This information is then transferred to the tagging submodel after which it is distributed among the tagged species, following their relative contribution. In Figure 6.5 a schematic overview is given of the most relevant submodels involved with the TAGGING submodel.

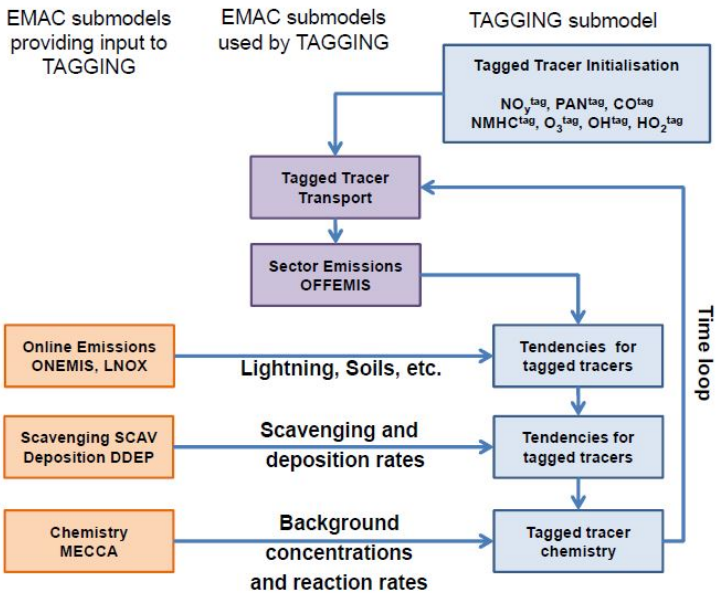


Figure 6.5: Representation of the EMAC physics, chemistry and diagnostic submodels applied (taken from [22]).

In the column on the right the TAGGING submodel is depicted. The middle column depicts the submodels of EMAC that are used by the TAGGING submodel for calculating the tagged trace transport and the contributions of offline emissions (OFFEMIS). In the column on the left other submodels of EMAC are depicted that provide input to the TAGGING model. ONEMIS is the submodel that calculates online 2D emissions for gas-phase tracers and it updates the tracer tendencies according to that. The LNOX submodel provides a parameterisation of the $NO_x$ produced by lightning and analogously to the ONEMIS submodel it feeds this information to the TAGGING model to update the tendencies for these tagged tracers. The simulation of wet deposition and liquid phase chemistry in precipitation fluxes is taken care of by the SCAV submodel. The gas phase and aerosol tracer dry deposition is simulated by the DDEP submodel. The outputs of the SCAV and DDEP submodels are also fed to the TAGGING submodel as input to update the tendencies for the tagged tracers. Finally the MECCA submodel plays a very important role in the TAGGING submodel chemistry module. This submodel calculates tropospheric and stratospheric chemistry. Its output consists of background concentrations and reaction rates which are fed to the TAGGING submodel for the tagged tracer chemistry simulation.

### 6.4.2. The Tagging and Tracing Method

To give a better understanding of the workings of the TAGGING submodel, the Tagging and Tracing method implemented in the submodel will be discussed in this subsection. This method is frequently used to assess the contribution of an emission source to specific concentrations. Each chemical species or family can be assigned a set of diagnostic tracers which experiences the same chemical conversions, sources and loss processes as the tracer that is being simulated. The sum of all tagged tracers must then equal the tracer that is simulated. Thus through this method the contribution of an emission sector, such as road traffic, to a concentration of a species is provided by this tagging method. The tagging method can be approached in various ways such as approaches that address a straight process chain from a specific emission species to a specific concentration, or a general tagging approach in which chemical reactions that compete in the production of the concentration to be analysed are taken into account. The first is the most frequently used tagging approach, but the latter approach allows the contribution of multiple emission sources to be determined, which is of interest for the thesis research at hand. Similarly, in the research of Grewe et al. (2017) it was of interest to investigate the contribution of different $NO_x$, $CO$ and $NMHC$ emission sectors to ozone and $HO_x$ chemistry [22]. For this end the general tagging approach was applied [18].

Implementing the general tagging scheme in the TAGGING submodel allows to monitor online the contribution of $NO_x$, $CO$, and $NMHC$ emissions sectors to ozone and $OH$ concentrations and it allows for a competition between the precursors of ozone while linearization is avoided. Furthermore the model is applicable in decadal simulations. For this implementation, the $NO_x$-ozone tagging approach by Emmons et al. (2012) and the VOC-ozone tagging approach by Butler et al. (2012) are combined [14] [8]. For the tagging approach, it is required that all sources of the species considered are quantified. Therefore, additional source categories are considered besides the emission sectors. The model setup described in this Section is obtained from Grewe et al. (2017) [22].

### 6.4.3. Basics on tagging method for tropospheric ozone production

As an example to set out the tagging approach the main reaction for tropospheric ozone production is taken, as explained in Grewe et al. (2017) (from Reaction 4.14, Section 4.2)[22]:

$$NO + HO_2 \rightarrow NO_2 + OH \tag{6.2}$$

$$NO_2 + h\nu \rightarrow NO + O \tag{6.3}$$

$$O_2 + O \rightarrow O_3 \tag{6.4}$$

In this chain, Reaction 6.2 (R6.1) is the rate limiting step, thus the production rate of ozone following this chain is dependent on the abundance of $NO$ and $HO_2$ and the reaction rate coefficient kR1 [3]. The concentration of nitrogen monoxide (NO) depends on emissions of this species from all the emission sources, for example industry and shipping with the respective concenrations $NO_x^{ind}$ and $NO_x^{sh}$, etc. Thus, the total ozone production rate $P_{R6.1}$ (introduced below) has to be distributed over all of these emission sectors, meaning a full partitioning of this production rate needs to be performed. This is done by a combinatorial reorganization of the concentrations following the tagged family and species of $NO_x$ and $HO_2$, respectively. This means that for all reactions involving combinations of $NO_x$ species and $HO_2$ species, the probability is calculated in the calculation of the production rate $P_{R6.1}$. This is illustrated in the following equations, where $i$ and $j$ denote a counter for all source categories, which is denoted by $N$:

$$\begin{aligned}
P_{R6.1} &= k_{R6.1} NOHO_2 \\
&= k_{R6.1} \sum_{i=1}^{N} NO^i \sum_{j\neq 1}^{N} HO_2^i \\
&= k_{R6.1} \sum_{i=1}^{N} \left( NO^i HO_2^i + \sum_{j\neq 1}^{N} \frac{1}{2} NO^i HO_2^j + \sum_{j\neq 1}^{N} \frac{1}{2} NO^j HO_2^i \right) \\
&= \sum_{i=1}^{N} \frac{1}{2} k_{R6.1} \left( \frac{NO^i}{NO} + \frac{HO_2^i}{HO_2} \right) \\
&= \sum_{i=1}^{N} P_{R6.1}^i
\end{aligned}$$

In these equations one can see the recurring factor $\frac{1}{2}$ which originates from the difference of the ozone production rate coefficients, which is equally attributed to emission category $i$ and $j$.
If for example the ozone production due to $NOx^{ind}$ from industry and due to $HO_x^{ind}$ from industry are taken the production rate becomes:

$$P_{R6.1}^{ind} = P_{R1} \frac{1}{2} \left( \frac{NO^{ind}}{NO} + \frac{HO_2^{ind}}{HO_2} \right) \tag{6.5}$$

Due to the factor $\frac{1}{2}$, double counting of reactions between $NO_x^{ind}$ and $HO_2^{ind}$ is prevented. However, this does not imply that in this reaction these species constitute to the same ozone production efficiency, as this is dependent on the chemical regime in which the reaction takes place (think of $NO_x$ sensitive vs. $NO_x$ saturated regimes [39]). The differential equation for the tagged species is then:

$$\frac{d}{dt} = O_3^{ind} = P^{ind} - D^{ind} \tag{6.6}$$

where $P^{ind}$ and $D^{ind}$ are the relevant production and loss terms of the ozone concentration by industry. Using this approach, it is shown that the when adding all emission contributions, the result equals the total concentration of the respective species. If this is done for all emission sectors, the sum of all these sectors equals the complete ozone concentration:

$$\sum_{i=1}^{N} O_3^i = O_3 \tag{6.7}$$

A different formulation can also be distinguished, which describes the right-hand side of expression 6.6 more generally. In this formulation the relative sensitivity of the individual production and loss terms with respect to the emission sector is considered:

$$P_{R1}^{ind} = P_{R1} \frac{\mathbf{s}^{ind\,T} \nabla s P_{R1}}{\mathbf{s}^T \nabla s P_{R1}}) \tag{6.8}$$

In this formulation, **s** denotes the vector of all the chemical compounds involved and $\nabla \mathbf{s} P_{R1}$ is the derivative of $P_{R1}$ with respect to this vector.

In summary, through the general tagging approach the different chemical fields can be divided and assigned to the contribution of their individual emission sectors. It should be noted that the tagging method itself is not a state-of-the-art method, but with the tagging approach described here the novelty lies in incorporating the competing effect of $NO_x$ and carbon compounds in producing ozone.

### 6.4.4. TAGGING chemistry

The TAGGING submodel distributes the chemical tendencies to the tagged tracers. In order to calculate the concentration changes as defined by the differential equation (Equation 6.6), the production and loss terms need to be determined. For this part, the ozone production and loss terms according to Crutzen and Schmaizl (1983) were used [11]. For the identification of ozone production and loss reactions, the tool ProdLoss is applied. This tool identifies the effective production and loss reactions for a tagged family in a selected chemical mechanism. In Appendix B the total chemistry overview of the TAGGING submodel is explained. Here, for simplicity, the production and loss terms according to Crutzen and Schmaizl (1983) are referred to as "ozone".

### 6.4.5. Sensitivities of the TAGGING scheme

The tagging scheme is investigated for sensitivity to changes in resolution and emissions by checking for plausibility and stability. For this end the horizontal resolution of the MECO(n) system was increased by roughly a factor of 5. A comparison was made between the original more coarse resolution and the finer resolution for the contributions of the individual emission sectors to the tropospheric ozone column as a mean over Europe, see Figures 6.6 and 6.7.

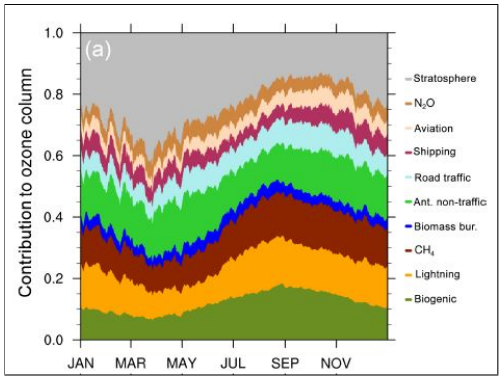


Figure 6.6: Contributions of emission sectors as indicated in the figure to the tropospheric $O_3$ concentration in Europe. A coarse resolution simulation with EMAC [22]

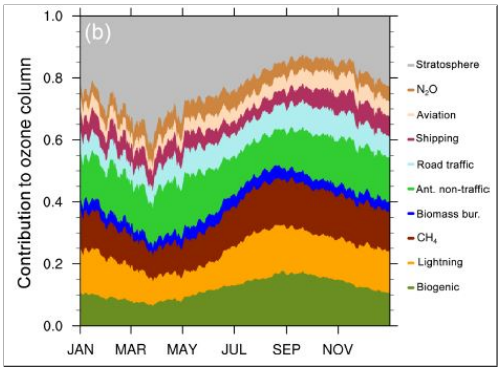


Figure 6.7: Contributions of emission sectors as indicated in the figure to the tropospheric $O_3$ concentration in Europe with a finer resolution simulation with MECO(n) [22]

From these figures it can be seen that the individual contributions show a similar behaviour with respect to their mean values and trends. The results for the finer resolution simulation show slightly finer-resolved structures in the horizontal. However, this does not affect the large-scale budgets, which are of interest for the current research. A same type of comparison was performed for the $OH$ and $HO_2$ contributions from shipping over the Mediterranean Sea. Again, the structures are similar. These comparisons clearly show that the tagging scheme is stable in its behaviour.

The TAGGING model was also investigated on its sensitivity to emission changes [22]. An additional global simulation was performed with EMAC where the emissions from the road traffic sector were reduced with 5%. It resulted that the chemical composition and the ozone productivity differs for the 5% road traffic emissions reduction from the base simulation. This lead to a 2-3% reduction in the said tagged ozone family. This lower reduction in ozone compared to the reduction in road traffic emissions is plausible since lowering surface $NO_x$ emissions will increase the ozone productivity. The relative change in tropospheric ozone induced by the 5% reduction in road traffic emissions was also considered.The total ozone change in this case amounts to 0.08%. This is a consequence of the 2-3% reduction in tagged road traffic ozone, which amounts to a reduction of the contribution of road traffic to the total tropospheric ozone by 0.16%. Thus, in total, the reduction in road traffic ozone change is a factor 2 greater than of the total ozone change. The compensating effects that are involved here result from other emission sectors which cause larger net ozone production rates.

Lastly, the TAGGING model has compromised its resolution significantly in order to limit memory demand. The tagging scheme for this model has therefore mapped the complex chemistry scheme onto a family concept which reduces the number of required tracers to a minimum. This results in a loss in accuracy and in and incidentally in unwanted side effects. These side effects could be overcome in the future by structuring the families in more detail.

# 7

# Methodology

In this chapter the methodology applied in the master thesis is discussed. After an introduction of the structure and methodology steps, the steps are detailed in Section 7.1 through 7.7. In Section 7.8 the analysis methods applied are discussed.
In Figure 7.1 the steps taken in this thesis are depicted in a flow chart. In this flowchart the tasks to be performed are depicted in the square boxes. The yellow arrows depict a moment in the process where a dataset is established with which further analysis is performed. Prior to the analysis a literature research was performed, which is depicted in the faded grey box. From the literature research the context for the research at hand was established, along with the constraints, Research Goals and Research Questions (see Chapter 2. The subjects researched during the literature study were covered in the Chapters 3 to 6. In the following subsections the steps depicted in the flowchart are discussed.

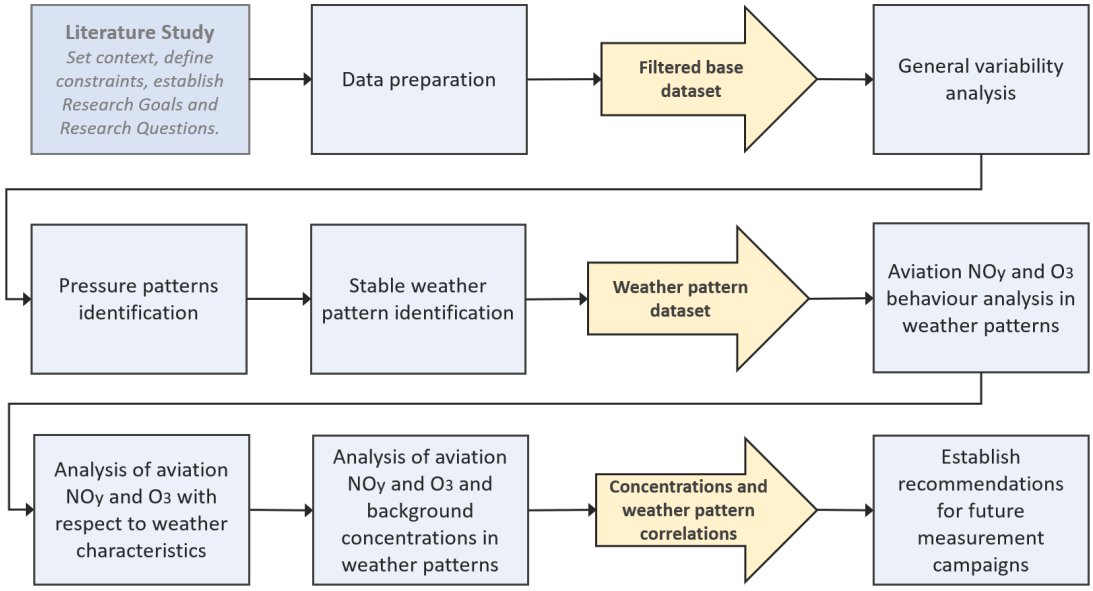


Figure 7.1: Overview of the steps taken to identify the correlations of aviation nitrogen oxides and ozone with specific weather patterns in order to establish recommendations for future measurement campaigns of aviation ozone.

## 7.1. Data preparation

Within the present study global three-dimensional atmospheric- and atmospheric chemical data is used. This data is made available by the DLR and the DKRZ and are stored at the supercomputer of the DKRZ to which access is granted for this project. The data employed is simulated by the EMAC model in the configuration detailed in Chapter 6. Due to the extensive amount of data and the high computing power needed, the data is selected, filtered and categorised first for further analysis. In this way only necessary input is analysed which reduces the computing power and time and targeted research is carried out.

The data provided consists of simulations from 2004 until 2015, of which the first two years serve as spin-up years. Therefore, data from years 2004 and 2005 are not considered. Since the most dense air traffic is found on the Northern Hemisphere and thus here the largest effect of aviation $NO_x$ and $O_3$ is found, the analysis focuses on the Northern Hemisphere and data from the Southern Hemisphere is excluded. Furthermore, weather patterns are most characteristics in the Northern Hemispheric Winter and Summer months, December, January and February (DJF) and June,

July and August (JJA), respectively, and less characteristic in the remaining months. The research of Wauben et al. suggested that the ozone perturbation due to aviation can be identified under specific meteorological conditions [42]. Correlations between weather patterns and concentrations are therefore expected to be more prominent during the DJA and JJA seasons where weather patterns are more characteristic, thus the remaining months are excluded from the analysis. Finally, data around flightlevel (175-300 hPa) is considered, as at these altitudes the aviation perturbation is most prominent [19]. An overview of the selected subsets of the data is given in Table 7.1

| **Dataset category** | **Selected data** |
|---|---|
| Years | 2006 - 2015 |
| Location | Northern Hemisphere (0°- 90°N and 0°- 360°E) |
| Season | December, January, February (DJF) and June, July, August (JJA) |
| Vertical dimension | Sigma hybrid pressure levels 69 - 75 (~175 - 300 hPa) |

Table 7.1: Selected subsets from simulation data

After the base dataset is filtered, the general variability of aviation $NO_x$ and $O_3$ in the atmosphere is assessed. This general variability is important to understand as it affects the behavior of these species' behaviour in weather patterns dependent on the season and its location.

## 7.2. General variability of aviation $NO_x$ and $O_3$ in the atmosphere

The general variability of aviation $NO_x$ and $O_3$ in the atmosphere is analysed with respect to latitude, longitude, season (DJF versus JJA) and altitude (200 hPa versus 225 hPa). For this the relative contributions with respect to background concentrations are assessed and the mixing ratios of the species are set out with respect to the parameters mentioned. This variability needs to be taken into account when examining the behaviour of aviation $NO_x$ and $O_3$ in weather patterns in different seasons and locations.

The $NO_x$ and $O_3$ mixing ratios are obtained from the TAGGING submodel and are given in [mol/mol]. The species are four dimensional, meaning that they can be obtained following the the dimensions time, level, latitude, and longitude. For $NO_x$ there is no separate tracer simulated but the $NO_y$ is simulated. Since $NO_x$ and $NO_y$ occur in the same ratio, for further analysis the $NO_y$ tracer is applied.

| Tagged Tracer [mol mol$^{-1}$] | Family |
|---|---|
| $NO_y^{lig}$, $O_3^{lig}$ | Lightning |
| $NO_y^{bio}$, $O_3^{bio}$ | Biomass |
| $NO_y^{soi}$, $O_3^{soi}$ | Soils |
| $NO_y^{ind}$, $O_3^{ind}$ | Industry |
| $NO_y^{tra}$, $O_3^{tra}$ | Transport |
| $NO_y^{shp}$, $O_3^{shp}$ | Shipping |
| $NO_y^{air}$, $O_3^{air}$ | Aviation |
| $NO_y^{n2o}$, $O_3^{n2o}$ | Nitrous oxide decomposition |
| $NO_y^{ch4}$, $O_3^{ch4}$ | Methane decomposition |
| $NO_y^{str}$, $O_3^{str}$ | Stratosphere |

In further analysis the mixing ratios of aviation $NO_y$ and $O_3$ are referred to as *foreground* parameters, whereas the other sources are referred to as *background* parameters. The foreground species are investigated to analyse the variability of the mixing ratios with respect to e.g. latitude and season. To analyse the relative contribution these foreground species are taken relatively to the sum of the background concentrations.

For the analysis of the general variability with respect to latitude and season the monthly mean average values are taken as this represents sufficiently the variability of these species over ten years of data.

## 7.3. Identification of pressure patterns

After the general variability analysis the research zooms in to a smaller scale to analyse the concentration changes within weather patterns. In order to do so, first weather patterns need to be established that can be analysed. For this the geopotential height anomalies are investigated at pressure level 200 hPa. These patterns are then analysed for positive anomalies larger than 200 gpm.

### 7.3.1. Geopotential height

In order to understand how geopotential height anomalies can identify weather patterns, the geopotential and the geopotential height needs to be explained. The geopotential height is an approximation of the elevation of a pressure level above mean sea level which is calculated using the geopotential. The geopotential is defined as the work needed to displace an air parcel from sea-level to a specific pressure height against gravitation and is given by:

$$\Phi(h) = \int_0^h g(\phi, z)\, dz \tag{7.1}$$

where $g(\phi, z)$ denotes the gravitational acceleration as a function of latitude and altitude. When the geopotential is normalized with respect to the Earth's standard gravitation ($g_0$) the geopotential height is obtained:

$$Z(h) = \frac{\Phi(h)}{g_0} \tag{7.2}$$

When the geopotential for a specific pressure level, say 200 hPa, is investigated, an air parcel with its pressure level at a higher altitude than average needs more work against gravitation than an air parcel with the pressure level at average altitude. Therefore, when normalizing with respect to the Earth's standard gravitation, the geopotential height of an air parcel containing an air pressure of 200 hPa at a higher altitude implies a larger geopotential height compared to an air parcel with an air pressure of 200 hPa at a lower altitude.

### 7.3.2. Geopotential height anomaly

In meteorology the geopotential height is applicable to identify weather patterns by assessing geopotential height anomalies. For this analysis, the geopotential height values of a certain pressure level are compared to monthly mean values. When the geoptential height deviates positively from the monthly mean (i.e. is larger), the anomaly is positive, whereas when it deviates negatively the anomaly is negative.

A positive geopotential height anomaly indicates that an air pressure level is located at a higher altitude than usual. According to the ideal gas law when an air parcel increases volume at a constant pressure, the temperature must increase as well. A constant pressure but an increase in volume results in a decrease in density, which causes the air parcel to rise. Therefore, a positive geopotential height anomaly means that the volume and thus temperature of the air parcel are also larger than usual. In this sense the geopotential height anomaly can be applied to identify air regions that are warmer or colder than usual. If such a region is stable for a longer period of time (at least 24 hours), one can speak of a stable weather pattern. In Figure 7.2 a contourfill map of the geopotential height anomalies at December 1st, 2007 at 00:00h is depicted. Here a clear high-pressure pattern is found around 190°E and 240°E and 45°N and 80°N, where the geopotential height anomaly is clearly positive. The blue regions indicate a negative geopotential height anomaly and thus low-pressure patterns.

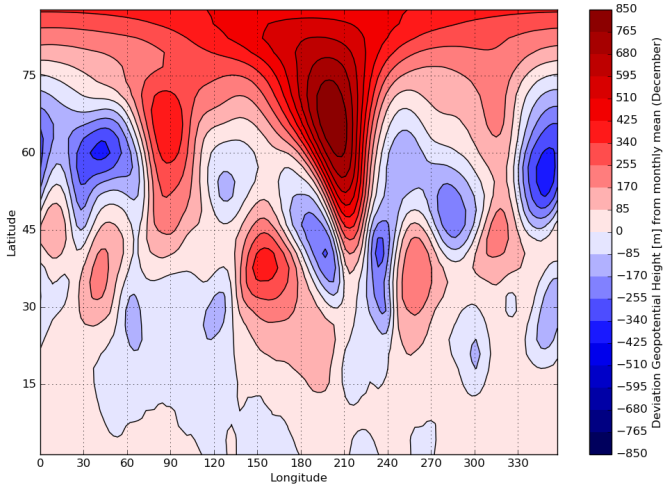


Figure 7.2: Geopotential height anomalies for December 1st 2007, 00:00

For the filtered years, location and season mentioned in Table 7.1 the geopotential height anomalies are calculated at pressure level 200 hPa. This data is then fed into a model that identifies patterns that are stable for more than two timesteps (one timestep covers 10 hours of simulation output, thus two timesteps covers 20 hours). This model is explained in the following subsection.

## 7.4. Stable weather pattern identification

A pressure pattern is worth analysing when it is stable over a longer period of time (at least two timesteps). If this is the case it can be called a weather pattern that constitutes certain weather characteristics throughout the lifetime of the weather pattern, i.e. certain relative humidity ($RH$) values and dry temperature values ($T_{dry}$) for example. It is expected that in a high-pressure system $NO_x$ from aviation accumulates which could potentially lead to an increase in ozone production. Therefore, the research focusses on stable high-pressure systems to test this hypothesis. In order to identify such pressure patterns a diagnostic model is developed that recognizes whether a pressure pattern survives to the next timestep. This diagnostic tool is discussed in this section.

### 7.4.1. General steps of the diagnostic tool

The tool identifies pressure patterns that last for at least two timesteps and outputs this into a dataframe that contains the coordinates of that pressure pattern, its timestep, its lifetime, and labels its location (East, West or Mid) which is relevant for further analysis. The pressure patterns obtained in Subsection 7.3 are fed into this model and the dataframe that results from the model is used to obtain data such as mixing ratios, production rates and weather variables from the EMAC model belonging to those weather patterns.

In Figure 7.3 an overview of the model is given in a flowchart. The square dashed box indicate datasets, the ellipses process steps and the yellow arrowed-boxes depict a filtering process step.

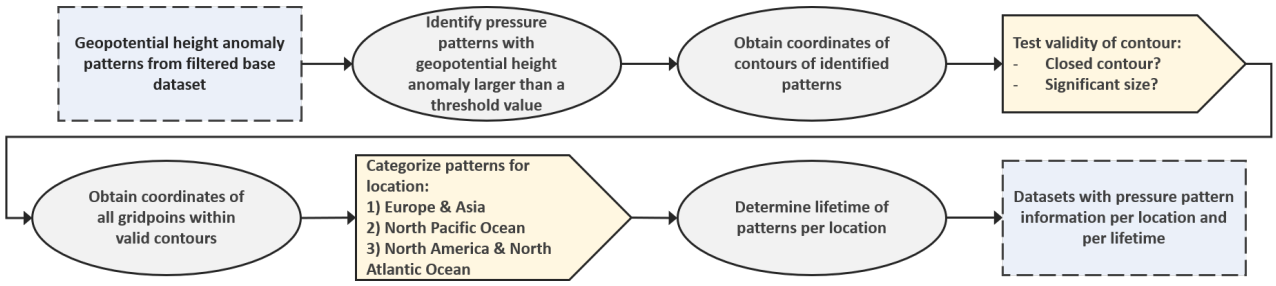


Figure 7.3: Flowchart depicting the algorithm for identifying stable weather patterns.

### 7.4.2. Diagnostic tool steps detailed

The steps illustrated in Figure 7.3 are discussed in the following text.

#### Filtering on geopotential height anomaly threshold value

Firstly regions which contain geopotential height anomalies larger than a predetermined threshold value are selected. The threshold value is set to 200 as this results in a sufficiently large set of strong pressure regions. Selecting a value lower than 200 results in a large dataset of weaker patterns with too noisy data. Selecting a value higher than 200 on the other hand yields too less patterns and reduces the size of the dataset such that patterns cannot be compared to each other.

#### Validating regions found

The regions found are highly variable in size and location. Some regions are of insignificant size (e.g. five gridpoints) such that no notable concentration changes can be identified there. Furthermore, some regions are cut off by the x- or y-boundaries of the contourplots. Therefore, only closed contours of sufficient size will be selected and filtered. The regions found need to satisfy two conditions:

- A region should constitute a closed contour
- A region should contain at least 20 by 20 gridpoints

#### Obtain gridpoint coordinates of regions

After validating and filtering the contours of the pressure patterns, the coordinates of the gridpoints within the contours are obtained. The pressure patterns are then categorised based on their location. The division of the longitudinal locations is depicted in Figure 7.4 where the three regions are numbered accordingly. This division is chosen due to the variability in air traffic density and atmospheric conditions between the regions. By dividing and analysing the weather patterns in these three groups it can be investigated whether this variability influences the perturbation of aviation $NO_x$ and $O_3$.

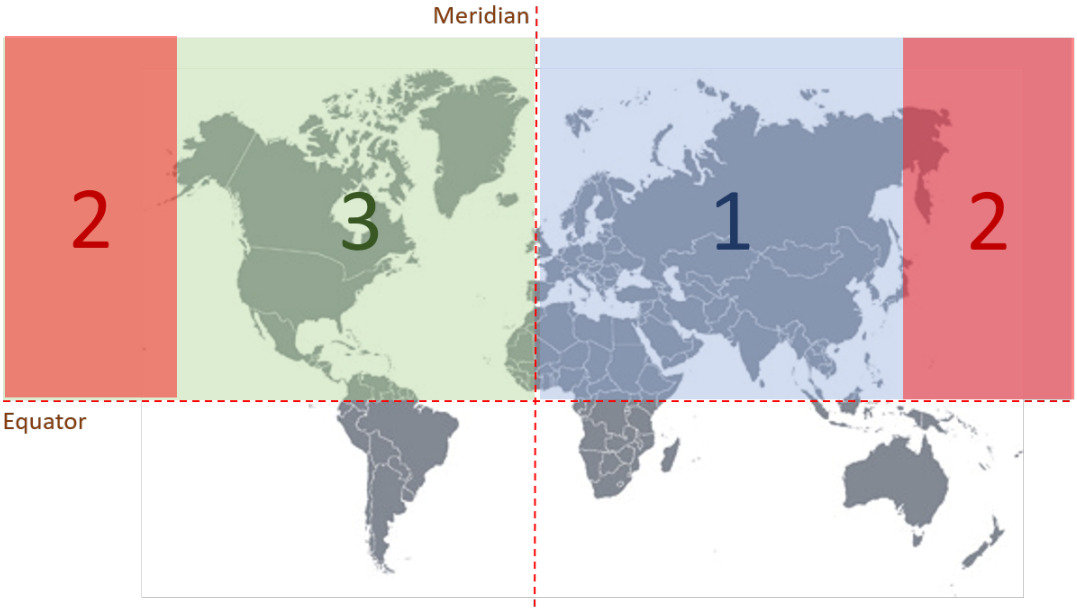


Figure 7.4: Worldmap with regions 1, 2 and 3 in which the pressure patterns are categorized

### Determine the lifetime of the patterns

After the region categorisation the lifetime of the pressure patterns are determined. This is done by investigating whether a pressure pattern survives to a next timestep. This is repeated until the pressure pattern does not survive to the next timestep. Since a pressure pattern never remains in a static state but changes form and drifts slowly with respect to time and the EMAC model outputs simulated data per 10 hours, this drift needs to be taken into account. Therefore, the model developed analyses whether 65% or more of the gridpoints of the pattern has survived to the next timestep.

The model outputs datasets with pressure pattern information per region and lifetime. The information contained in these datasets are needed to obtain the $NO_y$ and $O_3$ concentrations of aviation and weather characteristics per pressure pattern. Therefore it contains the 4 dimensions in which the EMAC model outputs data: time, level, latitude and longitude per pressure pattern per gridpoint. Additionally it contains labels with is region and lifetime.

### Calculate the pattern size

Lastly, to allow comparison between varying sizes of pressure patterns, the obtained mixing ratios (discussed in Subsection 7.5 and weather characteristic values (discussed in Subsection 7.6) are normalized with respect to pattern size. For this the surface area of each gridpoint is calculated and the total area per pattern is calculated and included in the dataset as well.

The area of each gridpoint is approximated by the area of a trapezium (Figure 7.5. The dimensions of the of the bases and tops of these trapezia are calculated by the circumference of the latitudinal bands at 200 hPa ($R$+$h_{lev}$). The height of the trapezia is approximated to be equal for each gridpoint. The total surface area of a pattern is then calculated by summing the area of all gridpoints belonging to that pattern.

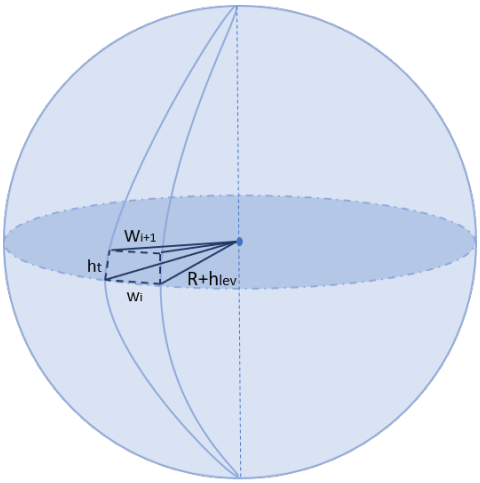


Figure 7.5: Illustration of gridpoint area approximation

To validate this approximation the total surface area of one longitudinal band is calculated following the formula of a wedge. The simulation divides the longitudinal dimension into 128 longitudinal bands of each 2.8125 degrees, or $\frac{2.8125}{2\pi}$ radians. Therefore the surface area of a wedge of $\frac{2.8125}{2\pi}$ is compared:

$$A = 2 \cdot \frac{2.8125}{2\pi} \cdot R^2 \tag{7.3}$$

Where R is the Earth's radius. For one longitudinal band on the Northern Hemisphere this comes down to a surface area of 1999325.46906 $m^2$. The approximated total surface area of all the gridpoints in this same longitudinal band equals 19998923.99315 $m^2$. This comes down to an acceptable error of 0.14 %.

## 7.5. $NO_x$ and $O_3$ behaviour in weather patterns

With the information from the developed model, the normalized mixing ratios per weather pattern can be determined. The concentration changes within a weather pattern can then be analysed. This analysis is carried out for each of the three regions at average cruise level (model hybrid pressure level 72), at lower cruise level (level 75) and at high cruise altitudes (level 69) to identify how the concentrations develop with respect to altitude in such a weather pattern. The analysis is carried out for weather patterns with a lifetime between 2 timesteps (T2) and 9 timesteps (T9). Analysing weather patterns with longer lifetimes result in highly variable results as these are rare and cannot constitute to a clear conclusion.

To assess the temporal development of the foreground concentrations in these weather patterns, the analysis for each pattern is commenced 5 timestep before the formation of the weather pattern until 5 timesteps after the the lifetime of a weather pattern. Beside the distinction in longitudinal location (region 1, region 2 and region 3) also a distinction in season is made in the analysis, therefore the Summer and Winter patterns are analysed seperately. Table 7.2 gives an overview of the selection of weather patterns analysed.

Table 7.2: Overview of weather pattern categories analysed

| Category | Analysed |
|---|---|
| Levels | 69, 72, 75 |
| Timesteps | t-5, t-4, t-3, t-2, t-1, t0, t2, ... , tn, t+1, t+2, t+3, t+4, t+5 |
| Locations | region 1, region 2, region 3 |
| Seasons | Winter (DJF), Summer (JJA) |

## 7.6. $NO_x$ and $O_3$ correlations with respect to weather variables

In Section 4.3 it was discussed that pressure, temperature, solar radiation and background concentrations influence the reaction productivity of ozone. These parameters can be translated into weather characteristics that influence the reaction productivity of ozone in the atmosphere. Therefore, it is investigated which weather variables affect the behaviour of aviation $NO_y$ and $O_3$. The weather variables taken into account are:

Table 7.3: Overview of weather variables analysed with respect to ozone and nitrogen oxides from aviation

| Name | Description | Source | Unit |
|---|---|---|---|
| geopot | Geopotential height | ECHAM5 | [$m^2 s^{-2}$] |
| tpot | Potential temperature | ECHAM5 | [K] |
| **tm1** | **Dry air temperature** | **ECHAM5** | **[K]** |
| um1 | Wind velocity in longitudinal direction | ECHAM5 | [$ms^{-1}$] |
| vm1 | Wind velocity in latitudinal direction | ECHAM5 | $ms^{-1}$ |
| **rhum** | **Relative Humidity** | **ECHAM5** | **[%]** |
| **PV** | **Potential vorticity** | **Tropop** | **[pvu]** |

Because dry air temperature, relative humidity and potential vorticity have shown a strong correlation to the foreground concentrations, these will be discussed further.

- **Dry Air Temperature**: the absolute temperature of an air parcel, given it is not influenced by radiation and with the absence of moisture, is given by the dry temperature ($T_{dry}$). This implies that the amount of heat within an air parcel and is thus proportional to the kinetic energy within the air parcel (Ahrens, 2012). As discussed in Section 4.3 the temperature in an air parcel could positively increase the production efficiency of avaition $O_3$. Therefore, it is investigated how the $T_{dry}$ affects the aviation $O_3$ in a weather pattern.
- **Relative humidity**: the ratio of partial pressure of water vapor to the equilibrium vapor pressure of water at a given temperature is given by the Relative Humidity of an air parcel. The Relative Humidity is given by the following equation ([29]):

$$U = \frac{q}{q_*} \times 100\% \tag{7.4}$$

  In this equation $U$ is the relative humidity, $q$ denotes the specific humidity and $q_*$ denotes the saturation-specific humidity, which is a function of temperature and pressure. The specific humidity is a measure of the mass of water vapor to the mass of air per unit volume. In the following text Relative Humidity is referred to as $RH$ instead of $U$. At 100% $RH$ the air has saturated and is at its dewpoint and precipitation is most likely to occur (though other factors such as condensation are required for precipitation to occur). From preliminary analysis RH showed a potential correlation to aviation ozone and it is therefore of interest to investigate how specific $RH$ values affect the production of aviation $O_3$ in a weather pattern.
- **Potential vorticity**: the absolute circulation within an air parcel enclosed by two isentropic surfaces is expressed by the potential vorticity [28]. An isentropic surface is a surface in the atmosphere with a constant potential temperature. The potential vorticity is expressed by the dot product of vorticity and stratification, meaning that if e.g. the column height over which the potential vorticity is calculated decreases, the vorticity increases such that the potential vorticity remains constant. At low latitudes low PV values are found (close to zero), which increases with latitude [6]. Additionally the PV also increases with altitude, and at flight levels the latitudinal variability of PV is even more present (ranging from 0 PVU at low latitudes up to 9 PVU at polar regions).

  When the isentropic surfaces between which the potential vorticity is analysed are close together, the potential vorticity is large. As such, above the tropopause the isentropic layers are closer together, thus elevated PV values are found here. If air parcels with elevated PV levels from above the tropopause are transported downward into the Troposphere where the isentropic surfaces are located further away from each other, the vorticity in the air parcel increases in order to conserve of the potential vorticity. Therefore, if the altitude of the tropopause decreases, the local vorticity increases, and Positive Vorticity Advection (PVA) takes place which leads to vertical movement in the troposphere [28]. Therefore, if air parcels with elevated PV values compared to the surrounding air are found in the troposphere, these air parcels have most likely been transported from above the tropopause into the troposphere. High-pressure systems generally contain low PV values as these contain air rising from lower altitudes with low PV values. As such, elevated PV values in high-pressure system indicate vertical transport from higher altitudes. As this variability in potential vorticity indicates vertical transport, it is of interest to investigate whether PV values in high-pressure systems are correlated to aviation $NO_x$ and $O_3$ concentrations.

## 7.7. $NO_x$ and $O_3$ and background concentration development in weather patterns

From the analysis of aviation $NO_x$ and $O_3$ changes with respect to weather patterns and weather characteristics, it is assessed whether correlations exist between said concentration changes and weather patterns. When these correlations have been established, it is investigated whether the concentration changes in aviation $O_3$ contribute to

detectable perturbations in the total $O_3$ budget in the weather patterns. For this, the concentration changes of those species per weather pattern are compared to the total $O_3$ concentrations in the weather pattern.
Firstly, the Spearman's correlation coefficient is calculated for the correlation between total ozone and aviation ozone, total ozone and stratospheric ozone, and stratospheric ozone and aviation ozone. This is done for each all the weather patterns at each level separately, because it is expected that the correlations vary per level due to the lifetimes of the precursors of these groups.

When the correlations are detected, the trends of the three groups are plotted to visualise the correlations. By then comparing the trend of aviation ozone versus total ozone for example, one can visualise this correlation. This is done according to the following steps:

1. Calculate the relative change of the total $O_3$ concentration per timestep (in percentages)

$$\Delta O_{3_{tot}} = \frac{O_{3_{tot}(i+1)} - O_{3_{tot}(i)}}{O_{3_{tot}(i)}} \cdot 100 \tag{7.5}$$

2. Calculate the relative change of the aviation $O_3$ concentration per timestep (in percentages) following Equation 7.5.
3. Compare the relative changes of the total and aviation concentrations by substracting the aviation ozone relative changes from the total ozone relative changes for each timestep.

If from this comparison a difference close zero results, it is concluded that the trend of aviation ozone behaves similarly to the total ozone. Ozone from the stratosphere ($O_{3_{str}}$) proved to have a large impact on the total ozone budget and therefore is also included in this analysis. If it results that the stratospheric ozone has a stronger similar trend as the total ozone, the total ozone is affected largest by the stratospheric ozone, due to the larger order of magnitude of stratospheric ozone in the atmosphere compared to aviation ozone.

## 7.8. Analysis methods used

### 7.8.1. Contour and contourfill plots

Contour and contourfill plots are used to visualise three-dimensional data on a two-dimensional plane. A contour plot graphs the x- and y- independent variables and the dependent third variable in z-direction as contours. A familiar example of a contourplot in meteorology are e.g. maps with isolines depicting isobars or isotherms. To emphasize values of regions enclosed by contour lines and the difference between two regions (for example positive versus negative values), the contourfill plots can be employed. These plots fill the contour lines in gradients of colours, according to the values found within a contour plot. In this way a clear distinction between negative and positive regions within a contourfill plot can be identified.

The contour- and contourfill plots are used to visualize the geopotential height anomalies at 200 hPa (see Subsection 7.3) and to identify weather patterns in these geopotential height anomaly plots (see Subsection 7.4).

### 7.8.2. Box- and whisker plots

Box- and whisker plots visualize the range of values of a large dataset in a compact manner. It depicts for a dataset the mean or median, the minimum and maximum, the first quartile and the third quartile, and outliers of the dataset. This way not only the range of values within a dataset is illustrated, but also its distribution. The amount of data analysed is rather large and also comparisons between subsets of the data need to be performed. Box- and whiskerplots provide an efficient and compact solution to understanding the range and distribution of a large dataset, but also its inter-variability between subsets of the data.

The box- and whiskerplots are applied to assess the variability of aviation $NO_x$ and $O_3$ with respect to latitude, season, location and with respect to the background concentrations. The boxplots are also used to assess the distribution and variability of weather characteristics within the weather patterns in order to find specific correlations with the aviation $NO_x$ and $O_3$ concentration changes.

### 7.8.3. Kernel Density Estimates (KDE) and joint KDE plots

A Kernel Density Estimate (KDE) is a non-parametric means of estimating the probability density function of a random continuous variable. The KDE is based on a finite dataset, for which the probability density function is estimated. A KDE provides a smooth graph that shows the shape of a dataset. A great advantage of the KDE is that When the correct variables are chosen to shape the KDE, it clearly represents the typical values around which the data accumulates.

Therefore the KDE is used to investigate whether specific combinations of aviation $NO_x$ and $O_3$ concentrations accumulate around specific values of weather characteristics such as relative humidity. If this is the case, it indicates a relationship between this variable and the concentration combinations.

Joint KDE plots are used to visualize two distributions against each other, in this case two distributions defined by the KDE. With the distribution of one variable along the x-axis and the distribution of another variable along the y-axis, the joint grid that the two distributions enclose shows the density areas where the two distributions coincide. Using density contour plots, an area where the distributions strongly correlate is coloured darker than the surrounding areas. This way it is clearly visualized how two distributions correlate to one another.

### 7.8.4. Spearman's rank correlation coefficients and correlation matrices

The Spearman's rank correlation coefficient is a non-parametric measure of rank correlation. It investigates the dependence between the rankings of two variables that do not need to be normally distributed. The Spearman's correlation is a statistical measure of the strength of a monotonic relationship between two variables. In a monotonic function it is never permitted that the dependent variable sometimes decreases and sometimes increases with the dependent variable, it always either decreases or increases with the dependent variable. The Spearman's coefficient is a value between -1 and +1, with -1 being a very strong negative relationship and +1 a very strong positive relationship.

To provide a clear overview of the correlation coefficients between the variables analysed, the coeffecients are put into a correlation matrix. A correlation matrix contains the variables analysed on the y- and x-axis and the correlation coefficient between specific variables at their intersection. A color pallette is often added for emphasize the strength of correlations between variables.

### 7.8.5. Scatterplots

Scatterplots are used to visualize the distribution of a dependent variable with respect to an independent variable. On the x-axis the independent variable is set out and on the y-axis the dependent variable. Scatterplots provide a clear illustration of the distribution and probable dependency between two variables. If the datapoints in a scatterplot accumulate over a specific region in the plot or over a certain trend, further investigation of the data can be performed to determine the dependency of the variables. For example fitting a trendline using linear or polynomial regression (see Subsection 7.8.6, indicates whether a correlation exists between the two variables.

A dependency on a third variable can also be investigated by expressing the third dimension in a colour range. The gradient of the colour range is linked to a specific value of the third variable dimension. This way, the correlations between three variables can be analysed.

Scatterplots are used to investigate the relationship of the $NO_y$ and $O_3$ of aviation in specific weather patterns and whether these correlate to specific weather characteristics. Furthermore they are used to investigate the relationship of specific weather characteristics within weather patterns and on different, for various altitudes.

### 7.8.6. Polynomial linear regression

Polynomial linear regression is a form of regression analysis in which the relationship between an independent and dependent variable is modelled as an $n$th degree polynomial in the dependent variable. For a set of independent (x) variables with respective dependent (y) variables a correlation can be found using polynomial linear regression. This is desirable when a scatterplot of two variables suggest the presence of a correlation, but it cannot be clearly deduced. Polynomial linear regression is given by the following formula:

$$y = b_0 + b_1 x_x + b_2 x_1^2 + ... + b_n x_1^n \tag{7.6}$$

A polynomial linearly regressed graph can be plotted over a scatter plot to indicate a correlation between the variables plotted over the x- and y-axis.

Polynomial linear regression is applied in this thesis to investigate whether a relationship exists between aviation $NO_x$ and $O_3$ in weather patterns and also with relation to weather variables.

# 8

# Variability Analysis of Aviation $NO_y$ and $O_3$ in the Northern Hemisphere

The variability of aviation $NO_y$ and $O_3$ over the Northern Hemisphere at flight level is analysed with respect to season and latitude. This variability is compactly visualized with boxplots as these offer a clear and concise overview of the distribution of various datasets. This is discussed in Section 8.1. The mixing ratios of these species are also analysed with respect to relative humidity, dry air temperature and potential vorticity. This analysis is carried out using Kernel Density Estimates, scatter plots, and joint KDE's, and is discussed in Section 8.2. This Chapter is concluded by a summary and discussion on the results in Section 8.3.
In this Chapter the results of the analysis of the variability of aviation $NO_y$ and $O_3$ is

## 8.1. Latitudinal and seasonal variability

In Chapter **ref** the current understanding in literature of the variability of aviation $NO_x$ and $O_3$ in the atmosphere was discussed. For the current research this variability is reassessed with the provided tagged data, as this variability influences the concentrations of specific weather patterns at specific locations that are analysed in the following steps. The average mixing ratios and relative contributions of aviation $NO_y$ and $O_3$ are considered in this text.

### 8.1.1. $NO_x$ and $O_3$ mixing ratio

In Figure 8.1 and 8.2 the distribution of mixing ratios of aviation $NO_y$ and $O_3$ are depicted in boxplots, respectively, for Region 1 at 200 hPa. For these figures, the monthly average values were taken over ten years, for both Summer and Winter months.

In these figures it can be seen that the aviation $NO_y$ and $O_3$ mixing ratios increase with latitude. The mixing ratios are lowest for low latitudes, as here the least air traffic takes place. For mid-latitudes the first and third quartiles of ozone and $NO_y$ show a large range, for both summer and winter. This is attributed to the gradual increase of aviation traffic from the mid-latitudes to higher latitudes. At higher latitudes the aviation $NO_y$ and $O_3$ both increase due to the large amount of air traffic taking place at these latitudes [32]. At high- to polar latitudes maximum values of $NO_y$ and $O_3$ are found although the highest air traffic is not found here. These maximum values are due to the horizontal transport of air from lower latitudes to the polar regions, resulting in the maximum values to appear here.

At higher latitudes, Winter show lower values of ozone and $NO_y$ compared to Summer. This is in agreement with results of $NO_x$ measurement campaigns that have been performed [43]. The lower values found for Winter are attributed to the 12% lower fuel burn in this season compared to Summer [32].

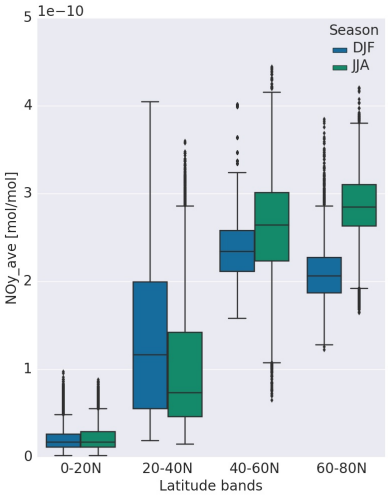


Figure 8.1: Boxplots showing the range of mixing ratios of aviation nitrogen oxides in Region 1 for winter (DJF) and summer (JJA)

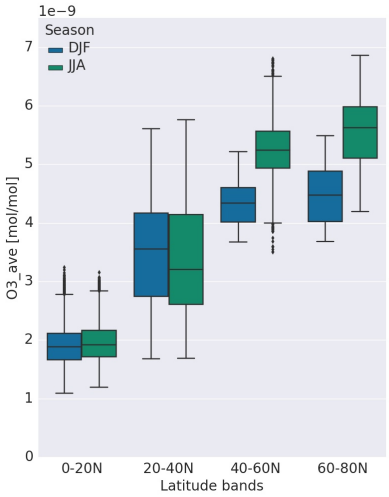


Figure 8.2: Boxplots showing the range of mixing ratios of aviation ozone in Region 1 for winter (DJF) and summer (JJA)

In Figures 8.3 until 8.6 the ranges of mixing ratios of aviation $NO_y$ and ozone are depicted for Region 2 and Region 3. These show a similar pattern as Region 1 with low values at low latitudes and maximum values towards the polar region.

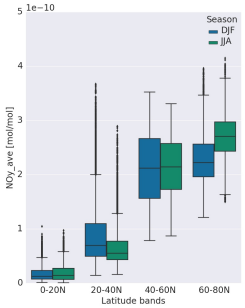

Figure 8.3: Boxplots showing the range of mixing ratios of aviation nitrogen oxides in Region 2 for winter (DJF) and summer (JJA)

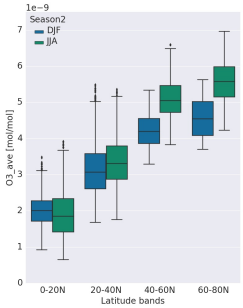

Figure 8.4: Boxplots showing the range of mixing ratios of aviation ozone in Region 2 for winter (DJF) and summer (JJA)

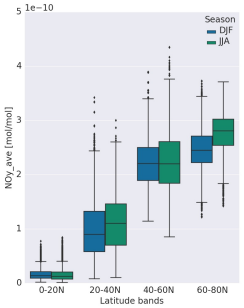

Figure 8.5: Boxplots showing the range of mixing ratios of aviation nitrogen oxides in Region 3 for winter (DJF) and summer (JJA)

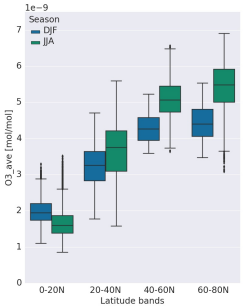

Figure 8.6: Boxplots showing the range of mixing ratios of aviation ozone in Region 3 for winter (DJF) and summer (JJA)

### 8.1.2. Aviation $NO_x$ and $O_3$ relative contribution

The average relative contributions of aviation $NO_y$ and $O_3$ are taken with respect to their total constituents ($NO_{y\,tot}$ and $O_{3\,tot}$), averaged over 10 years of data in the Northern Hemisphere. Again, the Winter season is compared to the Summer season for Region 1 in the boxplots given in Figures 8.7 and 8.8.

The relative contribution of $NO_y$ shows a similar pattern to the $NO_y$ mixing ratio distribution as it increases from low latitudes to high latitudes. The maximum values however are no longer found in the polar regions, but rather closer to latitudinal bands between 40deg N and 60deg N. This is attributed to the higher background concentrations found at the high- to polar latitudes due to horizontal transport in the atmosphere.

The relative contribution distributions of ozone exhibits a rather different trend compared to the ozone mixing ratio distributions. The relative contribution at low latitudes have increased to a close to equal value found at mid latitudes, while at high- to polar latitudes the relative contribution is relatively lower. Due to convection and horizontal transport the background concentrations of ozone at lower latitudes are lower and increase with latitude with a maximum at polar regions. Therefore, even though the mixing ratios at low latitudes are relatively lower at low latitudes compared to mid- and high latitudes, the relative contributions are close to the same range due to the equally lower background concentrations.

In Winter the relative contribution is higher than in Summer, while the mixing ratios resulted to be generally lower. This is due to the higher dynamical activity in the atmosphere in the Summer where more deep convection takes place, resulting in larger background concentrations. Therefore, with respect to the background concentrations, aviation $NO_y$ and $O_3$ have a larger relative contribution in Winter than in Summer. However, the climate impact of aviation is still larger in Summer due to the more efficient ozone production [41].

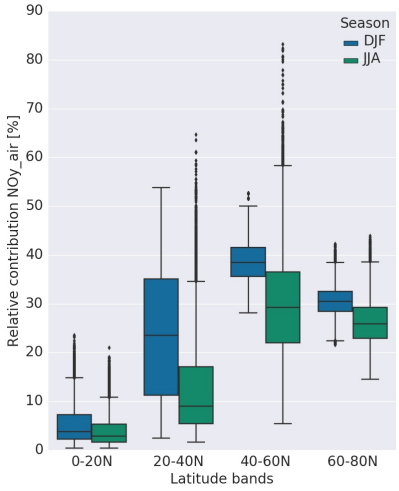


Figure 8.7: Boxplots showing the distribution of relative contributions of aviation nitrogen oxides in Region 1 for winter (DJF) and summer (JJA)

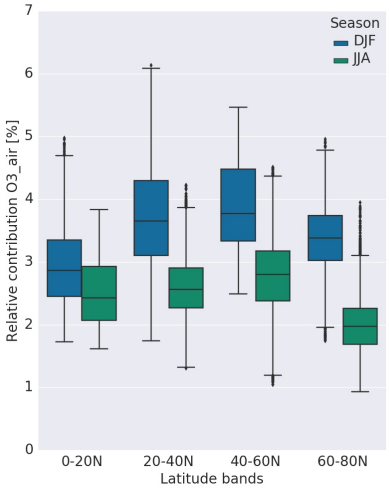


Figure 8.8: Boxplots showing the distribution of relative contributions of aviation ozone in Region 1 for winter (DJF) and summer (JJA)

In Figures 8.9 up to 8.12 the average relative contribution distributions of aviation $NO_y$ and $O_3$ are depicted for Region 2 and 3. Analogously to Region 1, the boxplots for Region 2 and 3 show an increase of relative contribution of aviation $NO_y$ with latitude towards polar regions. The relative contribution of aviation $O_3$ for Region 2 and 3 show a similar pattern to that of Region 1 as well. In all cases the relative contribution in Winter is higher than in Summer.

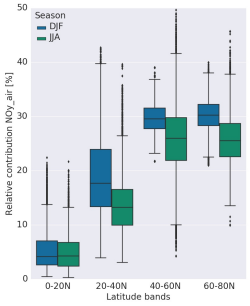


Figure 8.9: Boxplots showing the distribution of relative contributions of aviation nitrogen oxides in Region 2 for winter (DJF) and summer (JJA)

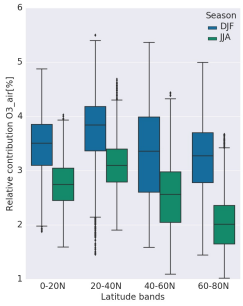


Figure 8.10: Boxplots showing the distribution of relative contributions of aviation ozone in Region 2 for winter (DJF) and summer (JJA)

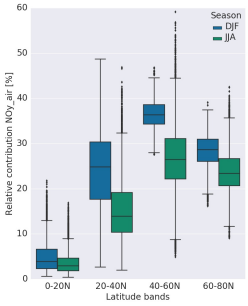


Figure 8.11: Boxplots showing the distribution of relative contributions of aviation nitrogen oxides in Region 3 for winter (DJF) and summer (JJA)

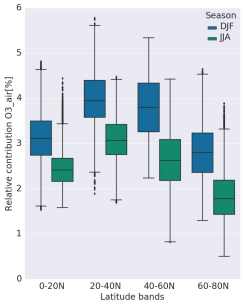


Figure 8.12: Boxplots showing the distribution of relative contributions of aviation ozone in Region 3 for winter (DJF) and summer (JJA)

## 8.2. Variability with respect to weather characteristics

Now that the general variability of aviation $NO_y$ and $O_3$ have been assessed, the general variability with respect to weather factors will be discussed. From a primary analysis it resulted that a strong relationship was found with respect to relative humidity, dry air temperature, and potential vorticity. Therefore, the variability with respect to these three factors will be discussed in this section.

### 8.2.1. Relative Humidity dependence

As discussed in Subsection 7.6 an air parcel with a high relative humidity contains relatively more water vapor under certain conditions than an air parcel with lower relative humidity under the same conditions. To assess whether Relative humidity affects the $NO_{y_{air}}$ - $O_{3_{air}}$ mechanism, the relative humidity values found in the study domain are

divided into low, medium and high relative humidity.

In Figure 8.13 all the relative humidity values at 200 hPa in the Northern Hemisphere over 10 years are summarized in a histogram for the Summer months. The same data is summarized in Figure 8.14 for the Winter months. In these figures it can be clearly seen that in the Summer season high relative humidity values of around 100% occur more frequently than in Winter. Low relative humidity values of around 0-15% occur more frequently in the winter season, and medium relative humidity values around 45-60% occur more frequently for Summer again. For the analysis the RH values have been divided into ranges of 0%-15%, 45%-60% and 85%-100% , for low RH, medium RH and high RH, respectively. This results in a larger dataset for high RH in Summer compared to Winter, but smaller datasets for low and medium RH in Summer. Overall, the size of the datasets are still within the same range and are sufficiently large to assess trends.

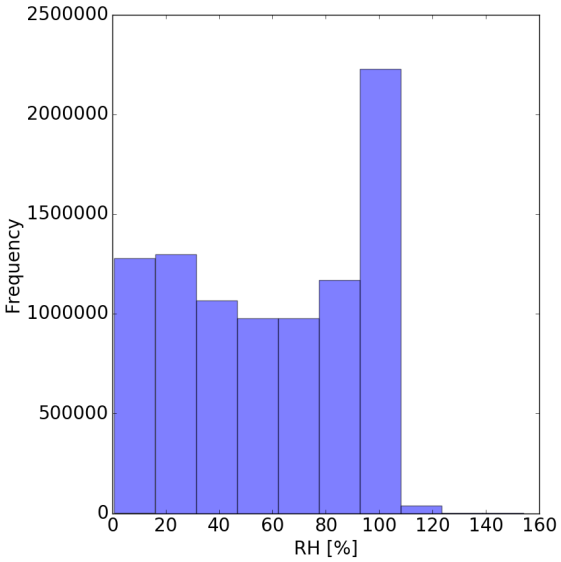


Figure 8.13: Relative humidity values found over 10 years on the Northern Hemisphere at cruise level 200 hPa for the Summer months JJA.

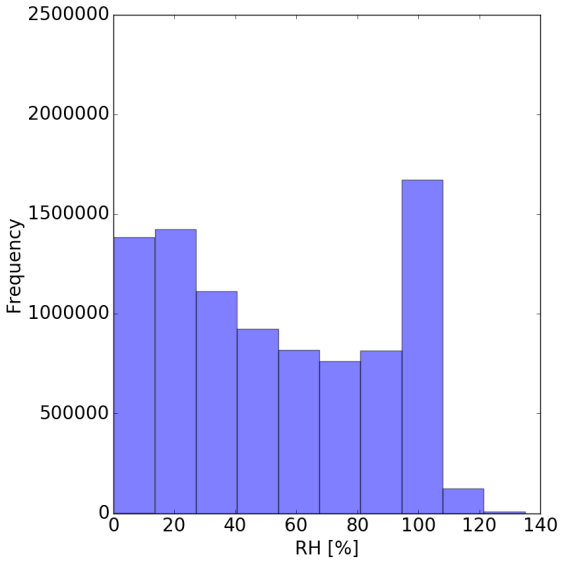


Figure 8.14: Relative humidity values found over 10 years on the Northern Hemisphere at cruise level 200 hPa for the Winter months DJF.

## Relative Humidity: KDE analysis

For the low, medium and high RH sets the aviation $NO_y$ and $O_3$ mixing ratios have been obtained for all gridpoints within the study domain. In the figures below (Figure 8.15 - 8.18) the Kernel Density Estimates (KDE) have been plotted for the aviation $NO_y$ and $O_3$ mixing ratios. The KDE estimates the probability that a certain value occurs in a finite dataset. Therefore, these figures show that if the KDE is high for a certain $NO_{y_{air}}$ or $O_{3_{air}}$ value, this value has a high probability of occuring in the atmosphere for that specific RH range.

In Figure 8.15 the KDE of $NO_{y_{air}}$ is depicted for low, medium and high RH in Winter. The most accumulation is found at very low values in the range of $1 \times 10^{-11}$ mol/mol, but a second peak takes shape at higher values, between $2 \times 10^{-10}$ and $3.5 \times 10^{-10}$ mol/mol, especially for low and medium RH. These peaks possibly represent different latitudinal regions, which will be discussed in the next part of this section. All three graphs show a similar pattern for the different RH regimes which indicates that the $NO_{y_{air}}$ mixing ratios do not have a correlation with the relative humidity values.

The KDE of $O_{3_{air}}$ for low, medium and high RH in Winter is depicted in Figure 8.16. The two peaks that were identified for the $NO_{y_{air}}$ values can be seen here as well. However, whereas the peaks for $NO_{y_{air}}$ were dominant for the lower values, the peaks in the KDE plots of $O_{3_{air}}$ are dominant for higher values. This implies that there is no linear relationship between $NO_{y_{air}}$ and $O_{3_{air}}$ in regions with specific RH values. The KDE lines of medium and high RH in this figure exhibit a similar pattern, while the KDE line for low RH deviates and is shifted to the left of the other two lines. While the KDE lines for $NO_{y_{air}}$ for low and high RH were similar, the KDE line of $O_{3_{air}}$ for low RH deviates from the high RH line. This suggests that the RH influences the aviation ozone concentration.

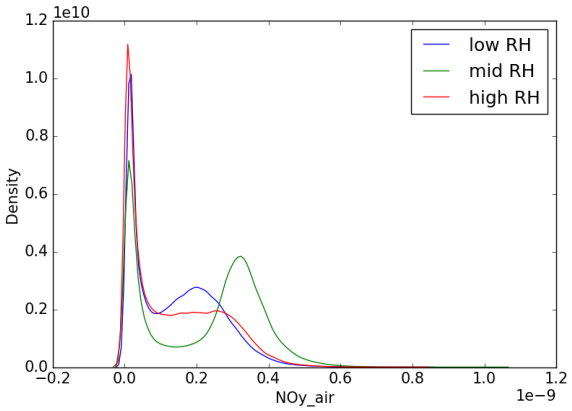


Figure 8.15: KDE of $NO_{y_{air}}$ for three relative humidity regimes, Winter

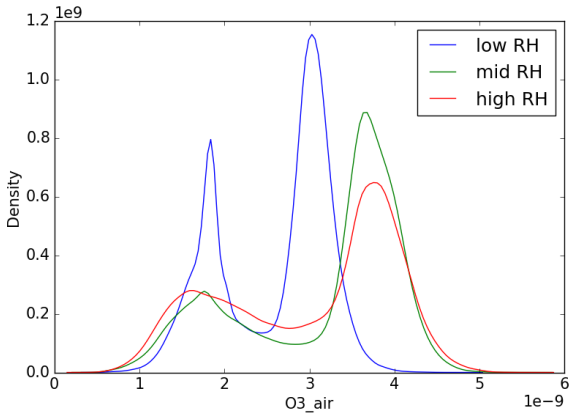


Figure 8.16: KDE of $O_{3_{air}}$ for three relative humidity regimes, Winter

The same graphs have been plotted for the Summer seasons in Figure 8.17 and 8.18. The Summer season exhibits a similar double peak for $NO_{y_{air}}$ (note the x-axis range being larger in the Summer graph), except for high RH. The peaks however do seem to be lower in Summer, even for high RH which contains a larger dataset than for Winter. This due to the higher values found in the data for Summer, as the $NO_{y_{air}}$ values range to up to $4 \times 10^{-9}$ mol/mol opposed to a maximum of $1.2 \times 10^{-9}$ mol/mol in Winter.

The aviation $O_3$ KDE plot for Summer shows a wider distribution of the data, up to $9 \times 10^{-9}$mol/mol opposed to $6 \times 10^{-9}$ mol/mol for Winter. The double peak is still present for low RH, but for medium and high RH the double peak trend is not very prominent. This could be attributed to the more variable weather in the Summer season and convection and transport having a large effect on the ozone production.

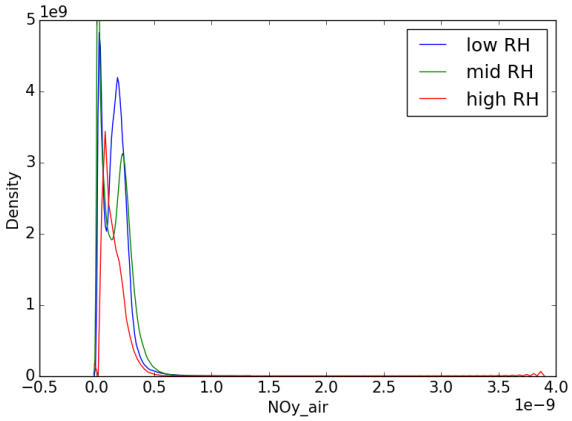


Figure 8.17: KDE of $NO_{y_{air}}$ for three relative humidity regimes, Summer

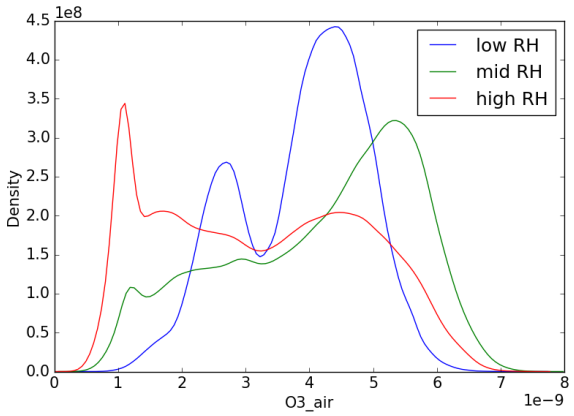


Figure 8.18: KDE of $O_{3_{air}}$ for three relative humidity regimes, Summer

## Relative Humidity: scatter plot analysis

As mentioned earlier, the peaks found in the KDE plots could potentially represent different latitudinal regions. Therefore, the aviation $NO_y$ and $O_3$ have been plotted against each other, and their respective latitude is expressed in the third dimension using a colormap. This was done for all 10 years, which is depicted in the figures below (Figure 8.19 - 8.24). Additionally, the data has been plotted for each individual year, which showed similar results.

The shapes of the scatter plots of the Winter months (top line) differ clearly from the shape of the Summer months where higher $O_3$ values are found for respective $NO_y$ values. Overall, for both seasons a relationship can be seen that for larger $NO_{y_{air}}$ values also larger $O_{3_{air}}$ values are found. For the Summer season clear regions of low- and high latitudes can be distinguished, whereas for the Winter months these regions are more blended.

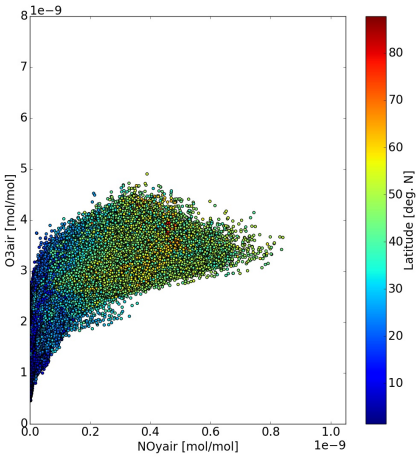


Figure 8.19: Aviation $NO_y$ versus $O_3$ with respect to latitude for the Winter season, over the whole Northern Hemisphere. Data for low relative humidity is shown.

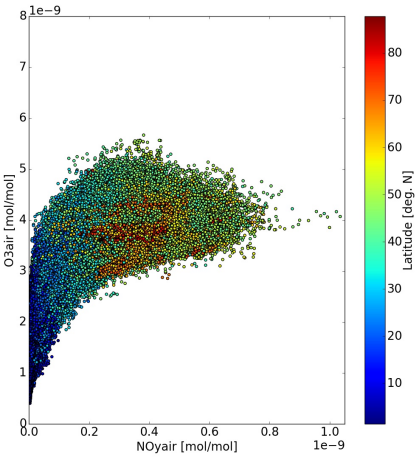


Figure 8.20: Aviation $NO_y$ versus $O_3$ with respect to latitude for the Winter season, over the whole Northern Hemisphere. Data for medium relative humidity is shown.

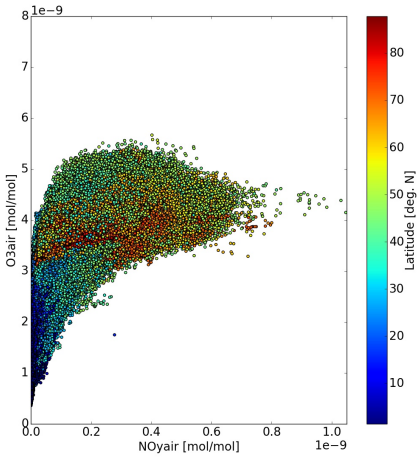


Figure 8.21: Aviation $NO_y$ versus $O_3$ with respect to latitude for the Winter season, over the whole Northern Hemisphere. Data for high relative humidity is shown.

The Winter months (depicted in Figures 8.19 - 8.21) show a clear low latitude region at the bottom left of the graph, where low $NO_{y_{air}}$ and $O_{3_{air}}$ values are found, in accordance with the findings of the variability analysis in Section 8.1. The graph then follows a rather square-root trend as $O_{3_{air}}$ increases with $NO_{y_{air}}$. As the mixing ratios of $NO_{y_{air}}$ and $O_{3_{air}}$ increase in this scatterplot, the latitude values also increase. For low RH the graph does not show any clear region of high latitudinal data points, which is actually expected for low RH values. For medium and high RH the high latitudes are blended throughout the middle of the pattern, which indicates that for these RH values, the largest $NO_{y_{air}}$ and $O_{3_{air}}$ are not found at the polar regions.

The Summer months also show a clear low latitude region at the bottom left of the graph, where the latitudinal values gradually increase with $NO_{y_{air}}$ and $0_{3_{air}}$. The scatter plots also follow a square-root trend as $O_{3_{air}}$ increases with $NO_{y_{air}}$, but slightly steeper. For low RH the higher latitudes can already be found at lower $NO_{y_{air}}$ values compared to medium and high RH. In contrast to the Winter months where high latitudinal points were rather blended throughout the plot, the Summer season shows a clear region of high latitudinal data points at the top left of the graph. This implies that for each RH category, larger $O_{3_{air}}$ values are found for respective $NO_{y_{air}}$ values at higher latitudes. Also, interesting to note is that for medium and high RH a cluster of polar latitudes can be found in the bottom left of the scatter plots. These clusters indicate low $NO_{y_{air}}$ and $O_{3_{air}}$ values at polar regions, which are potentially transported from the tropics to the polar regions.

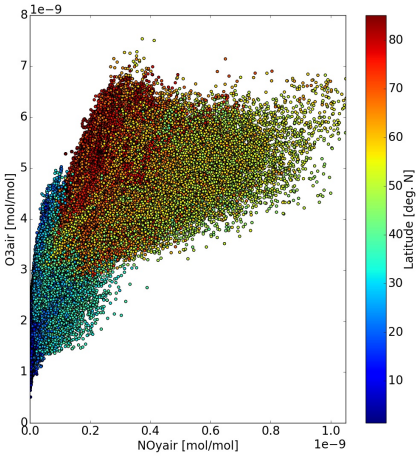


Figure 8.22: Aviation $NO_y$ versus $O_3$ with respect to latitude for the Summer season, over the whole Northern Hemisphere. Data for low relative humidity is shown.

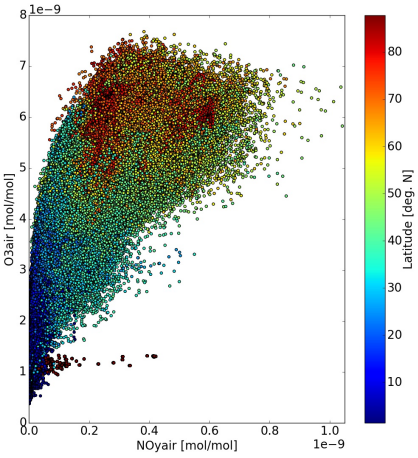


Figure 8.23: Aviation $NO_y$ versus $O_3$ with respect to latitude for the Summer season, over the whole Northern Hemisphere. Data for medium relative humidity is shown.

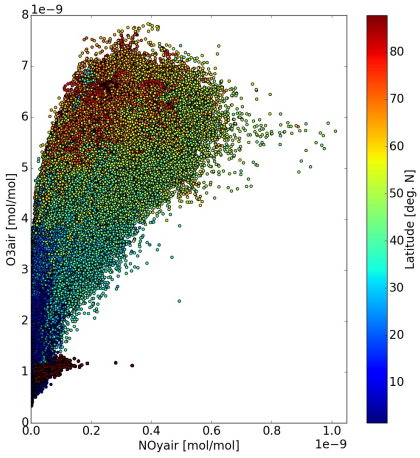


Figure 8.24: Aviation $NO_y$ versus $O_3$ with respect to latitude for the Summer season, over the whole Northern Hemisphere. Data for high relative humidity is shown.

From the scatter plots it can be concluded that there is a relationship between latitude and aviation $NO_y$ and $O_3$, and that this relationship differs also for the different RH regimes. For both seasons, data points with low $NO_{y_{air}}$ and low $O_{3_{air}}$ concentrations constitute low latitudinal values. In the Winter season less data points are found in high

latitudes, especially for low RH, whereas in Summer the high latitude data points constitute a prominent region of high $O_{3_{air}}$ values. However, with the scatter plots no clear regions can be attributed to the peaks found in the KDE plots.

## Relative Humidity: joint KDE analysis

In order to further investigate whether the peaks found in the KDE plots are correlated to certain latitudinal areas, joint plots are employed. Joint plots are used to visualize two distributions against each other. The distribution of one variable is then plotted along the x-axis, while the other distribution is plotted along the y-axis. On the joint grid that they share between the axes, the correlation can be visualized using a scatter plot, hexagonal bins, or contour density plots. Regions where both KDE's contain a high density are highlighted by a darker colour when making use of hexagonal bins or contour density plots, or by an accumulation of data points in the case of a scatter plot.

In Figures 8.25 - 8.30 the joint KDE plots are depicted for Winter and in Figures 8.31 - 8.36 for Summer. In these figures the KDE of the latitude values of all the data points is depicted on the x-axis, and the KDE of either the $NO_{y_{air}}$ or $O_{3_{air}}$ mixing ratios is depicted on the y-axis. Additionally the Pearson correlation coefficient and the according p-value is given in the figures. The Pearson correlation coefficient is a measure of the linear relationship between two variables and it returns a value between -1 and +1. If a positive linear relationship exists, the correlation coefficient will be close to +1, and if a negative linear relationship exists, this coefficient will be close to -1. The p-value indicates the significance of the correlation found between the variables. For this, the p-value is compared to a significance level, which is generally set to 0.05 (5%). If the p-value is less than or equal to the set significance level, then the correlation is statistically significant. If the p-value is larger than the significance level, the correlation is statistically insignificant. However, a p-value of 0 indicates that there is no linear relationship. The Pearson correlation analysis can only be applied to normally distributed data, which the data that is being investigated is not. This results in a p-value of 0 for each of the joint plots shown in this Chapter, which indicates that the Pearson correlation coefficient indicated as "pearsonr" in the figures is insignificant and can be ignored.

### $NO_{y_{air}}$ analysis with respect to RH, Winter

The joint KDE plots of $NO_{y_{air}}$ versus latitude for the Winter season are depicted in Figure 8.25 (low RH regime), Figure 8.26 (medium RH regime) and in Figure 8.27 (high RH regime). These three plots will now be individually discussed.

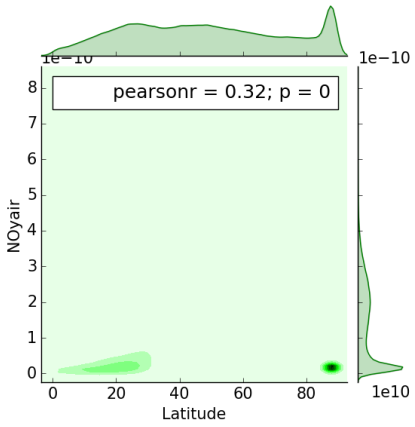


Figure 8.25: Joint Kernel Density Estimation of $NO_{y_{air}}$ and latitude for the Winter season, over the whole Northern Hemisphere. Data for low relative humidity is shown.

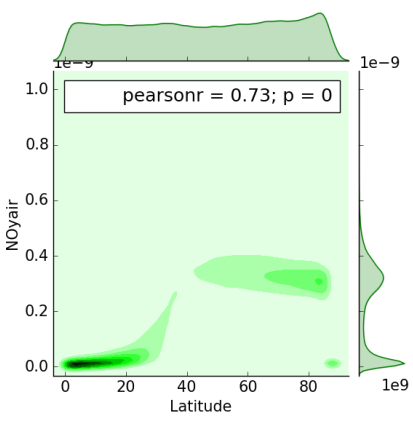


Figure 8.26: Joint Kernel Density Estimation of $NO_{y_{air}}$ and latitude for the Winter season, over the whole Northern Hemisphere. Data for medium relative humidity is shown.

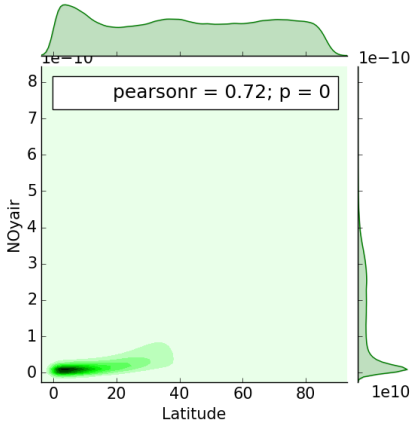


Figure 8.27: Joint Kernel Density Estimation of $NO_{y_{air}}$ and latitude for the Winter season, over the whole Northern Hemisphere. Data for high relative humidity is shown.

In the low RH regime the data points predominantly accumulate around high latitudinal values. This is in accordance with the dry climate that is found at the polar latitudes in Winter. Relative Humidity is dependent on both temperature and pressure, therefore as the temperature of the atmosphere is low at polar latitudes, low RH values are found here. A subtle accumulation can be found at lower latitudes and low $NO_{y_{air}}$ mixing ratios and a stronger accumulation is seen at polar latitudes in accordance with the peak of the latitudinal KDE. For low RH values low $NO_{y_{air}}$ values are found at polar latitudes. This is in contradiction with what was found in earlier research, that pointed out that at high latitudes, higher $NO_{y_{air}}$ values are found (see Section 5.1. This cluster of low $NO_{y_{air}}$ for low RH values could indicate air parcels that are transported from low latitudes to polar regions, resulting in low $NO_{y_{air}}$ mixing ratios at polar latitudes.

In the medium RH regime, two clear areas of accumulation can be distinguished: at latitudes between 0 °N and 20 °N, and at high latitudes from roughly 60 °N to 85 °N. The largest accumulation is found at lower latitudes for low mixing ratios, and at higher latitudes an accumulation is found for higher mixing ratios. The latitudinal KDE shows that the data points in this dataset are evenly distributed throughout this RH range over the Northern Hemisphere. Even though the data points are rather evenly distributed over the Northern Hemisphere, no gradual increase of $NO_{y_{air}}$ mixing ratios is found with respect to latitude, but two regimes are found for the mixing ratios. However, at higher latitudes elevated $NO_{y_{air}}$ levels are found compared to lower latitudes, which is in accordance with previous research (see Section 5.1). Again, an accumulation at high latitudes and low $NO_{y_{air}}$ mixing ratios is seen, albeit les prominent. This cluster is probably transported from low latitudes to polar regions, bringing low $NO_{y_{air}}$ mixing ratios to the polar latitudes.

The latitudinal KDE for high RH shows an accumulation around low latitudes, which is in accordance with the higher RH values found at low latitudes due to the elevated temperatures at low latitudes. In the high RH regime one clear region of accumulation is found for low latitudes and low $NO_{y_{air}}$ mixing ratios. This is in accordance with what was found in Section 5.1.

### $O_{3_{air}}$ analysis with respect to RH, Winter

The joint KDE plots of $O_{3_{air}}$ versus latitude for the Winter season are depicted in Figure 8.28 (low RH regime), Figure 8.29 (medium RH regime) and in Figure 8.30 (high RH regime). The KDE's of aviation ozone show a different pattern than the KDE's of aviation $NO_y$, while the latitudinal KDE's are identical for both sets.

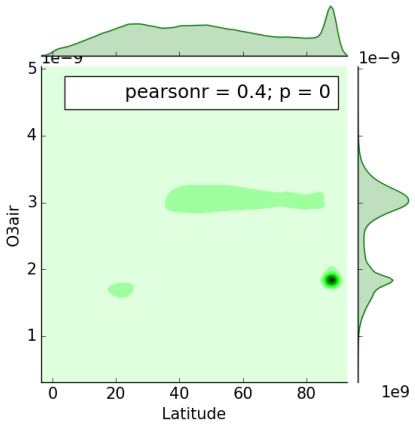


Figure 8.28: Joint Kernel Density Estimation of $O_{3_{air}}$ and latitude for the Winter season, over the whole Northern Hemisphere. Data for low relative humidity is shown.

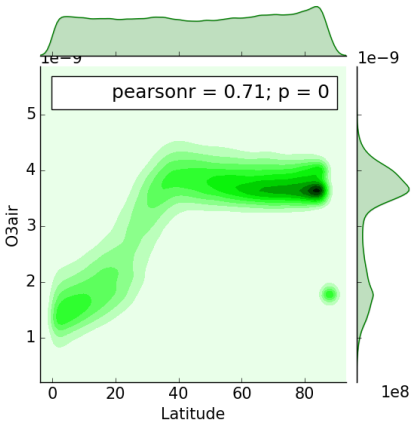


Figure 8.29: Joint Kernel Density Estimation of $O_{3_{air}}$ and latitude for the Winter season, over the whole Northern Hemisphere. Data for medium relative humidity is shown.

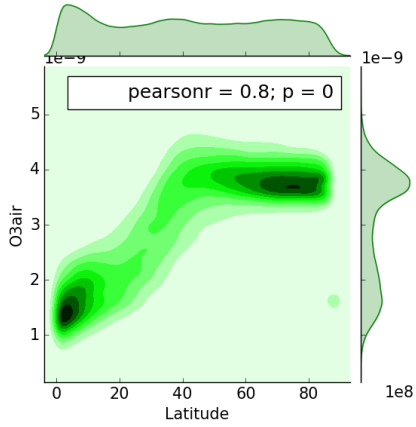


Figure 8.30: Joint Kernel Density Estimation of $O_{3_{air}}$ and latitude for the Winter season, over the whole Northern Hemisphere. Data for high relative humidity is shown.

For low RH, the KDE of $O_{3_{air}}$ shows two clear double peaks, which is identified in the joint KDE plot as well. A cluster of $O_{3_{air}}$ mixing ratios is found at high latitudes, analogously to the joint KDE of $NO_{y_{air}}$ for low RH, which represents the first peak in the KDE plot of this regime's $O_{3_{air}}$. The second peak is in accordance with an accumulation of higher $O_{3_{air}}$ mixing ratios over mid- to high latitudes. However, this accumulation is relatively weaker compared to the accumulation found at these regions for medium and high RH.

Whereas the KDE of $NO_{y_{air}}$ shows a strong peak for low mixing ratios, and a weaker peak for higher mixing ratios, the KDE of $O_{3_{air}}$ shows a stronger peak for higher mixing ratios, and a weaker peak for lower values. The strong peak is in accordance with high aviation ozone levels at mid- to high latitudes (40 °N to 85 °N) and the weak peak is in accordance with low latitudes and lower aviation ozone levels. This is in accordance with the latitudinal variability of these species discussed in Section 5.1.

The joint KDE for $O_{3_{air}}$ at high RH shows a similar pattern to the joint KDE of medium RH, but with stronger accumulations at high latitudes for high mixing ratios and at low latitudes for low mixing ratios. This is again in accordance with the latitudinal variability of aviation Ozone that was discussed in Section 5.1.

In all three RH regimes an accumulation at polar latitudes for low $O_{3_{air}}$ mixing ratios is seen, which is most strong for the low RH regime. To determine whether this cluster of low aviation ozone mixing ratios at polar latitudes has developed from the cluster of low $NO_{y_{air}}$ at these latitudes, further research is required.

### $NO_{y_{air}}$ analysis with respect to RH, Summer

The joint KDE plots of $NO_{y_{air}}$ versus latitude for the Summer season are depicted in Figure 8.31 (low RH regime), Figure 8.32 (medium RH regime) and in Figure 8.33 (high RH regime). The joint KDE of the medium RH regime for Summer shows a similar pattern to the joint KDE of the medium RH regim for Winter and therefore will not be discussed in detail. The transition of low-to mid latitudes and low to high aviation $NO_y$ mixing ratios however, is more gradual.

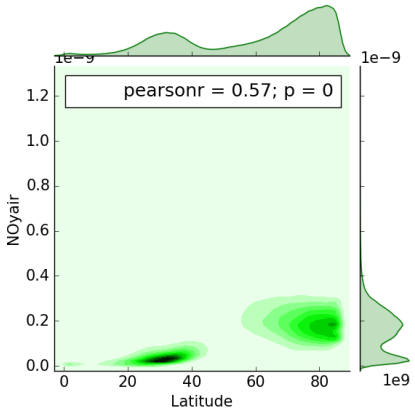


Figure 8.31: Joint Kernel Density Estimation of $NO_{y_{air}}$ and latitude for the Summer season, over the whole Northern Hemisphere. Data for low relative humidity is shown.

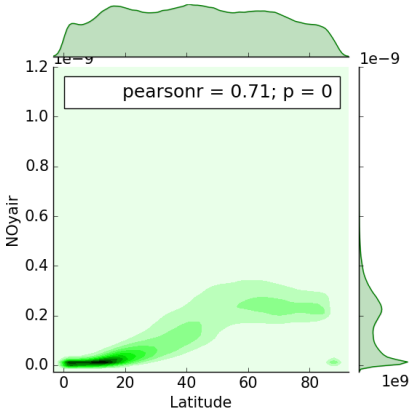


Figure 8.32: Joint Kernel Density Estimation of $NO_{y_{air}}$ and latitude for the Summer season, over the whole Northern Hemisphere. Data for medium relative humidity is shown.

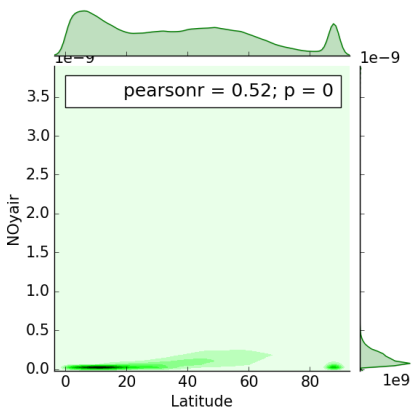


Figure 8.33: Joint Kernel Density Estimation of $NO_{y_{air}}$ and latitude for the Summer season, over the whole Northern Hemisphere. Data for high relative humidity is shown.

For the low RH regim two clear peaks are found in both the latitudinal KDE and in the $NO_{y_{air}}$ KDE. These correspond to low mixing ratios at low to mid latitudes (first peak) and high mixing ratios at high- to polar latitudes. The increase in mixing ratio with latitude is in accordance with the latitudinal variability of $NO_{y_{air}}$ discussed in Section 5.1.

The high RH regime shows an accumulation for low $NO_{y_{air}}$ mixing ratios at low latitudes, analogous to the Winter season. However, in the Summer season a peak at high latitudinal values occurs in the latitudinal KDE, which was not present in the Winter season. It is not clear where this peak originates from, but potentially represents air parcels that are transported from low latitudes regions to high latitudes, resulting in high RH values at polar regions. To determine this, further research is required.

### $O_{3_{air}}$ analysis with respect to RH, Summer

The joint KDE plots of $O_{3_{air}}$ versus latitude for the Summer season are depicted in Figure 8.34 (low RH regime), Figure 8.35 (medium RH regime) and in Figure 8.36 (high RH regime). The joint KDE'S of aviation ozone for Summer show a different behaviour compared to the Winter and will be discussed in this section.

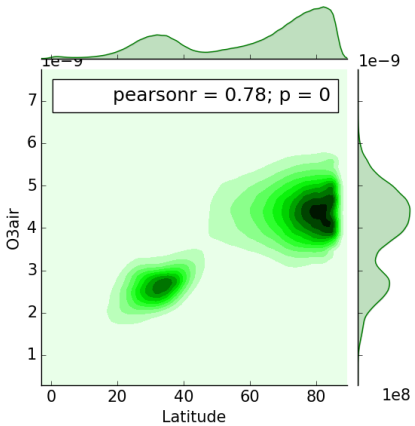


Figure 8.34: Joint Kernel Density Estimation of $O_{3_{air}}$ and latitude for the Summer season, over the whole Northern Hemisphere. Data for low relative humidity is shown.

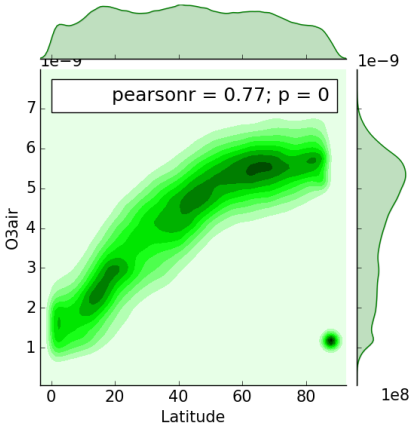


Figure 8.35: Joint Kernel Density Estimation of $O_{3_{air}}$ and latitude for the Summer season, over the whole Northern Hemisphere. Data for medium relative humidity is shown.

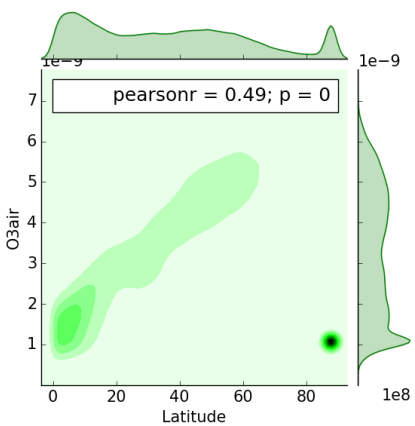


Figure 8.36: Joint Kernel Density Estimation of $O_{3_{air}}$ and latitude for the Summer season, over the whole Northern Hemisphere. Data for high relative humidity is shown.

In the low RH regime (left figure), two clear regions are identified: low mixing ratios for mid-latitudes, and high mixing ratios for higher latitudes, both in accordance with the regions identified for $NO_{y_{air}}$. However, the accumulation at higher latitudes is stronger for $O_{3_{air}}$ compared to $NO_{y_{air}}$. From the figures it is not clear what causes this.

The medium RH regime (middle figure) shows a clear gradual increase of the mixing ratios found with respect to latitude, which is in agreement with the latitudinal variability discussed in Section 5.1. In the high RH regime a similar pattern is found, albeit weaker than for medium RH.

For both medium- and high RH, the accumulation of low $O_{3_{air}}$ mixing ratios at polar latitudes is rather strong, while it is absent for low RH. From the data presented up until now, it is not clear what causes the accumulation of data around this region. Especially for medium RH this cluster is very peculiar, as the latitudinal KDE does not show a peak at these high latitudes.

### 8.2.2. Dry temperature dependence

In Section 7.6 it was discussed that the dry air temperature of an air parcel ($T_{dry}$) potentially positively affects the production efficiency of aviation $O_3$ To assess this, $NO_{y_{air}}$ and $O_{3_{air}}$ mixing ratios have been analysed with respect to $T_{dry}$. The dry air temperatures found in the study domain have been divided into two groups for Winter and Summer each.

In Figure 8.38 and 8.37 the histograms of the dry air temperature values in the study domain have been plotted for Winter and Summer, respectively. The Winter season shows a moderate distribution from 200 K up to 225K, while a large amount of data points is found for $T_{dry}$ around 220 K in Summer. Therefore two different sub-groups are defined for the Winter- and Summer season:

**Winter:**

- low $T_{dry}$: 205 K - 215 K
- high $T_{dry}$: 215 K - 225 K

**Summer:**

- low $T_{dry}$: 215 K - 225 K
- high $T_{dry}$: 225 K - 235 K

This results into subsets of unequal size, however each subset is still sufficiently large to allow for the identification of trends.

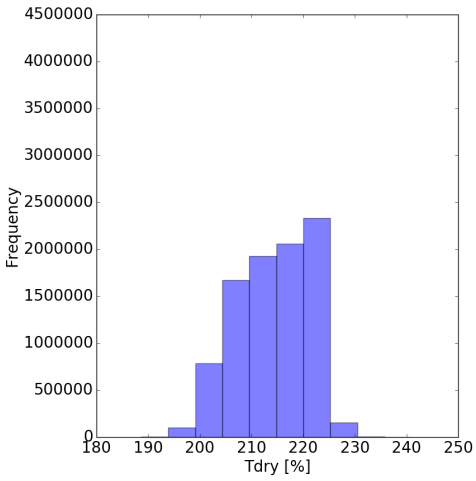


Figure 8.37: Dry air temperature values found over 10 years on the Northern Hemisphere at cruise level 200 hPa for the Winter months DJF

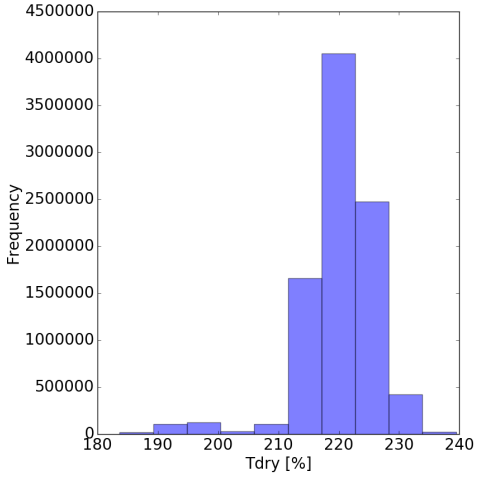


Figure 8.38: Dry air temperature values found over 10 years on the Northern Hemisphere at cruise level 200 hPa for the Summer months JJA

The KDE of $NO_{y_{air}}$ and $O_{3_{air}}$ are plotted for Winter in Figure 8.39 and Figure 8.40, respectively. For high dry air temperatures, a strong peak accumulates around low values of $NO_{y_{air}}$ around $2 \times 10^{-11}$ and a subtle second peak appears for higher values around $2 \times 10^{-10}$. For low dry air temperatures the peaks are located at the same mixing ratios, but

they are reversed, meaning that the primary peak for low dry air temperatures is found at higher mixing ratios, and the secondary peak is found at lower mixing ratios. The graphs for low and high $T_{dry}$ show different patterns and therefore it can be concluded that the dry air temperature regions influence the $NO_{y_{air}}$ mixing ratios.

Similar to the KDE's of $NO_{y_{air}}$, the KDE's of $O_{3_{air}}$ show two peaks. For high dry air temperatures the primary peak is found around $1.834 \times 10^{-9}$ mol/mol and the secondary peak is found around $3.091 \times 10^{-9}$ mol/mol. For low dry air temperatures the primary peak is located at higher mixing ratios, namely around $3.647 \times 10^{-9}$ mol/mol, and a secondary peak is found at lower mixing ratios of $O_{3_{air}}$, albeit less present than was found for $NO_{y_{air}}$. The two temperature regimes show distinctively different patterns in the KDE plots, indicating that these regimes a different constellation of mixing ratios. However, for the two regimes the KDE plots for aviation $NO_y$ and aviation $O_3$ showed similar patterns, indicating that dry air temperature correlates in a similar fashion to aviation $NO_y$ as it does with respect to aviation $O_3$.

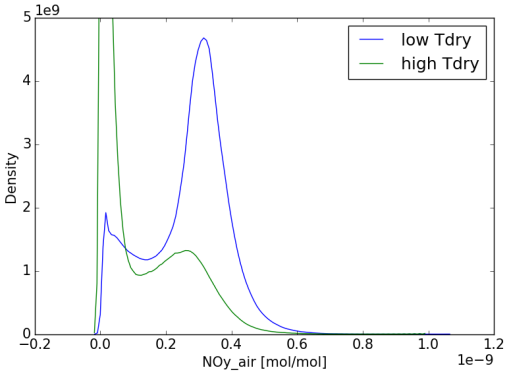


Figure 8.39: KDE of $NO_{y_{air}}$ for two temperature regimes, Winter

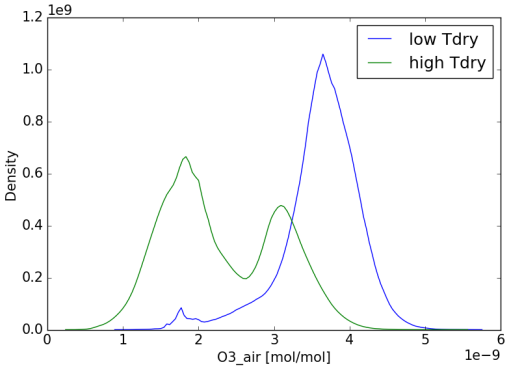


Figure 8.40: KDE of $O_{3_{air}}$ for two temperature regimes, Winter

The KDE's of aviation $NO_y$ in Summer shows two similar patterns for the low- and high dry air temperature regimes, while the KDE's of aviation $O_3$ show two distinctive patterns for the two regimes. The two KDE lines of aviation $O_3$ for low and high $T_{dry}$ different distributions, analogously to the Winter set, which means that aviation $O_{3_{air}}$ behaves differently in the two temperature regimes. Therefore, it can be concluded that for the Summer season the dry air temperature does not have an influence on the aviation $NO_y$, but it does influence the aviation $O_3$

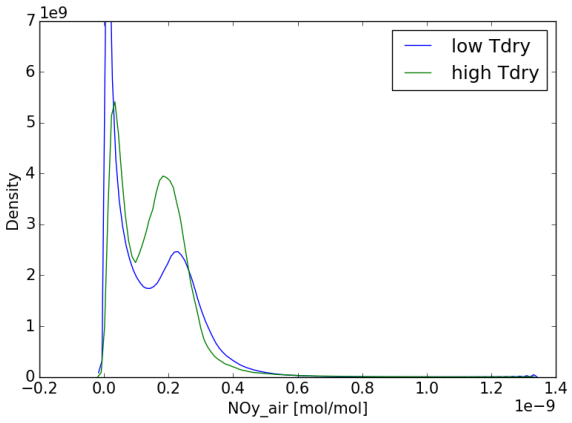


Figure 8.41: KDE of $NO_{y_{air}}$ for two temperature regimes, Summer

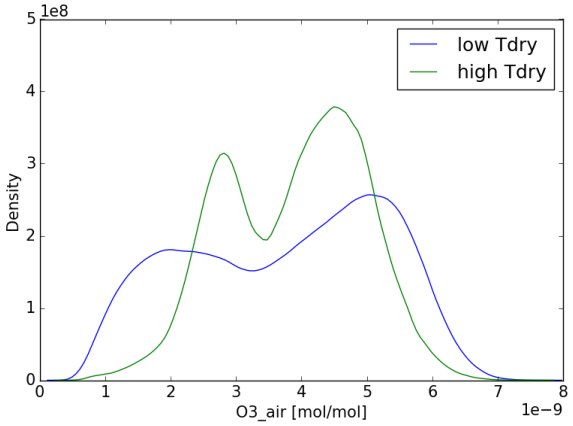


Figure 8.42: KDE of $O_{3_{air}}$ for two temperature regimes, Summer

The aviation $NO_{y_{air}}$ and $O_{3_{air}}$ have been set out against each other with respect to latitude for low and high $T_{dry}$ in Figures 8.43 through 8.46. These scatter plots show a resemblance with the low- and high RH scatter plots from Subsection 8.2.1. In the Winter scatter plots the latitude values are lowest at the left-bottom part of the plot and increase gradually towards the right top. However, around the middle part of the plot less high latitude values are found in the scatter plots for both low and high dry air temperature, compared to the scatter plots for RH.

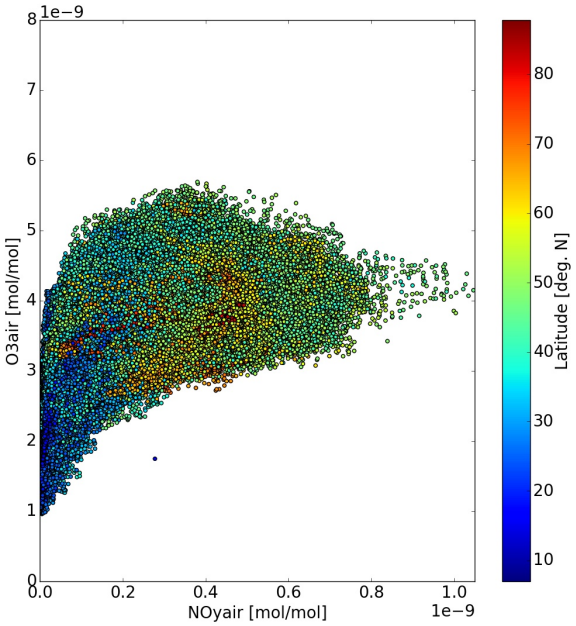


Figure 8.43: Aviation $NO_y$ versus $O_3$ with respect to latitude for the Winter season, over the whole Northern Hemisphere. Data for low dry air temperatures is shown.

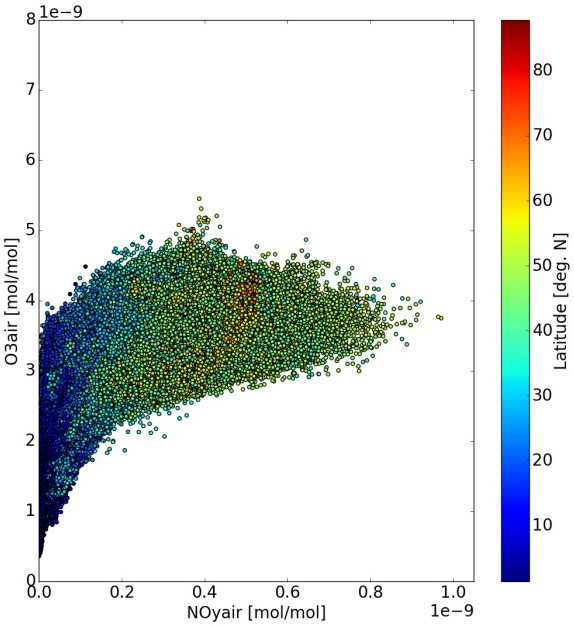


Figure 8.44: Aviation $NO_y$ versus $O_3$ with respect to latitude for the Winter season, over the whole Northern Hemisphere. Data for high dry air temperature values is shown.

In the Summer plots (Figures 8.45 and 8.46) the latitudinal regions are more prominent and higher $NO_{y_{air}}$ and $O_{3_{air}}$ are found compared to Winter. At the bottom left part of the plot for low $NO_{y_{air}}$ and low $O_{3_{air}}$ low latitudes are found, and the latitude values increase gradually with increasing mixing ratios. On the top-left part of the scatter plot a clear cluster of high latitudes can be seen. The $NO_{y_{air}}$ mixing ratios at these high latitude levels is lower than mixing ratios found at lower latitudes, as the contribution of aviation $NO_y$ is lower at polar latitudes. However, elevated aviation $O_3$ are found in these region, which is due to transport from lower latitudes, resulting in higher $O_{3_{air}}$ mixing ratios at high latitudes. Furthermore, in contrast to the Summer scatter plots for medium and high RH, in the high $T_{dry}$ scatterplot no cluster of high latitudinal data points is found in the bottom left of the plot containing low mixing ratios.

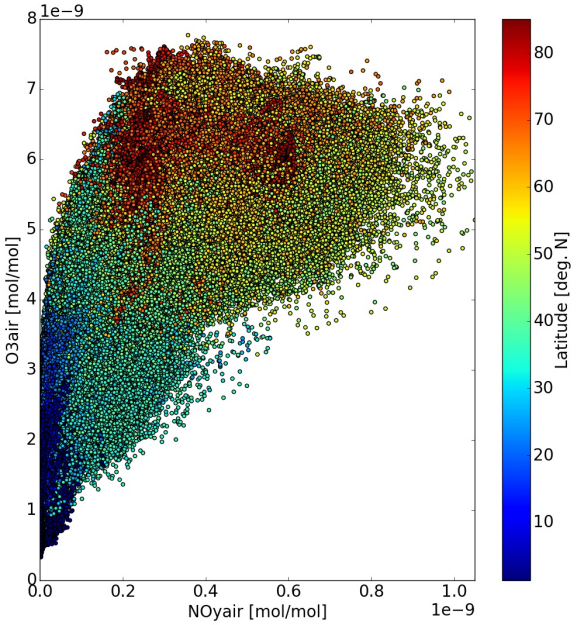


Figure 8.45: Aviation $NO_y$ versus $O_3$ with respect to latitude for the Summer season, over the whole Northern Hemisphere. Data for low dry air temperatures is shown.

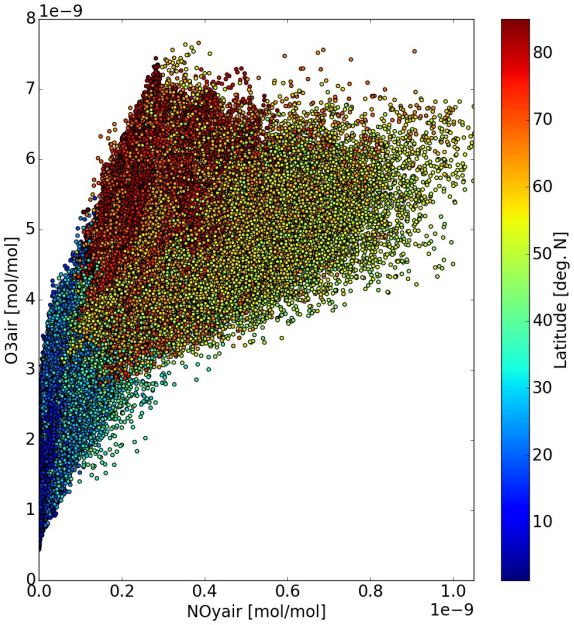


Figure 8.46: Aviation $NO_y$ versus $O_3$ with respect to latitude for the Summer season, over the whole Northern Hemisphere. Data for high dry air temperatures is shown.

Joint KDE plots are developed to further investigate the correlation between the aviation $NO_y$ and $O_3$ mixing ratios with respect to dry air temperature and latitude. This is discussed in the following text.

### $NO_{y_{air}}$ analysis with respect to $T_{dry}$, Winter

The joint KDE plots of $NO_{y_{air}}$ versus latitude for the Winter season are depicted in Figure 8.47 (low $T_{dry}$ regime) and in Figure 8.48 (high $T_{dry}$ regime).

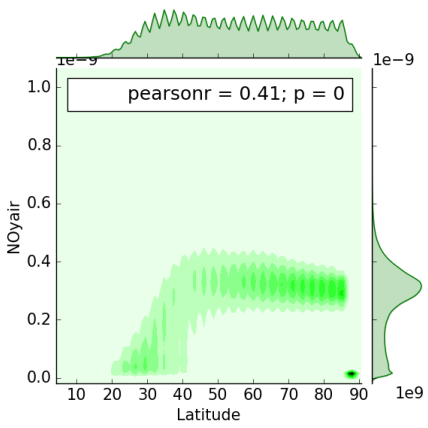


Figure 8.47: Joint Kernel Density Estimation of $NO_{y_{air}}$ and latitude for the Winter season, over the whole Northern Hemisphere. Data for low dry air temperature is shown.

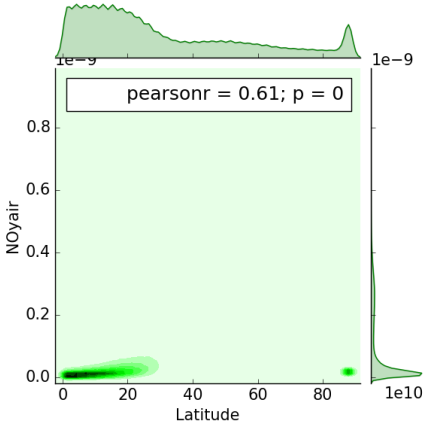


Figure 8.48: Joint Kernel Density Estimation of $NO_{y_{air}}$ and latitude for the Winter season, over the whole Northern Hemisphere. Data for high dry air temperature is shown.

The low $T_{dry}$ regime (left figure) extends from low-latitudes (20 °N) up to polar latitudes. The mixing ratios of aviation $NO_y$ show an accumulation around low mixing ratios for low latitudes, and it gradually increases to higher mixing ratios of around $3 \times 10^{-10}$), which is in agreement with the latitudinal variability of these species discussed in Section 5.1. No data points are found for latitudes from 0°N to about 20°N for low dry air temperatures.

For the high $T_{dry}$ regime (right figure) the data points accumulate at lower latitudes, which is in accordance with the higher dry air temperatures found at low latitudes (roughly 0°N up to 20 °N). Low mixing ratios are found at these low latitudes, which is in accordance with the primary peak at low mixing ratios. As was discussed in Section 5.1 the mixing ratios of aviation $NO_y$ is lowest at low latitudes, which is confirmed in this graph. Less straightforward is the peak in the KDE plot for latitude values. This peak shows an accumulation of data points at polar latitudes which was also present in the latitudinal KDE plot for the low RH regime in Winter (Figure 8.25) and in the latitudinal KDE plot for the high RH regime in Summer (Figure 8.33).

For both the low and high dry air temperature regimes a cluster of low mixing ratios is found at polar latitudes. This cluster was not identified in the scatter plots (Figure 8.43 and 8.44), but it explains the secondary peak that is found in the KDE of low dry air temperature in Winter (Figure 8.39).

### $O_{3_{air}}$ analysis with respect to $T_{dry}$, Winter

The joint KDE plots of $O_{3_{air}}$ versus latitude for the Winter season are depicted in Figure 8.49 (low $T_{dry}$ regime) and in Figure 8.50 (high $T_{dry}$ regime).

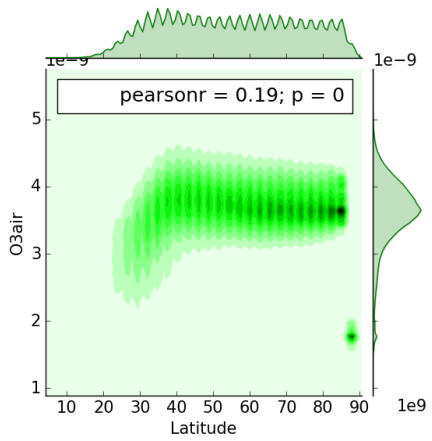


Figure 8.49: Joint Kernel Density Estimation of $O_{3_{air}}$ and latitude for the Winter season, over the whole Northern Hemisphere. Data for low dry air temperature is shown.

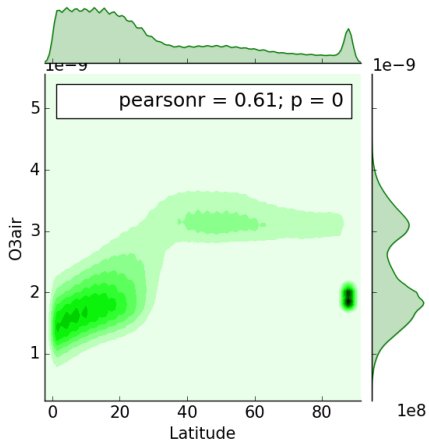


Figure 8.50: Joint Kernel Density Estimation of $O_{3_{air}}$ and latitude for the Winter season, over the whole Northern Hemisphere. Data for high dry air temperature is shown.

For the low dry air temperature regime (left figure) the mixing ratios accumulate mostly around elevated values of about $3.5 \times 10^{-9}$ - $4 \times 10^{-9}$ mol/mol. This accumulation is found for mid- to high latitudes from roughly 40 °N up to 85 °N. For lower latitudes, lower mixing ratios are found, which is in accordance with the latitudinal variability of aviation ozone as was discussed in Section 5.1.
For the high dry air temperature regime the mixing ratios accumulate over two regions: low latitudes (roughly 0°N up to 20 °N), which is in accordance with the two peaks found in the KDE of aviation ozone for Winter for this regime (see Figure 8.40). The latitudinal KDE for this regimes shows an accumulation at polar latitudes which is unexpected as high dry air temperatures are not typically found at this latitudinal region. This accumulation at high latitudes shows a strong accumulation of data points around lower aviation ozone mixing ratios, which is also found for low dry air temperatures. However, this cluster of high latitudinal data points was not found in the scatter plots. In order to explain this cluster at polar latitudes, which was also found the joint graphs of relative humidity, further investigation is needed.

### $NO_{y_{air}}$ analysis with respect to $T_{dry}$, Summer

The joint KDE plots of $NO_{y_{air}}$ versus latitude for the Summer season are depicted in Figure 8.51 (low $T_{dry}$ regime) and in Figure 8.52 (high $T_{dry}$ regime). In Summer higher dry air temperatures are and the distribution of the data points in the two temperature regimes differs to that from Winter. The KDE of the low dry air temperature region for Summer shows a distribution of the data points over a range from 0 °N up to 90 °N latitude, decreasing from low to high latitudes. The KDE for high dry air temperatures shows a different distribution where the data points accumulate at mid-latitudes of around 20°N up to 40 °N, and at high latitudes from roughly 75 °N up to 90 °N.

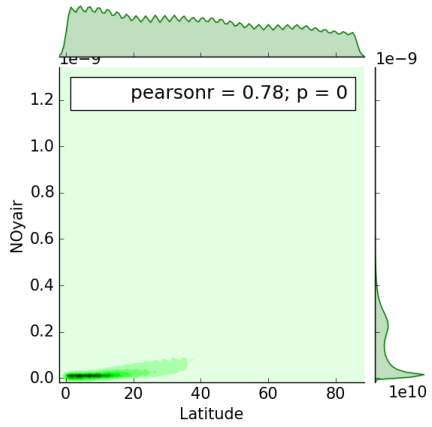


Figure 8.51: Joint Kernel Density Estimation of $NO_{y_{air}}$ and latitude for the Summer season, over the whole Northern Hemisphere. Data for low dry air temperature is shown.

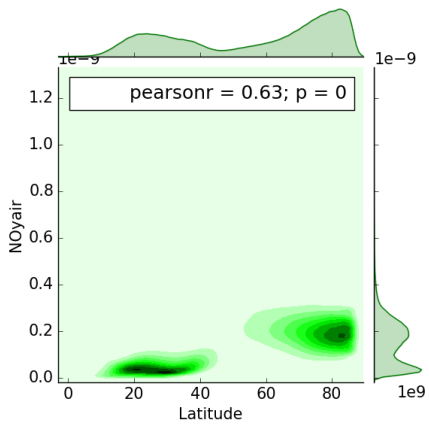


Figure 8.52: Joint Kernel Density Estimation of $NO_{y_{air}}$ and latitude for the Summer season, over the whole Northern Hemisphere. Data for high dry air temperature is shown.

For low dry air temperatures (left figure) the data points accumulate around low latitudes andlow $NO_{y_{air}}$ mixing ratios. The KDE of the $NO_{y_{air}}$ suggests an accumulation at higher mixing ratios, but this is not depicted in the joint KDE

plot. This might be due to the fact that the low dry air temperatures is well distributed over the rest of the latitude range, leading to no clear accumulation with respect to latitude.

For high dry air temperatures the KDE distribution of the latitude values is similar to the KDE pattern found with respect to latitude of the dataset for low RH in Summer (Figure 8.31 and 8.34). The joint KDE plot of $NO_{y_{air}}$ is also similar to the on depicted in Figure 8.31. This means that similar data points are found for the low RH and high $T_{dry}$ regimes in Summer. This is due to the fact that RH and $T_{dry}$ are inversely related: when the temperature of an air parcel increases, the saturation specific humidity $q_*$ increases as well [29], resulting in a decrease of RH.

**$O_{3_{air}}$ analysis with respect to $T_{dry}$, Summer**

The joint KDE plots of $O_{3_{air}}$ versus latitude for the Summer season are depicted in Figure 8.49 (low $T_{dry}$ regime) and in Figure 8.54 (high $T_{dry}$ regime).

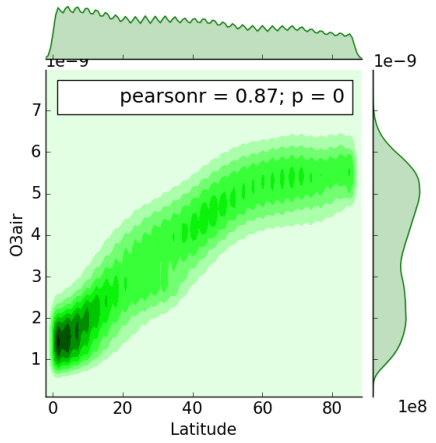


Figure 8.53: Joint Kernel Density Estimation of $O_{3_{air}}$ and latitude for the Summer season, over the whole Northern Hemisphere. Data for low dry air temperature is shown.

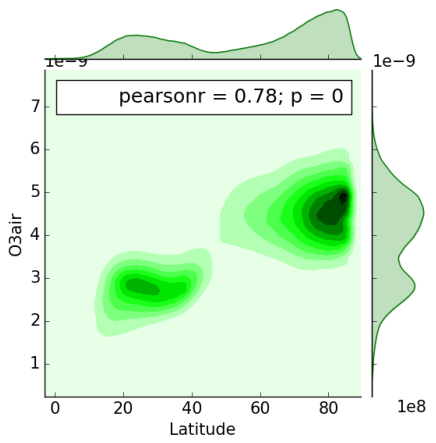


Figure 8.54: Joint Kernel Density Estimation of $O_{3_{air}}$ and latitude for the Summer season, over the whole Northern Hemisphere. Data for high dry air temperature is shown.

The joint KDE for the low $T_{dry}$ regime (left figure) shows a gradual increase of aviation $O_3$ mixing ratios with respect to latitude, which is in accordance with the variability of these species discussed in Section 5.1. A stronger accumulation however, is found for low latitudes and low mixing ratio, in accordance with the accumulation found for low $NO_{y_{air}}$ mixing ratios at low latitudes for Summer (Figure 8.51).

The joint KDE for the high $T_{dry}$ regime depicted in the figure on the right, shows a similar pattern as was found for $NO_{y_{air}}$ in this regime. However, the second peak is at higher mixing ratios is more dominant compared to the peak at lower latitudes, in contrast to the KDE of $NO_{y_{air}}$.

### 8.2.3. Potential Vorticity dependence

Potential vorticity (PV) is a measure of the stability and rotation of an air column. A high potential vorticity indicates higher dynamic activity compared to a low potential vorticity of a same size air column. Therefore, it is expected that air parcels with higher PV have higher dynamical activity. As discussed in Section 7.6 the potential vorticity increases with latitude. As the concentrations of $NO_{y_{air}}$ and $O_{3_{air}}$ also increase with latitude, it is expected that a positive correlation is found between the mixing ratios of these species and PV.

In Figure 8.55 and 8.56 the PV values of the study domain are plotted in a histogram for Winter and Summer, respectively. In these figures it can be seen that for Summer relatively more data points with a low PV value close to zero are found, and that in Summer the maximum PV is larger than in Winter. In Winter however higher PV values around 6-9 pvu are more prominent compared to Summer. For the analysis, the PV is divided into three groups for both Winter and Summer analysis: 0-1.5 pvu, 4.5-6 pvu and 8.5-10 pvu.

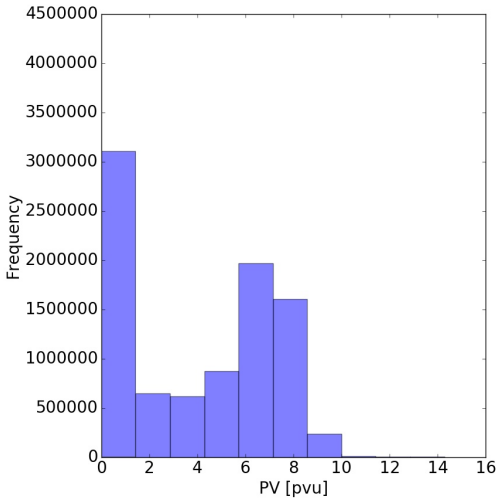


Figure 8.55: Potential vorticity values found over 10 years on the Northern Hemisphere at cruise level 200 hPa for the Winter months DJF

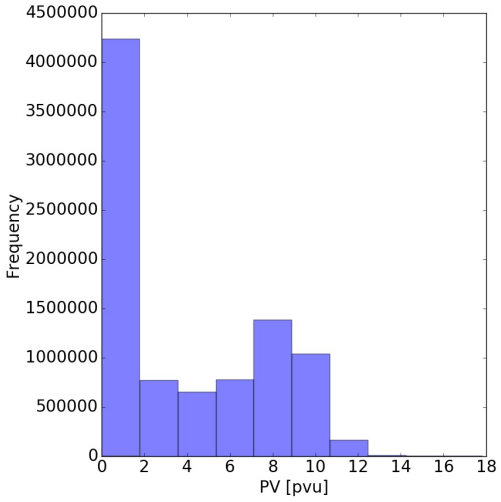


Figure 8.56: Potential vorticity values found over 10 years on the Northern Hemisphere at cruise level 200 hPa for the Summer months JJA

In Figure 8.57 and Figure 8.58 the KDE is plotted for the Winter season for low, medium and high PV, for $NO_{y_{air}}$ and $O_{3_{air}}$ respectively. These KDE plots exhibit a different pattern than was found for the RH and $T_{dry}$. The double peaks are still found for high PV values, but the low and medium PV values show one clear peak for $NO_{y_{air}}$ and $O_{3_{air}}$

In Figure 8.57 the graph for low PV clearly shows a peak at low $NO_y$ values, whereas the high PV graphs shows one peak at low $NO_y$ values and a subtle lower peak at higher $NO_y$ values. The medium PV graph shows one moderate peak for higher $NO_{y_{air}}$ values. The peak for low PV is attributed to the fact that low (close to zero) PV values are found at low latitudes, where also the $NO_{y_{air}}$ mixing ratios are relatively low. With increasing latitude also the PV increases, which is expressed in the peak at higher $NO_{y_{air}}$ values for medium PV. High PV values related to low $NO_{y_{air}}$ values need to be further analysed, as this could be attributed to air parcels with high PV at low latitudes, or air parcels with high PV at higher latitudes but with transport from the stratosphere, resulting in a higher PV, but in lower $NO_{y_{air}}$ levels.

The KDE plots of aviation $O_3$ in Figure 8.58 show a similar dependency. The high PV graphs also exhibits two peaks and the low PV graph shows an accumulation at low $O_{3_{air}}$ regions and the medium PV graph shows an accumulation around higher $O_{3_{air}}$ values.

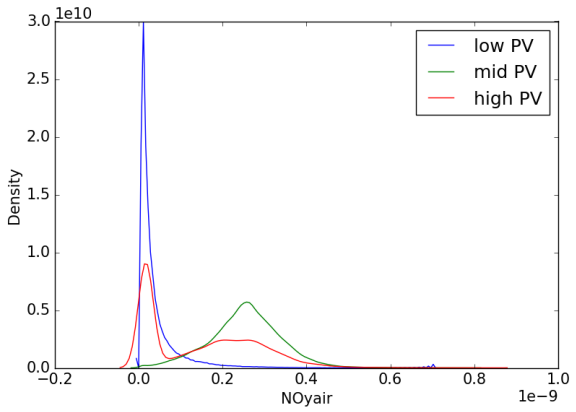


Figure 8.57: KDE of $NO_{y_{air}}$ for two PV regimes, Winter

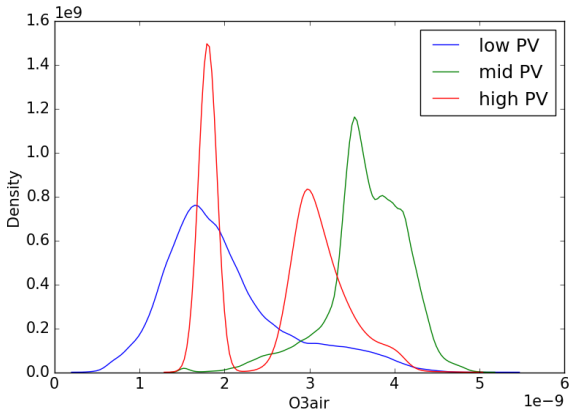


Figure 8.58: KDE of $O_{3_{air}}$ for two PV regimes, Winter

In Figure 8.59 and Figure 8.60 the KDE's are plotted for the Summer season for $NO_{y_{air}}$ and $O_{3_{air}}$ respectively. These KDE plots exhibit a different pattern than was found for the Winter months. The double peaks are now found for medium PV values, and the low and high PV values show one clear peak for $NO_{y_{air}}$ and the $O_{3_{air}}$ values.

In Figure 8.59 the graph for low PV clearly shows a peak at low $NO_y$ values, whereas the high PV graphs shows a peak at higher $NO_y$ values. The medium PV graph shows two peaks in both regions, indicating that the $NO_y$ values of this subset are found in both regions. This suggests that $NO_{y_{air}}$ increases with PV.

The KDE plots of aviation $O_3$ in Figure 8.60 show a similar pattern as were found in the KDE plots for $NO_{y_{air}}$. The medium PV plot exhibits two peaks, analogously to its $NO_{y_{air}}$ constituent, and the low- and high PV graphs show also one peak for lower and higher ozone values, respectively.

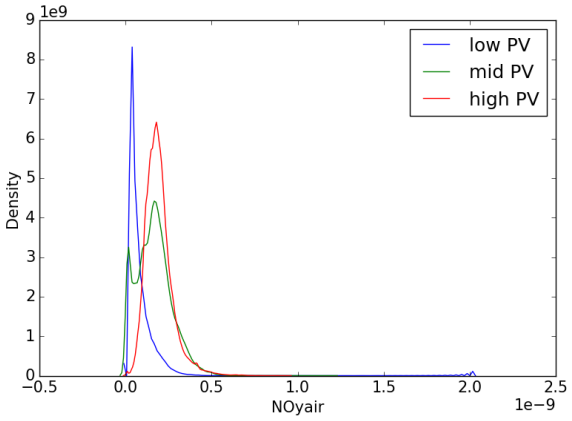


Figure 8.59: KDE of $NO_{y_{air}}$ for two PV regimes, Summer

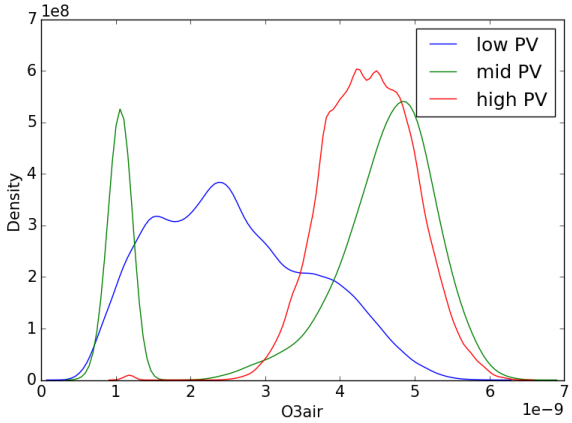


Figure 8.60: KDE of $O_{3_{air}}$ for two PV regimes, Summer

For both the Winter and Summer season similar patterns are found for $NO_{y_{air}}$ and $O_{3_{air}}$ for each subset. This means that a strong relationship between these species and potential vorticity is present.

The scatter plots depicting the distribution of $NO_{y_{air}}$ and $O_{3_{air}}$ pairs with respect to latitude for the three PV regions show a different pattern compared to the scatter plots for RH and $T_{dry}$. Figure 8.61 through 8.63 depict the scatter plots for Winter for low, medium and high PV.

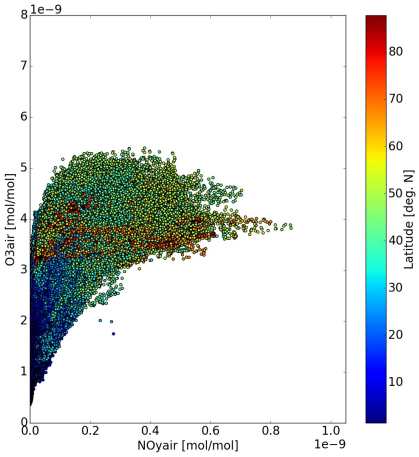


Figure 8.61: Aviation $NO_y$ versus $O_3$ with respect to latitude for the Winter season, over the whole Northern Hemisphere. Data for low PV values is shown.

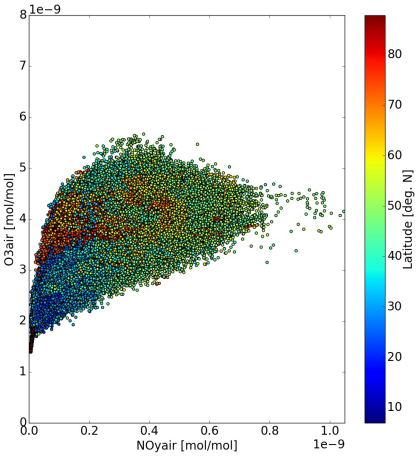


Figure 8.62: Aviation $NO_y$ versus $O_3$ with respect to latitude for the Winter season, over the whole Northern Hemisphere. Data for medium PV values is shown.

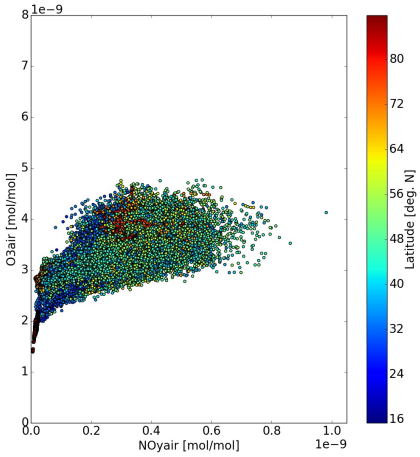


Figure 8.63: Aviation $NO_y$ versus $O_3$ with respect to latitude for the Winter season, over the whole Northern Hemisphere. Data for high PV values is shown.

Figure 8.61 shows the data points with low PV. Here the square-root pattern increase that was found in the RH and $T_{dry}$ plots is clearly visible. This graph shows mainly data points found for low to mid-latitudes, in accordance with this region containing low PV values. On the lower left of the scatter plot low mixing ratios of both $NO_{y_{air}}$ and $O_{3_{air}}$ are found for low latitudes. With increasing mixing ratios the latitudinal values appear to be rather blended than to show clear regions.

For medium PV the "tail" of low $NO_{y_{air}}$ and $O_{3_{air}}$ is not present. The graph shows data points for the whole range of latitudes, including a cluster of high latitudes at the top left part of the scatterplot. When zooming in (see Figure 8.64) a small cluster data points is found with polar latitude values and low mixing ratios of $NO_{y_{air}}$ and $O_{3_{air}}$. This cluster was not found in the Winter scatter plots of RH or $T_{dry}$ and requires further investigation.

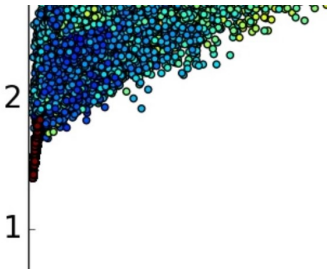


Figure 8.64: Zoomed in frame of aviation $NO_y$ versus $O_3$ with respect to latitude for the Winter season for medium PV. This frame shows a detailed part of the lower left region of Figure 8.62.

For high PV (Figure 8.63) even less low $NO_{y_{air}}$ or low $O_{3_{air}}$ values are present and a clear region of high latitude is visible. Additionally, no clear region with high latitude data points is found in the left top part of the graph, that was found for the medium PV region. Some high latitudinal data points are still found, but are more blended into the middle region of the scatterplot. In Winter time the dataset for high PV is relatively smaller compared to low and medium PV, resulting in a scatterplot with fewer data points. However, it is clear that no low $NO_{y_{air}}$ and $O_{3_{air}}$ pairs are found for high PV. When zooming to the lower part of the graph, analogously to the medium PV regime, a small cluster data points is found with polar latitude values and low mixing ratios of $NO_{y_{air}}$ and $O_{3_{air}}$ (see Figure 8.65). The discussion of this cluster will follow after the discussion of the Summer season scatter plots.

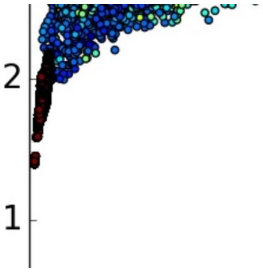


Figure 8.65: Zoomed in frame of aviation $NO_y$ versus $O_3$ with respect to latitude for the Winter season for high PV. This frame shows a detailed part of the lower left region of Figure 8.63.

Figure 8.66 through 8.68 depict the scatter plots for Summer for low, medium and high PV. These plots exhibit larger aviation $O_3$ values compared to Winter, analogously to the patterns found for RH and $T_{dry}$. However, these scatter plots show an interesting pattern that was not seen before in the other plots. Most prominently is that for each PV regime, the scatter plots take different shapes. Furthermore, no clear high-latitude regions are found in the upper-left part of the graphs, but the data points wit high latitude values are rather blended throughout the upper part of the graphs. Additionally, a clear cluster with polar latitude values is found at the bottom left of each graph.

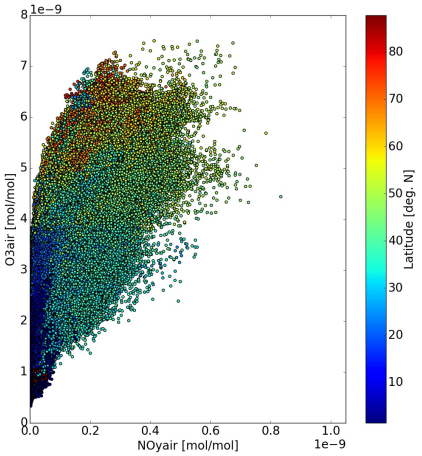


Figure 8.66: Aviation $NO_y$ versus $O_3$ with respect to latitude for the Summer season, over the whole Northern Hemisphere. Data for low PV values is shown.

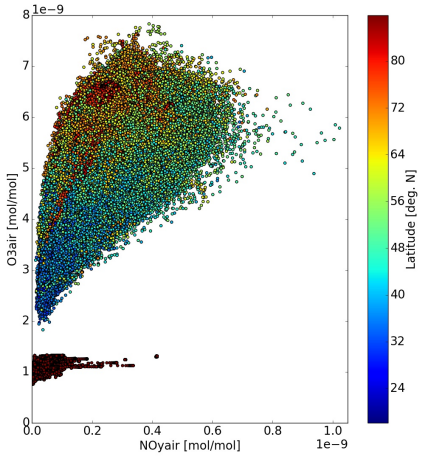


Figure 8.67: Aviation $NO_y$ versus $O_3$ with respect to latitude for the Summer season, over the whole Northern Hemisphere. Data for medium PV values is shown.

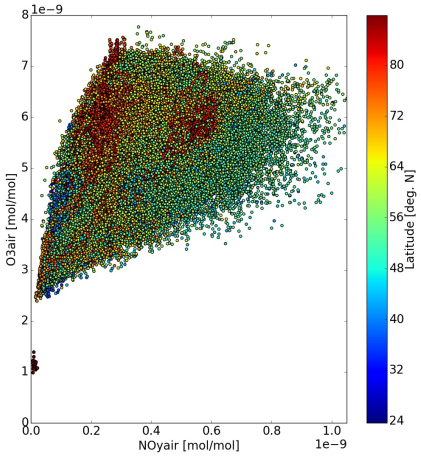


Figure 8.68: Aviation $NO_y$ versus $O_3$ with respect to latitude for the Summer season, over the whole Northern Hemisphere. Data for high PV values is shown.

Figure 8.66 depicts the $NO_{y_{air}}$ and $O_{3_{air}}$ for low PV. Here a gradual transition can be seen from low latitudes to mid-latitudes with increasing aviation $NO_y$ and $O_3$ values. When comparing this figure to the two on the right of it, it is evident that no high $NO_{y_{air}}$ mixing ratios are found for the low PV regime. High latitudes are not present in this dataset, analogously to the Winter scenario. However, as mentioned before, in the lower left of the graph a small cluster of polar latitude values is located. Figure 8.69 shows a this part of the graph in more detail, where the cluster can be better distinguished.

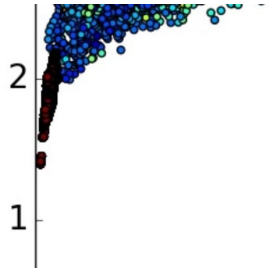


Figure 8.69: Zoomed in frame of aviation $NO_y$ versus $O_3$ with respect to latitude for the Summer season for low PV. This frame shows a detailed part of the lower left region of Figure 8.66.

In Figure 8.67 the distribution of the species can be seen with respect to latitude for medium PV. The tail of low latitude, low $NO_{y_{air}}$ and low $O_{3_{air}}$ is absent, and a gradual transition from lower to higher latitudes is seen for increasing $NO_{y_{air}}$ and $O_{3_{air}}$, analogously to the Winter scenario. For this regime, the maximum $NO_{y_{air}}$ and $O_{3_{air}}$ are higher compared to the low PV regime. The cluster of polar latitudinal data points located at low $NO_{y_{air}}$ and $O_{3_{air}}$ is even more prominent here. This cluster needs further research as it is not clear why high latitudinal values are associated with medium PV and low $NO_{y_{air}}$ and $O_{3_{air}}$ values.

Finally in Figure 8.68 the distribution of aviation $NO_y$ and $O_3$ can be seen with respect to latitude for high PV. A sharp increase in $O_3$ constituents can be seen for increasing $NO_y$. No low latitude data points are found in this subset, and overall no gradual transition from low to high latitudes is established with increasing $NO_{y_{air}}$ of $O_{3_{air}}$. This indicates that the $NO_{y_{air}}$ - $O_{3_{air}}$ behaviour is not dependent on latitude for high PV. Compared to low- and medium PV, the maximum $NO_{y_{air}}$ of this subset is highest, bu the maximum $O_{3_{air}}$ is comparable t that of medium PV.

In general it can be concluded that for the Summer season higher $NO_{y_{air}}$ and $O_{3_{air}}$ mixing ratios are found for higher PV regimes. For both seasons, a correlation is found with respect to latitude. For the low PV regime more data points are found with low latitudes compared to the subsets of medium PV and high PV. The medium PV regime shows a range from mid-latitudes to high latitudes (see the colorbar that with labels that extend from 24 N up to 80 °N for Summer). For the high PV range, the amount of data points at high latitudes is even higher than for medium PV.

To take a closer look at the possible correlations between latitude and the mixing ratios of aviation $NO_y$ and $O_3$ for the three PV regimes, the joint KDE plots for each regime will be discussed in the following text.

### $NO_{y_{air}}$ analysis with respect to PV, Winter

The joint KDE plots of $NO_{y_{air}}$ versus latitude for the Winter season are depicted in Figure 8.70 (low PV regime), Figure 8.71 (medium PV regime) and in Figure 8.72 (high PV regime). As discussed in Section 7.8 the potential vorticity increases with latitude. In accordance with this, the latitudinal KDE's show an accumulation of the data points around low latitudes for the low PV regime and an accumulation of the data points around high latitudes for the high PV regime. The KDE of the latitude values in the medium PV regime show a range from mid-latitudes (approx. 30 °N) up to high latitudes (approx. 85 °N), with subtle peaks at approximately 40°N and 75°N that indicate that the data points are not evenly distributed over the Northern Hemisphere for the medium PV range.

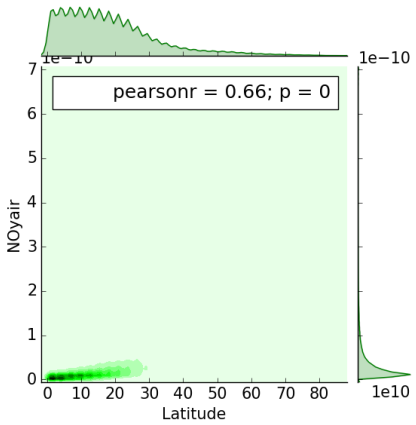


Figure 8.70: Joint Kernel Density Estimation of $NO_{y_{air}}$ and latitude for the Winter season, over the whole Northern Hemisphere. Data for low potential vorticity is shown.

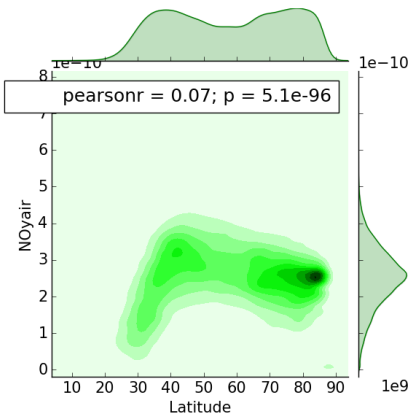


Figure 8.71: Joint Kernel Density Estimation of $NO_{y_{air}}$ and latitude for the Winter season, over the whole Northern Hemisphere. Data for medium potential vorticity is shown.

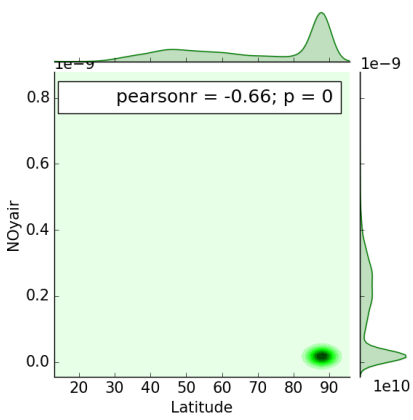


Figure 8.72: Joint Kernel Density Estimation of $NO_{y_{air}}$ and latitude for the Winter season, over the whole Northern Hemisphere. Data for high potential vorticity is shown.

In Figure 8.70 the joint KDE plot shows an accumulation of the data points at low mixing ratios for low latitudes. As discussed earlier, low PV values are found at low latitudes, which is reflected by the KDE for the latitude values of the dataset. The low mixing ratios that are found at these latitudes is in accordance with the latitudinal variability of these species discussed in Section 5.1.

The joint KDE for the medium PV regime is shown in Figure 8.71. In this figure it can be seen that the data points accumulate at high mixing ratios of around $2-3\times10^{-10}$ mol/mol from mid- to high latitudes, with an emphasized accumulation at high latitudes. The graph shows a correlation of increasing mixing ratio with latitude, however at high latitudes, from around 60°N on wards, the accumulation of the data points seem to decrease to lower mixing ratios, and a strong accumulation at mixing ratios below the maximum is seen at latitudes around 70°N - 85 °N. This is in accordance with what was found in the scatterplot for medium PV in Winter which was depicted in Figure 8.62. In the scatterplot a clear region of data points with high latitudes was found on the left side of the plot, indicating lower $NO_{y_{air}}$ mixing ratios than the maximum in the dataset.

In the high PV regime the joint KDE plot shows an accumulation at low mixing ratios for polar latitudes. This is not reflected in the scatterplot of this regime (Figure 8.63). The subtle secondary peak in the KDE of aviation $NO_y$ in this regime (see Figure 8.57) does not correspond to a specific accumulation in the joint KDE plot, which means that the data points with elevated aviation $NO_y$ mixing ratios is not restricted to a specific latitudinal range.

### $O_{3_{air}}$ analysis with respect to PV, Winter

The joint KDE plots of $O_{3_{air}}$ versus latitude for the Winter season are depicted in Figure 8.73 (low PV regime), Figure 8.74 (medium PV regime) and in Figure 8.75 (high PV regime). At first sight one can see that these joint KDE plots show similar accumulation regions as the joint KDE's of aviation $NO_y$ discussed in the previous Section (Figures 8.70 - 8.72).

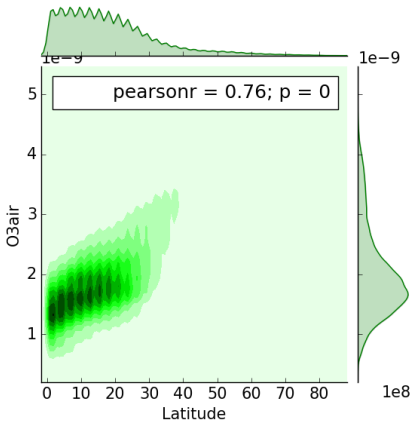


Figure 8.73: Joint Kernel Density Estimation of $O_{3_{air}}$ and latitude for the Winter season, over the whole Northern Hemisphere. Data for low potential vorticity is shown.

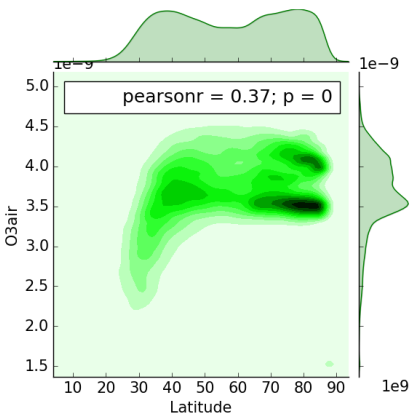


Figure 8.74: Joint Kernel Density Estimation of $O_{3_{air}}$ and latitude for the Winter season, over the whole Northern Hemisphere. Data for medium potential vorticity is shown.

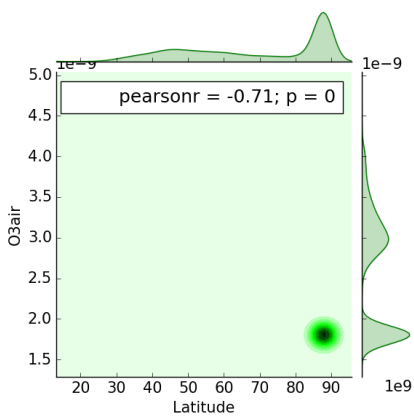


Figure 8.75: Joint Kernel Density Estimation of $O_{3_{air}}$ and latitude for the Winter season, over the whole Northern Hemisphere. Data for high potential vorticity is shown.

In the joint KDE plot for low PV values (left figure), an accumulation for low- to medium mixing ratios is found for latitudes up to approximately 30 °N. Whereas the $NO_{y_{air}}$ mixing ratios were quite concentrated at very low mixing ratios for this regime, the $O_{3_{air}}$ mixing ratios show a larger range of values for the low latitude region.

For the medium regime (middle figure), two strong regions of accumulations are identified, both for high latitudes. The first accumulation is found for mixing ratios around $3.5 \times 10^{9}$ mol/mol at latitudes from approximately 70 °N up o 90 °N and the second accumulation is concentrated around $4 \times 10^{-9}$ mol/mol a 80 °N to 90 °N. For lower latitudes a weaker accumulation is located around $3.5 - 4 \times 10^{-9}$ mol/mol. Overall, the pattern in this graph shows a sharp increase in mixing ratios with increasing latitude at mid-latiudes. However, at high latitudes, from 70 °N on wards, the accumulation of the data points seem to decrease to lower mixing ratios, analogously to what was found in the $NO_{y_{air}}$ joint KDE of this regime.

The high PV regime joint KDE plot in the figure on the right shows an identical behaviour as the joint KDE of $NO_{y_{air}}$ for this regime. However, this cluster of low $NO_{y_{air}}$ and low $O_{3_{air}}$ mixing ratios in the polar region was not identified in the scatter plot for Winter (Figure 8.63)

### $NO_{y_{air}}$ analysis with respect to PV, Summer

The joint KDE plots of $NO_{y_{air}}$ versus latitude for the Winter season are depicted in Figure 8.76 (low PV regime), Figure 8.77 (medium PV regime) and in Figure 8.78 (high PV regime). These joint KDE plots show that the KDE of the latitude values of the medium PV subset shows a different shape than the one found for Winter. In Summer a dominant peak is found at polar latitudes for medium PV, that was absent in the Winter analysis. For the low PV regime the KDE of the latitude values shows a high density for low latitude values and for the high PV regime the density increases to a maximum at high latitudes. This is in agreement with the latitudinal variability of PV discussed in Chapter 7.

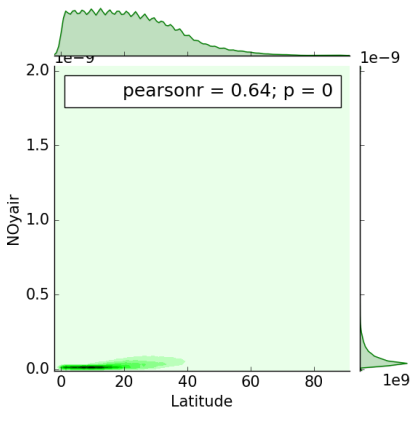


Figure 8.76: Joint Kernel Density Estimation of $NO_{y_{air}}$ and latitude for the Summer season, over the whole Northern Hemisphere. Data for low potential vorticity is shown.

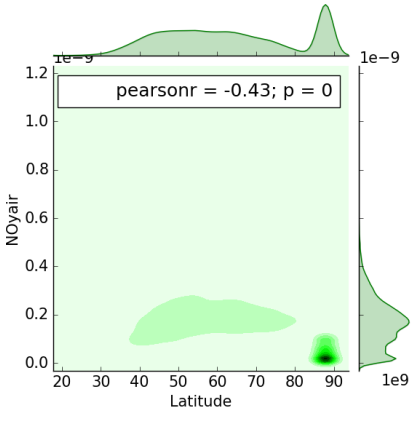


Figure 8.77: Joint Kernel Density Estimation of $NO_{y_{air}}$ and latitude for the Summer season, over the whole Northern Hemisphere. Data for medium potential vorticity is shown.

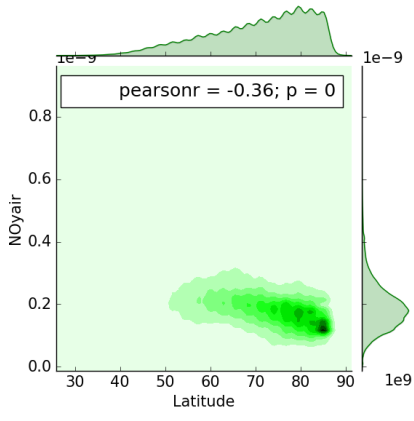


Figure 8.78: Joint Kernel Density Estimation of $NO_{y_{air}}$ and latitude for the Summer season, over the whole Northern Hemisphere. Data for high potential vorticity is shown.

Figure 8.76 shows the joint KDE plot for the low PV regime in Summer. Here it can clearly be seen that the single dominant peak found at low mixing ratios is in accordance with low latitude values.

In the medium PV range the distribution of $NO_{y_{air}}$ mixing ratios with respect to latitude is less straightforward. The primary peak in the KDE of the latitudes is in accordance with very low mixing ratios. This accumulation that is represented by the dark black dot on the bottom right of the joint plot respresents the cluster of low mixing ratios at polar latitudes that was identified in the scatter plots as well (see e.g. Figure 8.67). A second accumulation of data points is found at mid- to high latitudes (40 °N - 80 °N) with higher mixing ratios.

The KDE of the latitudes for the high PV regime (Figure 8.78) shows an increasing density for high latitudes. The high latitudes are paired with higher mixing ratios of up to $3 \times 10^{-}10$ mol/mol. After 80 °N latitude however, the data points accumulate at lower mixing ratios, with a strong accumulation around $1.8 \times 10^{-10}$ mol/mol.

The three joint KDE plots show clearly the correlation between PV and latitude: at low latitudes low PV values are prominent, which increase with latitude. Also the $NO_{y_{air}}$ mixing ratios increase with higher PV, which is correlated to its variability with respect to latitude. The cluster of low mixing ratios for polar latitudes is clearly present in the joint KDE plot for medium PV, which was also identified in the scatterplot for said scenario.

### $O_{3_{air}}$ analysis with respect to PV, Summer

The joint KDE plots of $O_{3_{air}}$ versus latitude for the Winter season are depicted in Figure 8.79 (low PV regime), Figure 8.80 (medium PV regime) and in Figure 8.81 (high PV regime). These joint KDE plots show similar patterns to the $NO_{y_{air}}$ joint plots, but the accumulation regions are more stretched out.

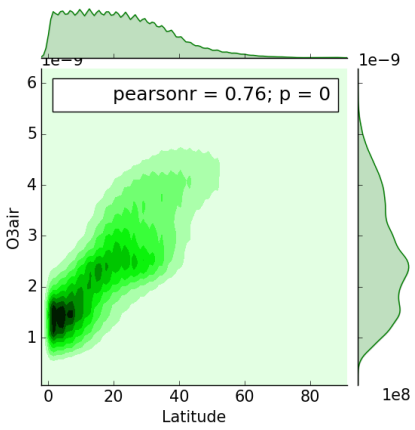


Figure 8.79: Joint Kernel Density Estimation of $O_{3_{air}}$ and latitude for the Summer season, over the whole Northern Hemisphere. Data for low potential vorticity is shown.

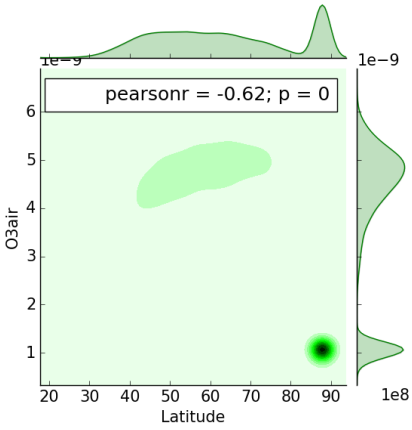


Figure 8.80: Joint Kernel Density Estimation of $O_{3_{air}}$ and latitude for the Summer season, over the whole Northern Hemisphere. Data for medium potential vorticity is shown.

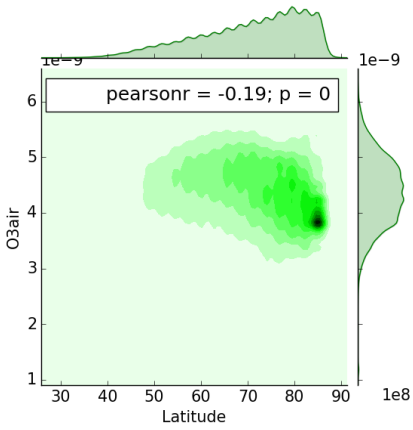


Figure 8.81: Joint Kernel Density Estimation of $O_{3_{air}}$ and latitude for the Summer season, over the whole Northern Hemisphere. Data for high potential vorticity is shown.

The figure on the left shows that for the low PV regime (left figure) low mixing ratios (starting at $1 \times 10^{-9}$ mol/mol are found at low latitudes. The mixing ratios increase with respect to latitude to a maximum of approximately $4.5 \times 10^{-9}$ at 60 °N, as expected from the latitudinal variability of aviation $O_3$ discussed in Section 5.1.

For medium PV the mixing ratios accumulate around $4 \times 10^{-9}$ mol/mol to $5 \times 10^{-9}$ mol/mol from mid-latitudes (40 °N) up to approximately 80 °N. The mixing ratios increase subtly with respect to latitude, as is expected from the latitudinal variability of this species. Again, at polar latitudes the accumulation of low mixing ratios is found, analogously to the $NO_{y_{air}}$ joint plot for this regime.

For the high PV regime a clear accumulation is seen for high latitude values, but the mixing ratios decrease with respect to latitude at high latitudes. This is in accordance with the variability of aviation $O_3$ at high latitudes, which states that the contribution of aviation $O_3$ decreases at polar latitudes.

These three joint KDE plots show that aviation $O_3$ increases with respect to latitude until it reaches approximately 80 °N. At medium PV a clear cluster of low mixing ratios is found at polar latitudes, which represents the cluster of data points that was found in the scatter plots as well.
In the scatter plots of all PV regimes (except of low PV in Winter), a cluster of data points with low mixing ratios at polar latitudes was found. This cluster was also found in some scatter plots depicting the distribution of the data points

with respect to relative humidity. This cluster was also found in the majority of the joint KDE plos. These data points could potentially represent air parcels containing low mixing ratios that have been transported from lower latitudes to polar latitudes. This could explain why the cluster is most prominent for medium PV and not for high PV in Summer, while at polar latitudes higher PV values are expected. Lower (than usual) PV values in the polar region indicate that the data points with these PV values have been transported there from lower latitudes. Additionally, this cluster was also found for the medium RH and high RH range, while at these latitudes higher mixing ratios are expected.

## 8.3. Discussion of results: aviation $NO_y$ and $O_3$ variability in the Northern Hemisphere

To conclude this Chapter, this Section summarizes the findings and highlights the results that were found in the analysis of the variability of aviation $NO_y$ and aviation $O_3$. Firstly the latitudinal and seasonal variability are discussed, after which the variability with respect to the weather variables is detailed.

### 8.3.1. Concluding the latitudinal and seasonal variability of aviation $NO_y$ and $O_3$ in the Northern Hemisphere

In Section 8.1 the general seasonal and variability of the mixing ratios and relative contributions of aviation $NO_y$ and $O_3$ was analysed. From this analysis it resulted that in general, the mixing ratios of aviation $NO_y$ and $O_3$ increase with latitude due to the increasing air traffic activity and horizontal transport through the atmosphere which transports these species to higher latitudes. The analysis was performed for latitudes from 0°N up to 80 °N where air traffic density is largest [26]. The mixing ratios found for Winter are generally lower than for Summer which is attributed to the higher air traffic density in Summer compared to Winter [17]. The relative contributions of these species on the other hand are larger in Winter compared to Summer, due to larger background concentrations in Summer which are attributed to higher deep convection and vertical mixing in the atmosphere. These results found are in agreement with the research performed by Wauben et al. (1997) and Köhler et al.(2012) [25][42].

### 8.3.2. Concluding the variability of aviation $NO_y$ and $O_3$ with respect to weather variables

The variability of aviation $NO_y$ and $O_3$ was assessed in Section 8.2 by means of KDE's, scatter plots and joint KDE plots. The KDE of the data over the Northern Hemisphere does not show a normal distribution for any of the subsets. Rather, two or more peaks are found in the KDE's which are potentially correlated to the latitudinal variation of the species. However, in the majority of the cases the data does not show a repeating pattern for the different study regimes, which suggests that the mixing ratios behave differently in the study regimes. In order to investigate this further, the data is visualized using scatter plots and joint KDE plots. In the following text variability with respect to each weather variable is summarized. Table 8.1 summarizes the values of the mixing ratios around which the data accumulates for each study subset analysed.

Table 8.1: Overview of mixing ratios around which the data accumulates in the subsets analysed. The primary peak refers to the largest peak in the KDE plots, and the secondary peak refers to the weaker peaks present in the KDE plots. The boxes highlighted in yellow indicate scenarios where the primary peak is at a larger value than the secondary peak. The boxes highlighted in red indicate scenarios where the highlighted peak represent the cluster containing low mixing ratios at polar latitudes.

| | **Summer** | | | |
|---|---|---|---|---|
| Regime | $NO_{y_{air}}$ primary peak ($\times 10^{-11}[mol/mol]$) | $NO_{y_{air}}$ secondary peak ($\times 10^{-11}[mol/mol]$) | $O_{3_{air}}$ primary peak ($\times 10^{-9}[mol/mol]$) | $O_{3_{air}}$ secondary peak ($\times 10^{-9}[mol/mol]$) |
| Low RH | 2.164 | 18.16 | 4.399 | 2.699 |
| Medium RH | 1.356 | 22.58 | 5.363 | 1.189 |
| High RH | 7.427 | - | 1.107 | 4.471 |
| Low $T_{dry}$ | 1.832 | 22.92 | 5.068 | 1.973 |
| High $T_{dry}$ | 3.394 | 18.29 | 4.495 | 2.816 |
| Low PV | 3.876 | - | 2.374 | 1.542 |
| Medium PV | 16.73 | 1.832 | 4.832 | 1.058 |
| High PV | 17.96 | - | 4.221 | - |
| | **Winter** | | | |
| | $NO_{y_{air}}$ primary peak ($\times 10^{-11}[mol/mol]$) | $NO_{y_{air}}$ secondary peak ($\times 10^{-11}[mol/mol]$) | $O_{3_{air}}$ primary peak ($\times 10^{-9}[mol/mol]$) | $O_{3_{air}}$ secondary peak ($\times 10^{-9}[mol/mol]$) |
| Low RH | 1.845 | 19.93 | 3.029 | 1.839 |
| Medium RH | 1.168 | 32.29 | 3.678 | 1.764 |
| High RH | 0.875 | 19.34 | 3.754 | 1.636 |
| Low $T_{dry}$ | 31.51 | 1.679 | 1.772 | 3.647 |
| High $T_{dry}$ | 1.361 | 25.95 | 3.091 | 1.834 |
| Low PV | 1.149 | - | 1.956 | - |
| Medium PV | 25.76 | - | 3.530 | 1.520 |
| High PV | 1.411 | 20.29 | 1.793 | 2.974 |

### Variability with respect to relative humidity summarized

The data showed a correlation between mixing ratios and latitude for all RH regimes. For both seasons the mixing ratios increase with latitude, with a clear region of low latitude values for low mixing ratios. The mixing ratios increase with latitude and especially in Summer a clear region data points with high latitude values is seen at the top of the graph which entail high aviation $NO_y$ and $O_3$ mixing ratios at high latitudes which is in agreement with the latitudinal variability found and discussed in Section 5.1. The scatter plots and joint KDE plots clearly show less data points present at low latitudes for low RH, as here higher RH values are generally found. In the joint KDE graphs for Winter an accumulation of the data points is seen for polar latitudes and low mixing ratios in all RH regimes for $O_{3_{air}}$, but only for low and medium RH for $NO_{y_{air}}$. This accumulation is not identified in the scatter plots. In the Summer joint KDE plots this cluster is also distinctive for medium and high RH. Additionally, this cluster is clearly seen in the respective scatter plots for this season. The peaks in the KDE's of $NO_{y_{air}}$ and $O_{3_{air}}$ for these cases is highlighted in Table 8.1 in red. The discussion on this cluster of data points follows later.

The scatter plots for all RH regimes show a similar pattern for each season separately. For the low RH regime less data points are found at low latitudes, which is attributed to elevated RH levels at low latitudes. In general, the behaviour of $NO_{y_{air}}$ is similar in all RH regimes which follows the variability of RH with respect to latitude. The behaviour of $O_{3_{air}}$ seems different for each RH regime, due to varying shapes of the KDE's for each regime. After closer examination it became evident that the deviation of the KDE plots is attributed to the cluster of low mixing ratios at polar latitudes (which are highlighted in red in Table 8.1). Interesting to note, is that for low RH, relatively lower $O_{3_{air}}$ mixing ratios are found compared to medium and high RH, while low RH is mostly found at higher latitudes where the aviation ozone mixing ratios should actually be higher than in the other regimes. This could indicate that low RH has an effect on the production of ozone from $NO_y$ as higher $O_{3_{air}}$ mixing ratios are expected for this regime.

### Variability with respect to dry air temperature summarized

The Winter subset shows distinctive behaviour in the low- and high $T_{dry}$ regimes for both $NO_{y_{air}}$ and $O_{3_{air}}$. In Summer this distinction is less present, especially for $NO_{y_{air}}$. This is due to the fact that in Winter the contrast between the temperatures is larger. As discussed in Section 8.2.2 the low $T_{dry}$ range for Winter extends from 205 K to215 K, the high $T_{dry}$ range for Winter is equal to the low $T_{dry}$ range for Summer which extends 215 K to 225 K, and the high $T_{dry}$ range for Summer extends from 225 K to 235 K. The KDE's of the high $T_{dry}$ range in Winter and of the low $T_{dry}$ range in Summer are therefore similar. When comparing the low dry air temperature regimes to the high dry air temperature regimes, different behaviour of the species is identified. From this it is concluded that aviation $NO_y$ and aviation $O_3$ behaves differently in each temperature regime, and the species are therefore correlated to dry air temperature.

For both Winter and Summer the scatter plots showed similar behaviour of aviation $NO_{y_{air}}$ and $O_{3_{air}}$ mixing ratios with respect to latitude. Data points in the bottom left of the graph depict low mixing ratios at low latitudes. As the mixing ratios increase, the latitude also increases. In the Winter season few data points with high latitudes are seen, which are quite blended throughout the scatter plot. Furthermore, for high dry air temperatures the data seems to accumulate at low latitudes, which is confirmed by the joint KDE plot (Figure 8.48) which shows elevated densities at low latitudes in the latitude KDE. For Summer the gradual transition from low to high latitudes is more present from low to high mixing ratios. Additionally, the mixing ratios in Summer of both species attain higher maxima, which is in agreement with the seasonal variability discussed in Section 8.1.

In the scatter plots however, it cannot be clearly distinguished where the two peaks found in the KDE plots originate from. In the joint KDE plots it becomes evident that the peaks of the KDE plots are attributed to the accumulation of the data points at specific latitudinal regions. Additionally, in the joint KDE plots for Winter the accumulation of data points around low mixing ratios (for both $NO_{yair}$ and $O_{3_{air}}$ at polar latitudes is present again. These clusters, cannot be distinguished in the scatter plots, but they are visible as small irregularities in the KDE plots of these subsets. The influence of this cluster is most notable in the $O_{3_{air}}$ KDE for the low $T_{dry}$ regime in Winter and the value of this secondary peak is highlighted in red in Table 8.1.

#### Variability with respect to potential vorticity summarized

The KDE plots of $NO_{y_{air}}$ and $O_{3_{air}}$ show distinctive patterns for each PV regime. This suggests that in each PV regime, the distribution of these species is different and therefore the magnitude of PV affects the behaviour of aviation $NO_{y_{air}}$ and $O_{3_{air}}$. In general it is concluded that a correlation is found between the PV regimes and latitudinal ranges in which the data points lie. This is related to the mixing ratios found in each subset as well. As discussed in Section 7.6, PV increases with latitude, which is confirmed by the joint KDE plots, where the latitude KDE's show an increase in density with increasing latitude for increasing PV. It is expected that the KDE's of the species show peaks higher mixing ratios for higher PV values. In Table 8.1 the elevated mixing ratios around which the data accumulates is highlighted in yellow. In Winter this is true for the low PV versus medium PV regime, but the high PV regime seems divided over the two ranges. In the Summer season the low PV regime is in agreement with low mixing ratios and the high PV regime is in agreement with high mixing ratios. The medium PV regime shows agreement with both low and high mixing ratios, which is expected. To better understand the behaviour of the species and explain why the high PV regime in Winter behaves differently than expected, the data is further analysed by means of scatter plots and joint KDE plots.

In the Summer months higher maximum mixing ratios of both species are found compared to Winter, which is in agreement with the seasonal variability discussed in Section 8.1.In the scatter plots of all PV regimes (except of low PV in Winter), a cluster of data points with low mixing ratios at polar latitudes was found. This cluster was also found in some scatter plots depicting the distribution of the data points with respect to relative humidity. Additionally, this cluster occurs in the majority of the joint KDE plots. These data points potentially represent air parcels containing low mixing ratios that have been transported from lower latitudes to polar latitudes. This explains why the cluster is most prominent for medium PV and not for high PV in Summer, while at polar latitudes higher PV values are expected. Lower (than usual) PV values in the polar region indicate that the data points with these PV values have been transported there from lower latitudes. Additionally, this cluster was also found for the medium RH and high RH range, while at these latitudes in these RH regimes, higher mixing ratios are expected. This cluster appeared as well for all years individually, meaning that it is not a random cluster of data points. In the Summer season this cluster is most prominent, which is attributed to higher convective activity. Due to the higher convective activity, more air parcels could be transported towards the polar region. However, to confirm that this cluster originates from lower latitudes, further research is needed. The cluster of data points could be tracked and traced individually to determine where it orginates from.

# 9

# Weather Pattern Analysis

In the previous Chapter the variability of the mixing ratios of aviation $NO_y$ and aviation $O_3$ were analysed with respect to latitude, season, relative humidity, dry air temperature and potential vorticity. However, this was for data over the total Northern Hemisphere, over 10 years of data. It is possible that the variability with respect to the weather variables differs in weather patterns. To analyse whether high-pressure systems and aviation $NO_y$ and aviation $O_3$ are correlated, the behaviour of these species are analysed in different weather patterns. Additionally the variability with respect to the weather variables is assessed again, to investigate the correlations with respect to these variables closer. For this end, high-pressure systems have been selected and filtered using a diagnostic tool. This resulted in a subset of Winter patterns and a subset of Summer patterns with lifetimes ranging from 2 up to 9 timesteps (where one timestep covers 10 hours of data). In Section 9.1 the selected weather patterns are detailed and in Section 9.2 it is shortly discussed why low-pressure systems are not analysed. Section 9.3 covers the discussion of the analysis of the behaviour of aviation $NO_y$, aviation $O_3$ and stratospheric $O_3$ in the weather patterns selected, for weather patterns with short, average, and long lifetimes. In Section 9.4 the variability of the species with respect to the weather variables within the weather patterns is discussed. Finally, Section 9.5 summarizes the findings of this Chapter.

## 9.1. Weather patterns selected

In total 228 high-pressure weather patterns have been found for the DJF and JJA seasons together, over all three regions. The exact amount of weather patterns per season and region can be found in Table 9.1, where the lifetimes per patterns are indicated in the left column as $T[..]$, where $[..]$ indicates the number of timesteps the pattern has survived.

Table 9.1: Number of weather patterns identified for the DJF and JJA season per region. The first column states the lifetimes of the weather patterns.

| | **Region 3** | | **Region 2** | | **Region 3** | |
|---|---|---|---|---|---|---|
| | DJF | JJA | DJF | JJA | DJF | JJA |
| T2 | 11 | 4 | 13 | 1 | 16 | 3 |
| T3 | 10 | 4 | 4 | 4 | 14 | 7 |
| T4 | 12 | 6 | 9 | 2 | 19 | 3 |
| T5 | 9 | 1 | 4 | 2 | 9 | 1 |
| T6 | 8 | 1 | 7 | 1 | 4 | 1 |
| T7 | 4 | 3 | 3 | 0 | 5 | 2 |
| T8 | 1 | 3 | 7 | 0 | 2 | 0 |
| T9 | 1 | 1 | 2 | 0 | 4 | 0 |
| **total** | 56 | 23 | 49 | 10 | 73 | 17 |

In Table 9.1 it can be seen that for the Summer (JJA) season, fewer patterns have been found (50 patterns) compared to in the Winter (DJF) season(178 patterns). This is due to weaker weather patterns in Summer which is illustrated in Figure 9.1 and 9.2 [15]. The Winter weather situations show more distinctive high- and low pressure patterns as can be seen for the Winter example situation which can be seen on the left, whereas the Summer weather situation show a more moderate variability as can be seen in the Summer example situation on the right. For each of the weather patterns included in Table 9.1 the $NO_y$ and $O_3$ behaviour is analysed. This analysis is discussed in the following section (Section 9.3). As fewer Summer patterns were found and the behaviour in the Summer patterns were highly variable, the low amount of Summer data leads to inconclusive results. Therefore, only the Winter patterns are discussed.

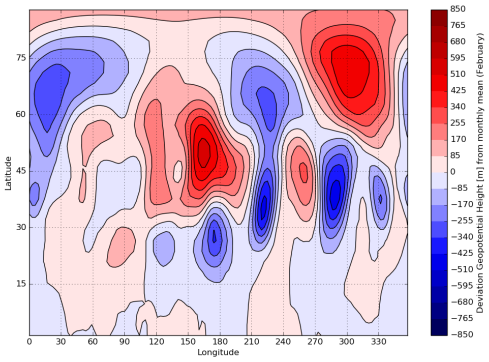


Figure 9.1: An example of a Winter weather situation (27th of February 2006, 08:00

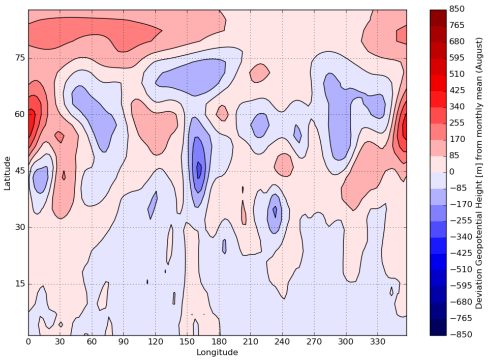


Figure 9.2: An example of a Summer weather situation (5th of August 2006, 22:00

## 9.2. $NO_y$ and $O_3$ development in low-pressure weather patterns

To validate the decision to analyse high-pressure weather systems an initial test is performed to check whether indeed in low pressure systems aviation $NO_y$ does not accumulate and aviation $O_3$ does not increase. In Figure 9.3 the temporal development of aviation $NO_y$ and $O_3$ are plotted over four analysis levels for a steady low pressure system. Here it can be seen that during the low-pressure system the aviation $NO_y$ exhibits some variable behaviour and it even seems to increase slightly. This is due to the high PV values involved in a low pressure pattern which causes additional aviation $NO_{y_{air}}$ to be transported to the location of the low-pressure pattern. However, due to the high vorticity these species do not accumulate here, thus no increase in aviation $O_3$ takes place. This is reflected in the blue lines which depict the temporal development of aviation ozone: these remain unresponsive. Therefore, no increase in aviation $O_3$ takes place in low-pressure patterns and these will thus not be further analysed.

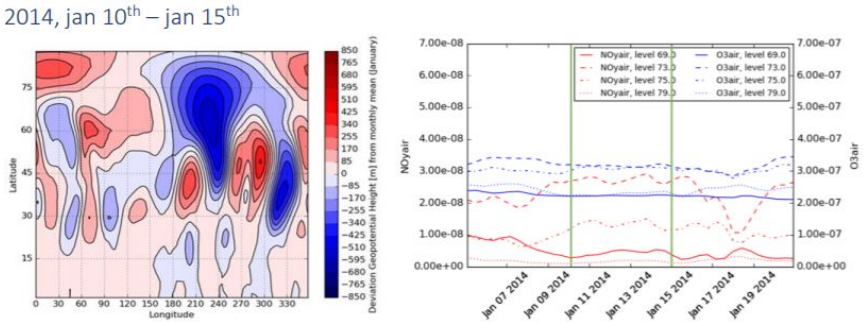


Figure 9.3: Temporal development of mixing ratios of $NO_{y_{air}}$ (red) and $O_{3_{air}}$ (blue) in a low-pressure weather pattern.

## 9.3. $NO_y$ and $O_3$ development in high-pressure weather patterns

In the following text the high-pressure weather patterns for the Winter season are discussed. The Summer weather patterns displayed highly variable trends due to the dynamic weather in Summer. Additionally, due to the higher background concentrations in Summer, it will be unlikely that aviation ozone will be detectable in Summer. Therefore, the current discussion focuses on the Winter patterns. The figures in this text show the normalized temporal development of aviation $NO_y$ and $O_3$ in each weather pattern found. For practical purposes only the plots from Region 3 are included in this discussion as these patterns display the variable behaviour best. The behaviour of weather patterns found in Region 3 and 2 are similar and can be found in the Appendix (D). In the following context the levels that are referred to are the model hybrid pressure levels and are as follows: level 69 indicates higher cruise levels ($\tilde{1}$75 hPa), level 72 indicates average cruise levels ($\tilde{2}$00 hPa) and level 75 implies the lower cruise levels ($\tilde{3}$00 hPa).

### 9.3.1. Short lifetime weather patterns

For short lifetimes (two to four timesteps) a general decrease in $NO_y$ is found during the presence of the high-pressure system at average cruise levels. This is depicted for weather patterns with lifetime T3 in Figure 9.4 where the temporal developments of $NO_y$ and $O_3$ of aviation are depicted. Additionally the temporal development of stratospheric $O_3$ is depicted in this figure on the third line. Higher cruise levels on the other hand show a random temporal development of aviation $NO_y$ and at lower cruise levels the concentration of aviation $NO_y$ decreases largely due to the shorter

lifetime of these species at lower altitudes. The ozone mixing ratios seem unresponsive to the presence of the high-pressure system for all three altitude levels. The stratospheric ozone on the other hand exhibits a strong response to the high pressure system as it decreases strongly at higher levels and gradually less strong at lower levels. At lower flight altitudes the stratospheric ozone has decreased significantly, which means that the stratospheric ozone does not reach these levels. Furthermore, while aviation $NO_y$ and stratospheric ozone decrease at lower levels, aviation ozone seems to remain stable at lower levels compared to the higher levels.

Overall, for short lifetime weather patterns the aviation $NO_y$ and stratospheric ozone show a decrease in response to the high-pressure system. The aviation ozone behaviour remains undisturbed by the presence of high-pressure systems.

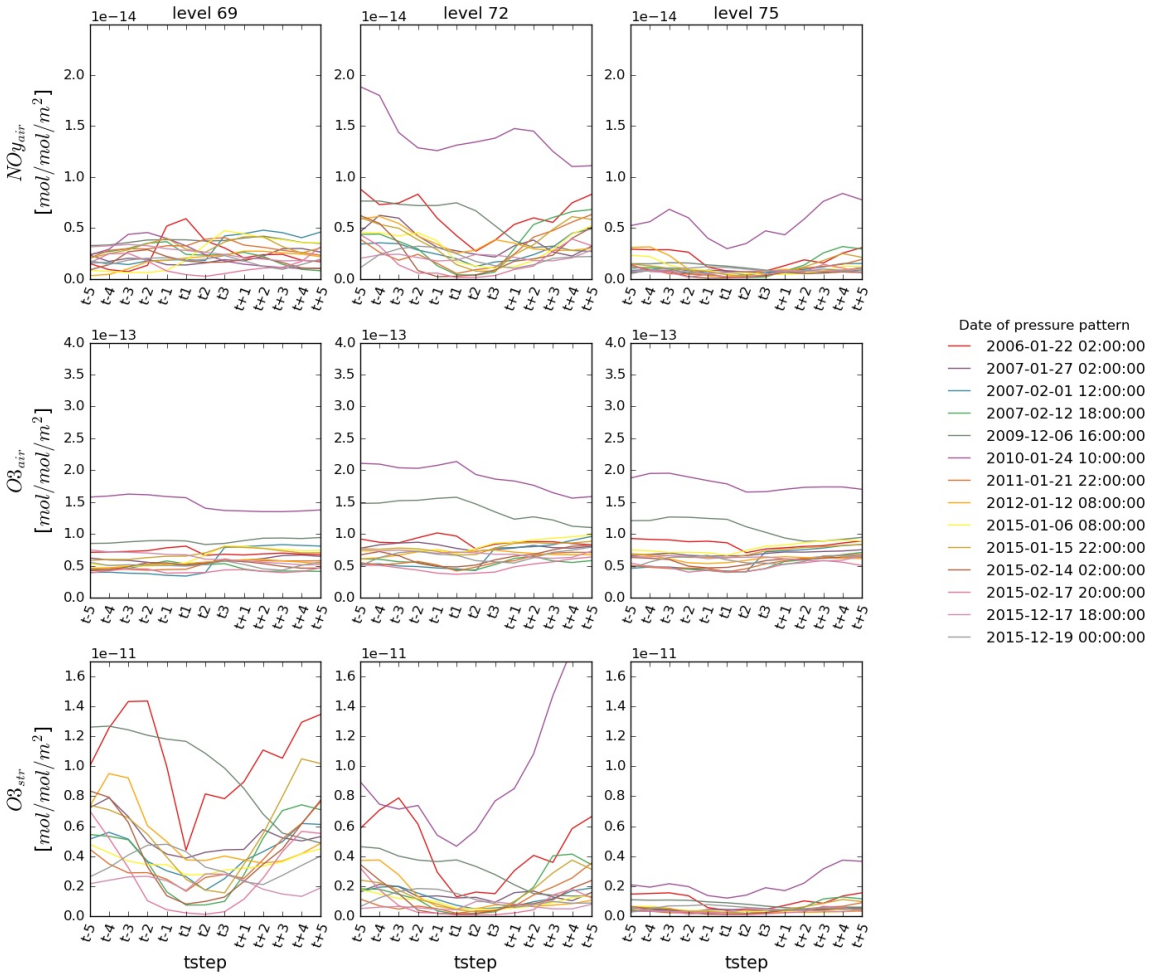


Figure 9.4: Temporal development of normalized mixing ratios of $NOy_{air}$ (top), $O3_{air}$ (middle) and $O_{str}$ (bottom) in weather patterns found in Region 3 with lifetime T3.

If the mixing ratios are normalized with respect to the value at $t_1$ it can be more clearly seen how the time series develop before and after the establishment of the high-pressure system. These normlaized timeseries are depicted in Figure 9.5. For the mixing ratios at all analysed levels, it becomes clear that for some patterns the mixing ratios increase (line continues above the dashed line) and for some patterns the mixing ratios decrease (line continues below the dashed line) after the establishment of the high-pressure system. The time series of the aviation ozone inside the weather patterns show that after the establishment of the high pressure system the mixing ratios deviate more from the normalized line than before the establishment of the high pressure system at $t_1$. This suggests that the aviation ozone responds to the high pressure system, as the lines before the $t_1$ are less variable. However, it does not show the same behaviour for each pattern, thus no conclusions can be drawn on the behaviour of aviation ozone with respect to the high-pressure system.

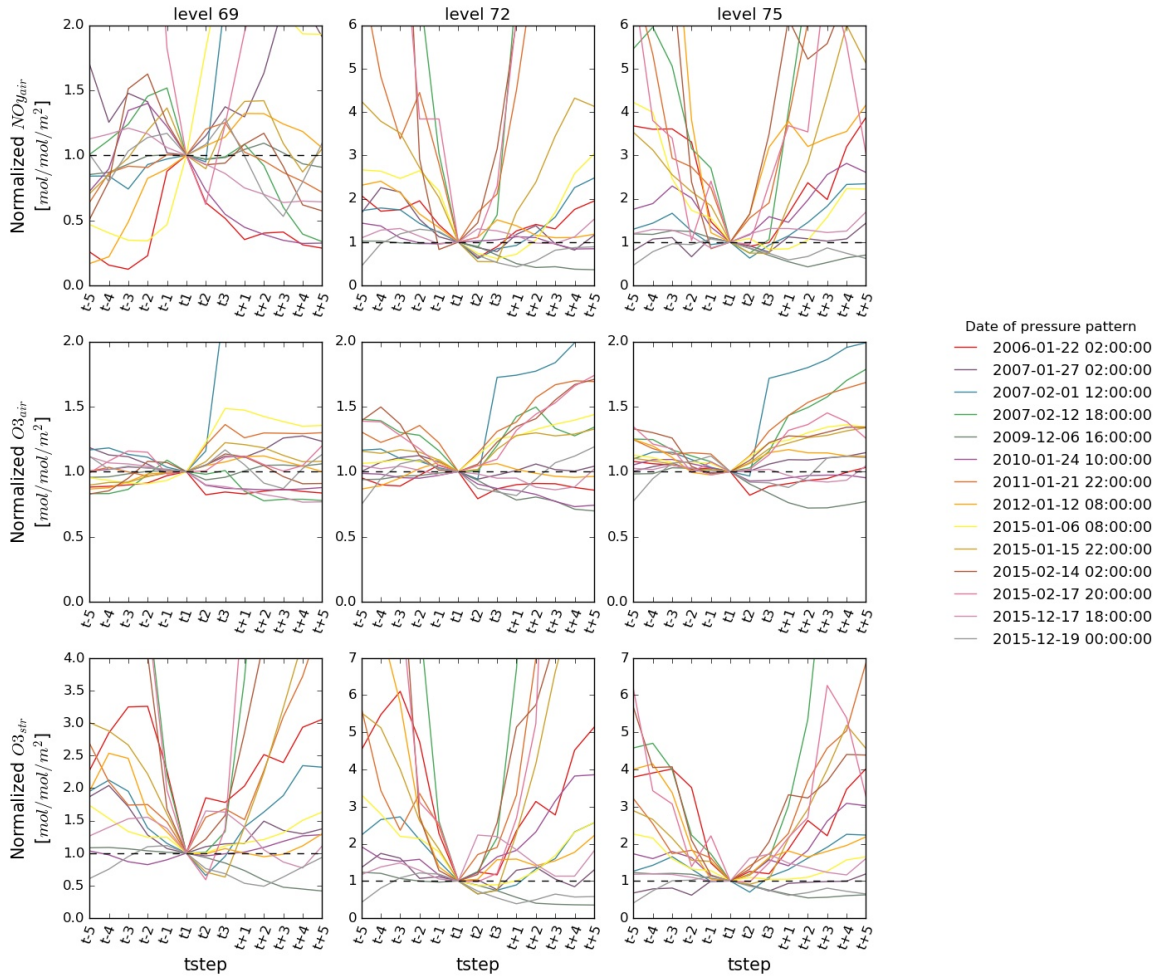


Figure 9.5: Temporal development of normalized mixing ratios of $NO_{y_{air}}$ (top), $O3_{air}$ (middle) and $O_{str}$ (bottom) in weather patterns found in Region 3 with lifetime T3.

### 9.3.2. Average lifetime weather patterns

For high-pressure weather systems of longer lifetime, the decrease in $NO_y$ makes place for some positive and negative peaks, as can be seen for patterns with lifetime T5 in Figure 9.6. Again, at lower cruise altitudes the $NO_y$ and stratospheric $O_3$ mixing ratios have decreased significantly, and the $NO_y$ mixing ratios of level 69 and 72 do not show a similar behaviour. However, the aviation ozone mixing ratios show a similar behaviour on all three levels, even on the lower cruise levels where the $NO_y$ and stratospheric ozone have reduced compared to the higher levels, analogously to the shorter lifetime patterns. The stratospheric ozone shows a highly dynamic response to the high-pressure pattern present.

This highly dynamic response shows a similar pattern to the aviation $NO_y$ pattern at average cruise level. Where peaks in aviation $NO_y$ are found with respect to time, also peaks in stratospheric $O_3$ are found at high and average cruise level. This means that where the aviation $NO_y$ increases, also ozone originating from the stratosphere increases, which suggests vertical downward transport from the Stratosphere into this stable high-pressure pattern. Although the aviation $O_3$ does not exhibit a direct response to these increases, it does exhibit a larger response compared to the shorter lifetime patterns. This means that the increase in aviation $NO_y$ in the pressure pattern possibly affects the production efficiency of aviation $O_3$.

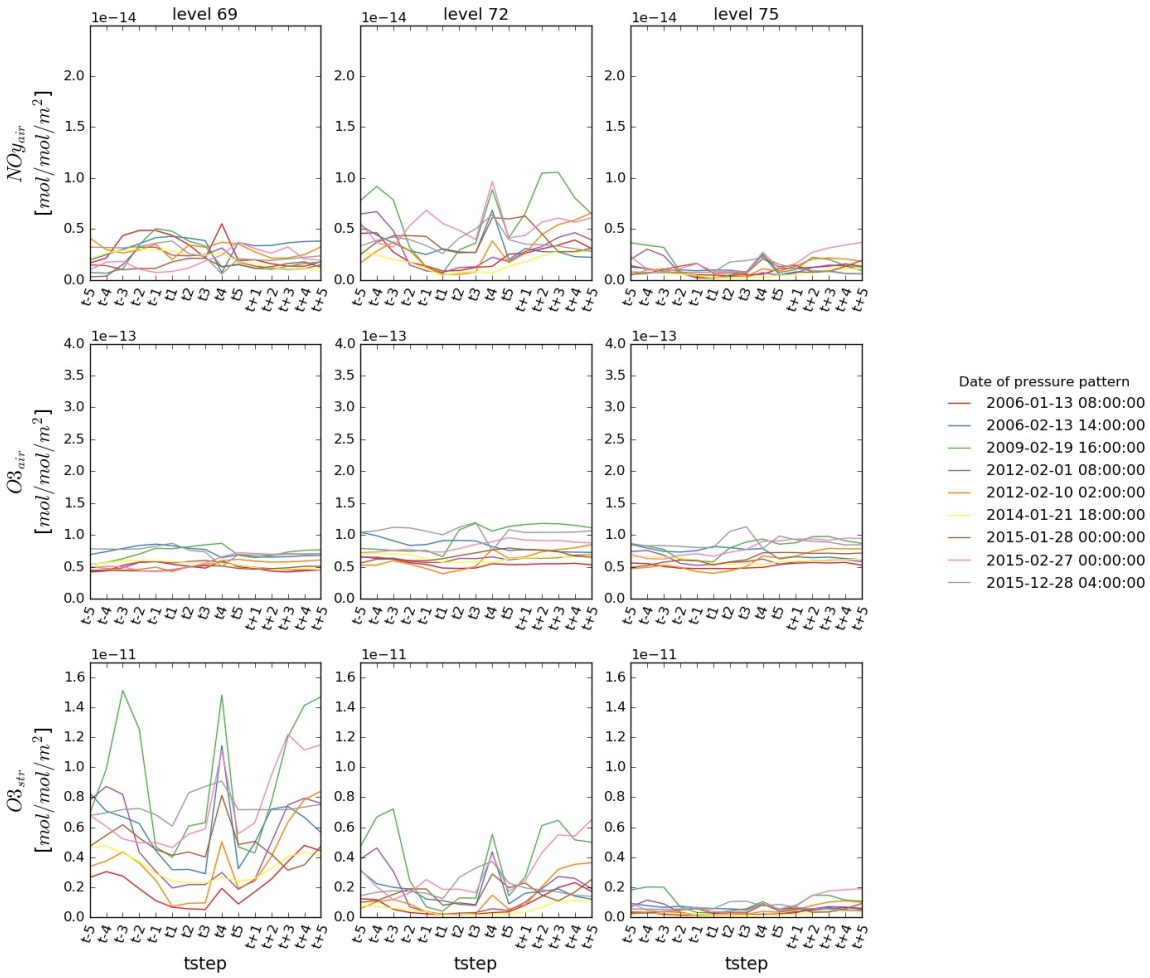


Figure 9.6: Temporal development of normalized mixing ratios of $NO_{y_{air}}$ (top), $O_{3_{air}}$ (middle) and $O_{str}$ (bottom) in weather patterns found in Region 3 with lifetime T5.

The mixing ratios normalized with respect to the value at $t_1$ are depicted in Figure 9.7. Here the response of the mixing ratios after the establishment of the pressure pattern can be seen better. At level 72 the graphs show that themixing ratios generally decrease towards $t_1$, but after $t_1$ the mixing ratios increase. This is valid for $NO_{y_{air}}$, $O_{3_{air}}$ as well as for $O_{3_{str}}$. Interesting to note is that at level 72 and level 75, the majority of the patterns show an increase in aviation $O_{3_{air}}$, which was not clearly visible in the non-normalized graphs.

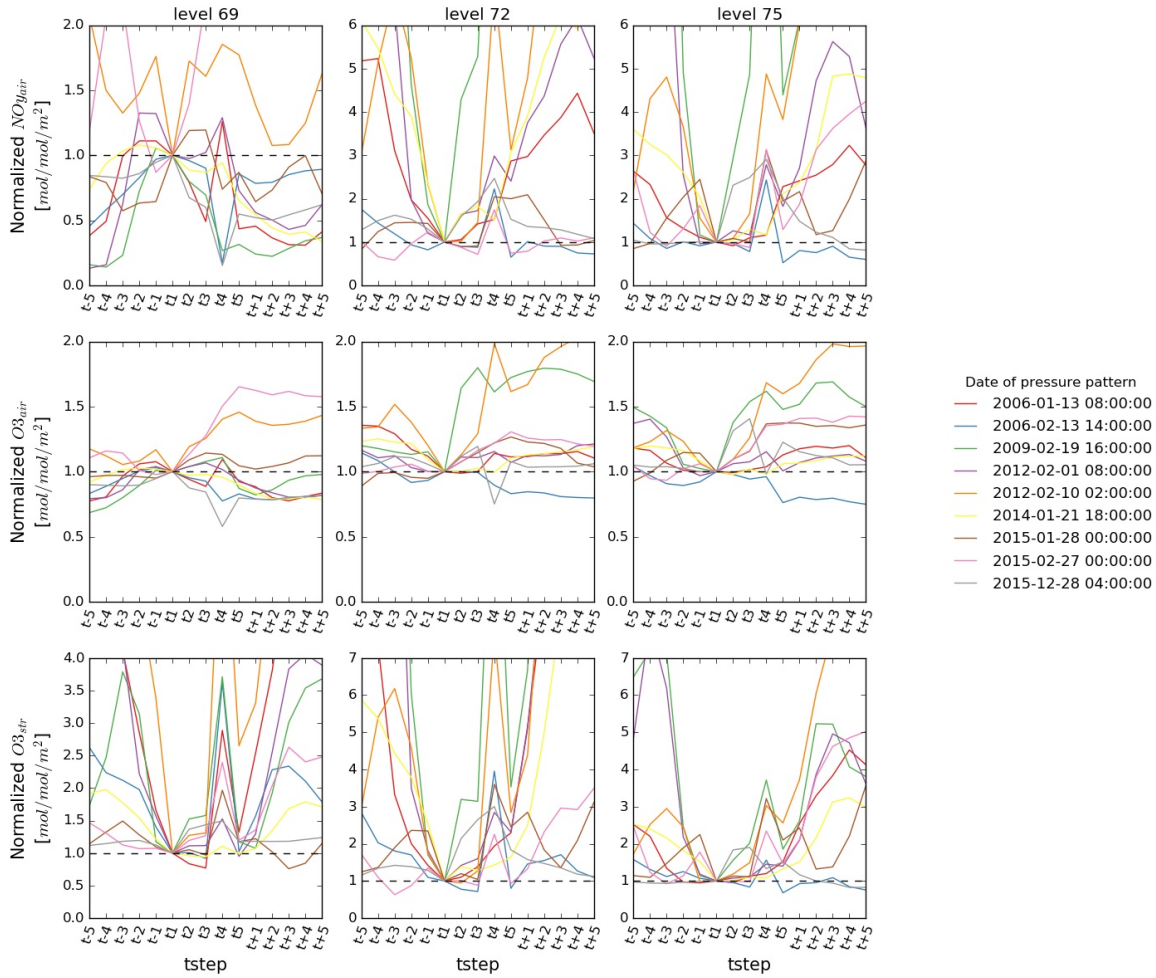


Figure 9.7: Temporal development of normalized mixing ratios of $NO_{y_{air}}$ (top), $O_{3_{air}}$ (middle) and $O_{str}$ (bottom) in weather patterns found in Region 3 with lifetime T5.

### 9.3.3. Long lifetime weather patterns

Weather patterns with a long lifetime (T7 - T9) show a large variable effect in aviation $NO_y$ and $O_3$, as can be seen in Figure 9.8. At average cruise level a clear accumulation can be seen for the majority of the weather patterns, and even at lower cruise level the accumulation is still noticeable. However, at higher cruise level the weather patterns do not exhibit peaks but dips are seen at the relative timesteps. At first glance, it seems that at high cruise level the opposite trend is found compared to average cruise level.

The aviation $O_3$ development is similar for all three levels plotted. Some subtle increases in these mixing ratios are found, although still no linear relationship is identified. However, the pattern of aviation $O_3$ is more stable over the three flight levels than that of the average lifetime weather patterns.

The stratospheric ozone exhibits once again a strong response to the high-pressure system at high cruise level. A similar, but less strong response is seen for average cruise level. This suggests strong downward motion for the weather patterns showing a large increase in stratospheric ozone at level 69 and level 72. This downward motion allows aviation $NO_y$ to accumulate at lower levels where it reacts to aviation $O_3$.

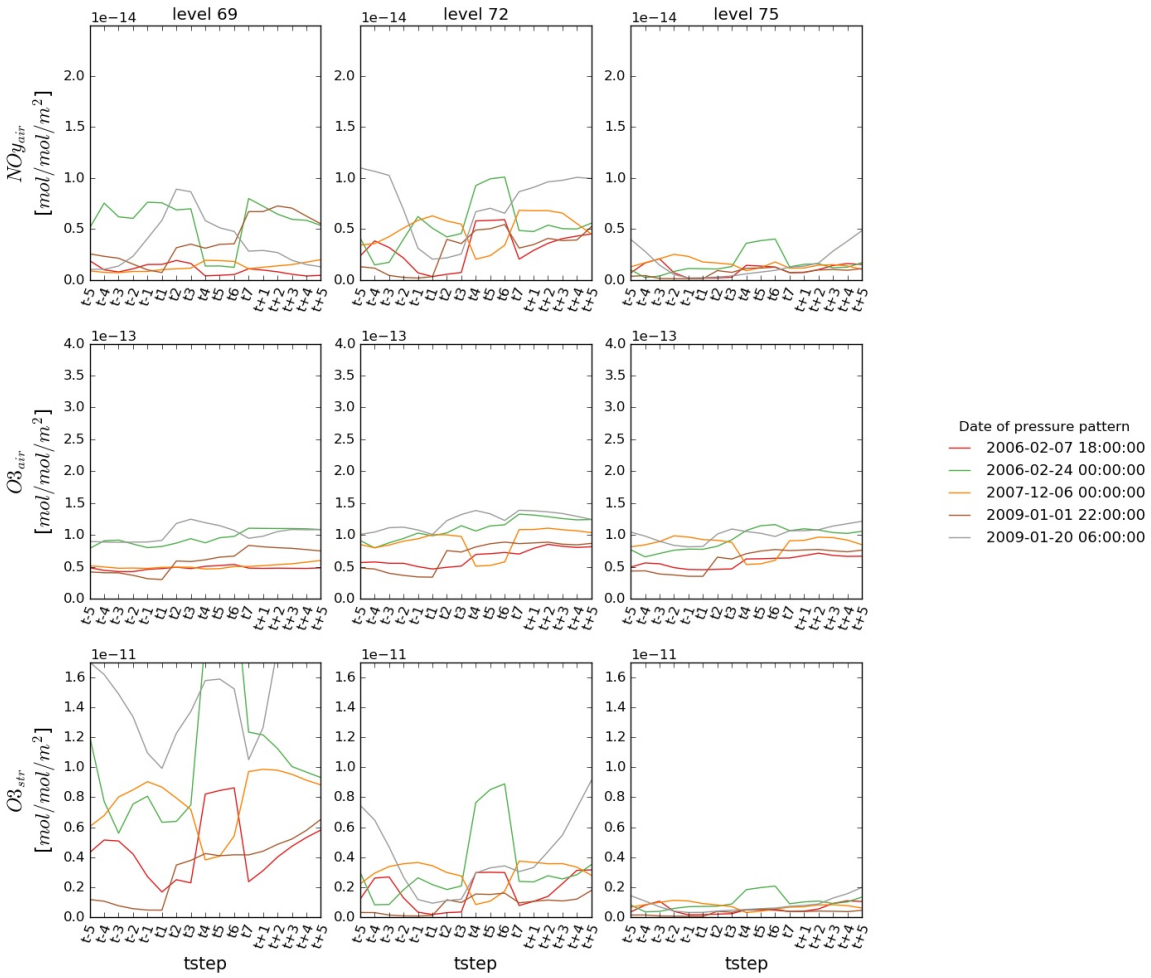


Figure 9.8: Temporal development of normalized mixing ratios of $NO_{y_{air}}$ (top), $O_{3_{air}}$ (middle) and $O_{str}$ (bottom) in weather patterns found in Region 3 with lifetime T7.

The mixing ratios normalized with respect to the value at $t_1$ for long lifetime patterns are depicted in Figure 9.9. Two scenarios are clearly seen at level 72 and level 75:

- $NO_{y_{air}}$ and $O_{3_{str}}$ decrease, and $O_{3_{air}}$ decreases as well (the yellow line).
- $NO_{y_{air}}$ and $O_{3_{str}}$ increase, and $O_{3_{air}}$ increases as well (the grey, red and green lines).

Interesting to see is that at level 69 the yellow line actually shows an increase, and the other lines show a decrease after an initial increase after the establishment of the high-pressure system.

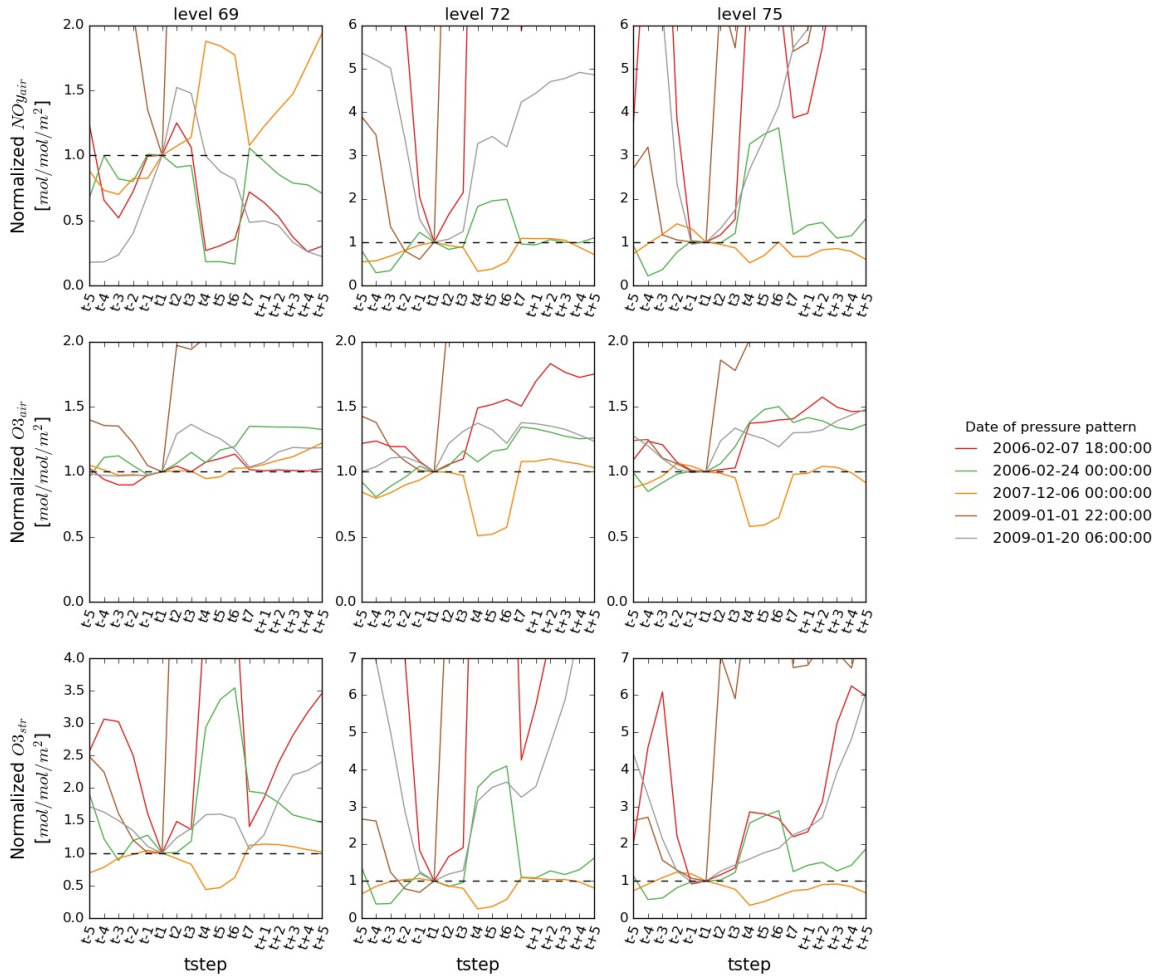


Figure 9.9: Temporal development of normalized mixing ratios of $NO_{y_{air}}$ (top), $O_{3_{air}}$ (middle) and $O_{str}$ (bottom) in weather patterns found in Region 3 with lifetime T7.

It resulted that these two scenarios were related to the potential vorticity values found in the weather patterns. Weather patterns with low PV values (below 1 pvu) at the establishment of the high-pressure system, and increasing PV values towards the end of the pressure system, showed an increase in $NO_{y_{air}}$ mixing ratios, and accordingly increasing $O_{3_{air}}$ mixing ratios. This is depicted in Figure 9.10 which shows the range of PV values expressed in boxplots for the red line from Figure 9.9. Weather patterns with relatively high PV values (larger than 1 pvu) at the establishment of the pressure system, and not increasing PV values, showed a decrease in $NO_{y_{air}}$ and $O_{3_{air}}$ mixing ratios. This is depicted in Figure 9.11 which shows the boxplots of the PV values for the yellow line form Figure 9.9. This analysis was done for all weather patterns found, and all weather patterns showed this behaviour.

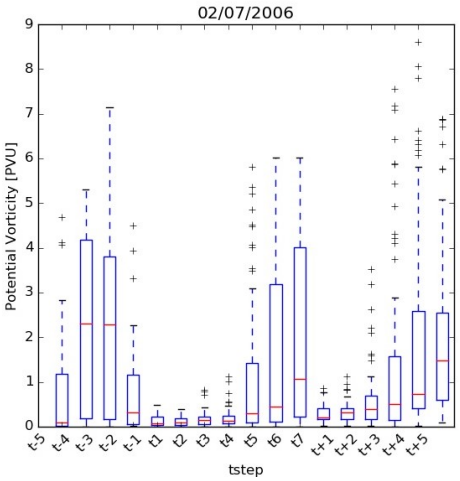


Figure 9.10: Boxplots of potential vorticity values in the weather pattern with the red line (07-02-2006)

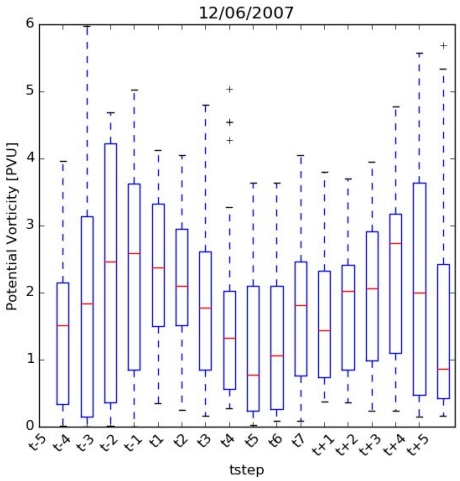


Figure 9.11: Boxplots of potential vorticity values in the weather pattern with the yellow line (06-12-2007)

From the weather patterns discussed in this section it is clear that the presence of a high-pressure system influences the aviation $NO_y$ - $O_3$ dynamics at flight level. However, not for all cases an increase in mixing ratios is found, sometimes even a decrease is found in aviation $NO_y$ and $O_3$. In Section 8.2 the general relationship of aviation $NO_y$ and $O_3$ was analysed with respect to potential vorticity, dry air temperature and relative humidity. From this analysis it resulted that the aviation $NO_y$ and $O_3$ values accumulate around one or two peaks for specific regimes of these weather factors, suggesting a relationship between the two. To further investigate this behaviour, the behaviour of these species with respect to weather factors is analysed.

## 9.4. Influence of weather variables on $NO_y$ and $O_3$ in weather patterns

In Section 8.2 it was concluded that there is a relationship between aviation $NO_y$ and $O_3$ behaviour and dry air temperature, relative humidity and potential vorticity. These relationships are now tested in specific weather patterns. To assess whether specific weather factors influence the behaviour of $NO_y$ and $O_3$, these factors are plotted against the $NO_y$ and $O_3$ mixing ratios found in the weather patterns. For this analysis the weather patterns have been split up in category 1, 2 and 3, for short (T2-T4), average (T5-T7) and long (T8-T9) lifetimes, respectively. Since there are less patterns found for the longer lifeetimes patterns, less data points are found for these plots. Furthermore, the results for Region 2 and 3 are similar, so for practical matters only the results for Region 3 are shown here as the previous analysis focused on the results for this Region as well. In Appendix D all the graphs for Region 1, 2 and 3 are given.

### 9.4.1. Relative Humidity

In this Subsection the relationship within weather patterns between relative humidity and aviation $NO_y$ and $O_3$ is assessed. Firstly the relationship with respect to aviation $NO_y$ is discussed, after which the relationship with respect to aviation $O_3$ follows. From the previous analysis it resulted that varying behaviour is found for short, average and long lifetimes. Therefore, the current analysis is also divided into these categories. Note however, that less weather patterns have been found for long lifetime patterns, therefore less data points are included in the scatter plots for the long lifetime patterns. In the following text all weather pattern variables are analysed belonging to Region 3. The results of Region 1 and 2 are similar but are not included in the discussion to omit repetition.

#### Relative Humidity versus $NO_{y_{air}}$

In Figure 9.12 the normalized relative humidity values found for each weather pattern are plotted against the normalized $NO_{y_{air}}$ values of each weather pattern, grouped together for short, medium and long lifetimes. From these scatter plots no clear pattern can be distinguished at first sight. However, the data points at level 69 seem clustered close to low $NO_{y_{air}}$ and low relative humidity values, whereas the data points at level 72 are more coarsely distributed. The data points for level 75 seem to be concentrated at lower $NO_{y_{air}}$ values, but over a larger RH range. These patterns are identified for all three weather pattern categories, albeit for the third categorie the pattern is weak due to a reduced number of data points.

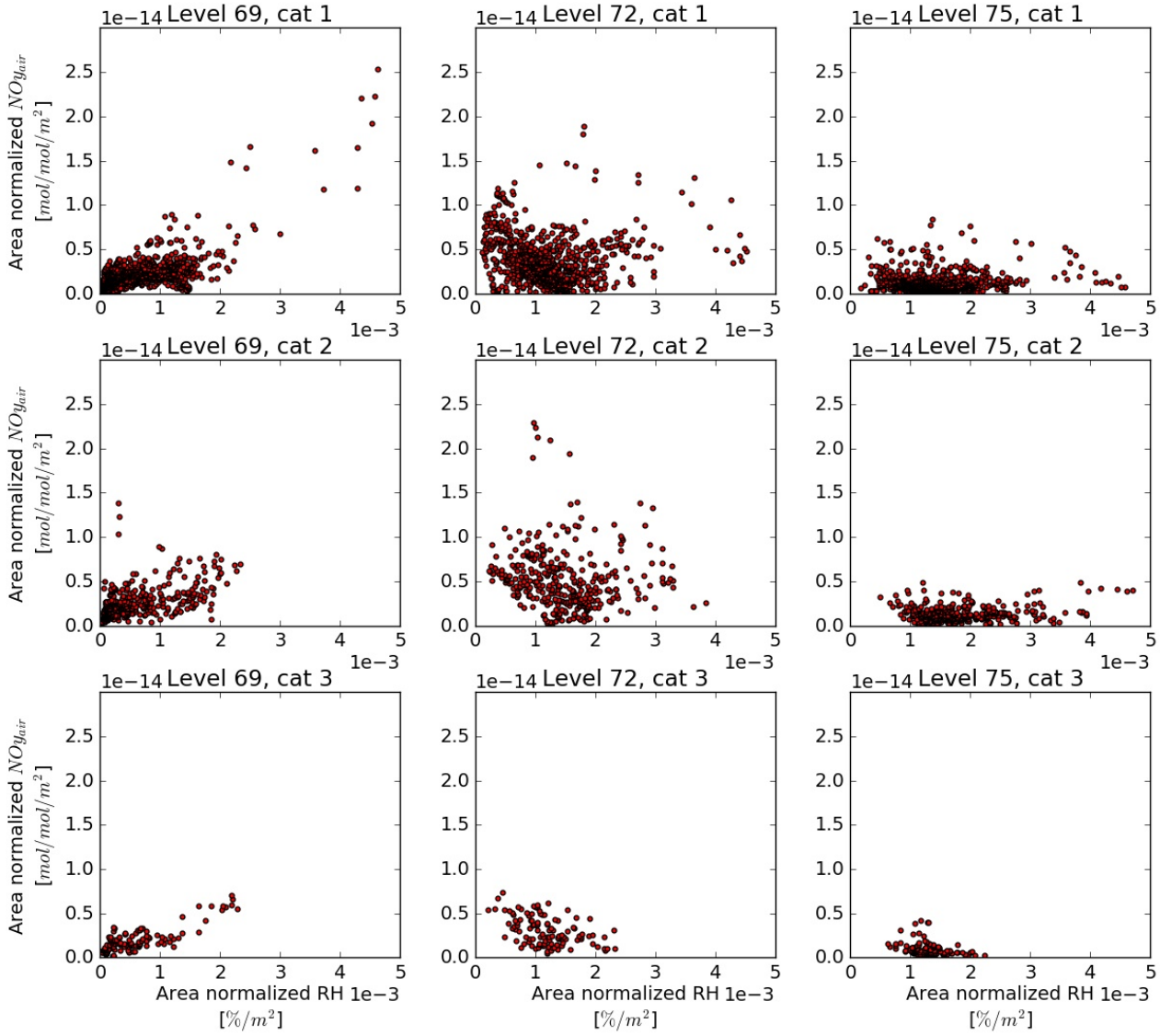


Figure 9.12: Normalized relative humidity versus normalized $NO_y$ from aviation for Region 3, category 1 (top line), category 2 (middle line), and category 3 (bottom line).

To investigate this closer the normalized relative humidity and normalized $NO_{y_{air}}$ have been plotted for eacht weather pattern separately. Subsequently, polynomial linear regression has been applied for each individual weather pattern to identify whether a correlation is present between RH and $NO_{y_{air}}$. This is depicted in Figure 9.13, where all the weather patterns found with lifetime T3 in Region 3 are shown in the upper line, and all the weather patterns found with lifetime T7 in Region 3 are shown in the bottom line.

Figure 9.13 shows that for both T3 and T7 patterns the data points at level 69 that are clustered in the left bottom corner show an increase of $NO_{y_{air}}$ with increasing RH. At level 72 on the other hand where the data points are more coarsely distributed, the majority of the patterns show a decrease in $NO_{y_{air}}$ with increasing RH, which is identified again for level 75, where the values of $NO_{y_{air}}$ have reduced overall. This relationship is found for all weather patterns in all three regions.

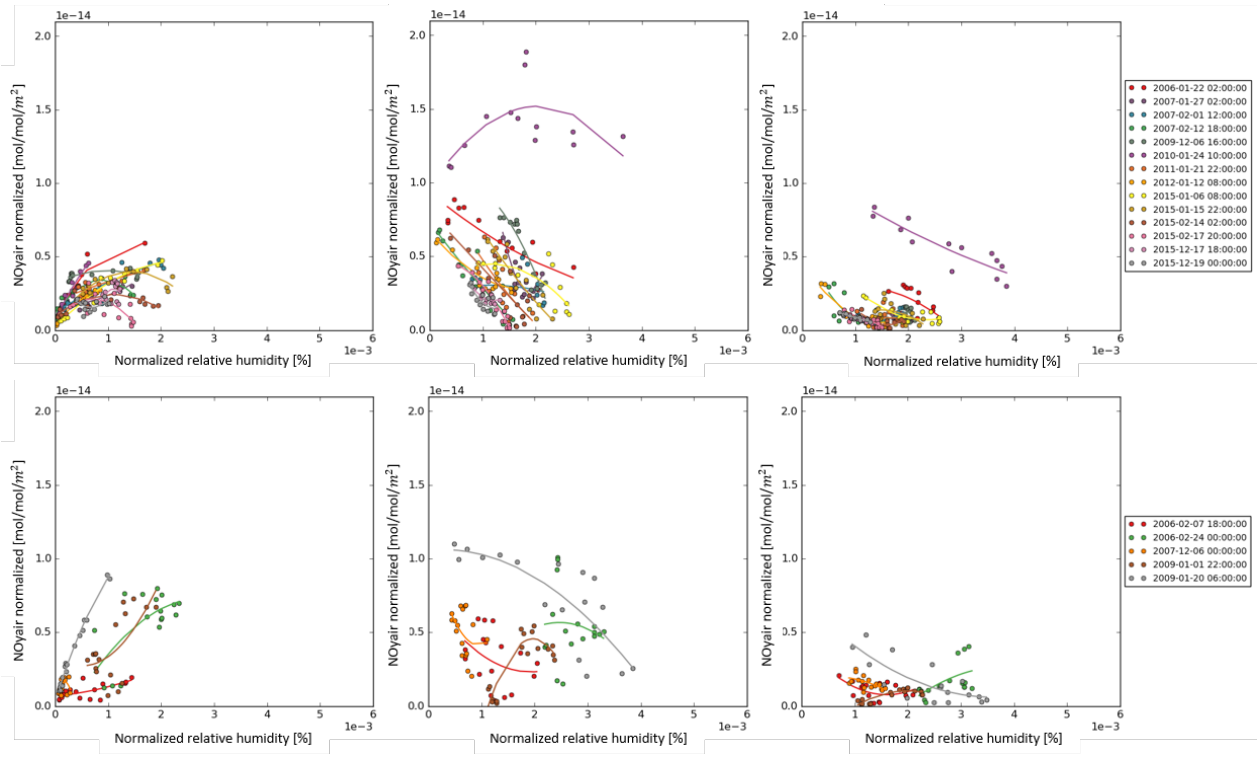


Figure 9.13: Normalized relative humidity versus normalized $NO_y$ from aviation for T3 in Region 3 (top line) and T7 for Region 3 (bottom line), for level 69 (left), 72 (middle) and 75 (right).

### Relative Humidity versus $O_{3_{air}}$

In Figure 9.14 the normalized relative humidity values found for each weather pattern are plotted against the normalized $O_{3_{air}}$ values of all the weather patterns in Region 3, grouped together for short, medium and long lifetimes. Analogously to the scatter plots depicting normalized RH against normalized $NO_{y_{air}}$, the data points at level 72 show a coarser distribution opposed to the data points of level 69 and 75. As was seen in Section 3.2, the aviation $O_{3_{air}}$ remains at stable levels at level 75 compared to level 72 and does not decrease like $NO_{y_{air}}$ does at these levels.

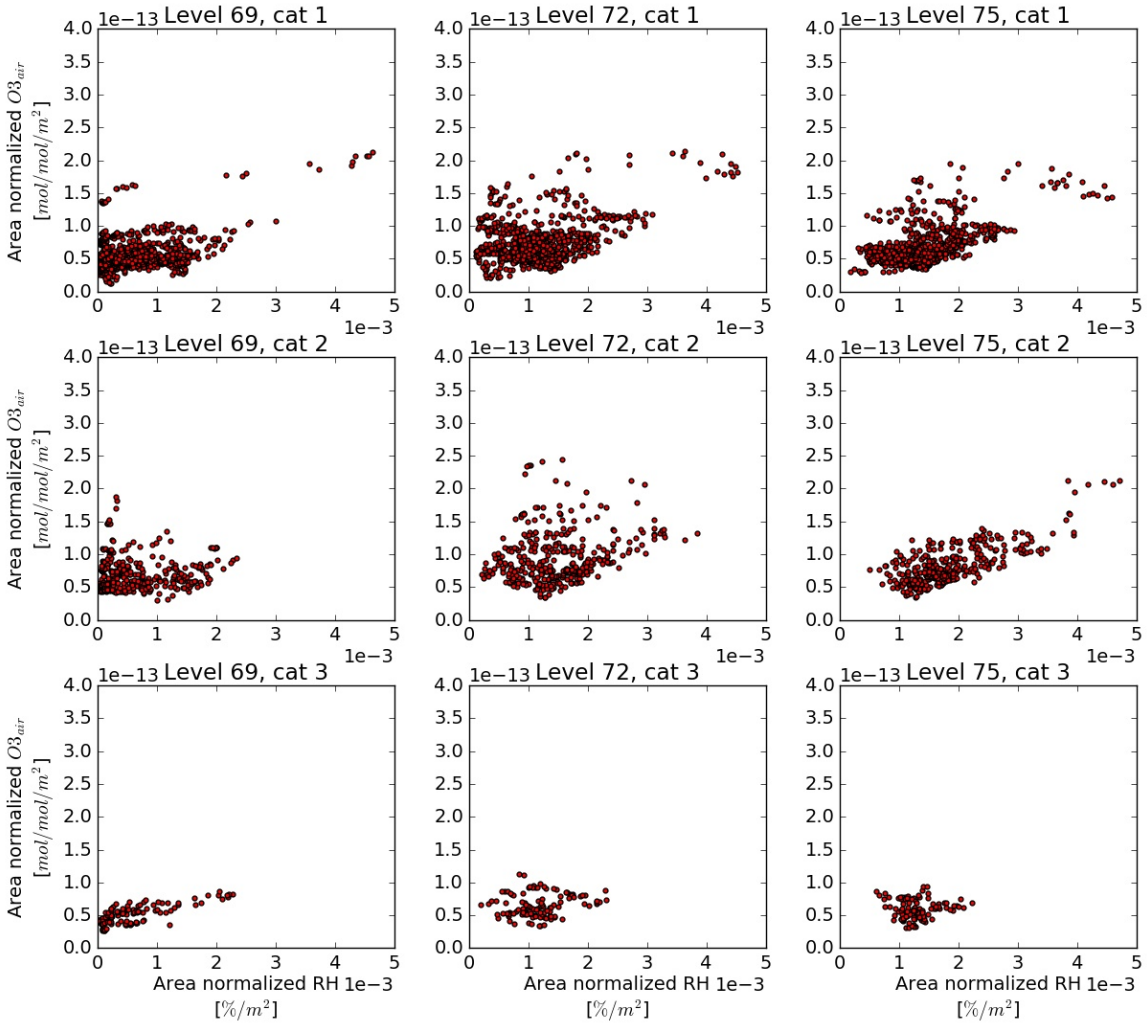


Figure 9.14: Normalized relative humidity versus normalized $O_3$ from aviation for Region 3, category 1 (top line), category 2 (middle line), and category 3 (bottom line).

After analysing these patterns closely and performing polynomial linear regression for each individual weather pattern, no relationship was found between RH and aviation $O_{3_{air}}$. Therefore, the detailed polynomial linear regression plots are not shown for this analysis. However, when examining the scatter plot of $NO_{y_{air}}$ versus $O_{3_{air}}$ with respect to RH, an interesting pattern is observed. This can be seen in Figure 9.15 for all weather patterns found in Region 3 at level 72.

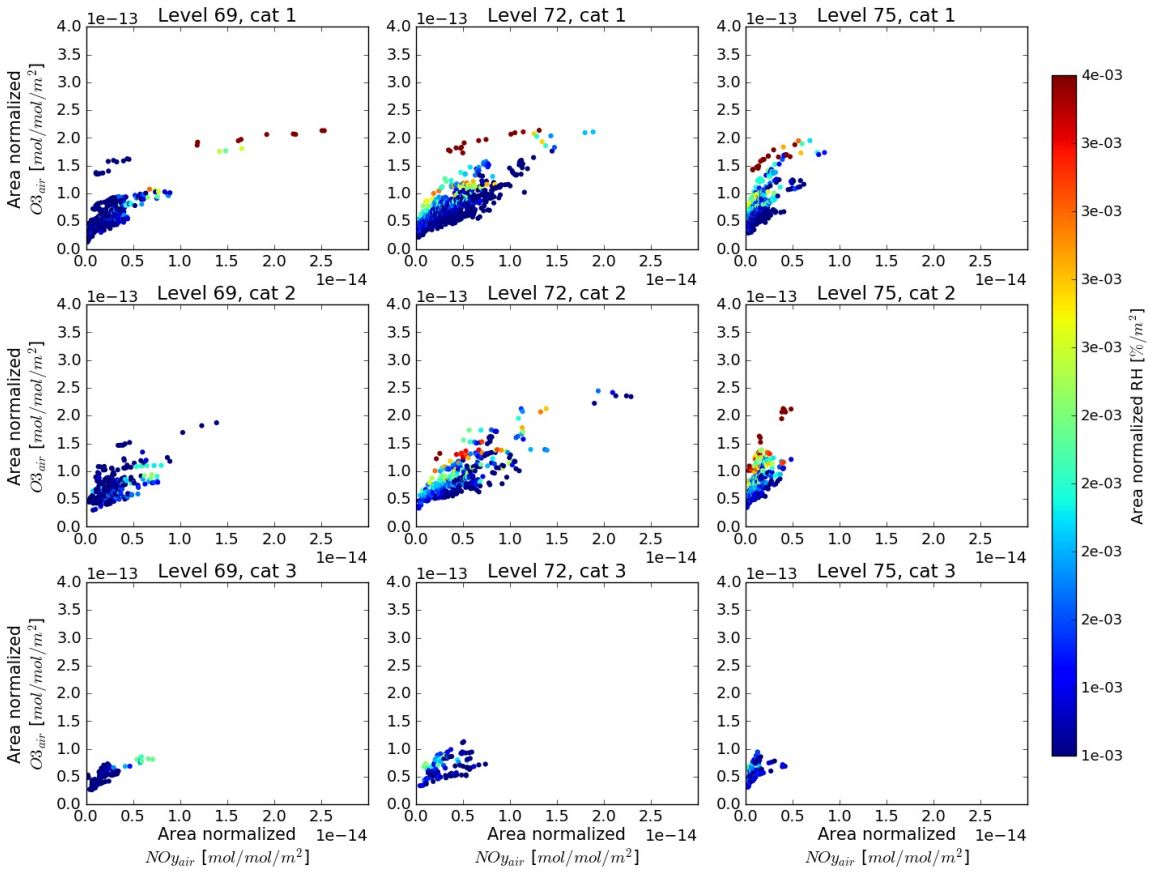


Figure 9.15: Normalized $NO_{y_{air}}$ in $[mol/mol/m^2]$ versus normalized $O_{3_{air}}$ in $[mol/mol/m^2]$ with respect to relative humidity in [%] for category 1 (left), 2 (middle) and 3 (right). All figures depict values taken at level 72.

For each category and level, it can be seen that the lower part of the distribution is attributed to low relative humidity values, whereas the data points at the top of the scatter plots belong to high relative humidity values. This implies that for higher relative humidity values, higher ozone mixing ratios are found in the weather patterns. The same trend is found for Region 2 and 3.

For all weather patterns found, the aviation $NO_{y_{air}}$ increases with relative humidity at higher cruise levels, whereas it decreases with relative humidity at average flight level as well as at low flight levels. Between aviation $O_{3_{air}}$ and relative humidity no conclusive relationship was found through the scatter plots of $O_{3_{air}}$ versus RH and through polynomial linear regression within the weather patterns. However, when plotting $NO_{y_{air}}$ versus $O_{3_{air}}$ with respect to RH, higher aviation $O_3$ have been found for higher RH values compared to lower aviation $O_3$ values for low RH values. This indicates that for specific $NO_{y_{air}}$ values the production efficiency of $O_{3_{air}}$ is potentially higher for higher RH values.

### 9.4.2. Dry air temperature

In this Subsection the relationship within weather patterns between dry air temperature and aviation $NO_y$ and $O_3$ is assessed. Firstly the relationship with respect to aviation $NO_y$ is discussed, after which the relationship with respect to aviation $O_3$ follows.

#### Dry air temperature versus $NO_{y_{air}}$

In Figure 9.16 the normalized dry air temperature values found for each weather pattern are plotted against the normalized $NO_{y_{air}}$ values of each weather pattern, categorized according to lifetime (short, medium and long). These scatter plots show a clustering for all levels and all categories except of category 3, which is attributed to the reduced dataset. No clear pattern is distinguished in these scatter plots, and after polynomial linear regression it resulted that the $T_{dry}$ values were constant for each weather pattern, with variable $NO_{y_{air}}$ values. This leads to the conclusion that the dry air temperature does not influence the concentration distribution of $NO_{y_{air}}$ in a weather pattern as the dry air temperature is rather constant in each weather pattern.

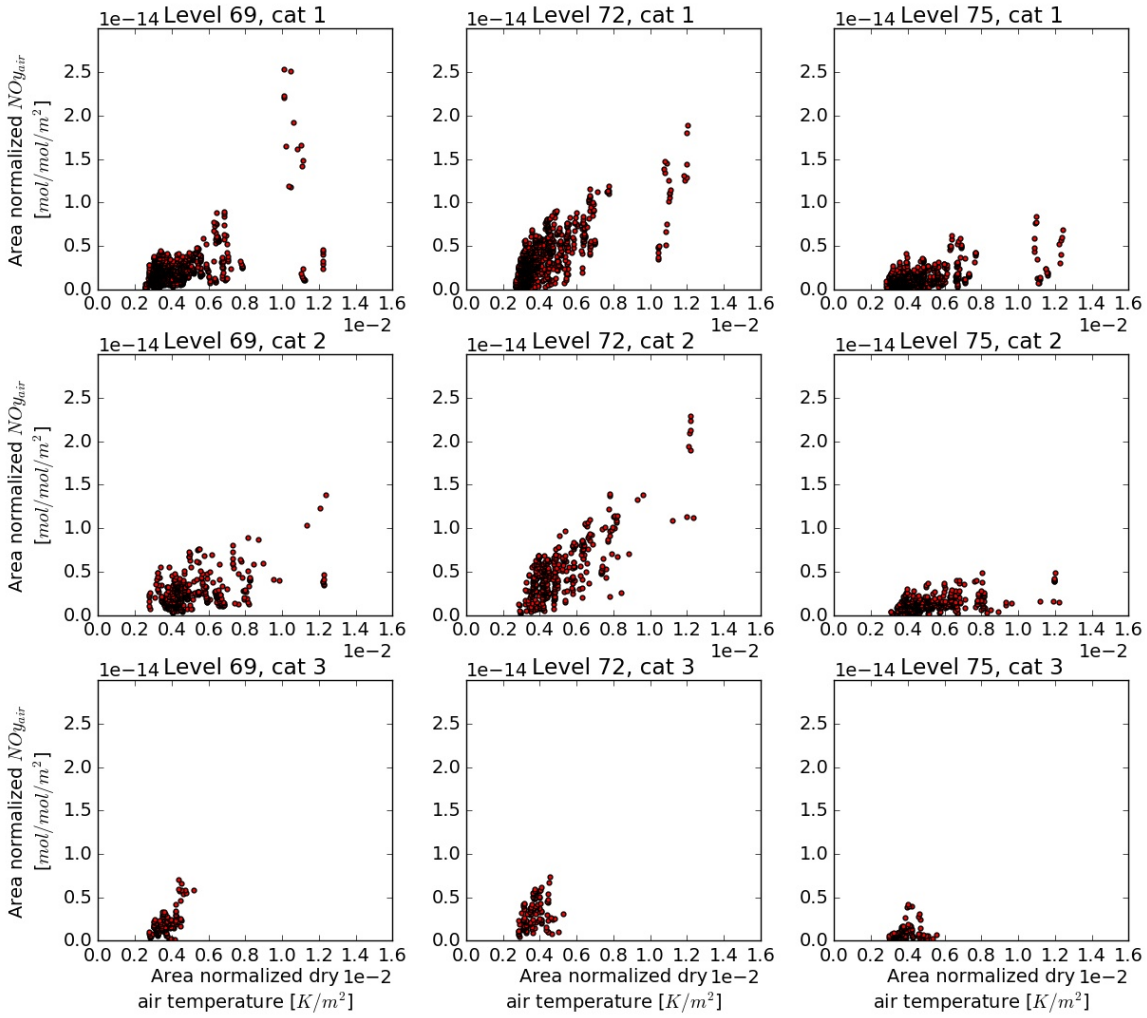


Figure 9.16: Area normalized dry air temperature versus normalized $NO_y$ from aviation for Region 3, all categories

### Dry air temperature versus $O_{3_{air}}$

In Figure 9.17 the normalized aviation $O_3$ values are plotted as a function of normalized dry air temperature for all weather patterns in Region 3, divided into the three analysis levels and lifetime subgroups. In contrast to the scatter plots with respect to $NO_{y_{air}}$, dry air temperature exhibits a strong linear correlation with aviation $O_3$. For each level and category the aviation $O_{3_{air}}$ increases with $T_{dry}$, and this relationship was also found for Region 2 and 3.

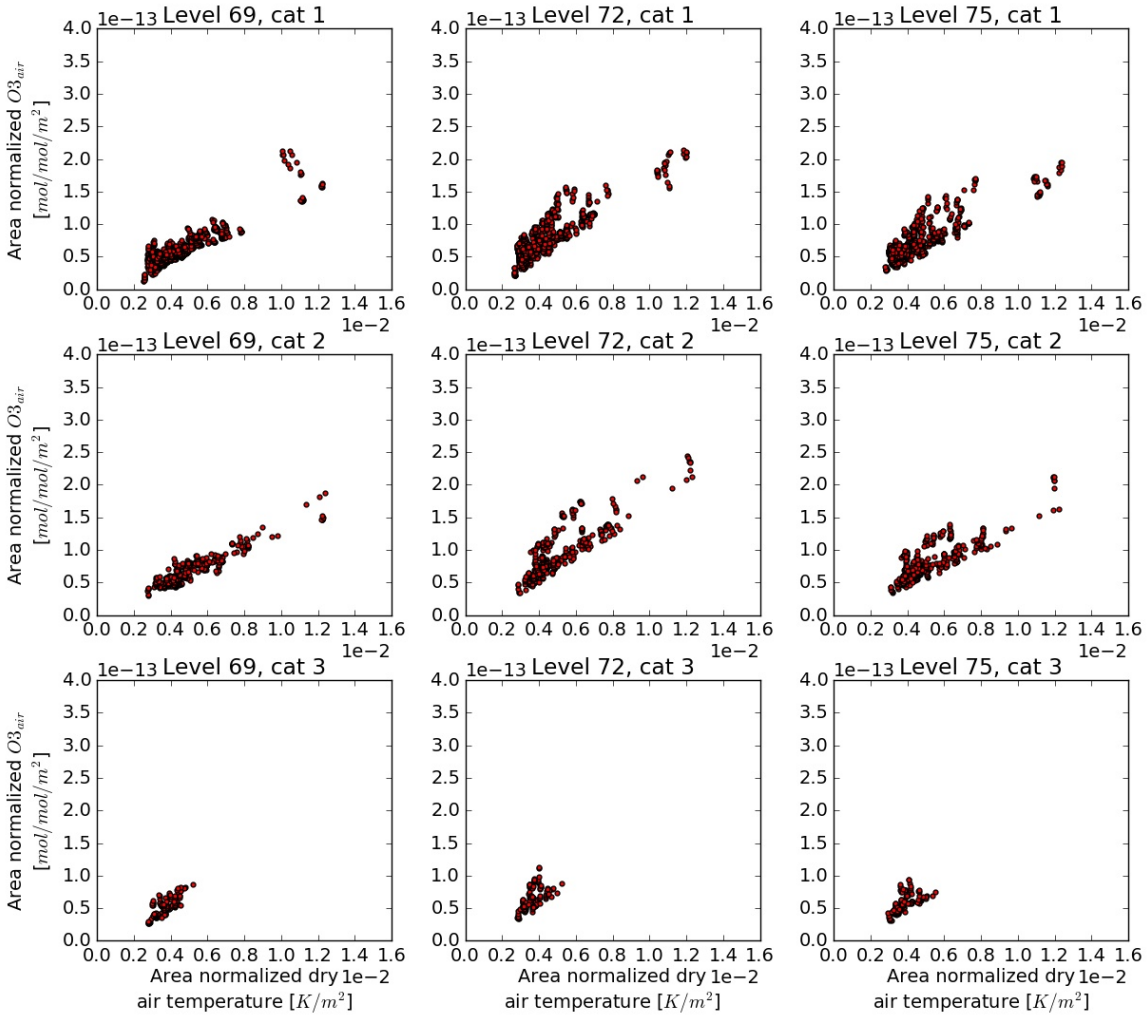


Figure 9.17: Normalized dry air temperature versus normalized $O_3$ from aviation for Region 3, all categories.

Polynomial linear regression was performed on the $O_{3_{air}}$ and $T_{dry}$ values of each weather pattern found to confirm this linear correlation. In Figure 9.18 this is plotted for weather patterns with lifetime T3 in Region 3, and in Figure 9.19 the same is plotted for weather patterns of the same region with lifetime T7. These figures confirm the linear relationship in more detail. Interesting to note is that for longer lifetimes the linear relationship is even notable within the weather pattern data points.

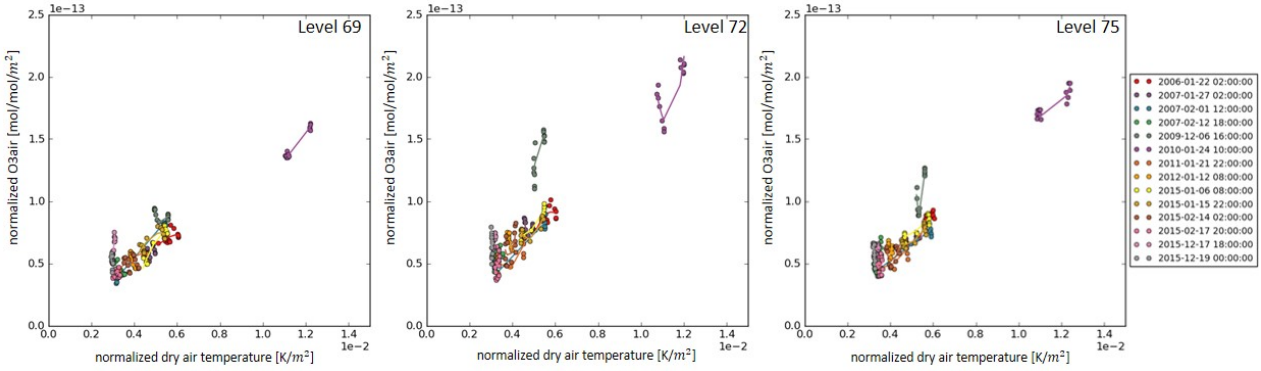


Figure 9.18: Polynomial linear regression lines plotted through the normalized dry air temperature versus normalized $O_3$ from aviation scatter points. The weather patterns considered in this plot are weather patterns with lifetime T3 in Region 3

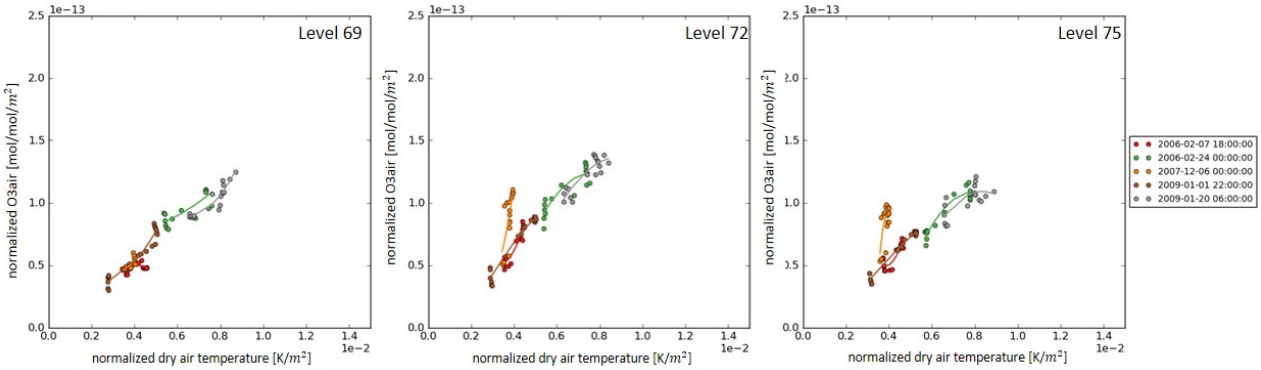


Figure 9.19: Polynomial linear regression lines plotted through the normalized dry air temperature versus normalized $O_3$ from aviation scatter points. The weather patterns considered in this plot are weather patterns with lifetime T7 in Region 3.

### 9.4.3. Potential Vorticity

In this Subsection the relationship within weather patterns between potential vorticity and aviation $NO_y$ and $O_3$ is assessed. Firstly the relationship with respect to aviation $NO_y$ is discussed, after which the relationship with respect to aviation $O_3$ follows.

#### Potential vorticity versus $NO_{y_{air}}$

In Section 8.2 it became evident that a strong correlation exists between potential vorticity and aviation $NO_y$. This relationship is further investigated in this subsection for each weather pattern. In Figure 9.20 the normalized potential vorticity values found for each weather pattern are plotted against the normalized $NO_{y_{air}}$ values of each weather pattern, grouped together for short, medium and long lifetimes. In this figure the linear correlation is identified for average cruise level and a weaker but present linear correlation is also found at lower cruise level. At higher cruise level the data shows a random distribution where for category the data seems clustered at low $NO_{y_{air}}$ values and low PV values, whereas the values for category 2 and 3 are more distributed over a larger PV range.

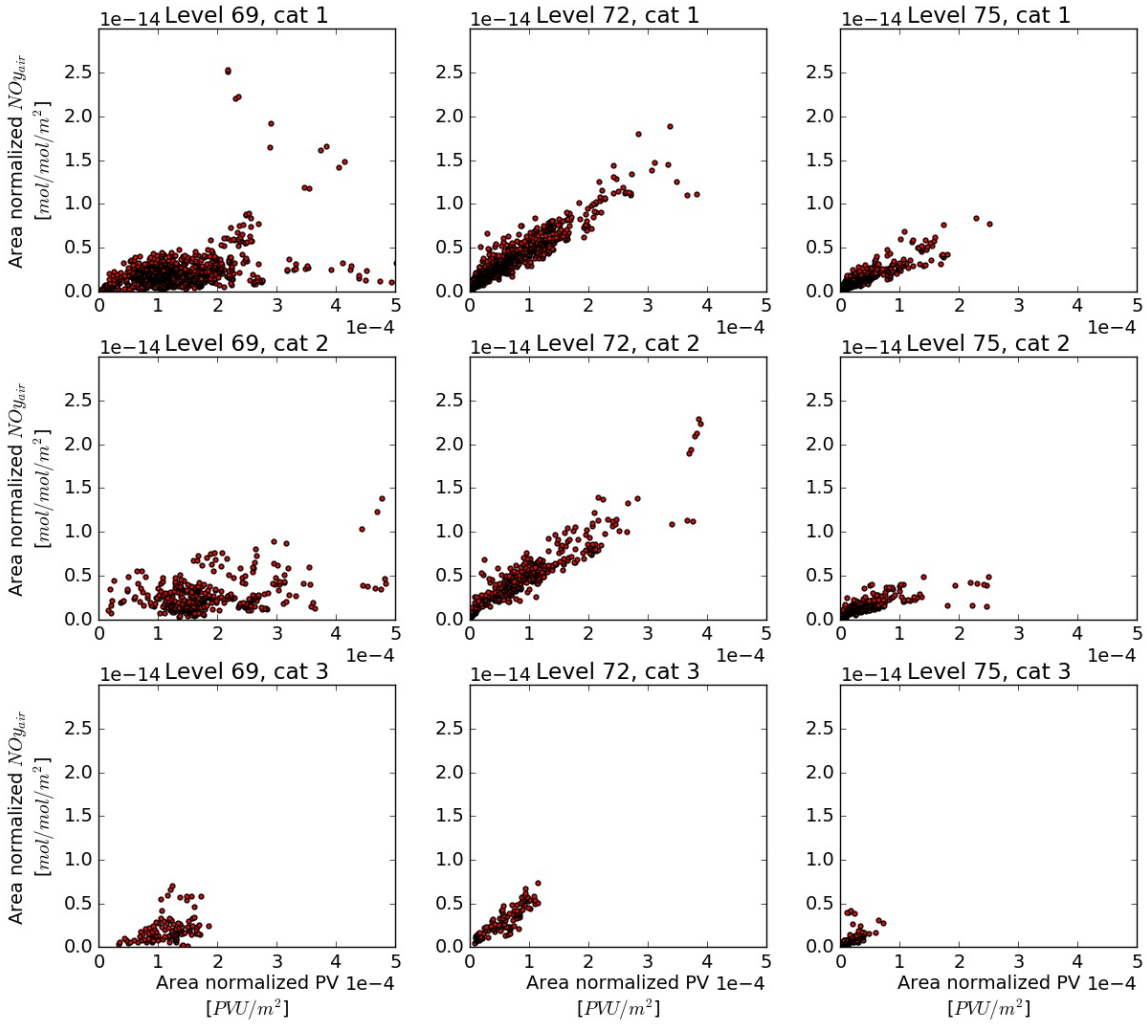


Figure 9.20: Normalized potential voriticity versus normalized $NO_y$ from aviation for Region 3. With the categories and levels as indicated in the subfigures.

The linear correlation that is prominent at average cruise level implies that $NO_{y_{air}}$ increases with PV. To test this, for each individual weather pattern the PV values and $NO_{y_{air}}$ values have been plotted for each gridpoint. From this it resulted indeed that in a weatherpattern with varying PV values the gridpoints with high PV value relate to a high $NO_{y_{air}}$ value. This is depicted in Figure 9.21. In this figure the $NO_{y_{air}}$ and PV for all gridpoints in a specific weather pattern have been plotted. The gripoints are arranged over the x-axis as they are numbered in the dataframe. This graph illustrates that gridpoints with high PV contain elevated $NO_{y_{air}}$ levels compared to low PV values, as was expected.

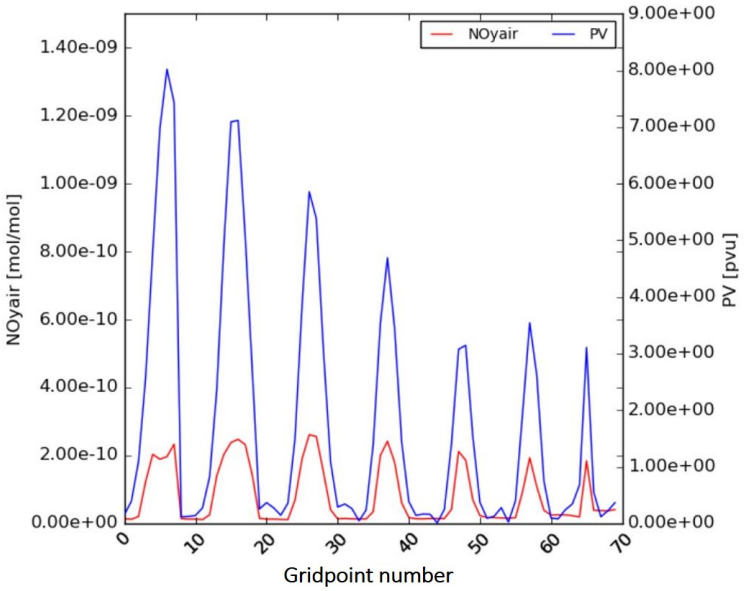


Figure 9.21: $NO_{y_{air}}$ and PV for all gridpoints (over the x-axis) for a specific weather pattern at one timestep.

High-pressure systems are characterized by a low PV that originate from the tropics. When transport from higher altitudes takes place in the high-pressure systems the PV increases. This explains the variable peaks found for average and long weather patterns discussed in Subsection 9.3.2 and 9.3.3. Here it was established that for the majority of the weather patterns an increase in $NO_{y_{air}}$ was found during the presence of a high-pressure weather pattern, while for some patterns no increase or even a decrease was found. After assessing the potential vorticity values for each specific weather pattern, it resulted that the increase in aviation $NO_y$ only takes place when the PV increases. This PV increase is also related to an increase in stratospheric ozone, indicating downward transport from higher altitudes. This relationship was also found for weather patterns in Region 1 and 2.

### Potential vorticity versus $O_{3_{air}}$

The normalized aviation $O_3$ and potential vorticity are plotted in Figure 9.22 for all weather patterns in Region 3, for each analysis level and lifetime category. At first glance, aviation $O_3$ exhibits a subtle linear correlation with respect to PV at all three analysis levels. However, this correlation is not as strong as the correlation between $NO_{y_{air}}$ with PV at high cruise levels. This means that aviation $O_3$ increases with PV, abeit not linearly.

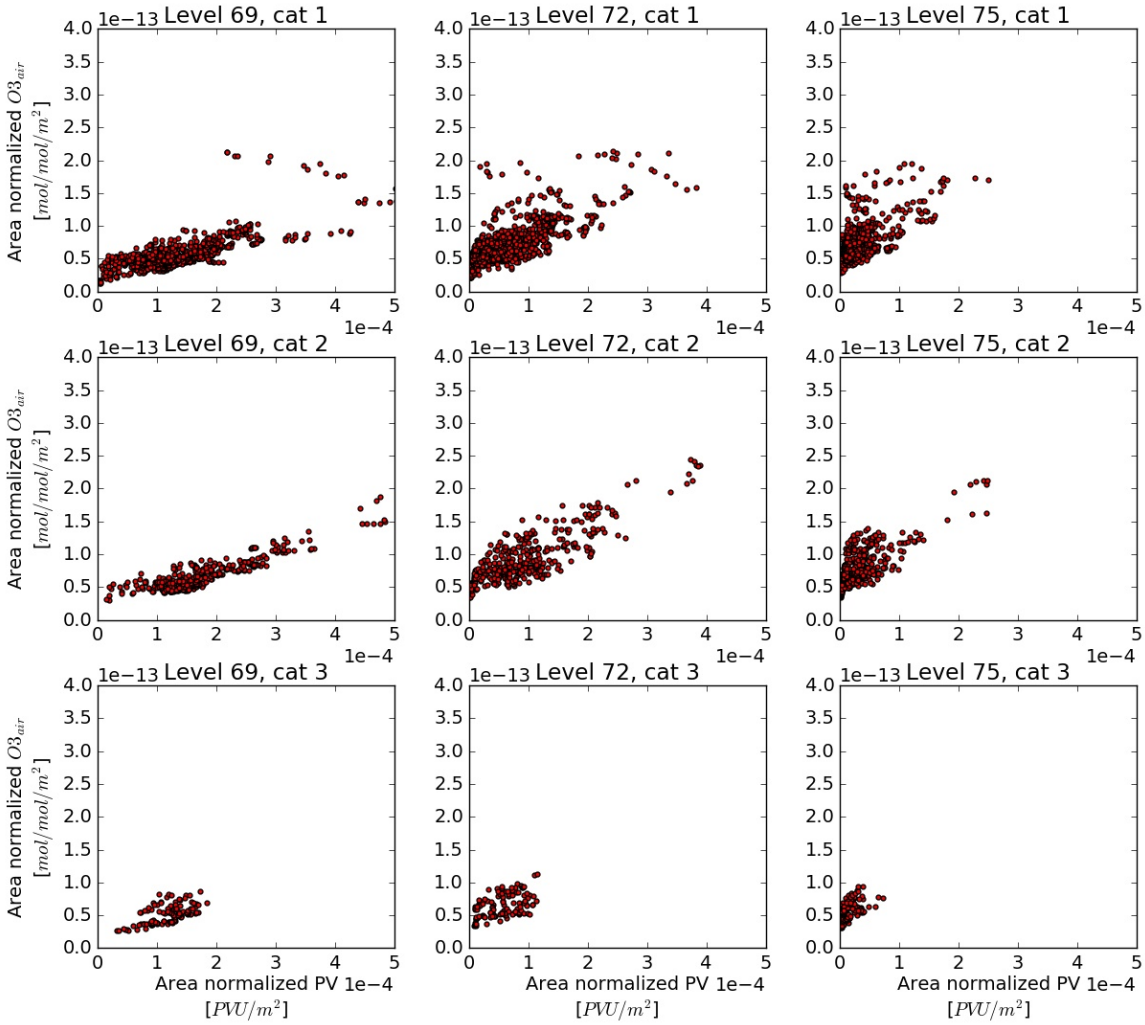


Figure 9.22: Normalized potential voriticity versus normalized $O_{3_{air}}$ from aviation for Region 3, with the categories and levels as indicated in the subfigures.

### 9.4.4. Summarizing weather factor correlations with Spearman's rank coefficient

The relationships found in the previous section are confirmed by analysing the Spearman's rank coefficient for each variable pair, at each level and for each category, for each Region seperately. This correlation coefficient indicates whether a monotonic relationship exists between two variables analysed, and its value lies between -1 and +1. A correlation coefficient of -1 indicates a negative monotonic relationship, meaning that the dependent variable always decreases while the independent variable increases. A correlation coefficient of 0 indicates that no monotonic relationship is present, and a correlation coefficient of +1 indicates a positive monotonic relationship, meaning that the dependent variable always increases when the independent variable increases. Therefore, a Spearman's rank coefficient close to either -1 or +1 indicates a strong correlation. The Spearman rank coefficients that have been calculated for Region 3 are depicted in Figure 9.23

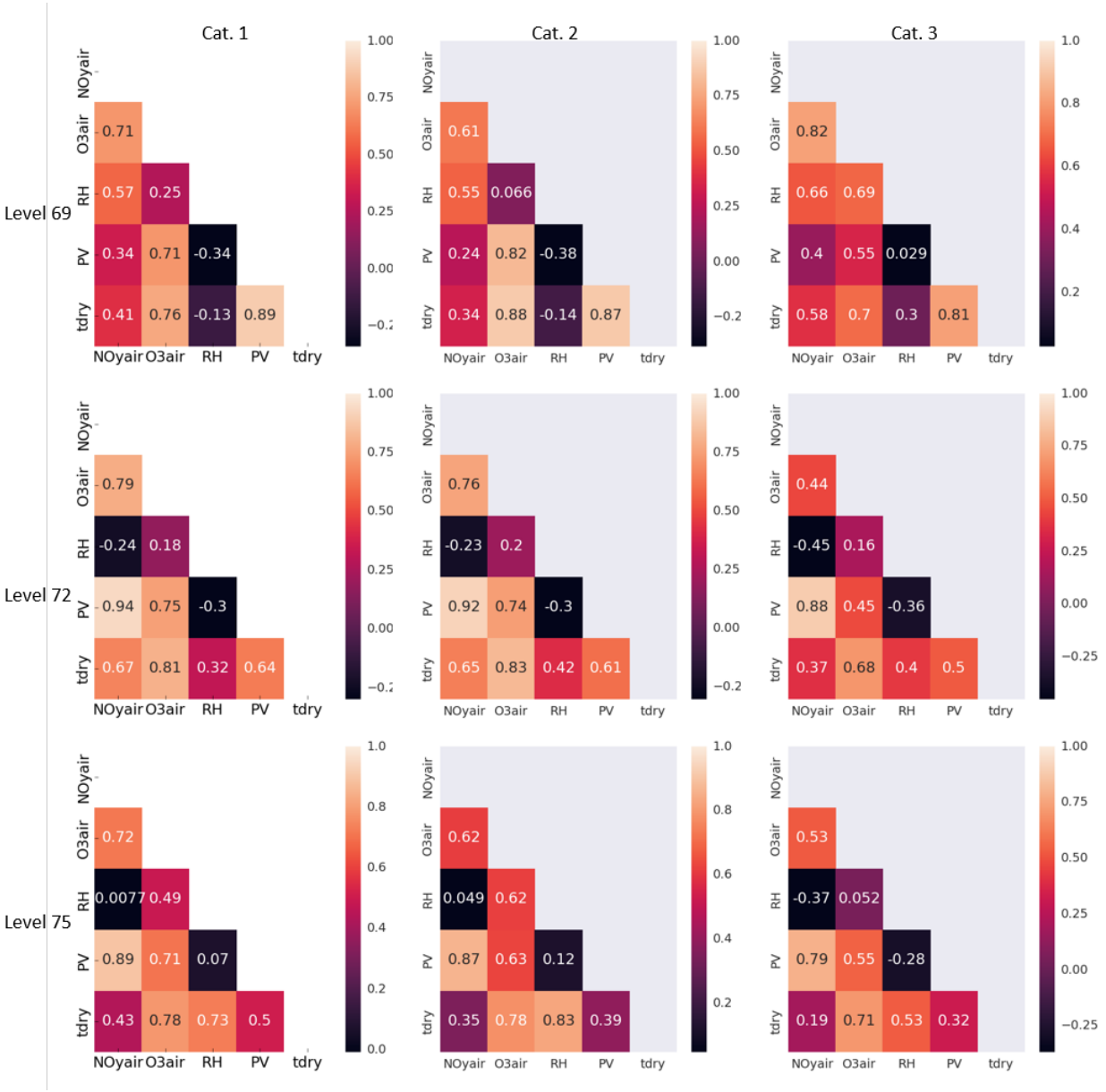


Figure 9.23: Spearman's rank coefficients for the correlations between the variables as indicated in the matrics. Weather patterns in Region 3 are included in this matrix.

In these matrices the correlation between $NO_{y_{air}}$ and $O_{3_{air}}$ is confirmed, as the Spearman's rank coefficient is rather high in all matrices (average of + 0.67). Also the strong correlation between $NO_{y_{air}}$ and PV at level 72 and 75 is confirmed by the Spearman's rank coefficients with an average value of + 0.88 and the moderate correlation between $O_{3_{air}}$ and PV over all levels is reflected by an average coefficient of +0.64. Furthermore, the correlation between $T_{dry}$ and $O_{3_{air}}$ over all levels and categories is confirmed by an average coefficient of +0.7.

The Spearman's rank correlations coefficients of the other variable pairs are either too variable between each set or too low to indicate a significant relationship. It was expected that some relationship exists between aviation $O_{3_{air}}$ and RH, as higher RH values yield higher $O_{3_{air}}$ for specific $NO_{y_{air}}$ values, but was not found using this method.

## 9.5. Discussion and summary of correlations

In the previous sections and in Chapter 8 various relationships have been found that help to better understand how aviation $NO_y$ and $O_3$ develop in specific weather patterns. Two scenarios resulted with respect to the temporal development of aviation $NO_y$ and $O_3$ in specific weather patterns, which are depicted in Figure 9.24.

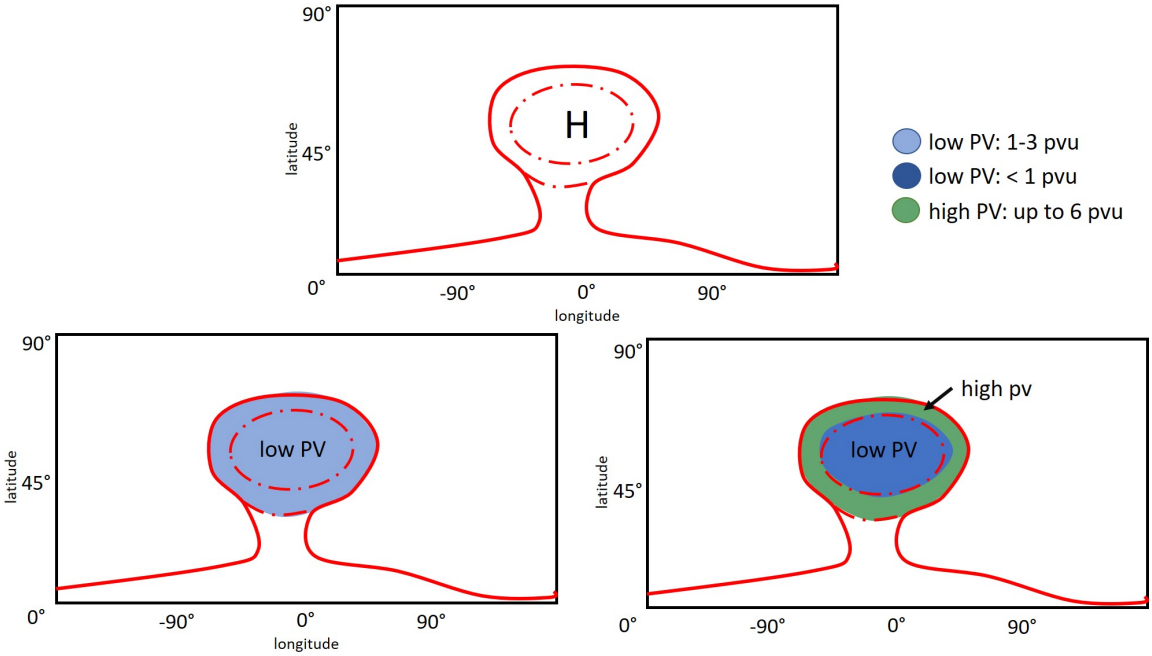


Figure 9.24: Illustration of the two scenarios established within a high-pressure system with respect to potential vorticity. The top picture depicts a high pressure system around Europe at mid-latitudes. The left bottom figure illustrates a high-pressure system with low (close to zero) PV values, the right bottom figure illustrats a high-pressure system with low and high PV values.

A very abstract description of the dynamics in a high-pressure system is that air flows from the core down and then out to low-pressure system. A high-pressure system contains generally low PV values that originate from the tropics, which is the scenario that is depicted on the left side of the figure. In other cases, the PV values can increase due to transport from either higher latitudes or from higher altitudes, which is the scenario depicted on the right.

If a high-pressure system contains solely moderately low (1 - 2 pvu) PV values, no increase in aviation $NO_y$ and aviation $O_3$ was found (see the end of Section 9.3.3). In this case the air inside the high-pressure system is rather stable, but does not constitute a closed system. This results to the fact that aviation $NO_y$ concentrations do not accumulate inside such a system if an aircraft flies over the high-pressure system and emits into the system. This scenario is illustrated in Figure 9.25.

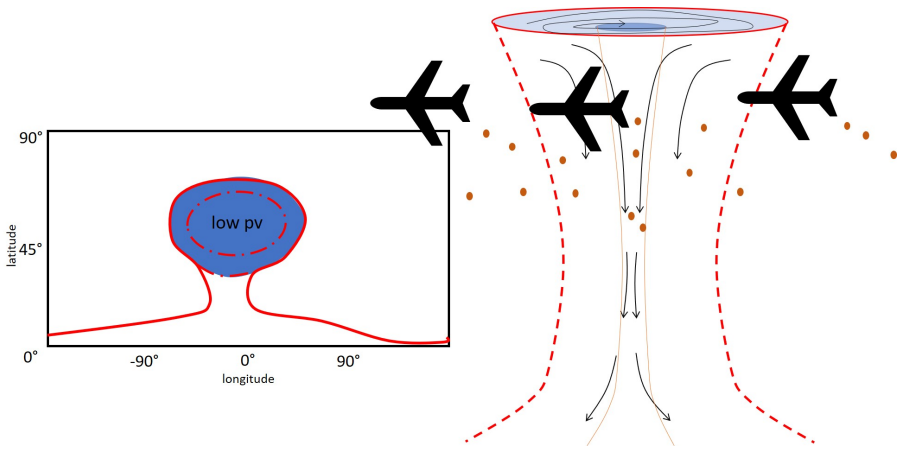


Figure 9.25: The low potential vorticitiy scenario is illustrated on the left and on the right a cross section of this pressure pattern is drawn.

If very low (close to zero) PV values are found at the establishment of the high-pressure system, the system constitutes a closed system. This provides an environment where emitted $NO_y$ from aviation could accumulate inside the high-pressure system. If during the lifetime of this system high PV values arise due to vertical transport from higher altitudes, the air in the high-pressure system is more dynamic. This is illustrated in Figure 9.26. The high PV values in these weather patterns are accompanied by increased stratospheric ozone concentrations, which indicate vertical transport into the high-pressure systems. The system is still a closed high-pressure system, but with increased transport from higher altitudes. In these cases the $NO_y$ emitted by aviation increases in the weather systems and lead to

increased $O_{3_{air}}$ in the system.

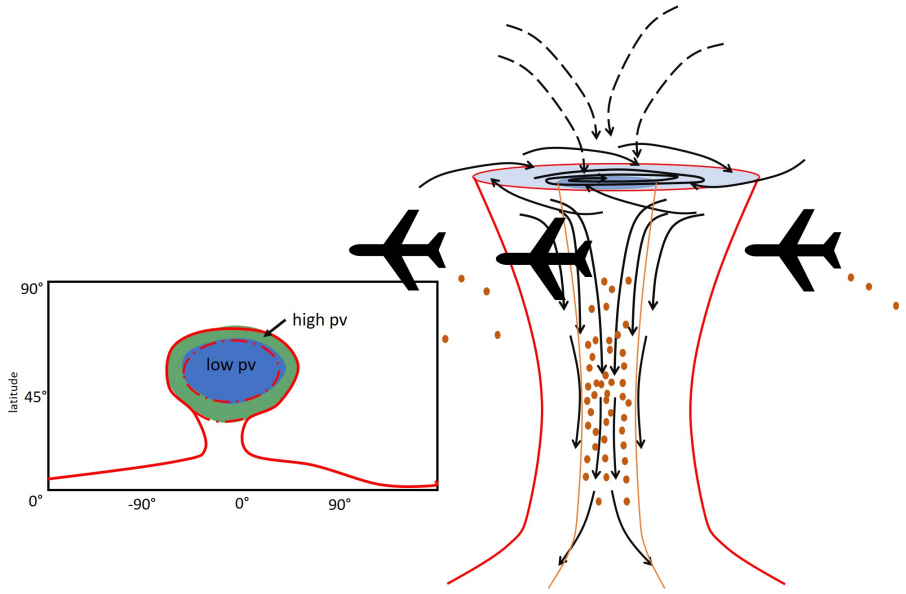


Figure 9.26: Illustration of the two scenarios established within a high-pressure system with respect to potential vorticity.

The mechanism of accumulation of $NO_{y_{air}}$ in the weather patterns and conversion to $O_{3_{air}}$ is influenced by the dry air temperature and relative humidity as well. The dry air temperature influences this process positively. For higher $T_{dry}$ values, elevated $O_{3_{air}}$ mixing ratios have been established. Thus, in weather patterns with higher dry air temperatures, the conversion of aviation $NO_y$ to ozone will be more efficient.

As was discussed in subsection 9.4.4 the relationship between RH and aviation $O_3$ is not yet properly understood. However, it was established that for higher RH, higher aviation ozone concentrations have been found for specific $NO_{y_{air}}$ concentrations compared to similar aviation $NO_y$ concentrations with lower RH. Therefore, in weather patterns with higher relative humidity values, the conversion of aviation $NO_y$ to ozone will be more efficient, although this influence is not as strong as that of dry air temperature.

Now the question rests whether the increased aviation $O_3$ mixing ratios in weather patterns due to the potential accumulation in $NO_{y_{air}}$ would be detectable . This question will be treated in the next chapter.

# 10

# Ozone Perturbation Analysis

In order to potentially measure aviation $O_3$ in the atmosphere, it must be investigated whether the increase in aviation $O_3$ due to accumulation in high-pressure weather systems can be detected. For this it is analysed whether the increase in aviation $O_3$ results in a similar increase in total ozone, which can then be measured. All figures in the following sections show results for Region 1. Weather patterns analysed for region 2 and Region 3 show similar behaviour and are therefore not included in the current analysis to omit repetition

## 10.1. Comparing aviation ozone to stratospheric ozone and total ozone mixing ratios

At flight altitude the most prominent contributors to the total ozone are aviation and stratospheric ozone. Therefore, an increase in total ozone would be most likely due to aviation ozone or stratospheric ozone. In order to determine this, the temporal developments of these constituents are analysed for all weather patterns. For the current analysis the weather patterns of Region 1 with lifetime T5 at level 72 and level 75 are depicted in Figure 10.1 and Figure 10.2, respectively.

At level 72, the total ozone and stratospheric ozone seem to follow a similar trend. However, the increase in stratospheric ozone is not exhibited in the stratospheric ozone graphs. The aviation ozone graphs exhibit no clear similarity with either stratospheric or total ozone. Therefore it is concluded that at level 72, an increase in aviation ozone can not be detected in the total ozone. If an increase in ozone is detected at this level, it is most likely due to an increase in stratospheric ozone.

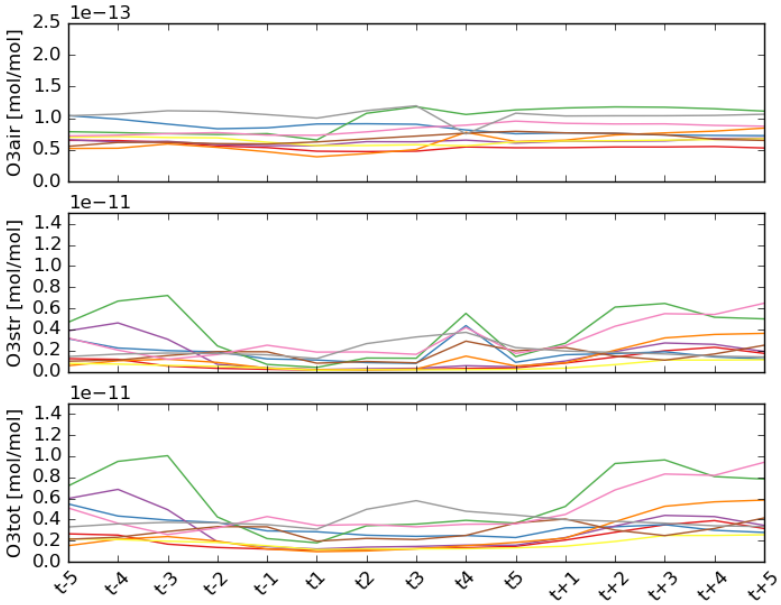


Figure 10.1: Temporal development of normalized aviation ozone (top), normalized stratospheric ozone (middle) and total ozone(bottom) at level 72 for weather patterns with lifetime T5 at Region 1.

At lower flight levels, level 75, the normalized stratospheric and total ozone concentrations have decreased to about half the concentrations at level 72. The normalized aviation ozone concentrations on the other hand have remained at a similar level as at higher flight levels. This could mean that the influence of aviation $O_3$ is larger at lower altitudes and thus a change in aviation $O_3$ could be detectable in total aviation ozone.

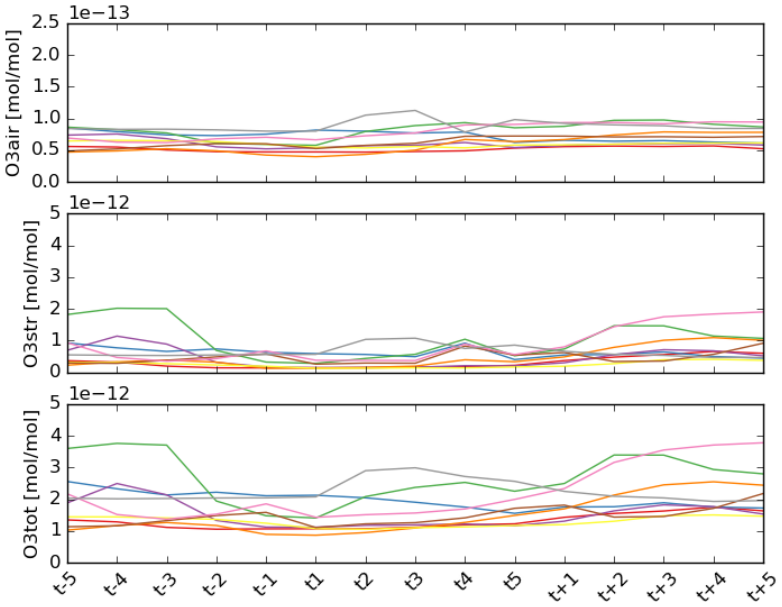


Figure 10.2: Temporal development of normalized aviation ozone (top), normalized stratospheric ozone (middle) and total ozone(bottom) at level 75 for weather patterns with lifetime T5 at Region 1.

To assess the correlation between the three ozone groups the Spearman's rank coefficients have been calculated for each of the analysis levels for all groups, and are depicted in Figure 10.3. In this Figure all weather patterns of Region 1 are included. The weather patterns of Region 2 and 3 yield similar correlation coefficients.

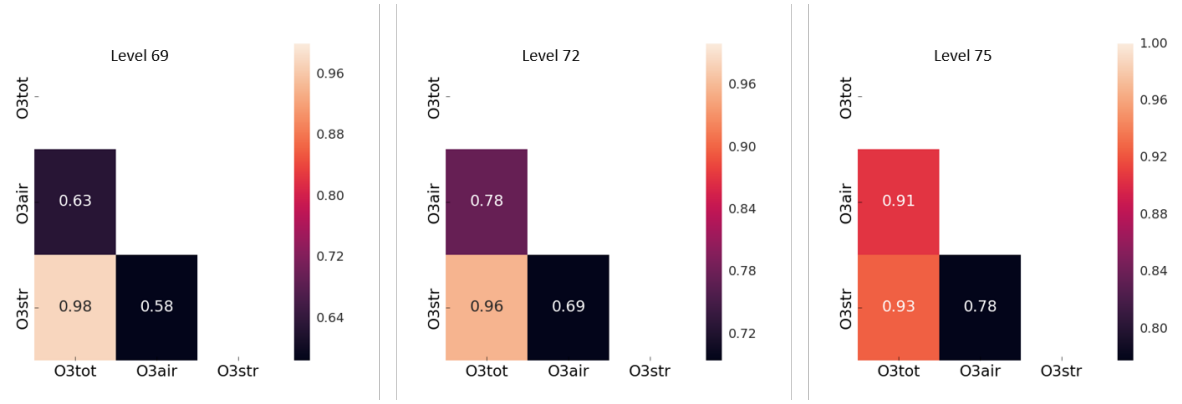


Figure 10.3: Spearman's rank coefficients indicating the correlation between the three ozone groups. All analysis levels and all weather patterns of Region 1 are included.

In this figure it is evident that at higher flight levels the stratospheric ozone has a high positive correlation with total ozone. Due to this strong correlation and their orders mixing ratios being in the same order of magnitude, it is highly likely that an increase or decrease in stratospheric ozone is detectable in the total ozone. Because the correlation between the two constituents is so strong at average and high flight levels, it is unlikely that an increase in aviation ozone can be detected in the total ozone trend at these levels. However, at lower levels the correlation coefficient between aviation ozone and total ozone increases largely, while the mixing ratios of stratospheric and total ozone decrease. Even though stratospheric ozone is at these levels still an order magnitude larger than that of the aviation constituent, the strong correlation between aviation ozone and total ozone suggest that large increases or decreases in aviation ozone could possible be detected in the total ozone mixing ratios.

To investigate these relationships further the trends of the three groups are compared to each other. This is discussed in the following section.

## 10.2. Comparing total, stratospheric and aviation ozone trends

The trends of the three groups are compared to each other to determine whether a change in the aviation ozone concentration relates to a change in the total ozone concentration. The method for comparing these trends is discussed in Chapter 7, Section 7.7. The compared trendlines for total ozone with respect to aviation ozone, total ozone with respect to stratospheric ozone, and stratospheric ozone versus aviation ozone are discussed. If a trendline remains close to zero, it can be concluded that the two groups follow similar trendlines. Following this method, the three analysis levels are discussed seperately in the following subsections. Again, in the following discussion the results for Region 1 are discussed. The comparative trendlines for Region 2 and 3 can be found in Appendix E

### 10.2.1. Ozone trend comparison at level 69

The ozone trends for level 69 that have been calculated and compared to each other are depicted in Figure 10.4 for all weather patterns with lifetime T2. In this Figure it can be clearly seen that the top and bottom graphs show large variabilities and do not depict similar trendlines. Therefore it can be concluded that at level 69 aviation ozone and total ozone do not follow similar trendlines, as well as aviation ozone and stratospheric ozone.

The graphs depicting the comparison between total ozone and stratospheric ozone also shows some variability, but a large majority of the lines remains close to zere. This confirms the strong correlation between the two groups that was identified by the Spearman's rank coefficient in the previous Section.

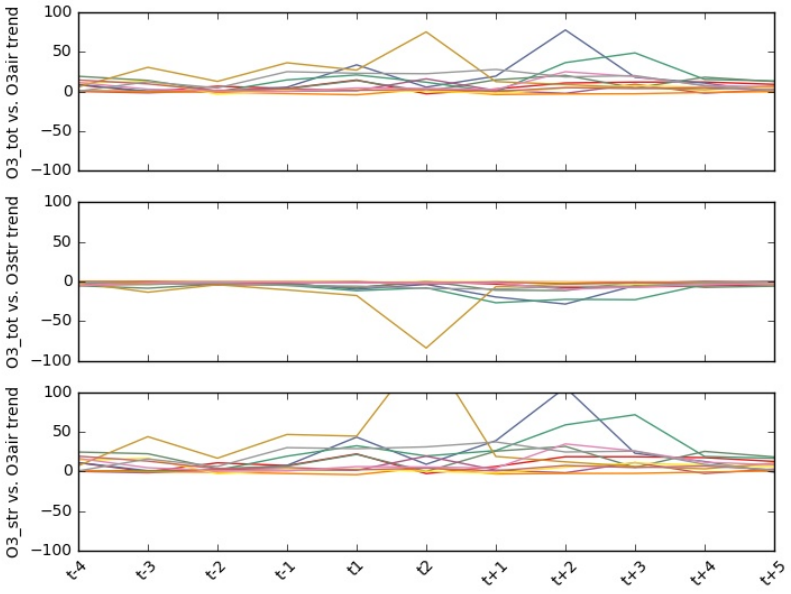


Figure 10.4: Trend comparison of aviation ozone versus total ozone (top), stratospheric ozone versus total ozone (middle) and stratospheric ozone versus aviation ozone (bottom) for T2 at level 69.

Similar results are found for weather patterns with longer lifetimes. In Figure 10.5 the results for weather patterns with lifetime T5 are given and in Figure 10.6 the results for weather patterns with lifetime T8 are given. These figures show similare results as were found for weather patterns with lifetime T2. However, the graphs for T5 do exhibit disruptions during the high-pressure system which are larger for the stratospheric versus total ozone graph than that of the aviation versus total ozone graph. The changes of stratospheric ozone are in this case larger than that of the total ozone which are the peaks in stratospheric ozone that can be seen in Figure 10.1, which are not present in the total ozone graph. The aviation ozone however is of such small magnitude that any changes in the aviation ozone are not noticeable in the total ozone concentrations, and additionally, the graphs of aviation ozone compared to total ozone do show a large variability still.

About the trendlines of T8 not much can be said as it contains only one weather pattern. However, the stratospheric ozone versus total ozone graph shows low variability, confirming the Spearman's rank coefficient.

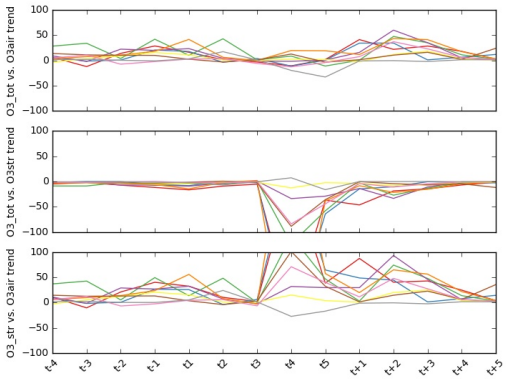


Figure 10.5: Trend comparison of aviation ozone versus total ozone (top graph), stratospheric ozone versus total ozone (middle graph) and stratospheric ozone versus aviation ozone(bottom graph) for T5 at level 69.

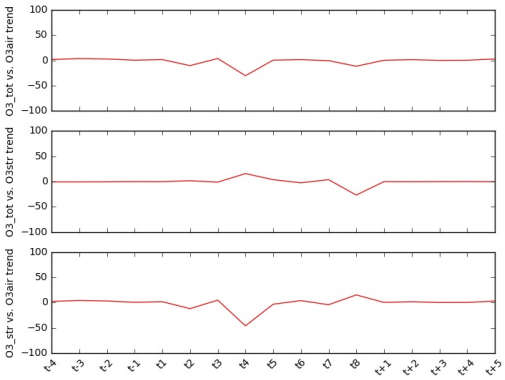


Figure 10.6: Trend comparison of aviation ozone versus total ozone (top graph), stratospheric ozone versus total ozone (middle graph) and stratospheric ozone versus aviation ozone(bottom graph) for T8 at level 69.

### 10.2.2. Ozone trend comparison at level 72

The ozone trends for level 72 that have been calculated and compared to each other are depicted in Figure 10.7 through 10.9 for all weather patterns with lifetime T2, T5 and T8, respectively. Compared to level 69, the graphs illustrating the comparison between stratospheric ozone and total ozone seems less stable. Also the graphs depicting the comparison between stratospheric ozone and aviation ozone is more unstable at level 72 compared to level 69. The graph depicting the comparison between total ozone and aviation ozone seems similar to that of level 69.

The trend in stratospheric ozone and total ozone are less similar at average flight altitudes. This attributed to the fact that the stratospheric ozone mixing ratios are decreased at these levels compared to the higher flight levels, which leads to a lesser impact on total ozone.

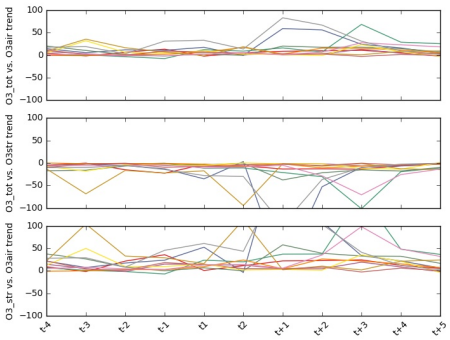


Figure 10.7: Trend comparison of aviation ozone versus total ozone (top), stratospheric ozone versus total ozone (middle) and stratospheric ozone versus aviation ozone (bottom) for T5 at level 72.

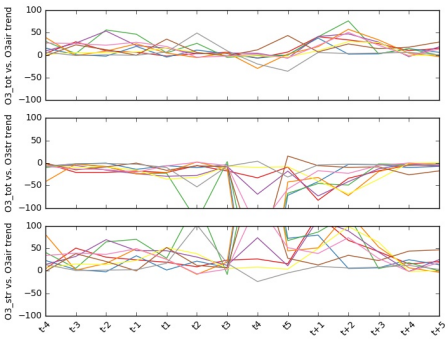


Figure 10.8: Trend comparison of aviation ozone versus total ozone (top), stratospheric ozone versus total ozone (middle) and stratospheric ozone versus aviation ozone(bottom) for T5 at level 72.

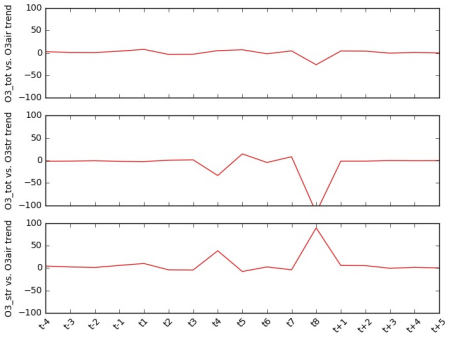


Figure 10.9: Normalized relative humidity versus normalized $O_3$ from aviation for Region 1, category 1 (top line), category 2 (middle line), and category 3 (bottom line) for T8.

### 10.2.3. Ozone trend comparison at level 75

The ozone trends for level 75 that have been calculated and compared to each other are depicted in Figure 10.10 through 10.12 for all weather patterns with lifetime T2, T5 and T8, respectively.

Compared to the previous analysed levels, the graphs illustrating the comparison between aviation ozone and total ozone exhibit a very stable pattern around zero, whereas the graphs of the other two correlations show a highly variable trend. This implies that at lower flight levels, the aviation ozone mixing ratios follow a similar trend as the total aviation ozone, more than the stratospheric ozone does. Additionally, the stratospheric ozone and total ozone mixing ratios have reduced largely, while the aviation ozone mixing ratios have remained around stable levels equal to the values found at level 72. This leads to the conclusion that at lower flight levels, a change in aviation ozone due to the accumulation in $NO_{y_{air}}$ can be potentially detected in the total ozone concentration changes.

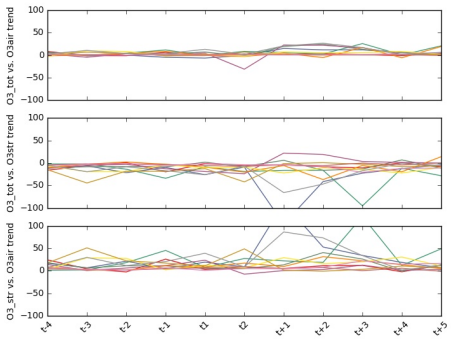


Figure 10.10: Trend comparison of aviation ozone versus total ozone (top graph), stratospheric ozone versus total ozone (middle graph) and stratospheric ozone versus aviation ozone(bottom graph) for T5.

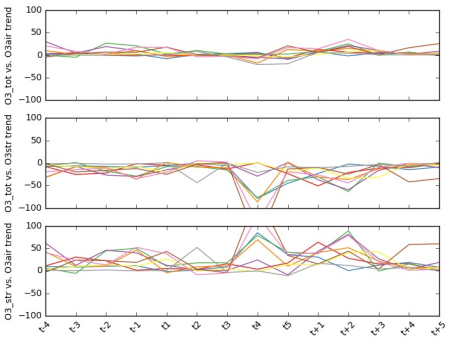


Figure 10.11: Trend comparison of aviation ozone versus total ozone (top graph), stratospheric ozone versus total ozone (middle graph) and stratospheric ozone versus aviation ozone(bottom graph) for T5.

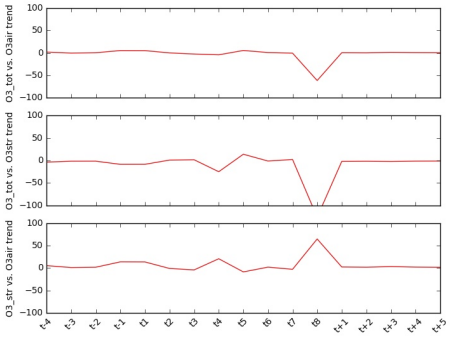


Figure 10.12: Normalized relative humidity versus normalized $O_3$ from aviation for Region 1, category 1 (top line), category 2 (middle line), and category 3 (bottom line) for T8.

## 10.3. Discussion of ozone perturbation analysis

The perturbation in total ozone due to aviation is generally smaller than the variability of the total ozone budget, which makes it unlikely to detect changes in the total ozone budget due to aviation. From the research performed it became evident that an increase in aviation ozone due to the accumulation in aviation nitrogen oxides in a high-pressure system might be detectable if under specific circumstances.

The accumulation of aviation $NO_y$ will only take place if the high-pressure system is stable over a longer period of time (at least 5 timesteps, thus 50 hours), and if the PV values increase during this period which allows the transport of aviation nitrogen oxides species to accumulate in the high-pressure system. A high dry air temperature and high relative humidity conditions positively influence this process. The aviation ozone increases at average flight levels and lower flight levels, while the background ozone does not increase at lower levels. Therefore at lower flight levels aviation ozone will likely have the largest impact, while at average flight levels the stratospheric ozone mixing ratios are most dominant. From the analysis performed in this chapter it resulted that at lower flight levels the aviation ozone and total ozone follow a similar trend, while the stratospheric ozone does not follow this same trend. Additionally, the mixing ratios of stratospheric ozone has decreased significantly at lower flight levels compared to average flight levels, while the mixing ratios of aviation ozone have remained at stable values on both levels. Therefore, it is potentially possible at lower flight levels to detect an increase in aviation ozone in the total ozone changes, under the condition that the accumulation takes place in a high-pressure stable weather system of at least 5 timesteps (50 hours) and transport from higher altitudes into the weather system takes place, increasing the PV values and allowing $NO_{y_{air}}$ to accumulate within the system.

# 11

# Assessing Possibilities for Future Measurement Campaigns

In this Chapter it is briefly discussed how the findings from this research could aid in designing aviation ozone measurement campaigns. First the conditions under which aviation ozone could be detected are discussed, after which various suitable measurement techniques are briefly discussed.

## 11.1. Conditions to detect aviation ozone in the atmosphere

In the previous Chapter it was discussed that aviation ozone is potentially detectable at lower flight altitudes for a specific set of conditions. These conditions are that the $NO_{y_{air}}$ takes place in a stable high-pressure weather system of at least 50 hours where the PV value increases such that transport into the weather system is possible. High dry air temperatures and high relative humidity conditions positively influence this mechanism and result in elevated aviation $O_{3_{air}}$ mixing ratios. Therefore, if a high pressure system with high relative humidity, high dry air temperature and high PV is analysed, it is likely that here accumulation of $NO_{y_{air}}$ takes place which results in a detectable increase in $O_{3_{air}}$.

To distinguish this increase in ozone due to aviation, measurements need to be performed at lower flight altitudes for the set of conditions described earlier. If measurements are performed at higher altitudes, the stratospheric ozone mixing ratios are dominant and any change in total ozone is most probably due to a change in stratospheric ozone.

## 11.2. Ozone measurement techniques

Ozone in the high troposphere and low stratosphere can be measured through in-situ measurement methods or through remote sensing methods. These methods include ozone sondes, UV back scatter satellites, radiometer satellites, ground based measurement systems or with on-board measuring instruments on aircraft. These measurement techniques are illustrated in Figure 11.1.

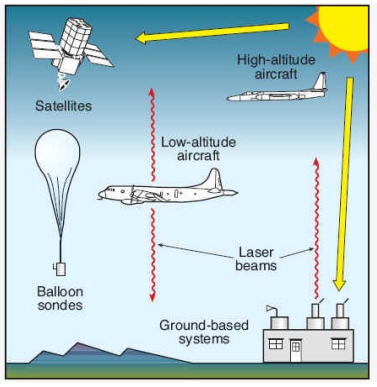


Figure 11.1: Illustration of different ozone measurement techniques. source: http://www.theozonehole.com/twenty.htm

These methods can either specifically measure a column of ozone over a large range of altitudes, or ozone layers in the atmosphere, or local ozone concentrations. For example, there are satellites that measure the stratospheric ozone specifically, while others are focused on measuring tropospheric ozone such as the TES[1]. Ozonesondes on the other

[1] https://tes.jpl.nasa.gov/

hand are a form of in-situ measurements and it measures the ozone concentration at the altitudes it passes on its upward path.

Since the perturbation of aviation ozone in weather patterns is very local, a measurement technique is needed which can locally measure the ozone changes with a high resolution. It should be able to detect the increase in total ozone at lower flight altitudes in a high-pressure system and distinguish this from surrounding ozone concentrations.

## 11.3. Summarizing future measurement campaign recommendations

In order to potentially measure the change in total ozone due to aviation ozone the following steps should be taken:

- Select potential stable high-pressure systems with high dry air temperatures and high relative humidity using weather forecasts
- Measure total ozone at low flight altitudes (around 300 hPa) in the potential high-pressure systems
- Compare the change of total ozone over time to ozone of surround areas which are not involved in a high-pressure system

To distinguish whether an increase in the total ozone is due to aviation, it needs to be further investigated to what extend aviation perturbs the total ozone budget. With the current information and results this has not been found. In order to determine this, the average increase of aviation ozone within high-pressure systems should be established. Additionally, the increase in Stratospheric ozone should be assessed, as this is a dominant contributor to the total ozone at flight levels. If it can be established that the increase in aviation ozone concentrations is more closely related than stratospheric ozone is to the change in total ozone and this can be quantified, then this quantification can be taken into account for future measurement campaigns.

# 12

# Conclusion and Recommendations

## 12.1. Conclusion

Aviation has a large impact on climate change through its emissions, particularly through $NO_y$[1]. By emitting $NO_y$ the background concentrations of $NO_y$, methane and ozone are disturbed. However, the impact of aviation $NO_y$ and ozone has not yet been successfully measured due to the dynamic properties of $NO_y$. Because $NO_y$ rapidly mixes with other $NO_y$ particles in the atmosphere it is up to date not possible to measure ozone emanating from aviation $NO_y$ in the atmosphere. In order to propose mitigation measures for the effects of aviation $NO_y$ and ozone, measuring these species would contribute largely to understanding this mechanism. Currently, the footprints of aviation $NO_y$ and $O_3$ have been successfully modelled in 3D climate-chemistry models which is a great aid in understanding their behaviour. The current understanding is that the background concentrations of $NO_y$ and ozone are probably larger than the perturbations caused by aviation $NO_y$ and ozone, making it hardly measurable in the atmosphere, except for under special meteorological conditions such as high-pressure systems.In this MSc. thesis the relationship between high-pressure weather patterns and the impact of aviation nitrogen oxides ($NO_{y_{air}}$) and aviation ozone ($O_{3_{air}}$) was investigated. It was investigated whether $O_{3_{air}}$ is detectable under high-pressure weather systems, and if so, if its perturbation is detectable in the total ozone concentration changes.

First a general variability analysis was performed where the variability of the mixing ratios of aviation $NO_y$ and $O_3$ was assessed with respect to latitude an season. The analysis showed that in general the mixing ratios of aviation $NO_y$ and $O_3$ increase with latitude due to the increasing air traffic activity and horizontal transport through the atmosphere which transports these species to higher latitudes. The mixing ratios found for Winter are generally lower than for Summer. The relative contributions of these species on the other hand are larger in Winter compared to Summer, due to larger background concentrations in Summer which are attributed to higher deep convection and vertical mixing in the atmosphere.
The variability of these species was also analysed with respect to dry air temperature, relative humidity and potential vorticity. Aviation $NO_y$ showed to be insensitive to relative humidity, but with respect to dry air temperature it was found that for each temperature regime, different behaviour for both $NO_{y_{air}}$ and $O_{3_{air}}$ was found. Low mixing ratios of $NO_{y_{air}}$ are correlated to higher dry air temperatures, whereas these temperatures are related to higher $O_{3_{air}}$ mixing ratios, implying that higher dry air temperatures positively affect the aviation $O_3$ concentrations. Furthermore, a strong positive correlation to potential vorticity was found for $NO_{y_{air}}$. Aviation $O_{3_{air}}$ also showed a correlation with potential vorticity, but less strong compared to the correlation of $NO_{y_{air}}$ with PV. Furthermore, the results suggested that relative humidity and dry air temperature influence the production of ozone aviation, as concentrations were found for elevated dry air temperature and relative humidity conditions. Finally, the $NO_{y_{air}}$ - $O_{3_{air}}$ ratio seems to be correlated to latitude independent of the RH and $T_{dry}$ regimes. High potential vorticity forms an exception here as for this regime the $NO_{y_{air}}$ - $O_{3_{air}}$ ratio is distributed over random latitudes. This answers the first research question posed in Section 2.1.

After analysing the temporal development of aviation ozone and nitrogen oxides for various weather patterns it resulted that an increase of $NO_{y_{air}}$ happens only if a high-pressure weather system is stable for at least 50 hours (T5 or longer). This increase then only happens for weather patterns where the PV values are initially close to zero, after which elevated PV values arise, which allows transport of additional $NO_{y_{air}}$ into the weather system from higher altitudes. The accumulation will then be located at average flight levels (around 225hPa). After analysing individual specific weather patterns it was concluded that the mechanism of accumulation of $NO_{y_{air}}$ in the weather patterns and the conversion to $O_{3_{air}}$ is influenced by the dry air temperature and relative humidity as well. For higher $T_{dry}$ and RH conditions elevated $O_{3_{air}}$ mixing ratios have been established. Thus, in weather patterns with higher dry air

[1]The model (EMAC model) with which the analysis data was simulated, outputted $NO_y$ concentrations and contributions and not $NO_x$. These species occur in the same ratio in the atmosphere, and therefore for the following text $NO_y$ is applied instead of $NO_x$.

temperatures and elevated RH conditions, the conversion of aviation $NO_y$ to ozone will be more efficient and increased aviation $O_3$ are found. The increased aviation ozone mixing ratios extend even to lower flight levels (down to 300hPa), while aviation nitrogen oxides have decreased at lower flight levels. This is in contrast to what was found in literature where it states that at lower levels the lifetime of $NO_{y_{air}}$ is shorter thus less $O_{3_{air}}$ is produced. This answers the second research question posed in Section 2.1.

The third research question posed in Section 2.1 was whether the increase in aviation $O_3$ is detectable in the total ozone concentration changes, and if so, if this result could aid in formulating recommendations for future measurement campaigns. The answer to this is that aviation $O_3$ concentration changes are potentially detectable at lower flight levels as here the influence of stratospheric ozone has largely reduced, and the ozone concentrations are still relatively large (although still smaller than stratospheric ozone). From these results it is assessed whether suggestions for future measurement campaigns could be formulated. Aviation ozone concentrations only increase at locations where a closed high-pressure system with low PV values is found. In order to achieve higher mixing ratios, increased PV values throughout the lifetime of the high-pressure system should arise which allow transport from higher altitudes. Only under these conditions an increase in aviation $NO_y$ takes place at flight levels. This increase translates into elevated aviation ozone mixing ratios at average flight levels and lower flight levels. Only at lower flight levels there is a possibility that the increase in aviation ozone is detectable by an increase in total ozone. In order to distinguish aviation $O_3$ from total $O_3$ an analysis must be performed to investigate the variability of aviation $O_3$ in such systems and compare this to the standard deviation of the total ozone in such weather patterns. If this is achieved and the perturbation of aviation ozone on the total ozone can be quantified, aviation ozone can be identified in high-pressure systems, if the measurements are performed in high-pressure systems that where $NO_{y_{air}}$ and $O_{3_{air}}$ increases. This concludes the answer to the third research question posed in Section 2.1.

## 12.2. Recommendations

The results of this thesis have lead to multiple recommendations for future research. As weather patterns are unique concepts, comparing weather patterns to each other always brings uncertainties, as conditions are never constant. Especially comparing weather patterns with long lifetimes is difficult as these are rare and a higher variability of weather conditions within the pattern are encountered. Therefore, to be able to draw more conclusive results it is recommended to analyse a larger set of weather patterns.

Furthermore in order to confirm the concept that species accumulate in high-pressure systems a detailed comparison could be carried out with respect to low-pressure systems. From an initial comparison it resulted that for low-pressure systems the aviation $NO_y$ increases due to the high PV, but it does not accumulate with the system, thus aviation $O_{3_{air}}$ does not increase for low-pressure systems. To confirm this a similar analysis should be performed as was done for the high-pressure weather systems.

For some cases the $NO_{y_{air}}$ increased in the high-pressure system, while no increase in aviation $O_{3_{air}}$ was established. This could be attributed to already high background $NO_y$ concentrations. This could be investigated in detail to classify for which background concentrations aviation $O_3$ increases and when not.

In order to distinguish aviation ozone from the total ozone, a closer analysis needs to be performed which looks at characteristic concentration changes with respect to the weather patterns. The variability of aviation ozone should be quantified, which must then be compared to the variability of the total ozone under the same conditions. If this is achieved, the next step into distinguishing aviation ozone from total ozone can be taken.

Lastly no analysis has been performed with respect to other chemical species such as OH or HCl. These species also take part in the production of ozone and could affect the production efficiency of aviation $O_3$ due to competing effects.

# Bibliography


[1] T. Berntsen and J. Fuglestvedt. Global temperature responses to current emissions from the transport sector. *Proceedings of the National Academy of Science U.S.A.*, 105:19154–19159, 2014.

[2] G.P. Brasseur and M. Gupta. Impact of aviation on climate change. *American Meteorological Society*, pages 461–463, 2010.

[3] G.P. Brasseur, R.A. Cox, D. Hauglustaine, I. Isaksen, J. Lelieveld, H. Listera, R. Sausen, U. Schumann, A. Wahner, and P. Wiesen. European scientific assessment of the atmospheric effects of aircraft emissions. *Atmospheric Environment*, 32(13):2329–2418, 1998.

[4] G.P. Brasseur, M. Gupta, B.E. Anderson, S. Balasubramanian, S. Barrett, D. Duda, G. Fleming, P.M. Forster, J. Fuglestvedt, A. Gettelman, and et al. Impact of aviation on climate: FAA's aviation climate change research initiative (ACCRI) phase II. *Bulletin of the American Meteorological Society*, 97:561–583, 2016.

[5] Brasseur G.P., Orlando J.J., Tyndall G.S. *Atmospheric Chemistry and Global Change*. Oxford University Press, Oxford, 1st ed. edition, 1999.

[6] S. et al. Brunamonte. Balloon-borne measurements of temperature, water vapor, ozone and aerosol backscatter on the southern slopes of the himalayas during StratoClim 2016-2017. *Atmospheric Chemistry and Physics*, 18: 15937–15957, 2018.

[7] U. Burkhardt and B. Karcher. Global radiative forcing from contrail cirrus. *Nature Climate Change Journal*, 1: 54–58, 2011.

[8] T.M. Butler, M.G. Lawrence, D. Taraborrelli, and J. Lelieveld. Multi-day ozone production potential of volatile organic compounds calculated with a tagging approach. *Atmospheric Environment*, 45:4082–4090, 2012.

[9] W.L. Chameides, F. Fehnsfeld, M.O. Rodgers, C. Cardelino, J. Marinez, D. Parrish, W. Lonneman, D.R. Lawson, R.A. Rasmussen, P. Zimmerman, J. Greenberg, P. Middleton, and T. Wang. Ozone precursor relationships in the ambient atmospere. *Journal of Geophysical Research*, 97(D5):6037–6055, 1992.

[10] P.J. Crutzen. The influence of nitrogen oxides on the atmospheric ozone content. *Quarterly Journal of the Royal Meteorological Society*, 96:320–325, 1970.

[11] P.J. Crutzen and U. Schmaizl. Chemical budgets of the stratosphere. *Planetary and Space Science*, 31:1009–1032, 1983.

[12] T Eames. Modelling ozone air quality in the netherlands and north-western europe in 2050. 2018.

[13] D. Ehhalt, M. Prather, F. Dentener, R. Derwent, Edward J. Dlugokencky, E. Holland, I. Isaksen, J. Katima, V. Kirchhoff, P. Matson, P. Midgley, M. Wang, T. Berntsen, I. Bey, G. Brasseur, L. Buja, W. J. Collins, J. S. Daniel, W. B. DeMore, N. Derek, R. Dickerson, D. Etheridge, J. Feichter, P. Fraser, R. Friedl, J. Fuglestvedt, M. Gauss, L. Grenfell, Arnulf Grubler, N. Harris, D. Hauglustaine, L. Horowitz, C. Jackman, D. Jacob, L. Jaegle, Atul K. Jain, M. Kanakidou, S. Karlsdottir, M. Ko, M. Kurylo, M. Lawrence, J. A. Logan, M. Manning, D. Mauzerall, J. McConnell, L. J. Mickley, S. Montzka, J. F. Muller, J. Olivier, K. Pickering, G. Pitari, G.-J. Roelofs, H. Rogers, B. Rognerud, Steven J. Smith, S. Solomon, J. Staehelin, P. Steele, D. S. Stevenson, J. Sundet, A. Thompson, M. van Weele, R. von Kuhlmann, Y. Wang, D. K. Weisenstein, T. M. Wigley, O. Wild, D.J. Wuebbles, R. Yantosca, Fortunat Joos, and M. McFarland. *Atmospheric Chemistry and Greenhouse Gases*. 2001.

[14] L.K. Emmons, P.G. Hess, J.-F. Lamarque, and G.G. Pfister. Tagged ozone mechanism for MOZART-4, CAM-chem and other chemical transport models. *Geoscientific Model Development*, 5:1531–1542, 2012.

[15] C. Frömming, M. Ponater, K. Dahlmann, V. Grewe, D.S. Lee, and R. Sausen. Aviation-induced radiative forcing and surface temperature change in dependency of the emission altitude. *Journal of Geophysical Research*, 117, 2012.

[16] J.S. Fuglestvedt, K.P. Shine, Cook J. Berntsen, T., D.S. Lee, A. Stenke, R.B. Skeie, G.J.M. Vleders, and I.A. Waitz. Transport impacts on atmosphere and climate: metrics. *Atmospheric Environment*, 44:4648–4677, 2010.

[17] R.M. et al. Gardner. The ancat/ec global inventory of $no_x$ emissions from aircraft. *Atmospheric Environment*, 31 (12):1751 – 1766, 1997.

[18] V. Grewe. A generalized tagging method. *Geoscientific Model Development*, 6:247–253, 2013.

[19] V. Grewe, M. Dameris, C. Fichter, and D.S. Lee. Impact of aircraft nox emissions. Part 2: Effects of lowering the flight altitude. *Meteorologische Zeitschrift*, 11(3):197–205.

[20] V. Grewe, T. Champougny, S. Matthes, C. Froemming, S. Brinkop, O. Amund Sovde, E.A. Irvine, and L. Halscheidt. Reduction of the air traffic's contribution to climate change: A REACT4C case study. *Elsevier*, pages 617–625, 2014.

[21] V Grewe, K. Dahlmann, J. Flink, C. Froemming, R. Ghosh, K. Gierens, R. Heller, J Hendricks, P Joeckel, S Kaufmann, K Koelker, F. Linke, T. Luchkova, B. Luehrs, J. Van Manen, S. Matthes, A. Minikin, M. Niklass, M. Plohr, M. Righi, S. Rosanka, A. Schmitt, U. Schumann, I. Terekhov, S. Unterstrasser, C. Vazquez-Navarro, M. Voigt, K. Wicke, H. Yamashita, A. Zahn, and H. Ziereis. Mitigating the climate impact from aviation: Achievements and results of the DLR WeCare Project. *Aerospace*, pages 4971–4993, 2017.

[22] V. Grewe, E. Tsati, M. Mertens, C. Froemming, and P. Joeckel. Contribution of emissions to concentrations: The TAGGING 1.0 submodel based on the modular earth submodel system (MESSy 2.52). *Geoscientific Model Development*, 10:2615–2633, 2017.

[23] L. Husain. Ozone transport from stratosphere to troposphere. *Geophysical Research Letters*, 4(9):363–365, 1977.

[24] E.A. Irvine, B.J. Hoskins, K.P. Shine, R.W. Lunnon, and C. Froemming. Characterizing north atlantic weather patterns for climate-optimal aircraft routing. *Royal Meteorology Society*, 2012.

[25] M.O. Kohler, G. Rädel, K.P. Shine, H.L. Rogers, and J.A. Pyle. Latitudinal variation of the effect of aviation $no_x$ emissions on atmospheric ozone and methane and related climate metrics. *Atmospheric Environment*, 64:1–9, 2012.

[26] M.O. Köhler, G. Rädel, O. Dessens, K.P. Shine, H.L. Rogers, O. Wild, and J.A. Pyle. Impact of perturbations to nitrogen oxide emissions from global aviation. *Journal of Geophysical Research*, 113:–, 2008.

[27] E. Lippert, J. Hendricks, and H. Petry. Development and application of a chemistry mechanism for mesoscale simulations of the troposphere and lower stratosphere., 1997.

[28] Maas, A. and Kleingeld, H. *Synoptische Meteorologie en Conceptuele Modellen*. KNMI, 2004.

[29] Marshall, J. and Plumb, R.A. *Atmosphere, ocean, and Climate Dynamics: An Introductory Text*. Elsevier Academic Press, 1st ed. edition, 2008.

[30] M. Mertens. The 1-way on-line coupled model system meco(n) – part 4: Chemical evaluation (based on messy v2.52). *Geoscientific Model Development*, 9(10):3545 – 3567, 2016.

[31] M. Mertens, V. Grewe, V.S. Rieger, and P. Joeckel. Revisiting the contribution of land transport and shipping emissions to tropospheric ozone. *Atmospheric Chemistry and Physics*, 18:5567–5588, 2018.

[32] S.C. Olsen, D.J. Wuebbles, and B. Owen. Comparison of global 3-d aviation emissions datasets. 2013.

[33] Research Triangle Institute. Investigation of Rural Oxidant Levels as Related to Urban Hydrocarbon Control Strategies, 1975.

[34] E. Roeckner, G. Bauml, L. Bonaventura, R. Brokopf, M. Esch, M. Giorgetta, S. Hagemann, I. Kirchner, L. Kornblueh, E. Manzini, A. Rhodin, U. Schlese, U. Schulzweida, and A. Tompkins. The atmospheric general circulation model echam5, part i. (349), 2003.

[35] E. Roeckner, G. Bäuml, L. Bonaventura, R. Brokopf, M. Esch, M. Giorgetta, S. Hagemann, I. Kirchner, L. Kornblueh, E. Manzini, A. Rhodin, U. Schlese, U. Schulzweida, and A. Tompkins. The atmospheric general circulation model ECHAM5. PART I: Model description. *MPI für Meteorologie*, (349), 2003.

[36] R. Sander, A. Kerkweg, P. Jöckel, and J. Lelieveld. Technical note: the new comprehensive chemistry module MECCA. *Atmospheric Chemistry and Physics*, (5):445 – 450, 2005.

[37] R. Sausen, R. adn Deckter, P. Jöckel, V. Aquila, U. Brinkop, S. ad Burkhardt, I. Cionni, M. Dall'Amico, M. Dameris, S. Dietmuller, V. Eyring, K. Gottschaldt, V. Grewe, J. Hendricks, M. Ponater, and M. Righi. Global chemistry-climate modelling with EMAC. *High Performance Computing in Science and Engineering*, 2010.

[38] Seinfeld, J.H. and Pandis, S.N. *Atmospheric Chemistry and Physics*. Wiley Interscience, 1997.

[39] S Sillman. The relation between ozone, $no_x$ and hydrocarbons in urban and polluted rural environments. *Atmospheric Environment*, 33:1821–1845, 1999.

[40] O.A. Søvde and et al. Aircraft emission mitigation by chaning route altitude: A multimodel estimate of aircraft $no_x$ emission impact on $o_3$ photochemistry. *Atmospheric Environment*, pages 1352–2310, 2014.

[41] D.S. Stevenson, R.M. Doherty, M.G. Sanderson, C.E. Collins, W.J.and Johson, and R.G. Derwent. Radiative forcing from aircraft $NO_x$ emissions: Mechanisms and seasonal dependence. *Journal of Geophysical Research*, 109, 2004.

[42] W.M.F. Wauben, P.F.J. Van Velthoven, and H. Kelder. A 3d chemistry transport model study of changes in atmospheric ozone due to aircraft $no_x$ emissions. *Atmospheric Environment*, 31(12):1879–1836, 1997.

[43] H. Ziereis, H. Schlager, P. Schulte, I. Köhler, R. Marquardt, and C. Feigl. In situ measurements of the nox distribution and variability over the eastern north atlantic. 1999.

# A

# Perturbation method

The perturbation approach is a method with which one can attribute certain concentration changes to changes in specific sources. Basically, the perturbation method assesses the impact of an emission sector on a species, while the tagging method assesses the contribution of an emission sector to a species (source apportionment).

The perturbation method basically compares two (or more) simulations, e.g. a perturbed simulation to a base simulation. The base simulation is a reference simulation where all emission source sectors are active, and the perturbed simulation could be a simulation where one emission source sector is inactive or simulated with perturbed emission values. In the case of linear relationships, this method is rather straightforward [**?** ]. A linear relationship between the function C and the three variables E1, E2 and E3 is taken with constant coefficients P1, P2 and P3:

$$C(E_1, E_2, E_3) = C(0,0,0) + P_1E_1 + P_2E_2 + P_3E_3 \tag{A.1}$$

For this relationship, the sensitivity of a concentration with respect to a change in one of the emission sources can be quantified as follows:

$$\frac{\delta C}{\delta E_1} = P_1 \tag{A.2}$$

$$\frac{\delta C}{\delta E_2} = P_2 \tag{A.3}$$

$$\frac{\delta C}{\delta E_3} = P_3 \tag{A.4}$$

Because a linear relationship is established, all higher-order derivatives are set to zero, as the impact of a change in one emission source is independent of the others. Furthermore this also means that the first-order partial derivatives are constant and can therefore be calculated with finite differencing between any couple of emission levels. The linearity in this relationship also entails that the concentration change resulting from a simultaneous reduction of all emission sources is equal to the sum of the emission source contributions.
In the case of nonlinear relationships however, this conclusion is invalid. In this case interaction terms must be accounted for. Since the relationship between $NO_x$ emission sectors and ozone concentration is non-linear, the focus of this section will be on the assessment of the perturbation method for non-linear relationships. The study by Mariano Mertens et al (2018) assessed the impact of land transport and shipping to tropospheric ozone by means of the perturbation method [31]. This was done by performing three simulations using the TAGGING submodel with the 10 tagging categories as stated in Chapter 6. The three simulations were the following:

- BASE simulation: the unperturbed simulation where all emission source categories are active
- LTRA95: perturbed simulation where the land transport emissions are reduced by 5%
- SHIP95: perturbed simulation where the shipping sector emissions are reduced by %

Since the $O_3$ chemistry is non-linear, one cannot simply subtract a perturbed simulation from the unperturbed simulation to analyse the ozone sensitivity to these perturbations. It is known that the ozone production efficiency depends on the NOx background concentrations. As such, the $O_3$ production efficiency is higher In order to analyse this sensitivity, the tangent approach in accordance with Grewe et al (2010) must be applied [18]. This approach calculates a linearized ozone production function such that a saturation indicator can be determined, which aids in analysing the ozone sensitivity further. This saturation indicator is a quantitative measure that indicates for a chemical regime how much an emission change in one specific sector is compensated for by increased ozone productivity in other sectors.

# B

# TAGGING Submodel Chemistry

For the ozone production, two production terms are identified (analogously to Section **??**), which are Reaction 4.14 and Reaction 4.12, with reaction rates PR4.14 and PR4.12 respectively. This is applied to any tagged ozone field except for stratospheric ozone.
The loss reaction terms are as follows:

$$OH + O_3 \rightarrow HO_2 + O_2 \tag{B.1}$$
$$HO_2 + O_3 \rightarrow OH + 2O_2 \tag{B.2}$$
$$D[NO_y] \tag{B.3}$$
$$RO_2 + O_3 \rightarrow RO + 2O_2 \tag{B.4}$$
$$OH + O_3 \rightarrow HO_2 + O_2 \tag{B.5}$$

Where Reaction B.3 denotes the effective ozone loss via $NO_y$. Analogously, to these reaction terms belong the reaction rates PRB.1 – PRB.5.
Using these production and loss terms, the production and loss terms of the tagged ozone fields then become:

$$PO_3^{tag} = \frac{1}{2} P_{R4.11}\left(\frac{NO_y^{tag}}{NO_y} + \frac{HO_2^{tag}}{HO_2}\right) \tag{B.6}$$
$$+ \frac{1}{2} P_{R4.9}\left(\frac{NO_y^{tag}}{NO_y} + \frac{NMHC^{tag}}{NMHC}\right) \tag{B.7}$$

$$DO_3^{tag} = \frac{1}{2} P_{RB.1}\left(\frac{OH^{tag}}{OH} + \frac{O_3^{tag}}{O_3}\right) \tag{B.8}$$
$$+ \frac{1}{2} P_{RB.2}\left(\frac{HO_2^{tag}}{HO_2} + \frac{O_3^{tag}}{O_3}\right) \tag{B.9}$$
$$+ \frac{1}{2} P_{RB.3}\left(\frac{NO_y^{tag}}{NO_y} + \frac{O_3^{tag}}{O_3}\right) \tag{B.10}$$
$$+ \frac{1}{2} P_{RB.4}\left(\frac{NMHC^{tag}}{NMHC} + \frac{O_3^{tag}}{O_3}\right) \tag{B.11}$$
$$+ P_{RB.5} \frac{O_3^{tag}}{O_3} \tag{B.12}$$

The principal relations between the tagged species is indicated in Figure B.1[22]. In this figure the blue rectangular boxes denote the tagged species, and the orange elliptic boxes denote other species. The arrows in this figure indicate the relationships between the species.

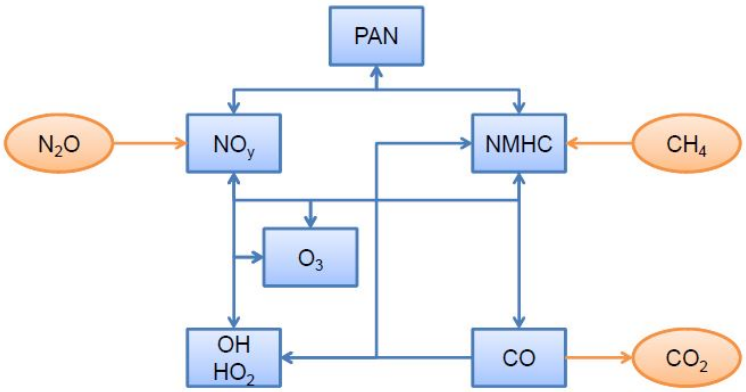


Figure B.1: Chemistry of tagged species in blue and the key relations to other species in orange. Stratospheric ozone is not included here. Source: [22]

As can be seen, methane is not tagged in the model. However, its chemical products are ($NMHC$) and are tagged as "NMHC from methane". Following the arrows one can see that the species in the NMHC family are eventually transformed into $CO$ (tagged) and then into $CO_2$ (not tagged). Furthermore, the decomposition of $N_2O$ is also not tagged, but it constitutes a source for stratospheric $NO_y$, which is tagged. Indicated in the figure is the product $PAN$ that results from the reaction between $NO_y$ and $NMHC$. $PAN$ is an important species which can be transported over long distances before it thermally decomposes.

# C

# Aviation $NO_y$ and $O_3$ for Region 1 and 2

In this appendix the temporal developments are shown for weather patterns found in Region 1 and 2. The weather patterns with lifetime T3, T5 and T7 are given.

## C.1. Region 1

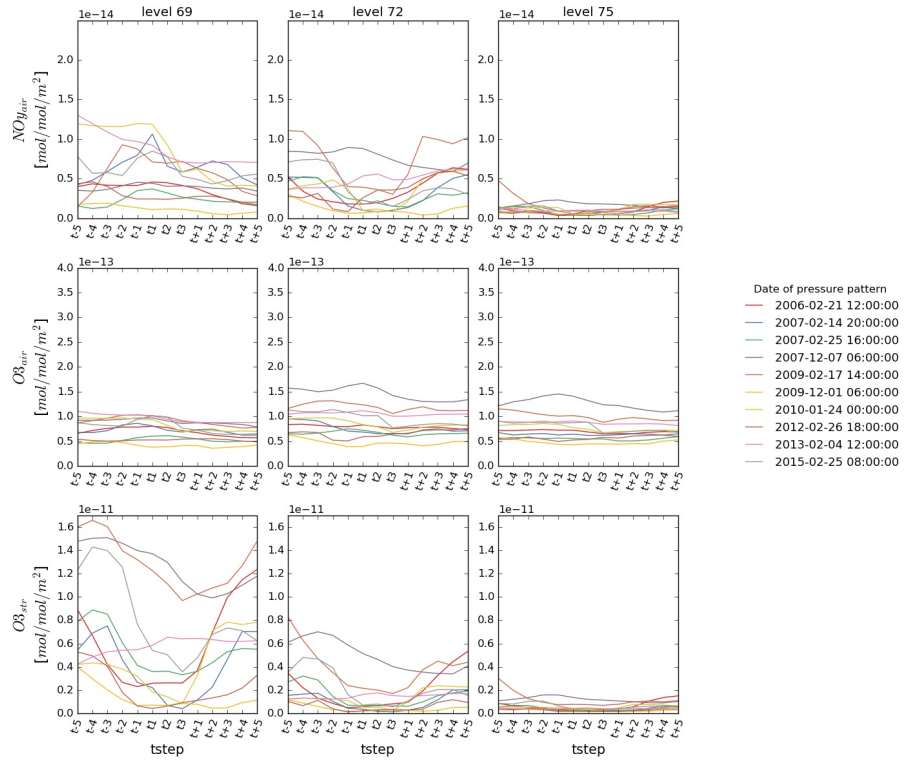


Figure C.1: Temporal development of area normalized mixing ratios of $NOy_{air}$ (top), $O_{3_{air}}$ (middle) and $O_{str}$ (bottom) in weather patterns found in Region 1 with lifetime T3.

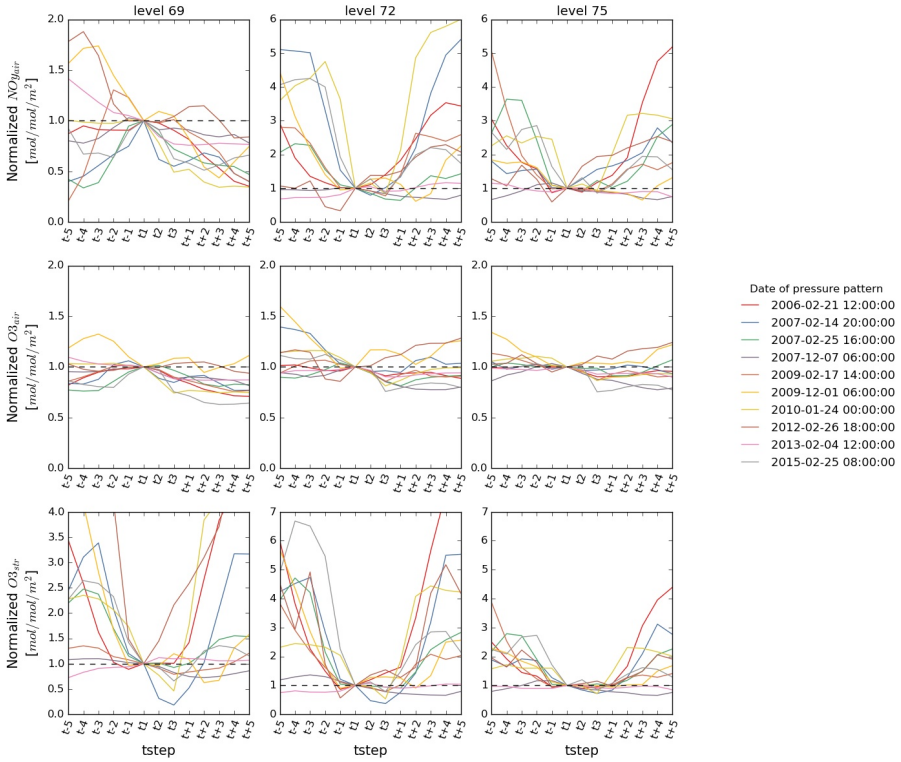


Figure C.2: Temporal development of area normalized mixing ratios of $NO_{y_{air}}$ (top), $O_{3_{air}}$ (middle) and $O_{str}$ (bottom) in weather patterns found in Region 1 with lifetime T3. These mixing ratios have been normalized with respect to the mixing ratio at $t_1$.

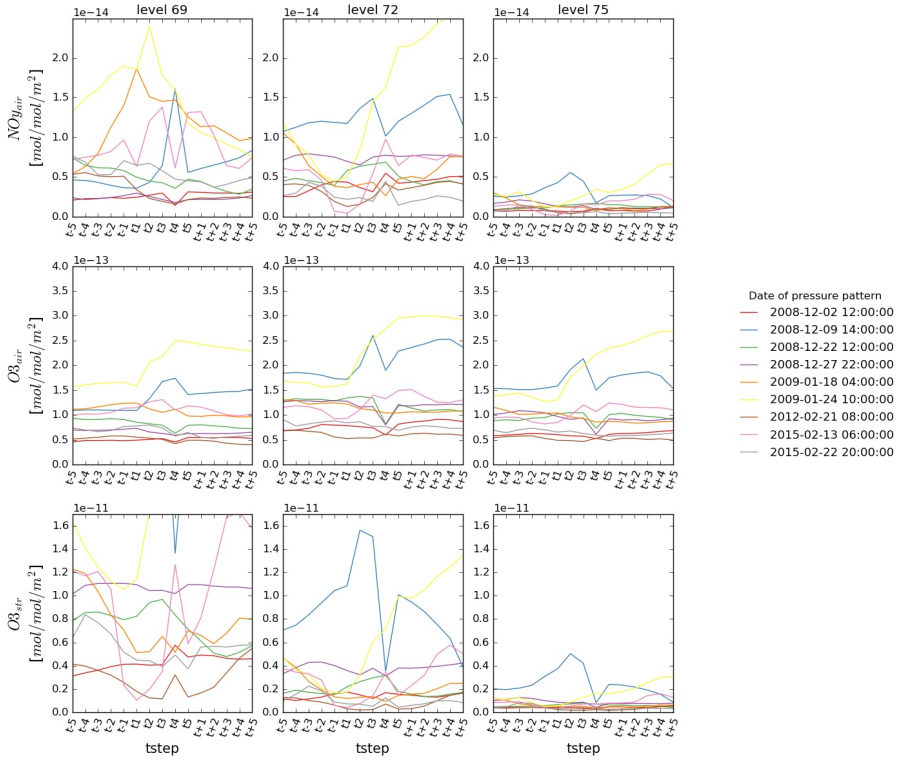


Figure C.3: Temporal development of area normalized mixing ratios of $NO_{y_{air}}$ (top), $O_{3_{air}}$ (middle) and $O_{str}$ (bottom) in weather patterns found in Region 1 with lifetime T3.

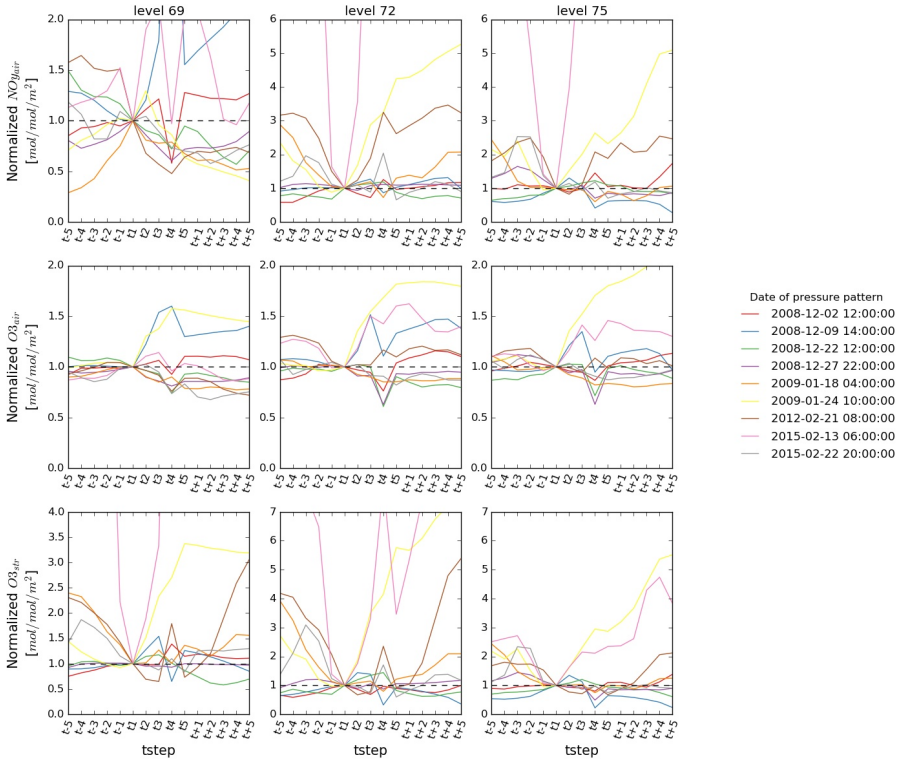


Figure C.4: Temporal development of area normalized mixing ratios of $NO_{y_{air}}$ (top), $O_{3_{air}}$ (middle) and $O_{str}$ (bottom) in weather patterns found in Region 1 with lifetime T3. These mixing ratios have been normalized with respect to the mixing ratio at $t_1$.

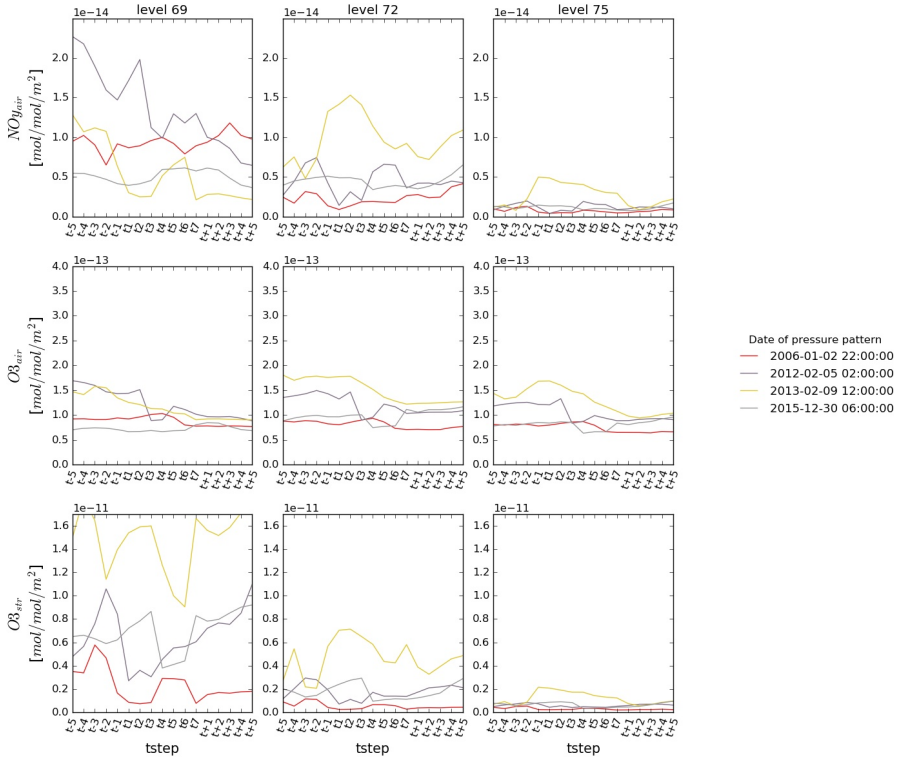


Figure C.5: Temporal development of area normalized mixing ratios of $NO_{y_{air}}$ (top), $O_{3_{air}}$ (middle) and $O_{str}$ (bottom) in weather patterns found in Region 1 with lifetime T3.

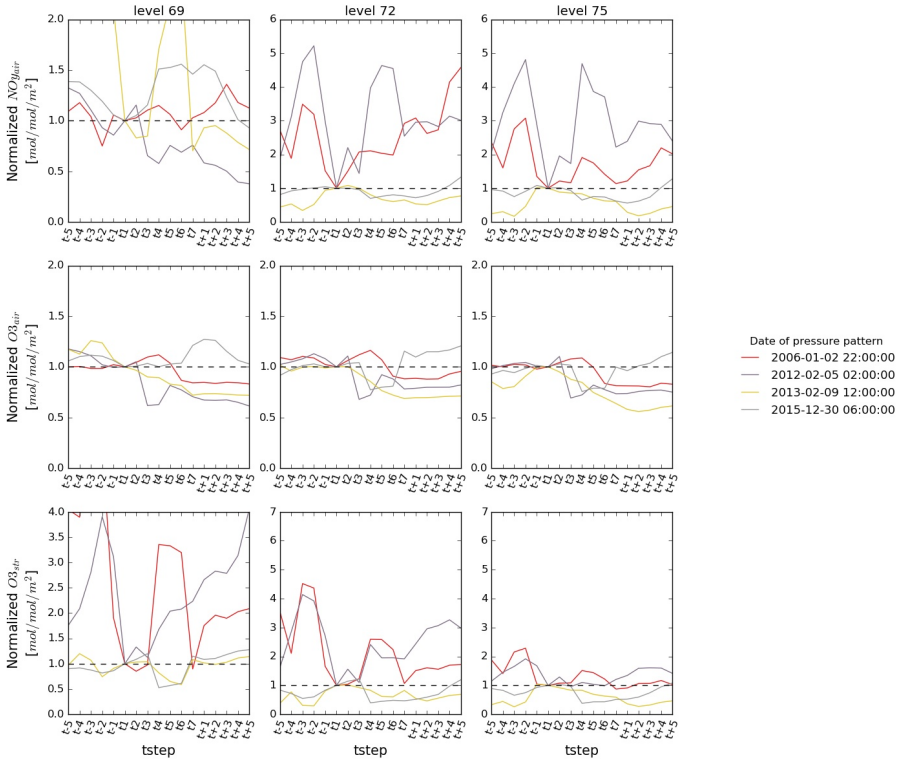


Figure C.6: Temporal development of area normalized mixing ratios of $NO_{y_{air}}$ (top), $O_{3_{air}}$ (middle) and $O_{str}$ (bottom) in weather patterns found in Region 1 with lifetime T3. These mixing ratios have been normalized with respect to the mixing ratio at $t_1$.

# C.2. Region 2

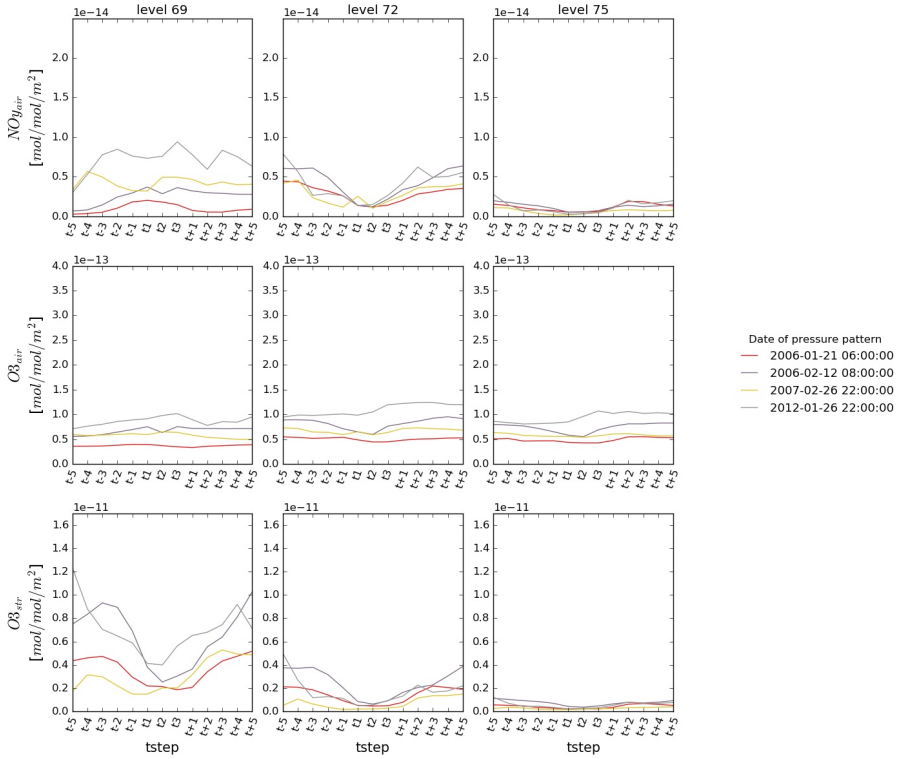


Figure C.7: Temporal development of area normalized mixing ratios of $NO_{y_{air}}$ (top), $O_{3_{air}}$ (middle) and $O_{str}$ (bottom) in weather patterns found in Region 2 with lifetime T3.

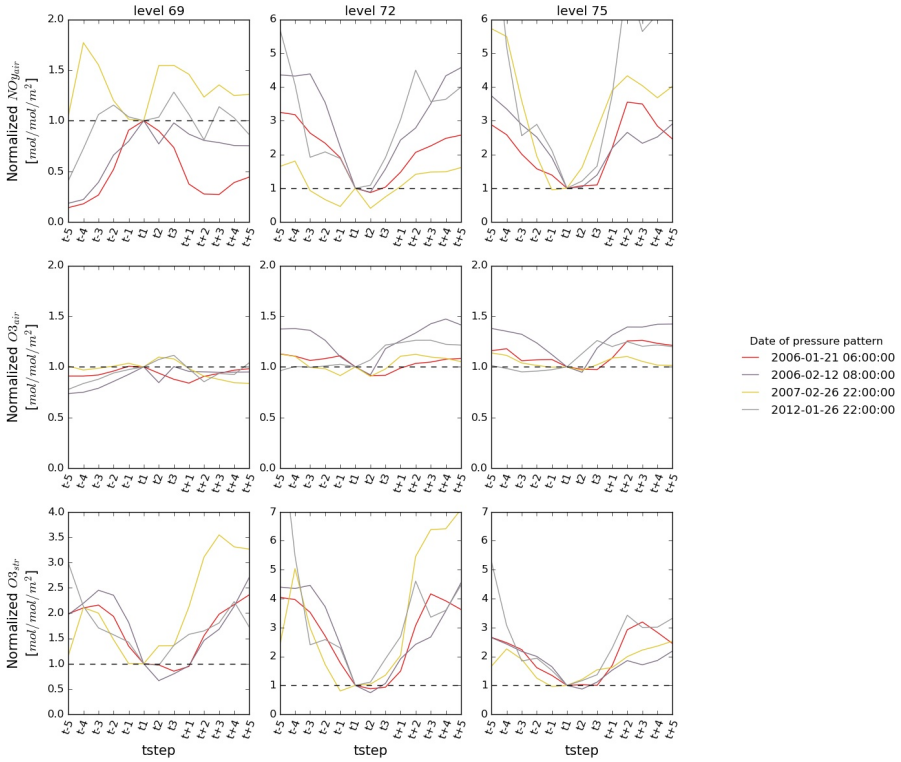


Figure C.8: Temporal development of area normalized mixing ratios of $NO_{y_{air}}$ (top), $O_{3_{air}}$ (middle) and $O_{str}$ (bottom) in weather patterns found in Region 2 with lifetime T3. These mixing ratios have been normalized with respect to the mixing ratio at $t_1$.

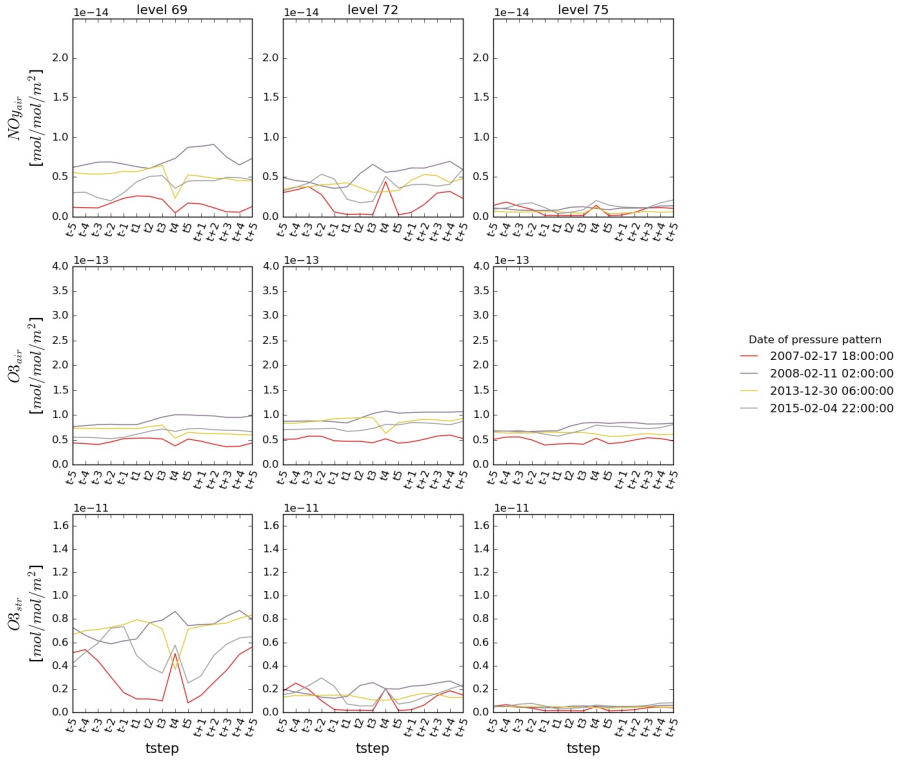


Figure C.9: Temporal development of area normalized mixing ratios of $NO_{y_{air}}$ (top), $O_{3_{air}}$ (middle) and $O_{str}$ (bottom) in weather patterns found in Region 2 with lifetime T5.

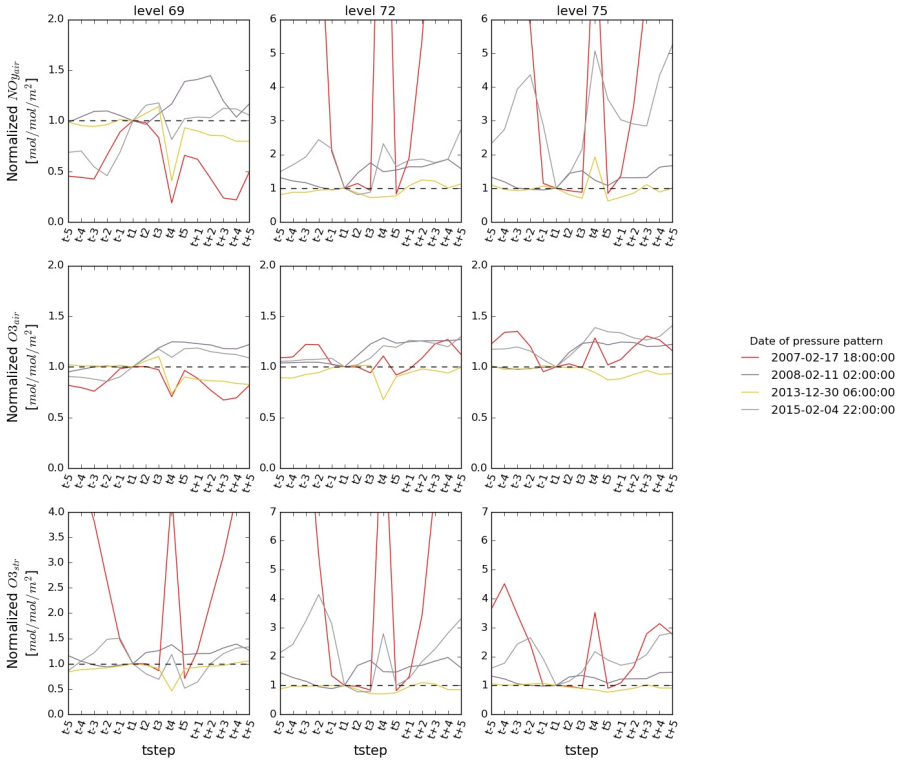


Figure C.10: Temporal development of area normalized mixing ratios of $NO_{y_{air}}$ (top), $O_{3_{air}}$ (middle) and $O_{str}$ (bottom) in weather patterns found in Region 2 with lifetime T5. These mixing ratios have been normalized with respect to the mixing ratio at $t_1$.

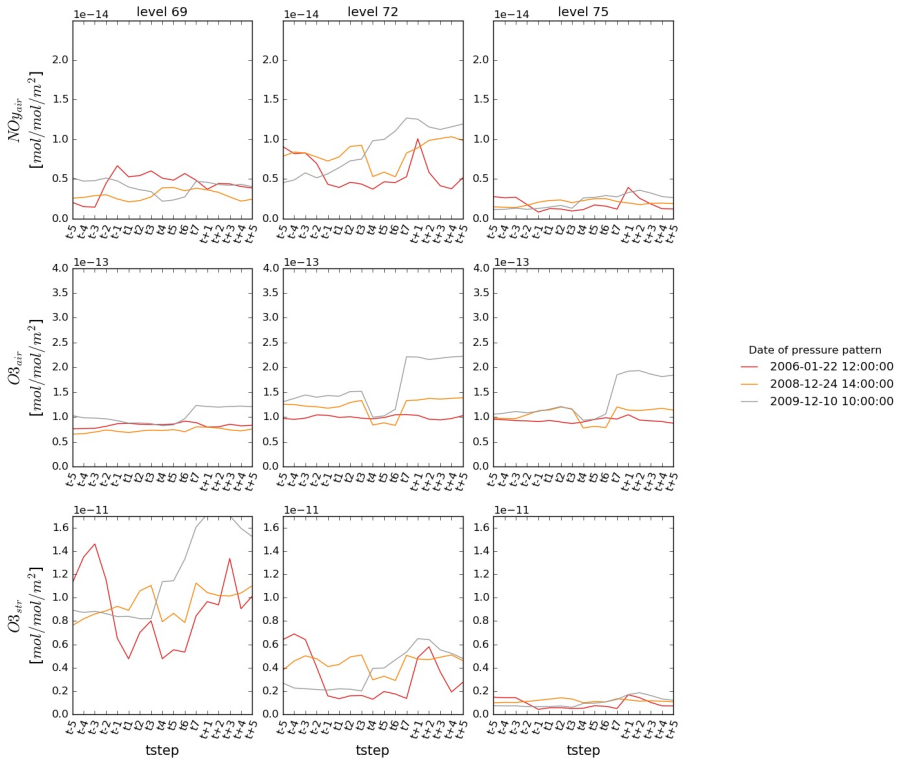


Figure C.11: Temporal development of area normalized mixing ratios of $NO_{y_{air}}$ (top), $O_{3_{air}}$ (middle) and $O_{str}$ (bottom) in weather patterns found in Region 2 with lifetime T7.

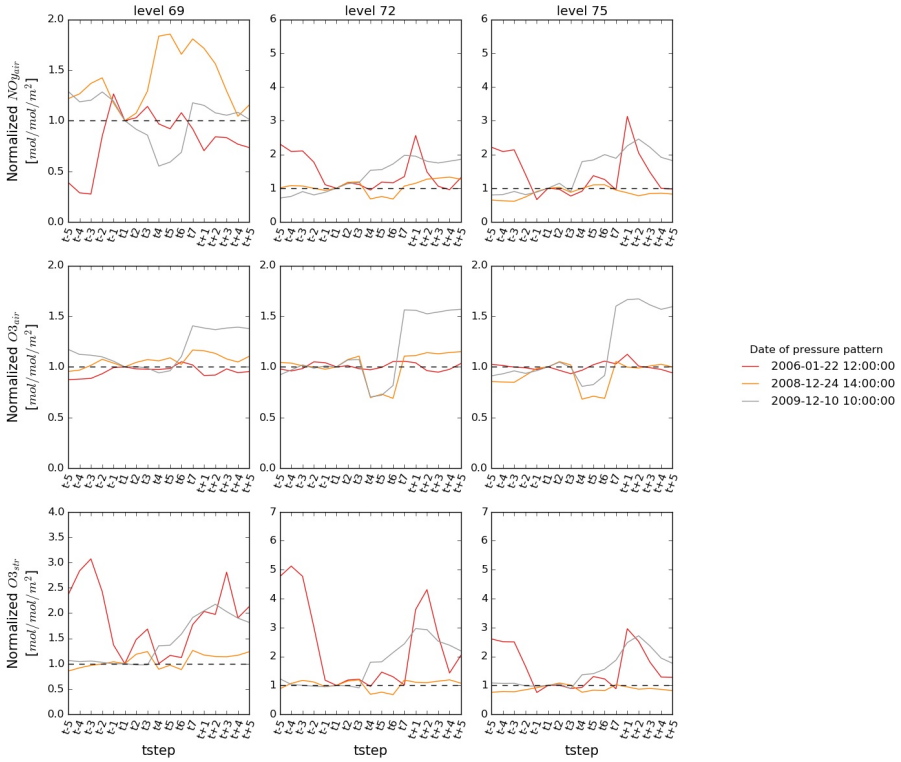


Figure C.12: Temporal development of area normalized mixing ratios of $NO_{y_{air}}$ (top), $O_{3_{air}}$ (middle) and $O_{str}$ (bottom) in weather patterns found in Region 2 with lifetime T7. These mixing ratios have been normalized with respect to the mixing ratio at $t_1$.

# D

# Aviation $NO_y$ and $O_3$ for Region 1 and 2 with respect to weather variables

In this appendix all graphs depicting the variability of aviation $NO_y$ and $O_3$ with respect to relative humidity, dry air temperature, and potential vorticity are included.

## D.1. Region 1

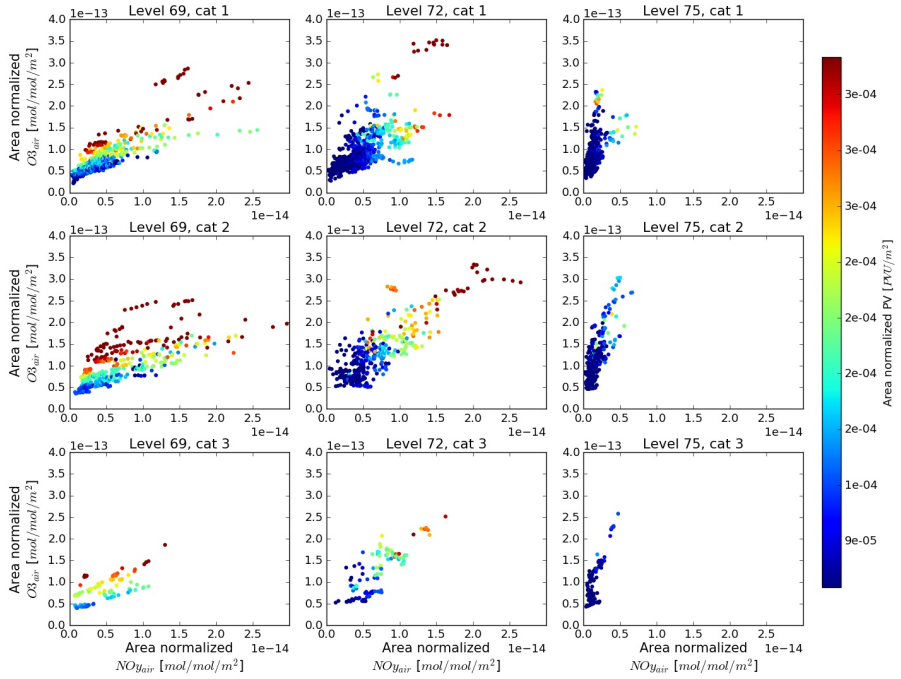


Figure D.1: Region 1: $NO_{y_{air}}$ versus $O_{3_{air}}$ with respect to potential vorticity

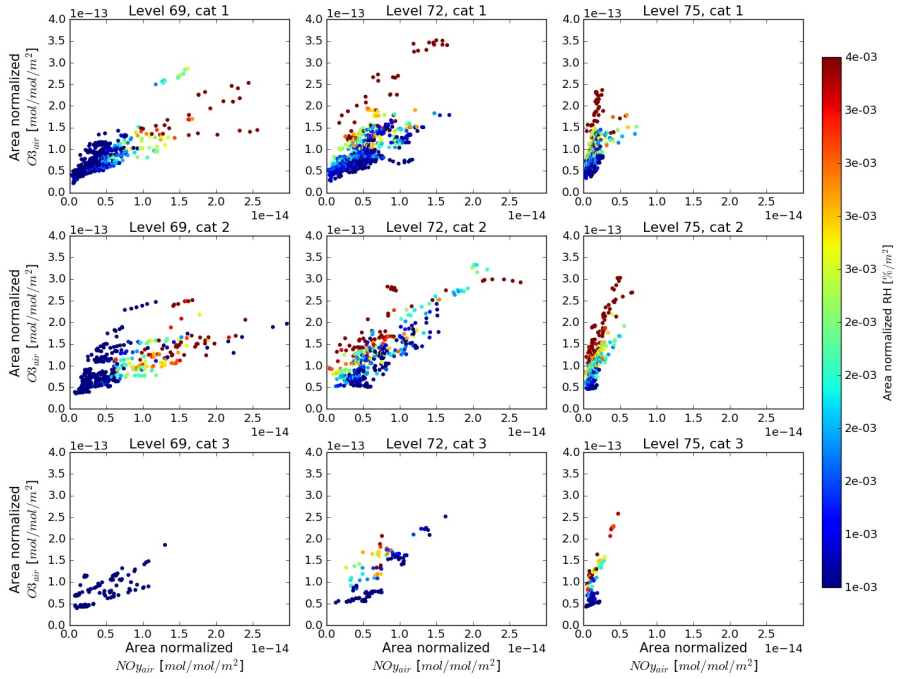


Figure D.2: Region 1: $NO_{y_{air}}$ versus $O_{3_{air}}$ with respect to relative humidity

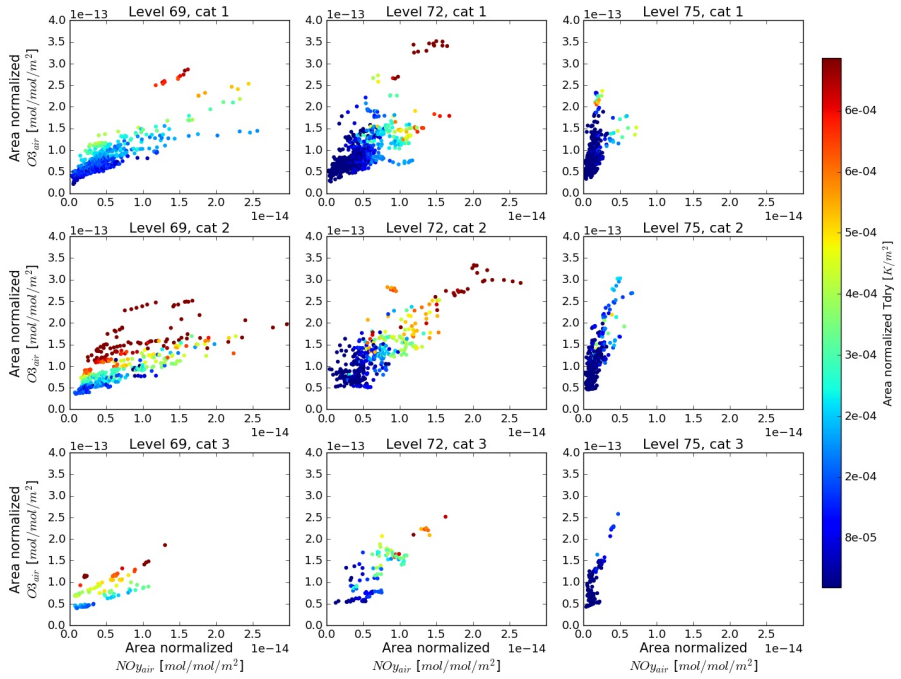


Figure D.3: Region 1: $NO_{y_{air}}$ versus $O_{3_{air}}$ with respect to dry air temperature

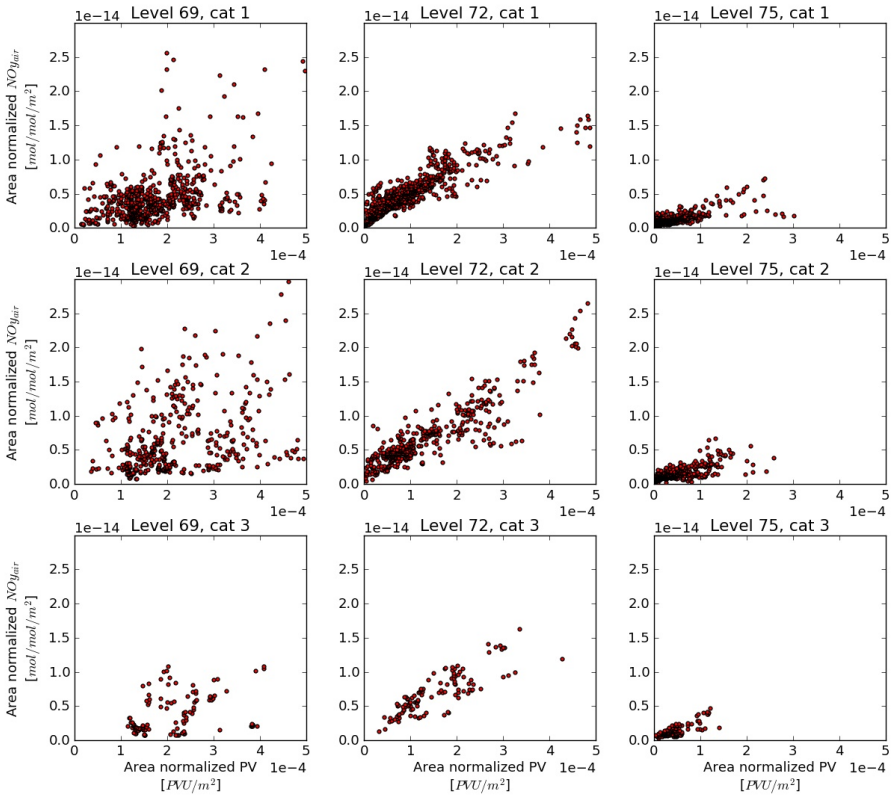


Figure D.4: Region 1: Potential vorticity versus $NO_{y_{air}}$

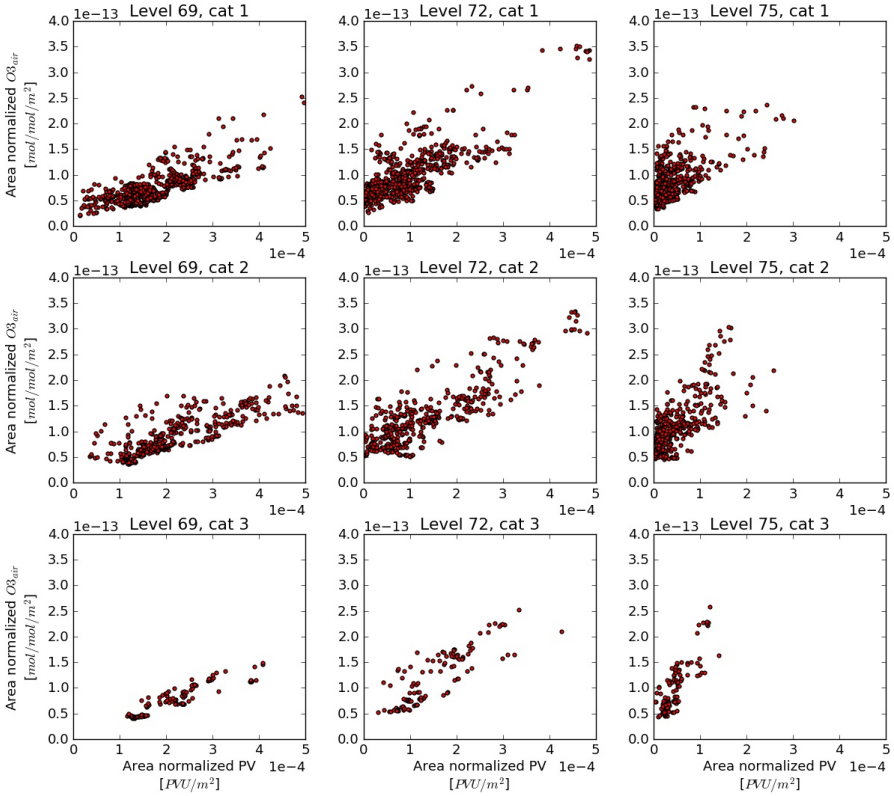


Figure D.5: Region 1: Potential vorticity versus $O_{3_{air}}$

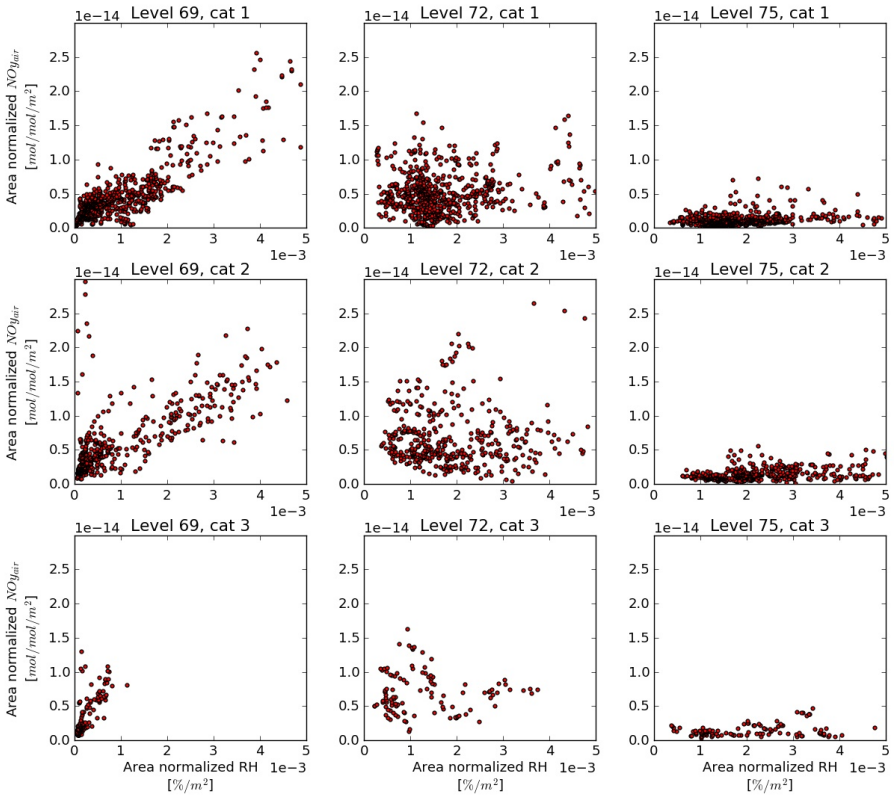


Figure D.6: Region 1: Relative humidity versus $NO_{y_{air}}$

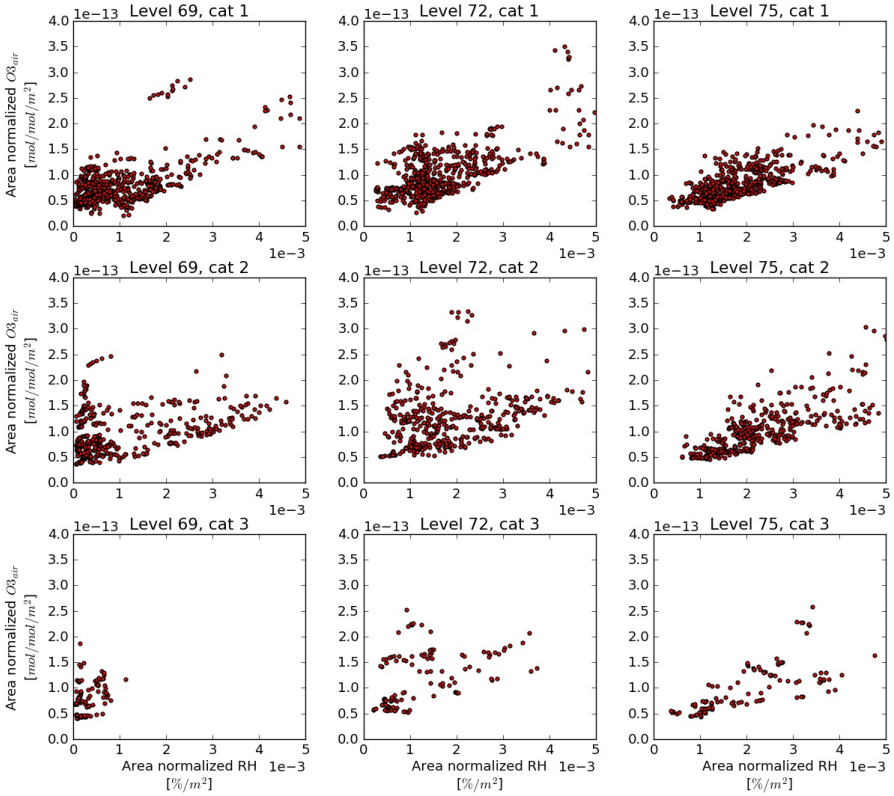


Figure D.7: Region 1: Relative humidity versus $O_{3_{air}}$

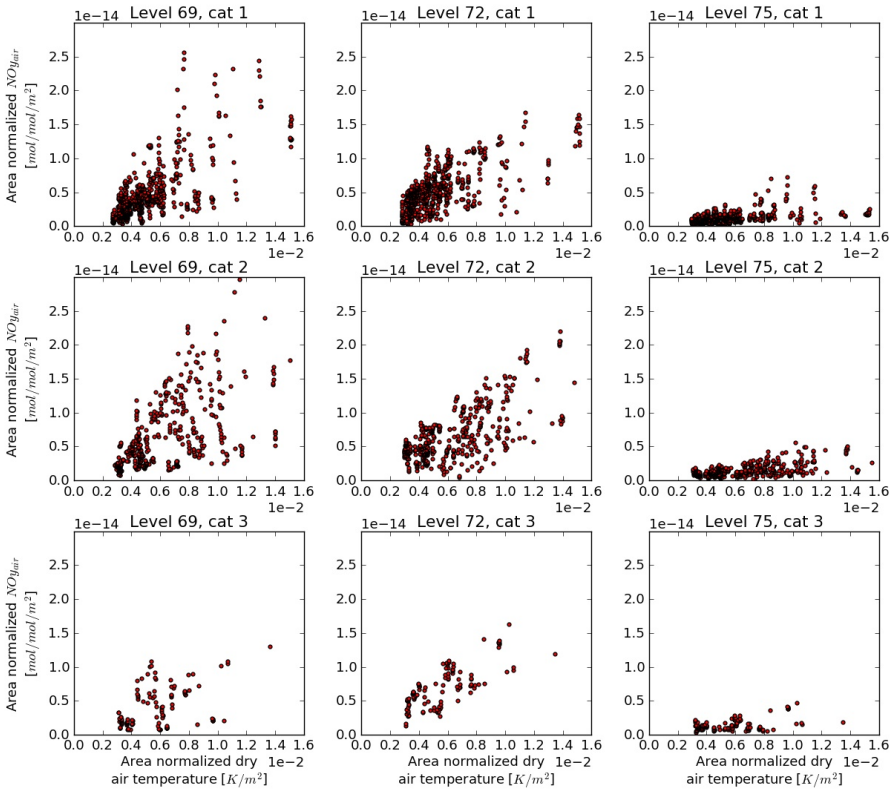


Figure D.8: Region 1: Dry air temperature versus $NO_{y_{air}}$

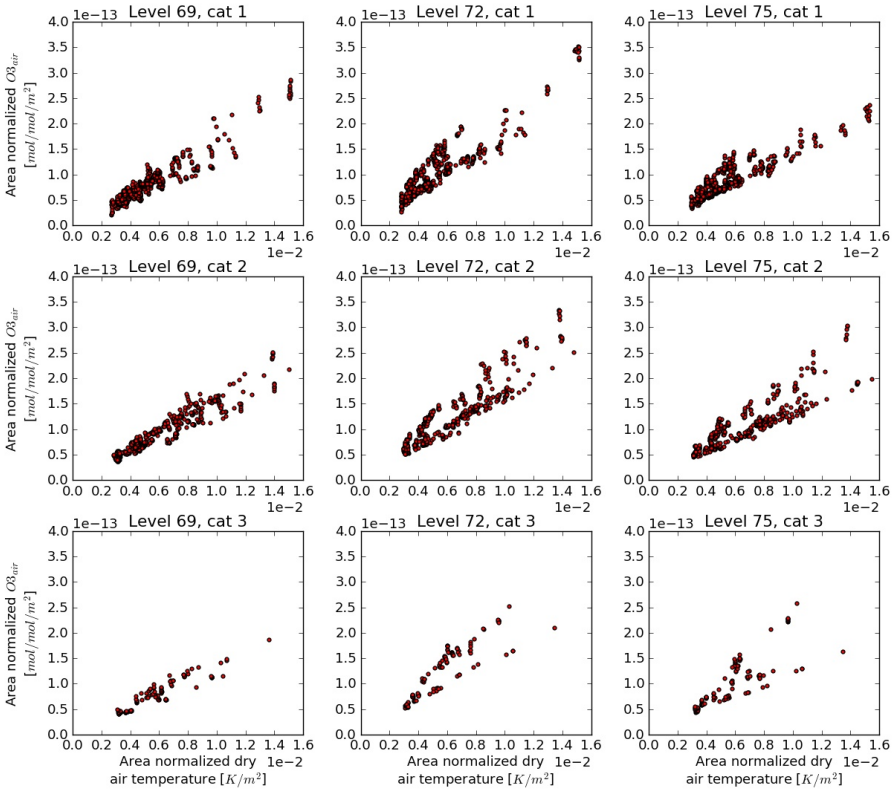


Figure D.9: Region 1: Dry air temperature versus $O_{3_{air}}$

## D.2. Region 2

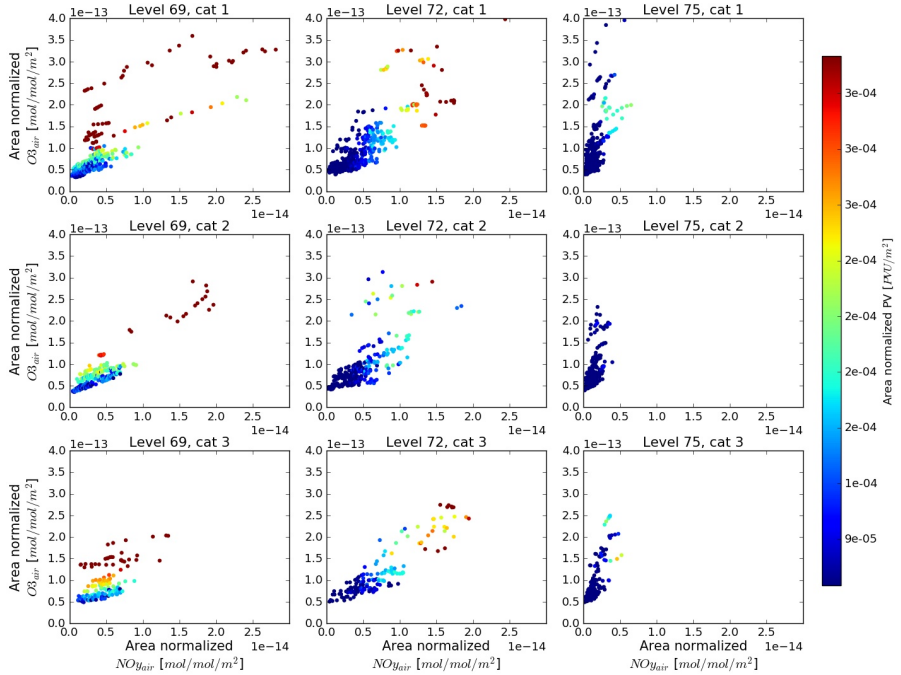


Figure D.10: Region 2: $NO_{y_{air}}$ versus $O_{3_{air}}$ with respect to potential vorticity

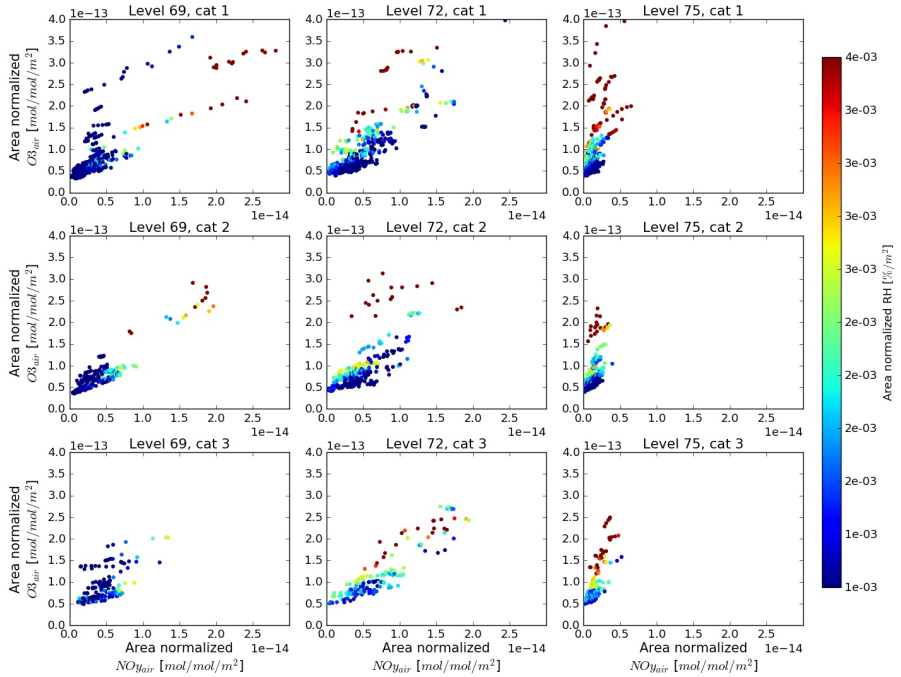


Figure D.11: Region 2: $NO_{y_{air}}$ versus $O_{3_{air}}$ with respect to relative humidity

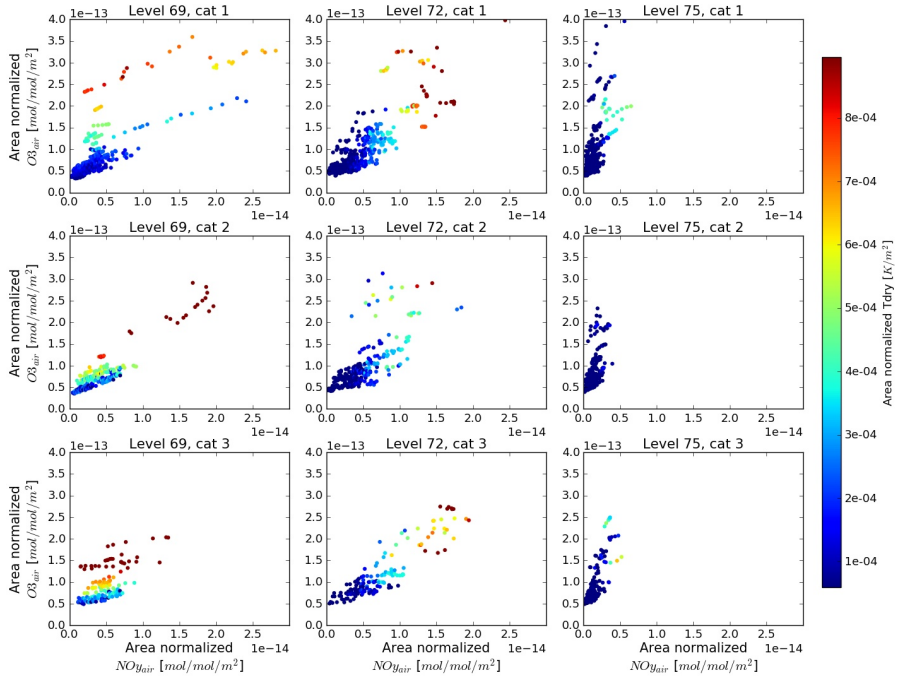


Figure D.12: Region 2: $NO_{y_{air}}$ versus $O_{3_{air}}$ with respect to dry air temperature

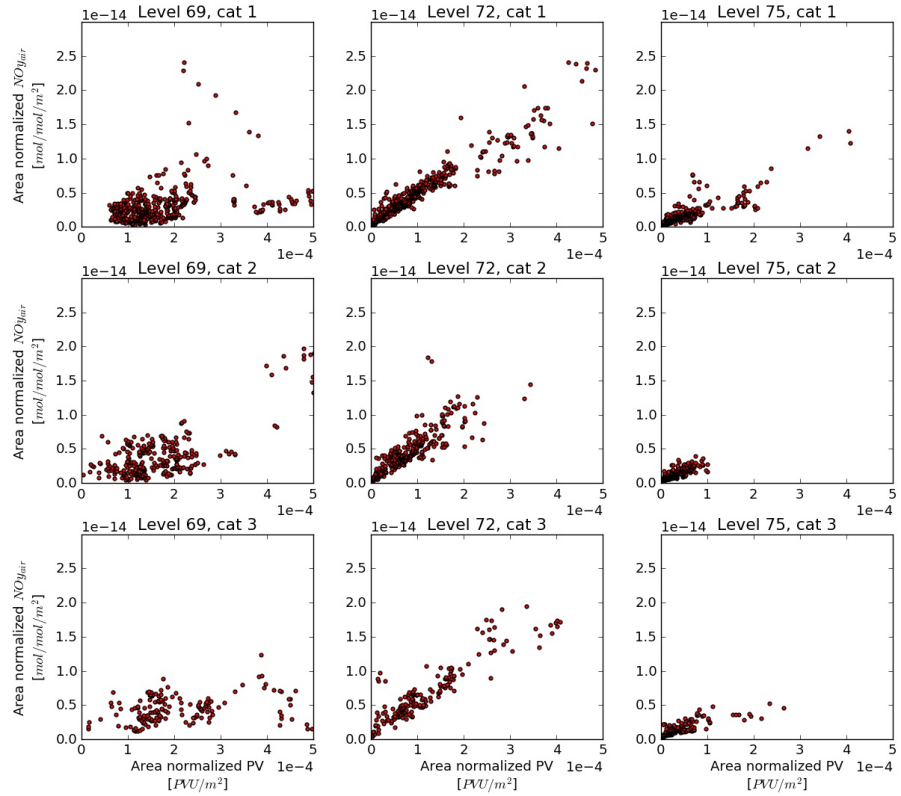


Figure D.13: Region 2: Potential vorticity versus $NO_{y_{air}}$

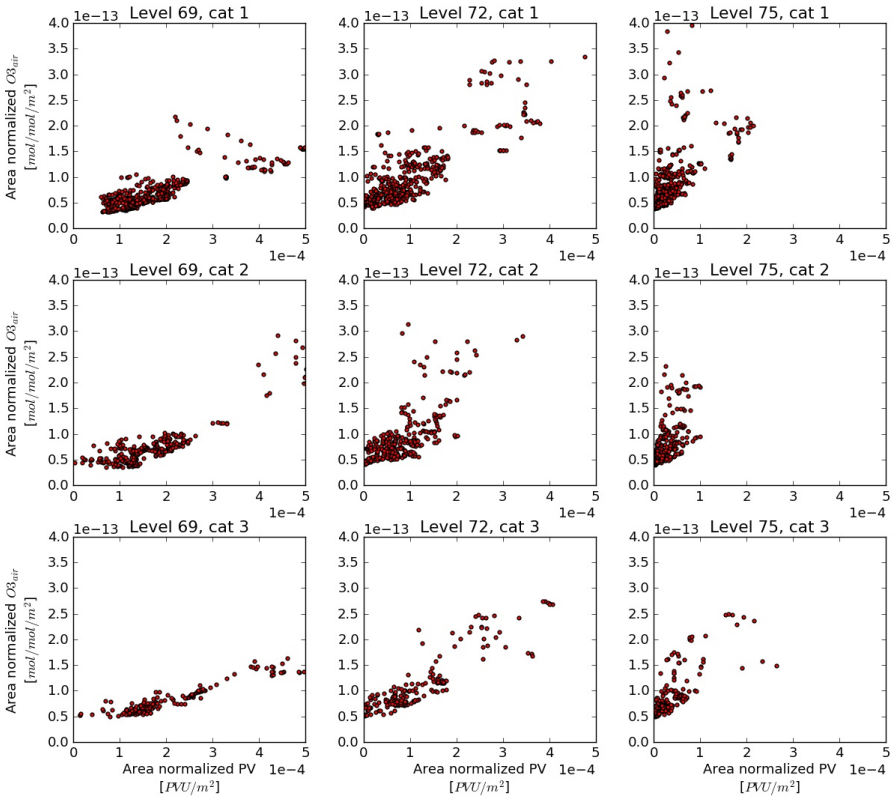


Figure D.14: Region 2: Potential vorticity versus $O_{3_{air}}$

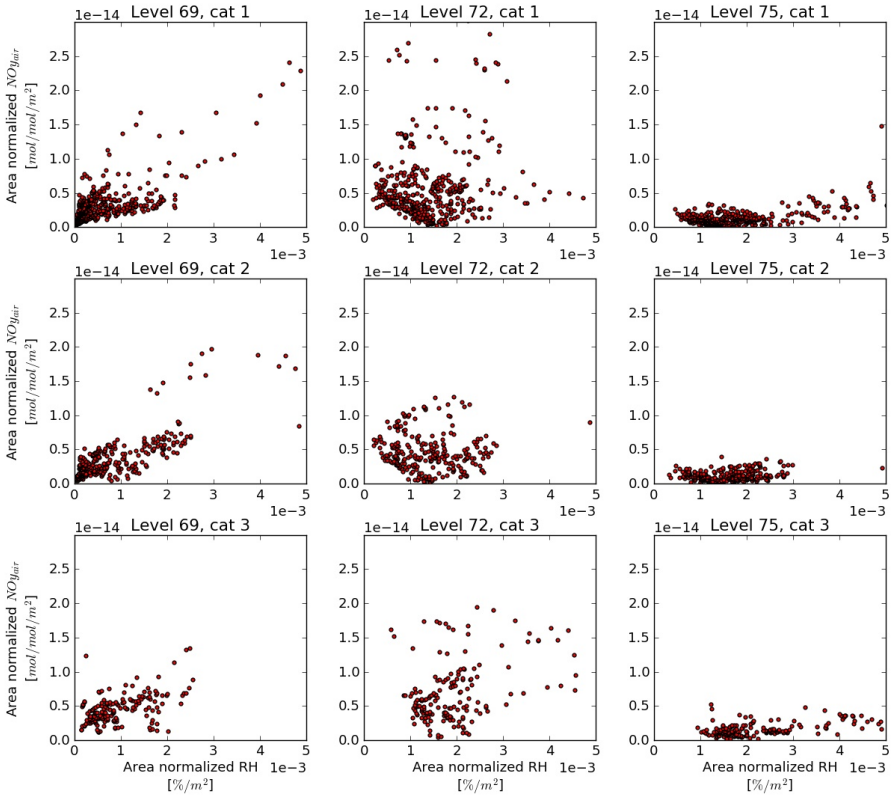


Figure D.15: Region 2: Relative humidity versus $NO_{y_{air}}$

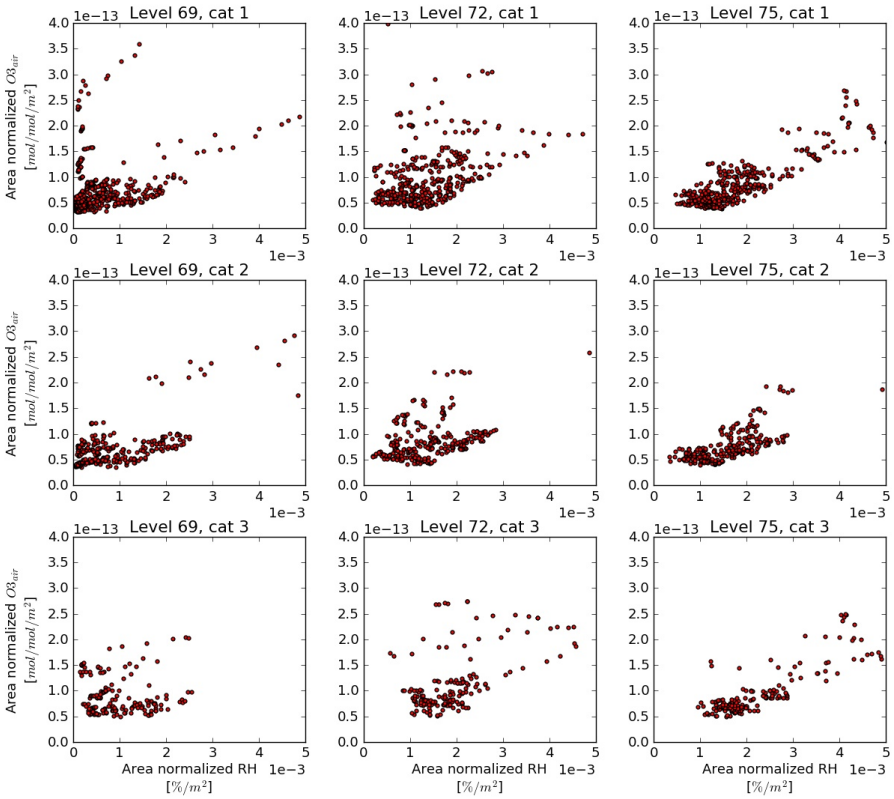


Figure D.16: Region 2: Relative humidity versus $O_{3_{air}}$

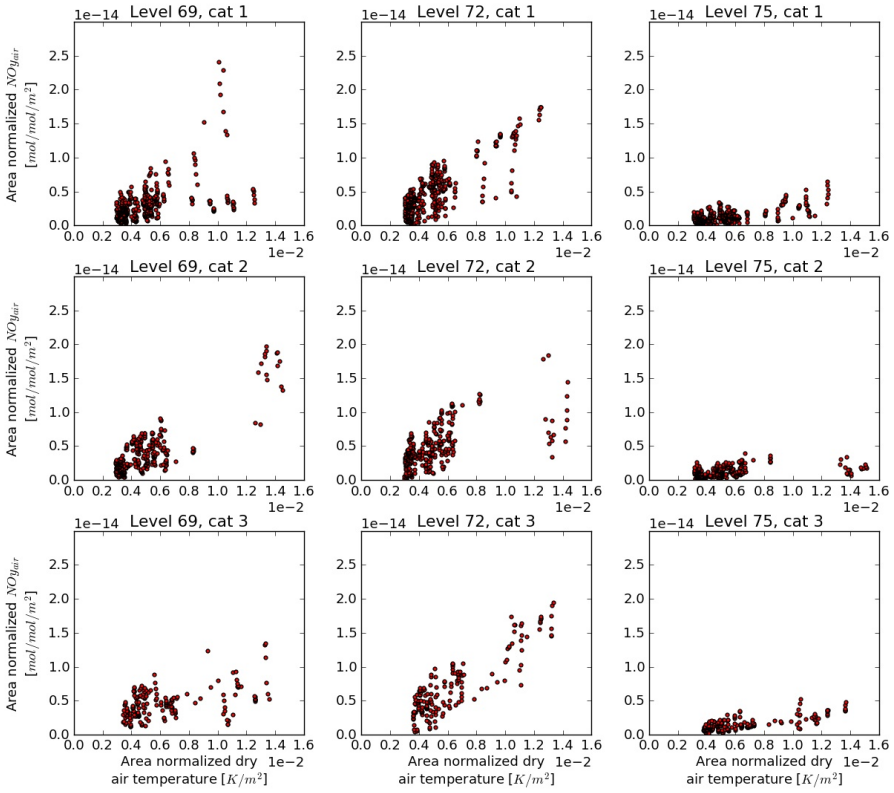


Figure D.17: Region 2: Dry air temperature versus $NO_{y_{air}}$

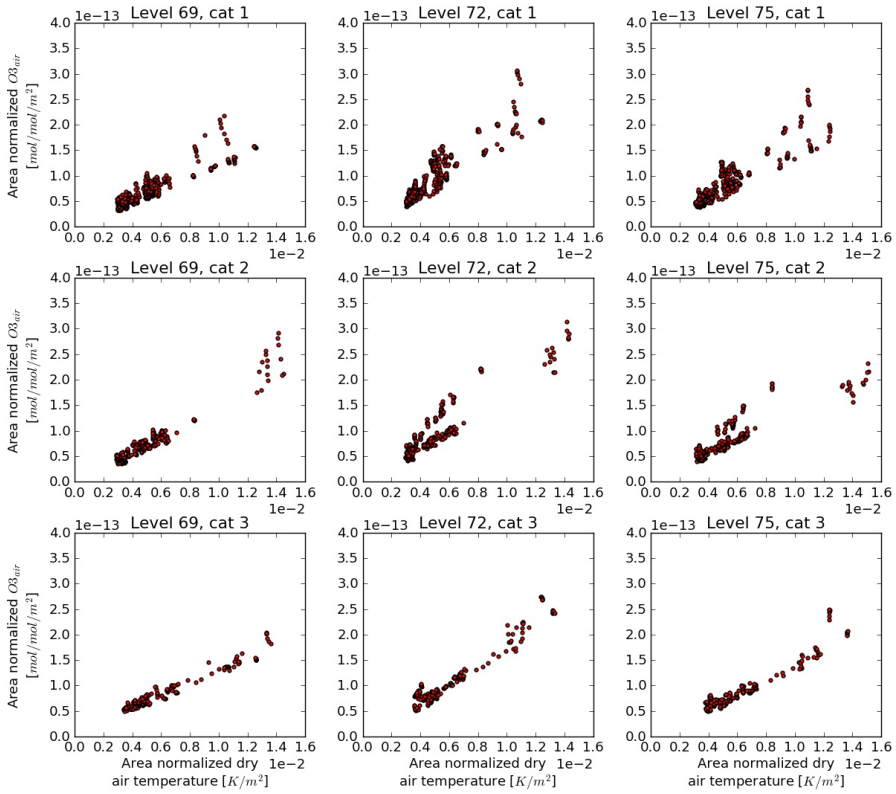


Figure D.18: Region 2: Dry air temperature versus $O_{3_{air}}$

# D.3. Region 3

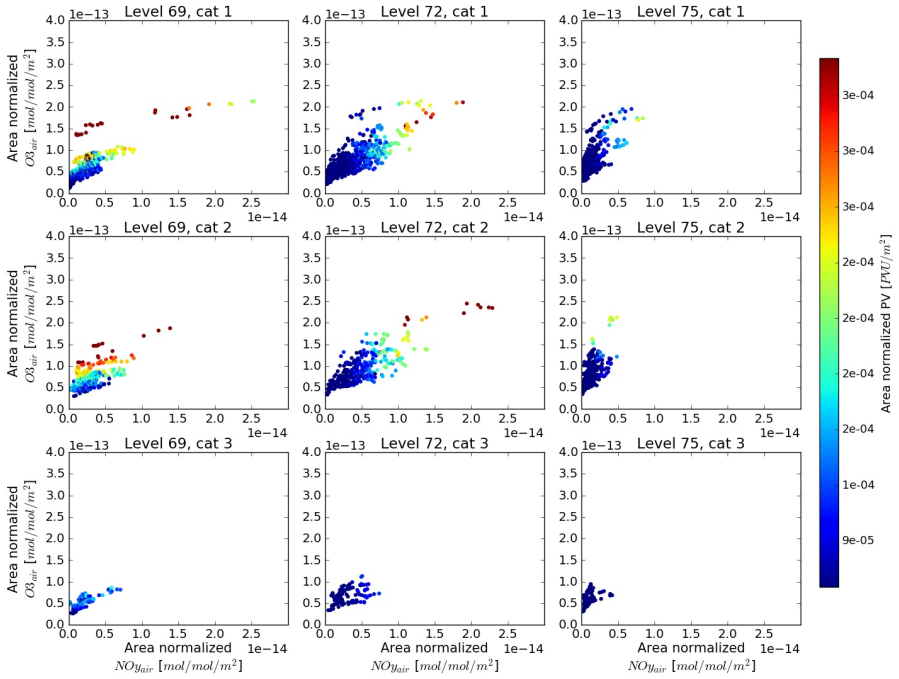


Figure D.19: Region 3: $NO_{y_{air}}$ versus $O_{3_{air}}$ with respect to potential vorticity

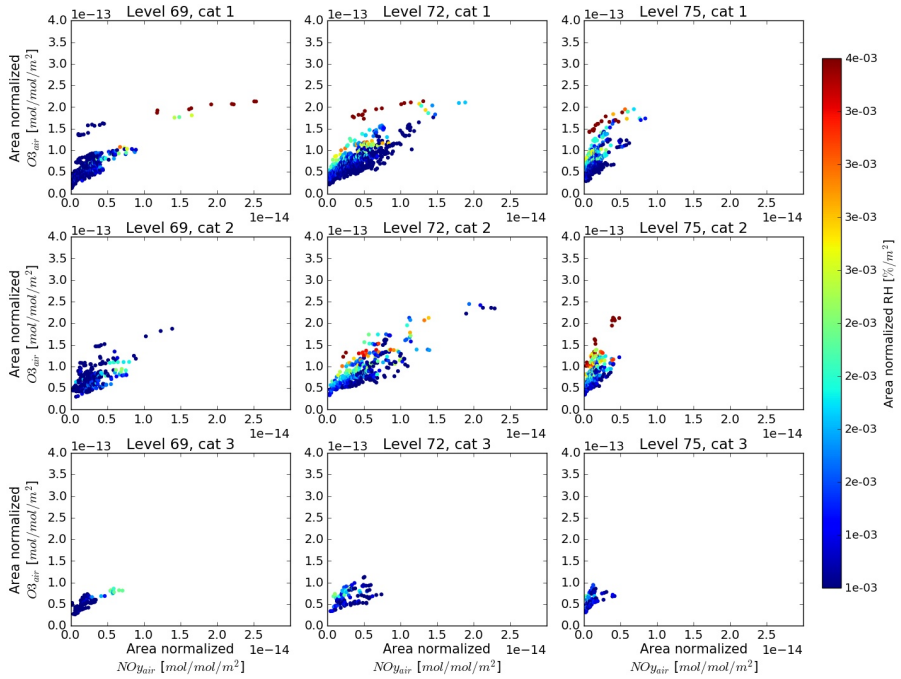


Figure D.20: Region 3: $NO_{y_{air}}$ versus $O_{3_{air}}$ with respect to relative huEASTity

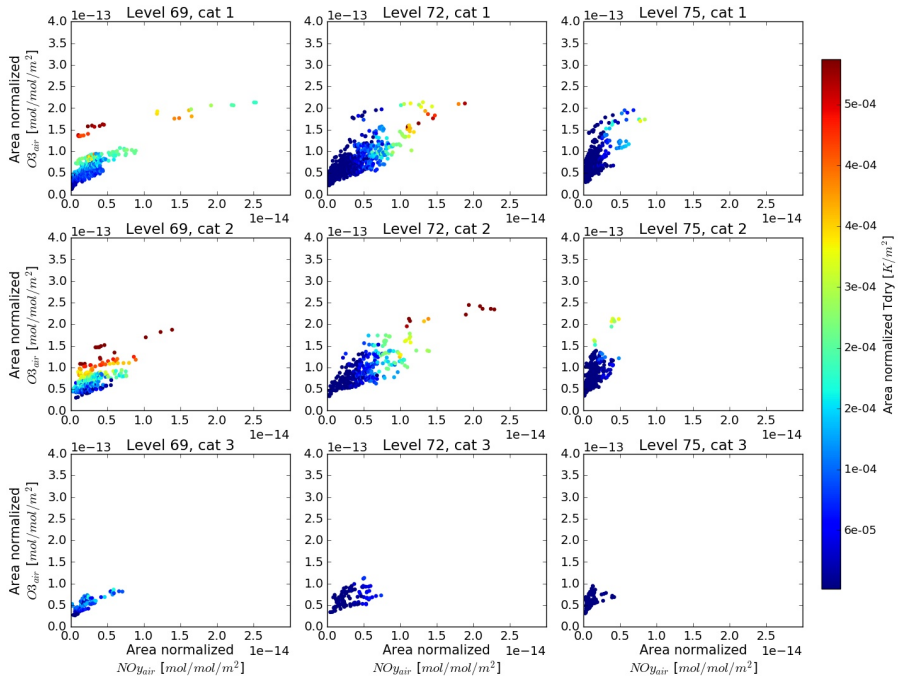


Figure D.21: Region 3: $NO_{y_{air}}$ versus $O_{3_{air}}$ with respect to dry air temperature

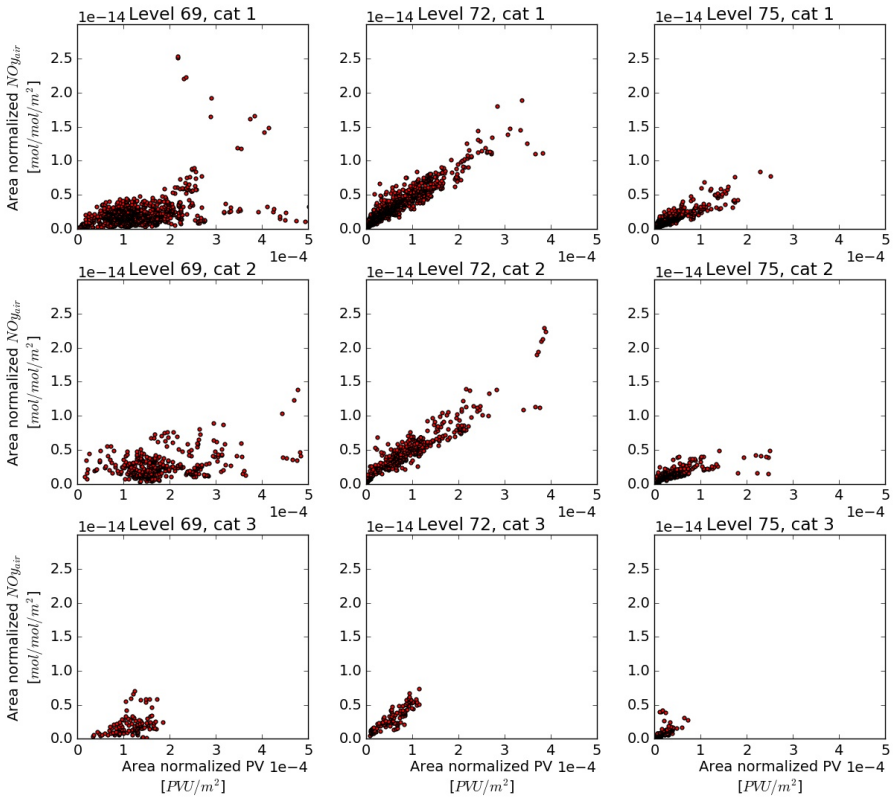


Figure D.22: Region 3: Potential vorticity versus $NO_{y_{air}}$

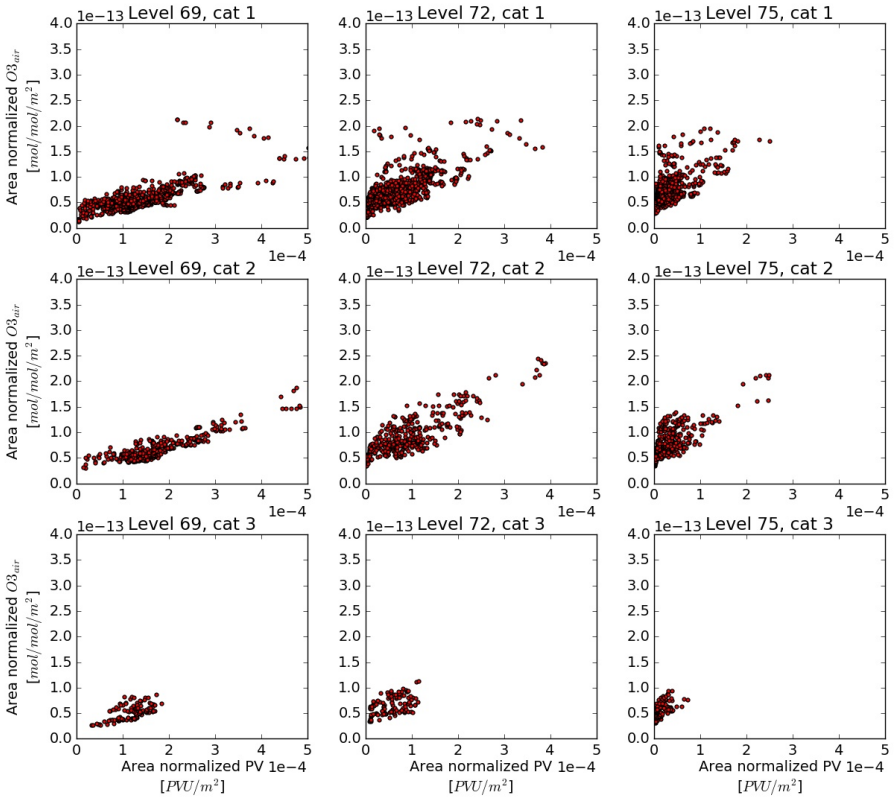


Figure D.23: Region 3: Potential vorticity versus $O3_{air}$

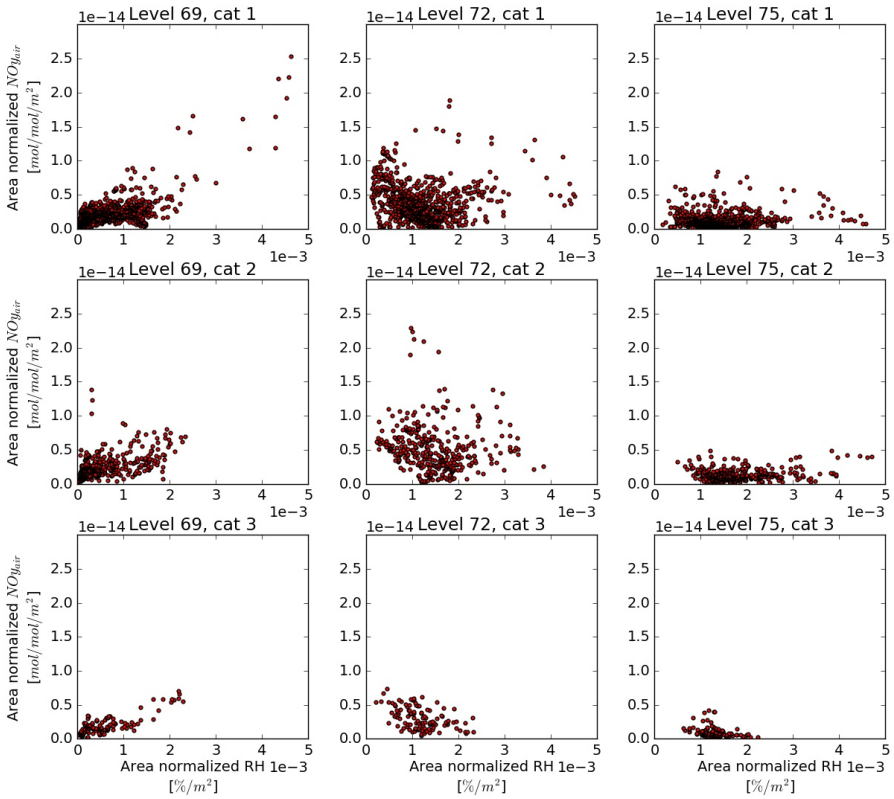


Figure D.24: Region 3: Relative huEASTity versus $NO_{y_{air}}$

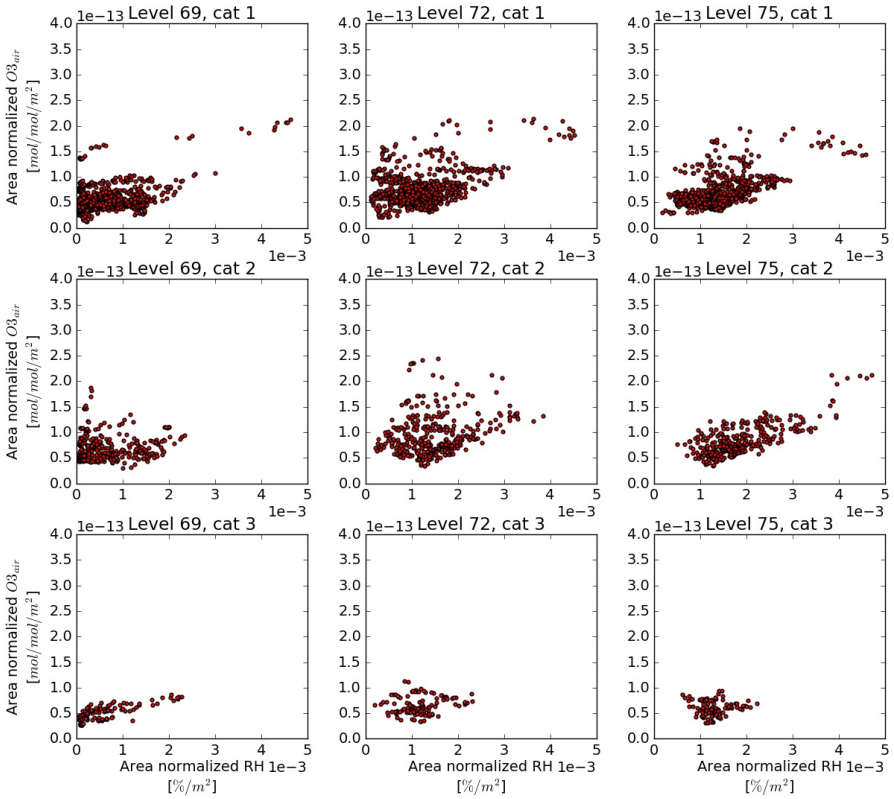


Figure D.25: Region 3: Relative huEASTity versus $O_{3_{air}}$

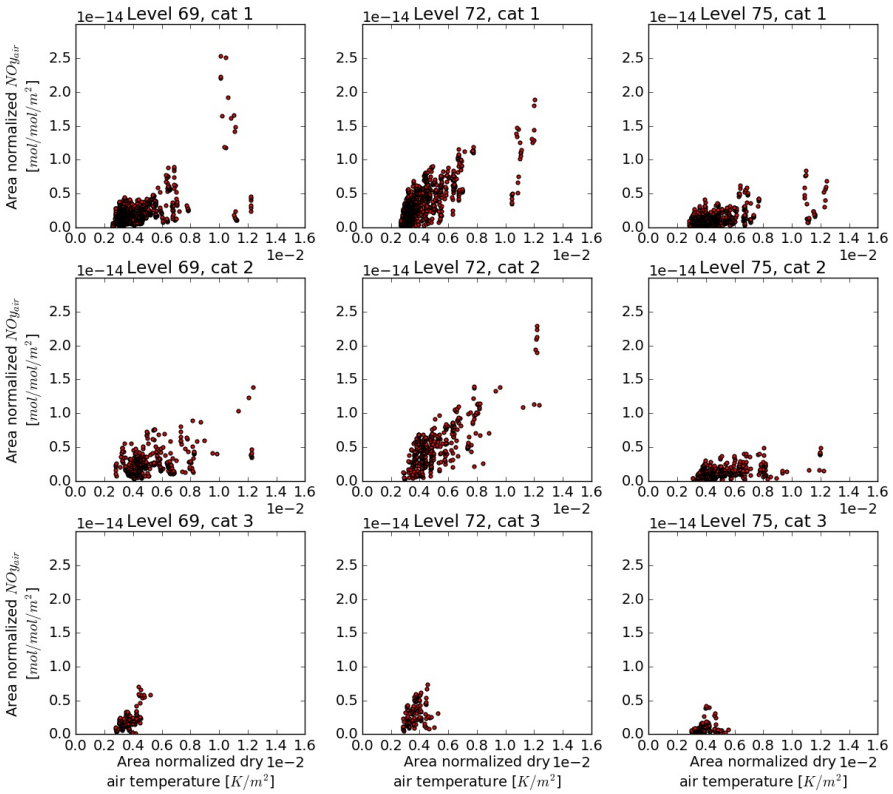


Figure D.26: Region 3: Dry air temperature versus $NO_{y_{air}}$

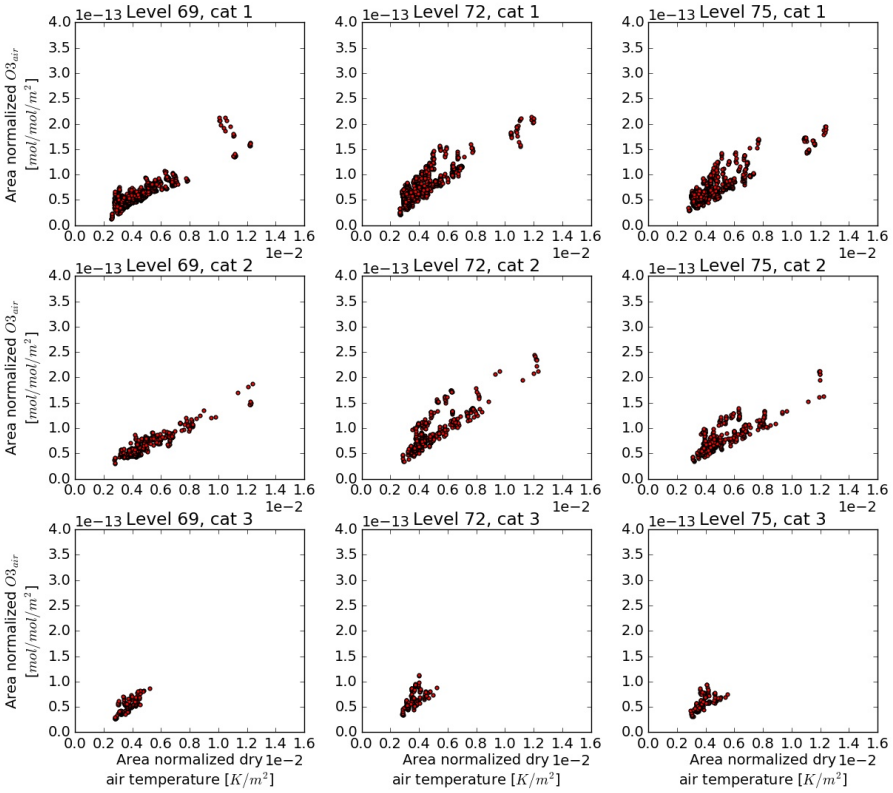


Figure D.27: Region 3: Dry air temperature versus $O_{3_{air}}$

# E

# Ozone trend comparative graphs for Region 2 and 3

In this appendix the comparative graphs for Region 2 and 3 are given. These trendline exhibit a similar pattern as was found for Region 1, therefore the conclusions drawn in Chapter 10 are valid for Region 2 and 3 as well.

## E.1. Region 2

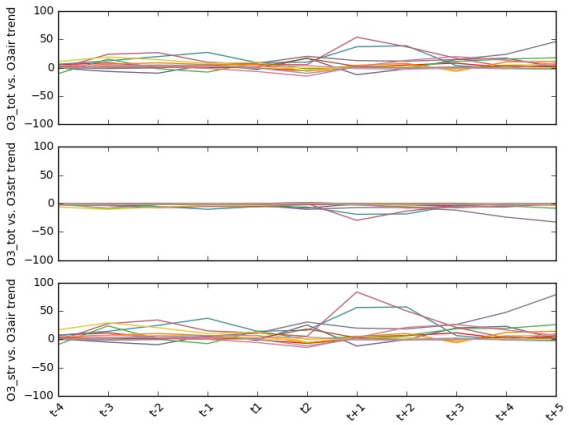


Figure E.1: Temporal development of normalized mixing ratios of $NO_{y_{air}}$ (top), $O_{3_{air}}$ (middle) and $O_{str}$ (bottom) in weather patterns found in Region 2 with lifetime T2, level 69.

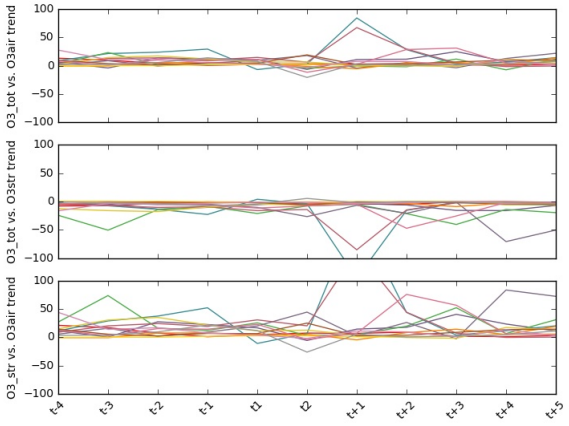


Figure E.2: Temporal development of normalized mixing ratios of $NO_{y_{air}}$ (top), $O_{3_{air}}$ (middle) and $O_{str}$ (bottom) in weather patterns found in Region 2 with lifetime T2, level 72.

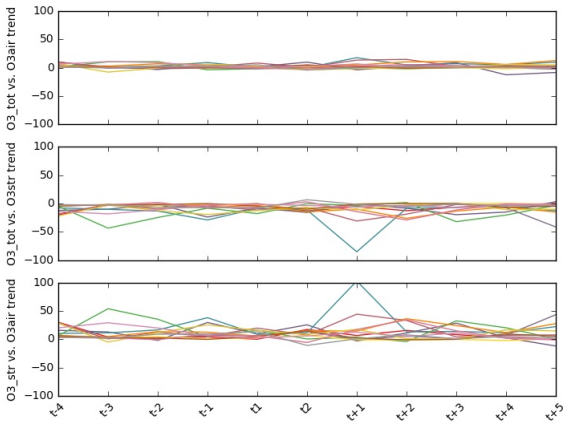


Figure E.3: Temporal development of normalized mixing ratios of $NO_{y_{air}}$ (top), $O_{3_{air}}$ (middle) and $O_{str}$ (bottom) in weather patterns found in Region 2 with lifetime T2, level 75.

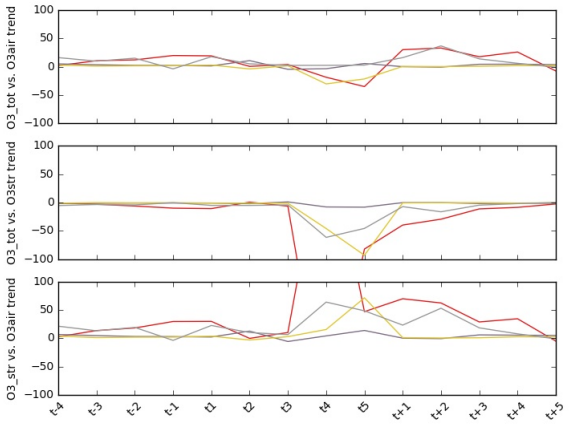


Figure E.4: Temporal development of normalized mixing ratios of $NO_{y_{air}}$ (top), $O_{3_{air}}$ (middle) and $O_{str}$ (bottom) in weather patterns found in Region 2 with lifetime T5, level 69.

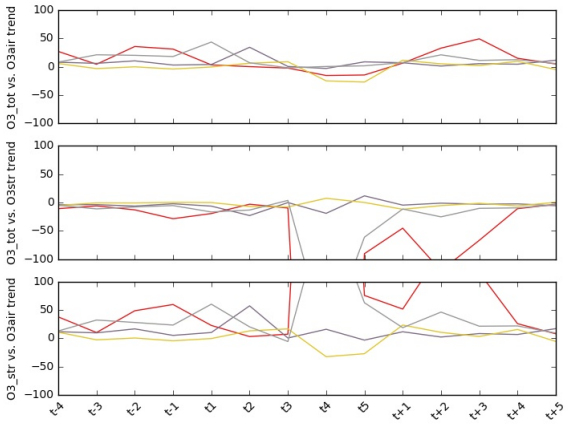


Figure E.5: Temporal development of normalized mixing ratios of $NO_{y_{air}}$ (top), $O_{3_{air}}$ (middle) and $O_{str}$ (bottom) in weather patterns found in Region 2 with lifetime T5, level 72.

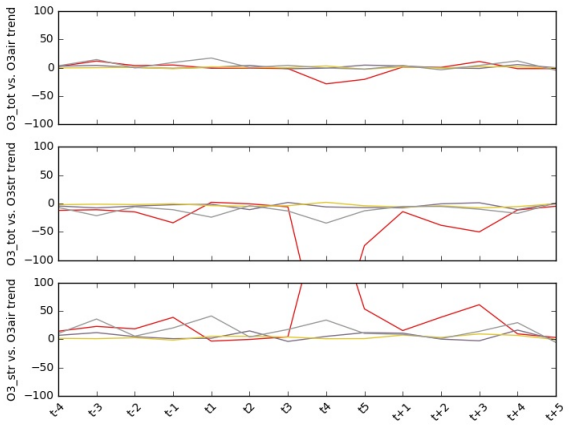


Figure E.6: Temporal development of normalized mixing ratios of $NO_{y_{air}}$ (top), $O_{3_{air}}$ (middle) and $O_{str}$ (bottom) in weather patterns found in Region 2 with lifetime T5, level 75.

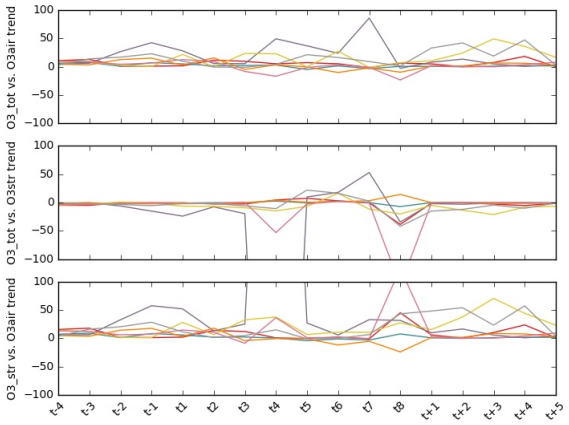


Figure E.7: Temporal development of normalized mixing ratios of $NO_{y_{air}}$ (top), $O_{3_{air}}$ (middle) and $O_{str}$ (bottom) in weather patterns found in Region 2 with lifetime T8, level 69.

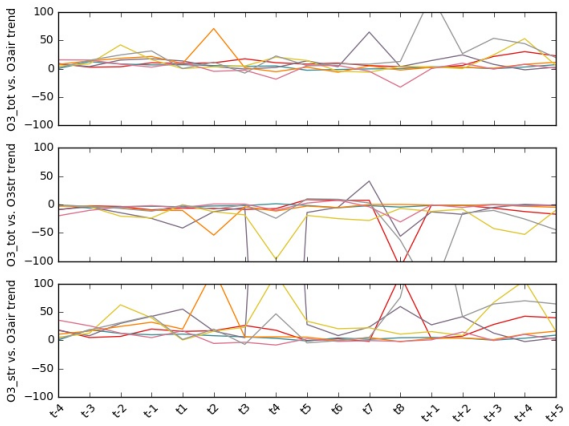


Figure E.8: Temporal development of normalized mixing ratios of $NO_{y_{air}}$ (top), $O_{3_{air}}$ (middle) and $O_{str}$ (bottom) in weather patterns found in Region 2 with lifetime T8, level 72.

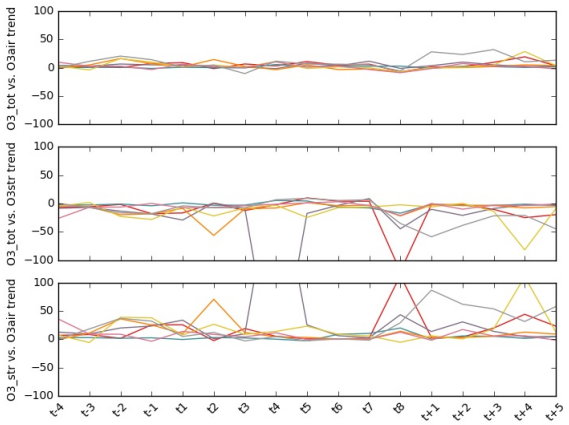


Figure E.9: Temporal development of normalized mixing ratios of $NO_{y_{air}}$ (top), $O_{3_{air}}$ (middle) and $O_{str}$ (bottom) in weather patterns found in Region 2 with lifetime T8, level 75.

## E.2. Region 3

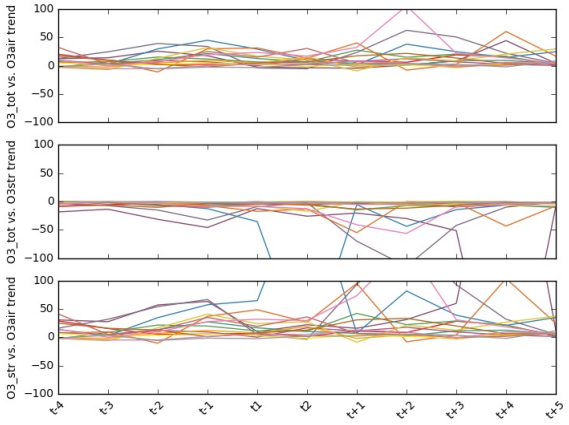


Figure E.10: Temporal development of normalized mixing ratios of $NO_{y_{air}}$ (top), $O_{3_{air}}$ (middle) and $O_{str}$ (bottom) in weather patterns found in Region 3 with lifetime T2, level 69.

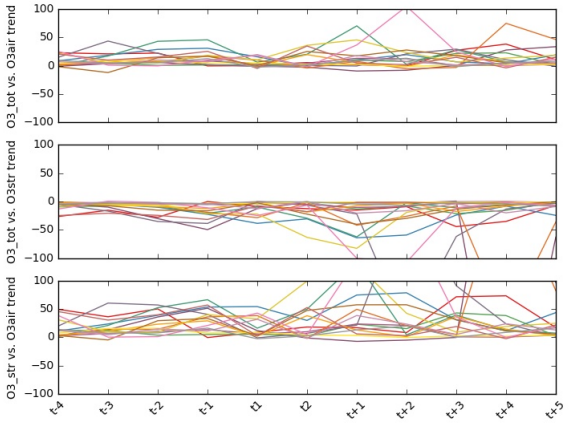


Figure E.11: Temporal development of normalized mixing ratios of $NO_{y_{air}}$ (top), $O_{3_{air}}$ (middle) and $O_{str}$ (bottom) in weather patterns found in Region 3 with lifetime T2, level 72.

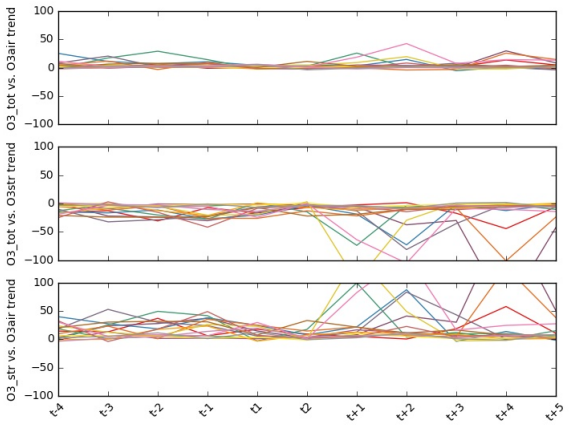


Figure E.12: Temporal development of normalized mixing ratios of $NO_{y_{air}}$ (top), $O_{3_{air}}$ (middle) and $O_{str}$ (bottom) in weather patterns found in Region 3 with lifetime T2, level 75.

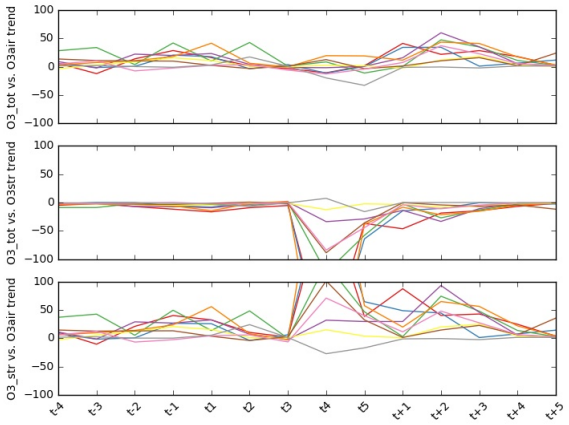


Figure E.13: Temporal development of normalized mixing ratios of $NO_{y_{air}}$ (top), $O_{3_{air}}$ (middle) and $O_{str}$ (bottom) in weather patterns found in Region 3 with lifetime T5, level 69.

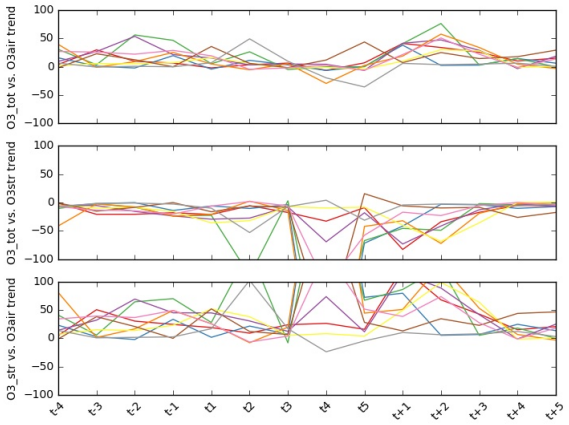


Figure E.14: Temporal development of normalized mixing ratios of $NO_{y_{air}}$ (top), $O_{3_{air}}$ (middle) and $O_{str}$ (bottom) in weather patterns found in Region 3 with lifetime T5, level 72.

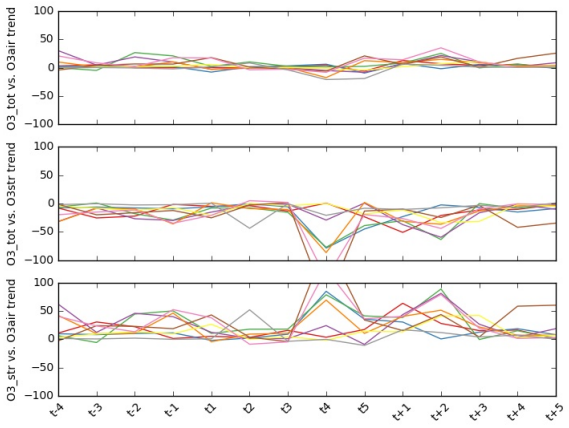


Figure E.15: Temporal development of normalized mixing ratios of $NOy_{air}$ (top), $O3_{air}$ (middle) and $O_{str}$ (bottom) in weather patterns found in Region 3 with lifetime T5, level 75.

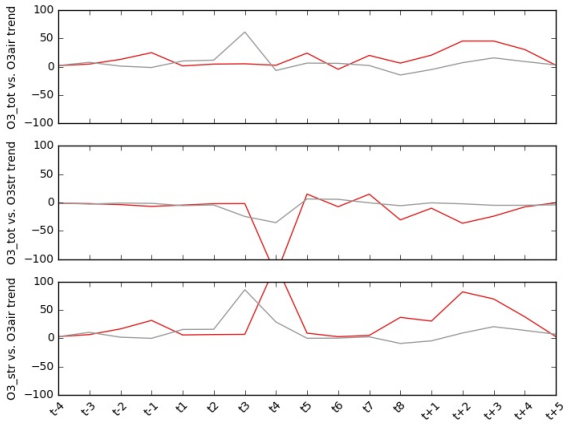


Figure E.16: Temporal development of normalized mixing ratios of $NOy_{air}$ (top), $O3_{air}$ (middle) and $O_{str}$ (bottom) in weather patterns found in Region 3 with lifetime T8, level 69.

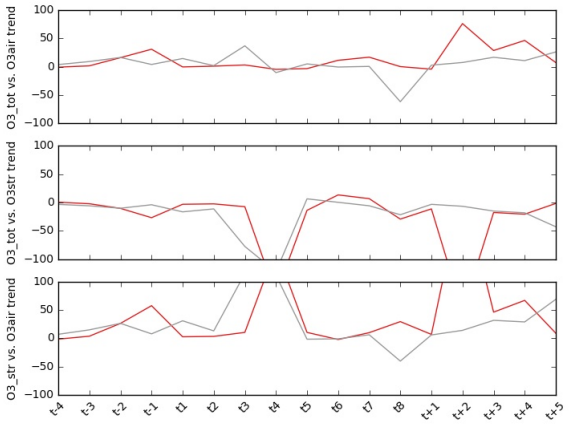


Figure E.17: Temporal development of normalized mixing ratios of $NOy_{air}$ (top), $O3_{air}$ (middle) and $O_{str}$ (bottom) in weather patterns found in Region 3 with lifetime T5, level 72.

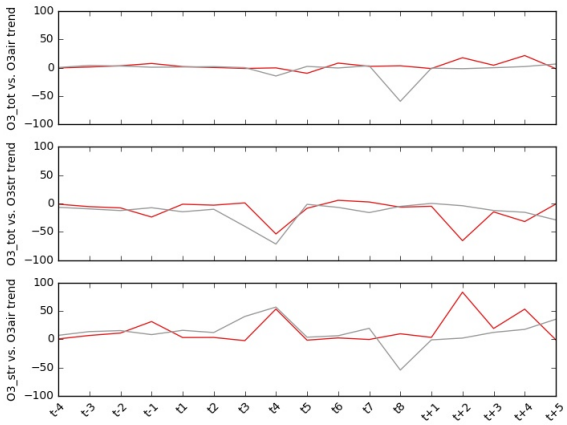


Figure E.18: Temporal development of normalized mixing ratios of $NO_{y_{air}}$ (top), $O_{3_{air}}$ (middle) and $O_{str}$ (bottom) in weather patterns found in Region 3 with lifetime T5, level 75.